Synthesis of nanoparticles in the gas phase for functional applications

Frank Einar Kruis

Synthesis of nanoparticles in the gas phase for functional applications

Vom Fachbereich Elektrotechnik der

Gerhard-Mercator-Universität Duisburg

Zur Erlangung der Lehrbefähigung im Lehrgebiet

Prozeßtechnik nanostrukturierter Materialien

genehmigte Habilitationsschrift

von

Dr.-Ing. Frank Einar Kruis

aus

Bergen op Zoom (Niederlande)

Table of Contents

1. Introduction

Nanoparticles have attracted the attention of an increasing number of researchers from several disciplines in the last ten years. The term ‘nanoparticle’ came into frequent use in the early 1990s together with the related concepts, ‘nanoscaled’ or ‘nanosized’ particle. Until then, the more general terms submicron and ultrafine particles were used. The term nanoparticle is generally used now in materials science community to indicate particles with diameters smaller than 100 nm (El-Shall and Edelstein, 1996). The term nanoparticles is used here interchangeably to refer to particles in aerosols and particles in other situations respectively. A closely related but not identical concept, ‘cluster’, indicates smaller nanoparticles with less than 10^4 molecules or atoms, corresponding to a diameter of only a few nanometers.

Nanomaterials or nanostructured materials have a characteristic length scale of less than 100 nm, and therefore also include uni-axially stacked multilayers and coatings. A further subset can be distinguished in these nanomaterials, i.e. the nanophase materials which have a three-dimensional structure with a domain size smaller than 100 nm. Nanophase materials are usually produced by compaction of a powder of nanoparticles. They are characterized by a large number of grain boundary interfaces in which the local atomic arrangements are different from those of the crystal lattice (Weissmüller, 1996).

The small size of nanoparticles, which is responsible for the different properties (electronic, optical, electrical, magnetic, chemical and mechanical) of nanoparticles and nanostructured materials with respect to the bulk material, makes them suitable for new applications. Having a size between the molecular and bulk solid-state structures, nanoparticles have hybrid properties which are incompletely understood today, creating a challenge for theoreticians as well. Some examples of these properties are lower melting temperature (Goldstein *et al.*, 1992), increased solid-solid phase transition pressure (Tolbert and Alivisatos, 1995), lower effective Debye temperature (Fujita *et al.*, 1976), decreased ferroelectric phase transition temperature (Ishikawa *et al.*, 1988), higher self-diffusion coefficient (Horvath *et al.*, 1987), changed thermophysical properties (Qin *et al.*, 1996) and catalytic activity (Sarkas *et al.*, 1993).

‘Nanocomposites’ consist of nanoparticles dispersed in an continuous matrix, creating a compositional heterogeneity of the final structure. The nanocomposites usually involve a ceramic or polymeric matrix and are not restricted only to thin films. These materials show interesting properties such as alloying of normally immiscible

materials (Linderoth and Moerup, 1990) and higher critical superconductor transition temperature (Goswami *et al.*, 1993).

The size-dependent properties of nanostructured materials make them interesting for potential technological applications. This has led before the 1990s to applications such as supported nanoscale catalysts and pigments, based mainly on the large surface area to volume ratio in these systems. After 1980, a renewed interest took place in nanomaterials research. Brus (1983) suggested quantum confinement effects to occur specifically in semiconductor nanoparticles. Birringer *et al.* (1984) developed a method for synthesizing amounts of weakly agglomerated nanoparticles for producing nanophase materials with a large volume fraction of grain boundaries. Improved mechanical properties of nanophase ceramics were observed in these materials, such as increased hardness by Koch and Cho (1992). Finally, one of many other important findings was the giant magnetoresistance in nanocomposites discovered by Carey *et al.* (1992).

This Habilitation Thesis concentrates on gas-phase processes for synthesizing nanoparticles. Methods for the synthesis of nanoparticles are also being developed in other than gas-phase processes such as colloidal systems where stabilization is used to prevent coagulation (Peled, 1997). However, gas-phase processing systems may prove better in some cases because of their following inherent advantages:

- Gas-phase processes are generally purer than liquid-based processes since even the most ultra-pure water contains traces of minerals, detrimental for electronic grade semiconductors. These impurities seem to be avoidable today only in vacuum and gas phase systems. Colloid chemistry has the advantage that nanoparticle aggregation can be avoided by the use of ligands. However, these molecules can lead to a change of the surface properties of the nanoparticles. This was shown clearly by Yu *et al.* (1997), who found that 'naked' SnO_2 nanoparticles formed by gas-phase synthesis showed the expected blue-shift in the absorption spectrum, whereas for ligand-stabilized SnO_2 nanoparticles an unexpected red-shift was detected which cannot be understood by quantum confinement theories.
- Aerosol processes have the potential to create complex chemical structures which are useful in producing multicomponent materials, such as high-temperature superconductors (Kodas, 1989).
- The process and product control are usually very good in aerosol processes. Particle size, crystallinity, degree of agglomeration, porosity, chemical homogeneity, stoichiometry, all these properties can be controlled with relative ease by either adjusting the process parameters or adding an extra processing step, e.g. sintering or size fractionation.
- Being a nonvacuum technique, aerosol synthesis provides a cheap alternative to expensive vacuum synthesis techniques in thin or thick film synthesis (Wang *et al.*,

1990). Furthermore, the much higher deposition rate as compared to vacuum techniques may enable mass production.

- An aerosol droplet resembles a very small reactor in which chemical segregation is minimized, as any phases formed cannot leave the particle (Kodas, 1989).
- Gas-phase processes for particle synthesis are usually continuous processes, while liquid-based synthesis processes or milling processes are often performed in a batch form. Batch processes can result in product characteristics which vary from one batch to another.

One important field of research deals with aerosol-assisted processes used for film synthesis in which liquid droplets dispersed in a gas are used as source and transport vehicles to the substrate. These processes are called aerosol-assisted chemical vapor deposition (AACVD) (Xu *et al.*, 1994), aerosol metal-organic CVD (A-MOCVD) (Fröhlich *et al.*, 1995), the pyrosol process (Blandenet *et al.*, 1981) and aerosol CVD (Tourtin *et al.*, 1995). Common to these processes is the evaporation of micron-sized droplets in proximity to the substrate to produce epitaxial or polycrystalline films (Jergel *et al.*, 1992). Small nanocrystallites might be found in the films but are not formed in the gas phase, therefore these processes are not considered here.

In this Habilitation Thesis, various processes and techniques which can be applied for the synthesis of functional nanomaterials are described. By using the word ‘functional’, the classical distinction which is made in ceramics between structural and functional applications is applied. The structural applications are based on the mechanical properties of the nanostructured or nanophase materials, leading to, e.g., superplastic ceramics or extremely hard metals, using the nanoparticles rather as passive basic building units. Functional applications however rely on a transformation of external signals, such as the filtering of incident light, the change of electrical resistance in different gas concentrations and luminescent behaviour when electrically activated. The functional applications dealt with in this work are mainly electronic and optical.

In order to clarify the methodological approach followed here, the various disciplines involved are shown in Fig. 1.1. The functional applications all base on the special properties of nanoparticles, which are studied in physics, materials science and chemistry. Essential for practical application are the synthesis and handling techniques, here in the gas phase. The handling of nanoparticles, which is bringing the produced nanoparticles in the desired condition for the application, is an often underestimated but essential field. Examples of handling techniques are post-synthesis conditioning such as controlled oxidation, crystallisation and mixing but also the deposition onto suitable substrates. Here, the input of several other disciplines is

essential, such as aerosol science for understanding particle behavior, materials science for understanding materials properties, aerosol instrumentation for process monitoring and process technology for process control and optimization.

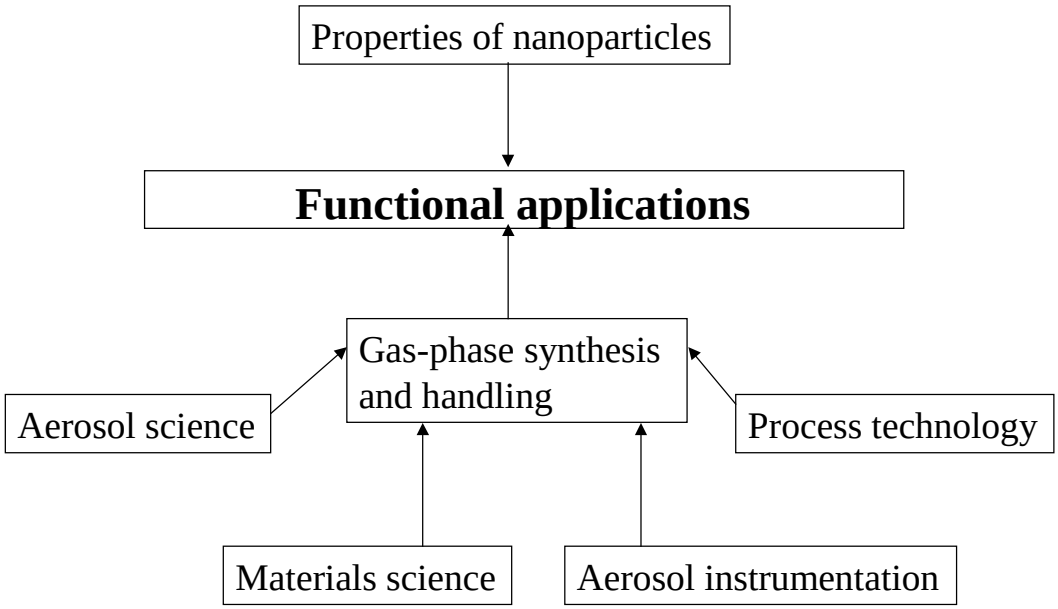

Fig. 1.1. The various disciplines contributing to functional applications based on gas-phase synthesized nanoparticles.

The organization of this Habilitation Thesis is as follows:

- *Chapter 2* gives an introduction into functional applications which are based on the special properties of nanoparticles. Electronic, optical and magnetic applications are discussed.
- *Chapter 3* gives an overview of the current synthesis methods of nanoparticles in the gas phase.
- *Chapter 4* concentrates on several physical phenomena occurring in the gas phase which are important for specific synthesis and handling methods of nanoparticles. The physical processes taking place during the evaporation-condensation synthesis technique applied in this work are modeled in order to understand the synthesis step and to facilitate synthesis of other materials. Aerosols are inherent instable, as the constituting particles tend to collect in flocs, so-called aggregates or agglomerates, when the temperature is below the melting point. This process is modeled by a Monte Carlo simulation technique in order to be able to describe complex systems, such as multi-component or multidimensional systems with several variables, e.g. particle size and charge. The method is useful for describing

the mixing of charged nanoparticles, which is an example of an handling technique and which is also studied experimentally in Chapter 7.

- *Chapter 5* reviews the various works done on the synthesis of nanoparticles in the gas phase for functional applications, arranged so as to emphasize the application rather than the method of preparation. The requirements for gas-phase processes suitable for functional applications are stated.
- *Chapter 6* describes experimental techniques which are important for the measurement and control of nanoparticle aerosols. These methods base on the transport of charged nanoparticle in an electric field. For obtaining charged nanoparticles, a new nanoparticle charger has been developed and characterized. Differential mobility analysis allows to fractionate charged nanoparticles according to their electrical mobility. This can be used for a direct particle size distribution analysis or for producing almost equal-sized nanoparticles (‘monodispersity’). Its potential for application at sub-atmospheric pressures will be investigated. An electrostatic precipitator suited for investigation of the electrical properties of thin nanoparticle films will be described.
- *Chapter 7* describes the synthesis of PbS and SnO_x nanoparticles which apply with the requirements for use in functional applications. Both materials are IV-VI semiconductors, where PbS is mainly interesting for its quantum confinement effects and SnO_x for its application in gas sensors. The quantum confinement effects in PbS are shown by means of a shift in the optical absorption spectrum. Furthermore, an experimental technique which allows the creation of nanoparticle pairs composed of two different chemical components is described. This can be used for the controlled doping of gas sensors.
- *Chapter 8* summarizes and concludes the work.

2. Electronic, optical and magnetic application of nanoparticles

In this chapter, the use of nanoparticles for electronic, optical and magnetic applications is discussed. A broad spectrum of materials including insulators, semiconductors, superconductors, metals and alloys, optical, and artificially structured materials can be used for these purposes. Most applications use films composed of nanoparticles, supported by a substrate material. Part of the material presented here has been published (Kruis *et al.*, 1998d). In this chapter the main phenomena making specific applications possible are reviewed, while in Chapter 5 examples of gas-phase synthesis methods aiming at these applications are given.

2.1 Microelectronic and optoelectronic applications of zero-dimensional structures (quantum dots)

Nanoparticles have been suggested recently for various potential applications in electronics where quantum confinement effects may be of advantage. When electrons are confined to a small domain such as a nanoparticle the system is called a ‘quantum dot’ or zero-dimensional (0-D) structure. Then the electrons are behaving like ‘particles-in-a-box’ and their resulting new energy levels are determined by quantum ‘confinement’ effects. These new energy levels give rise to a modification of the optoelectronic properties as compared to the corresponding properties determined by the bulk material electronic structure (Brus, 1983; Yoffe, 1993). As a result, discrete energy levels are needed to describe the electron excitation and transport in quantum dots. Quantum confinement effects lead for example to higher energy level transitions as compared to the bulk material observed as a shorter wavelength optical absorption edge, indicated by a spectral ‘blue shift’. An example is given in Fig. 2.1.

Quantum dots can be used also to produce light emitters of various colors by ‘band gap tuning’ using particle size effects rather than the current complex techniques of synthesizing compound semiconductors (Service, 1996). Another advantage of 0-D semiconductor structures stems from the very long life time of electrons in the excited states, which is an important requirement in laser optical applications (Weisbuch and Vinter, 1991).

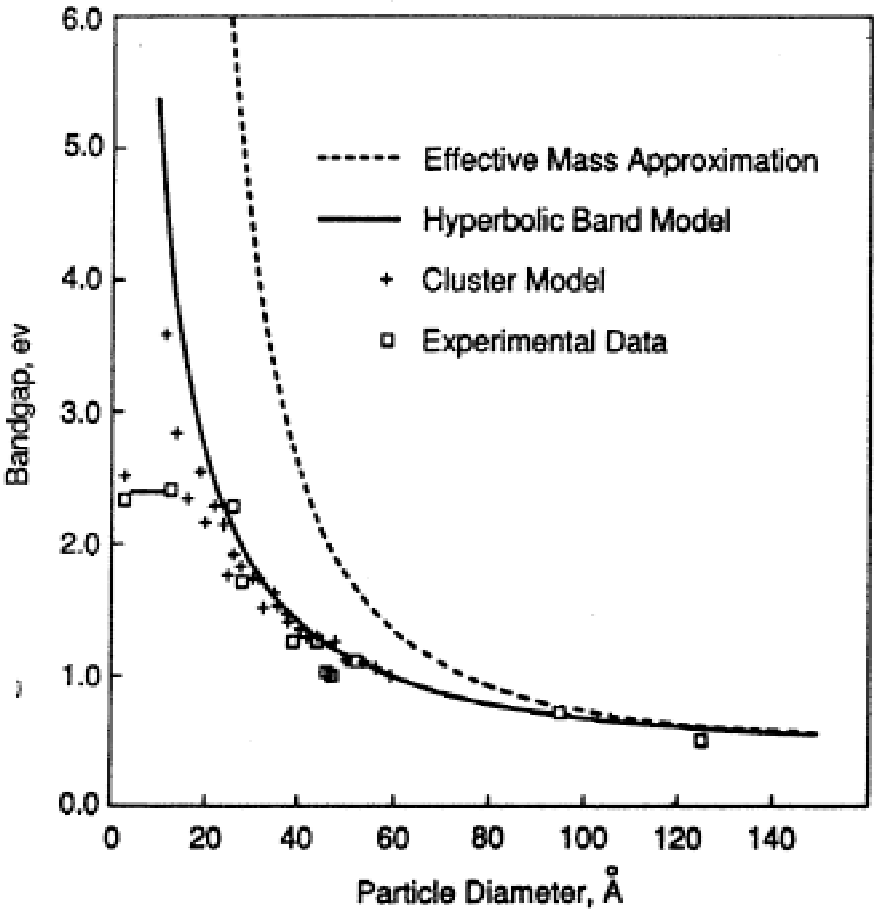

Fig. 2.1. Band gap of PbS as function of particle diameter (Wang et al., 1987)

Alivisatos (1996) produced light-emitting diodes (LED) with high conversion efficiencies (10 %) by using quantum dots embedded in polymer matrices. Moreover, quantum dots were employed in LEDs with a voltage-controlled, tunable output color by Colvin *et al.* (1994), as shown in Fig. 2.2, who assembled CdSe nanoparticles on the surface of an electroluminescent polymer (PPV). The LEDs emitted green light from the polymer and red light from the nanoparticle layer, being also color tunable as a function of the applied voltage. Finally, lasers based upon such structures are expected to have a higher gain and to lase at much lower electrical threshold as compared to current available laser technologies (Weisbuch and Vinter, 1991).

Although these applications seem very attractive, the processes for producing quantum dots devices are very demanding technologically. The preparation of the semiconducting nanoparticles need highly accurate steps during the production stages such as (Salata *et al*., 1994): 1) good controllability of the particle size, 2) monodispersivity, 3) passivation of the surface, 4) good control of the particle shape. A good stability against degradation is needed, as observed in many cases where

properties of the nanoparticles vary with time. A current technological approach to circumvent the inherent reactivity and instability of nanoparticles is by imbedding them in a glass (Ohtsuka *et al.*, 1992) or in a semiconductor having a wider band gap (Danek *et al*., 1994). These nanocomposite structures can then be used in real life optical and electrooptical applications.

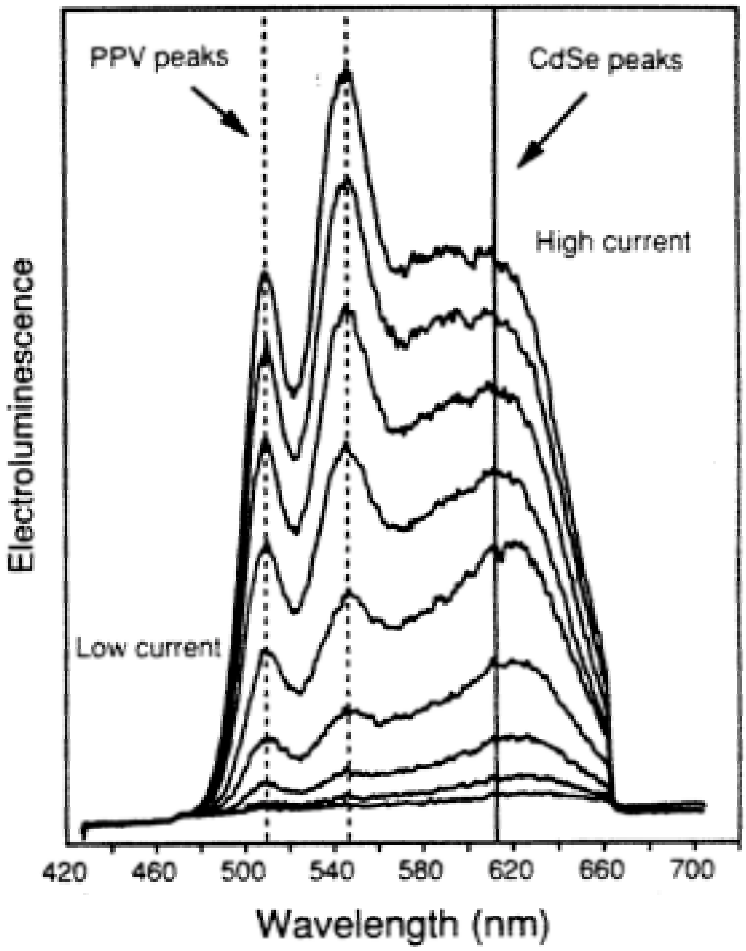

Fig. 2.2. Electroluminescence as function of current for use in LEDs with a voltage-controlled, tunable output color (Colvin et al., 1994).

Enhancement of the nonlinear optical properties by quantum size effects are also of great interest today. This effect has been applied already commercially for producing optical cut-off color filters based on CdS_xSe_{1-x} nanoparticles embedded in silicate glasses. It is expected also that nanoparticles such as CdS, CdSe, GaAs and Si dispersed in glasses will have applications in fast optical switches and optical fibers based on the nonlinear optical behavior (Yoffe, 1993). In nonlinear optical materials, the refractive index can be changed either by carrier injection or by applying electrical fields (Brus, 1991). This change in the refractive index allows electronic modulation of light, enabling for instance faster electro-optical switching as compared to electronical

switching.

Another potential application of quantum dots is the fabrication of optical memories. A 3-D array of quantum dots which are addressed optically can pack in the same volume much larger amounts of information than current planar-based microelectronic memory devices. This can be done for instance by spectral hole burning (Peyghambarian *et al.*, 1996), in which those quantum dots in resonance with a specific laser wavelength will be excited and thus 'bleach'. This enables thus 'writing' a '0' or a '1' memory 'state' with a resolution smaller than the size of the laser spot.

For semiconductor applications other than optical, the nanoparticles should be contacted electrically efficiently. This forms one main difficulty for producing electronic devices based on quantum dots. Since attaching electrical leads to an array of quantum dots is a formidable technological task, one way of making an efficient contact is by using a semiconductor structure consisting of an ensemble of quantum dots. The voltage-tunable LED described earlier is a successfully implemented example which uses a matrix of quantum dots. Another example of efficient contacts can be found in photovoltaics. Hodes *et al.* (1987) measured photocurrents arising from a film consisting of CdSe nanoparticles on glass and reported quantum effects. To allow conversion of significant quantities of light into an electrical current for obtaining an efficient solar cell, a rather 'thick' film up to twenty monolayers of particles had to be deposited. Increasing the contact area between nanoparticles and electrode to increase the signals is possible by depositing the nanoparticles on a very porous TiO_2 electrode. (Weller, 1993).

In microelectronics, the need for faster switching times calls for a reduction in the size of the electronic components. At present, one switching cycle in a transistor gives rise to the movement of many thousands of electrons, requiring a considerable amount of switching energy and producing excessive heat which can hardly be dissipated in high-frequency applications. This calls for developing single-electron devices, in which the switching occurs with the motion of only a single electron. Such a device may be realized by a quantum dot in which the charge of an added electron effectively blocks the flow of other electrons by the so-called 'Coulomb blockade'. Both switching, which performs logic operations, and storage of information are possible with these devices. Here again, one finds that electrical contacts are very hard to produce (Lüth, 1995). Such contacts were nevertheless obtained by Bezryadin *et al.* (1997), using an liquid-phase electrostatic trapping method of Pd nanoparticles between nanoelectrodes with a 4 nm gap.

2.2 Luminescent nanocrystalline silicon and other materials

Porous structures and other nanometer sized particles have found in the last decade a very important potential application for electrolumiscent silicon based devices. The interest in luminescent Si is due to the desire for integration of optoelectronic devices, based now mainly on III-V semiconductors which are not yet integrable monolithically with the dominant Si microelectronics (Kanemitsu, 1995). Light-emitting Si hence would open the way to optical and electrical functionality on one integrated monolithic Si chip. Silicon electroluminescence, in which the luminescence is controlled electrically, would enable also to implement new devices such as light-emitting diodes, with voltage tuned color, and also many other optoelectronic integrated circuits concepts. Being an indirect-gap semiconductor in which interband transitions need phonons (a quantum of energy associated with atomic vibrations), Si in its bulk form is not luminescent, as radiative transitions are of very low probability. Takagi *et al.* (1990) observed visible luminescence from Si nanocrystals at room temperature although the phenomenon was first observed in porous silicon. Until now, there is no generally accepted mechanism for visible luminescence although there are indications that the light absorption by the nanoparticle is influenced by quantum effects and the photoluminescence is dominated by the electronic states of the surface (Kanemitsu, 1995, Prokes, 1996).

Seraphin *et al.* (1996) reported that unpassivated Si nanoparticles exhibit no visible photoluminescence. As the particles age in air, the surface becomes passivated gradually with SiO_2 and exhibits a strong orange emission behavior. Koch and Petrova-Koch (1996) even reported luminescence from SiO_2 nanoparticles. Other nanoparticles of indirect-gap semiconductors such as Ge (Kanemitsu *et al.*, 1992) and SiC (Mimura *et al.*, 1994) showed also luminescence in the visible.

2.3 Gas sensors

Gas sensors have nowadays many established production technologies. It seems however that this field can take advantage from the nanoparticles recent developments as well. A gas sensor consist quite generally of a material with measurable physical properties such as electrical or optical, which change when a gas is present. A solid state chemical sensor selectively converts microscopic chemical interactions into a measurable electrical signal. Sensors should possess selective and reversible sensing properties and be compatible with the transducer device (Holtz *et al.*, 1996). The simplest ‘nanomaterials’ based sensor concept involves measuring the changes in the electrical resistance of a nanocrystalline metal when exposed to hydrogen. Volkening *et al.* (1995) used palladium nanoparticles (10-15 nm) for hydrogen sensing, since the Pd-H system is well understood in terms of the dissociative reactions of H_2 at the Pd

surface and the diffusive properties of H_2 into Pd. They found the response in the nanocrystalline material to be faster as compared to palladium with conventional micron-size particles, due to the smaller diffusion distances.

Traditionally, semiconducting oxides such as SnO_2, ZnO and Fe_2O_3 are used extensively in gas sensor technology (Göpel, 1996). Usually, the sensor is constructed as a porous sintered ceramic body, heated between 300 °C and 700 °C. The sensing behavior appears to be governed by the adsorption of oxygen in the neck regions between the grains. A positive space charge, also called depletion layer, develops in the oxide layer as electrons transfer to the adsorbed oxygen, and a negative charge accumulates on the surface. Reducing gases can remove some of the O^{2-} ions from the surface, thereby increasing the electrical conductivity (Moulson and Herbert, 1990).

The sensitivity of gas sensors can be increased by doping, usually with noble metal catalysts such as platinum, rhodium or palladium. Labeau *et al.* (1993, 1994) investigated the sensitivity of a nanocrystalline SnO_2 gas sensor doped with Pt and Pd nanoparticles. These particles probably act as a catalyst for the adsorption of CO and ethanol molecules, leading to a lower activation energy of the surface reactions. In the work of Gautheron *et al.* (1993), the CO sensitivity was increased by a factor of 30 by adding Pd nanoparticles.

2.4 Resistors and varistors

Nanometer particles have found new applications also in the production of resistors and varistors. Granular films consisting of small conducting particles embedded in an insulating matrix of ceramic or glass exhibit a great variability of the electrical conductivity. It was also shown that by a proper control of the volume fraction of W in Al_2O_3 stable, high-resistance films with a low temperature coefficient of resistivity(TCR) can be produced (Abeles *et al.*, 1975). When the particle size can also be controlled, a wider range of the electrical transport properties is attainable, making these materials suitable for thick film resistors production. The electrical resistance is modeled here by percolation and quantum effects such as electron tunneling (Kundu and Chakravorty, 1996). An example of thick film resistors whose resistivities can be controlled by changing the nanoparticle size is the LaB_6 nanoparticle-glass nanocomposite system, which is compatible with copper hybrid integrated circuits (Ito *et al.*, 1991).

Since varistors are voltage-dependent resistors, characterized by a very low resistance at high voltage, they are used for protection of low-power circuits from high-voltage transients. They are prepared from sintered ceramic materials such as ZnO or SiC with some added minor constituents. The resistance is assumed to be controlled by either direct grain-boundary contacts or by intergranular insulating layers

between the conducting grains. The use of nanoparticles with their large volume of grain boundaries in varistors is expected to improve their properties. Brankovic *et al.* (1994) investigated ZnO based varistors. Using particles with sizes below 100 nm, a varistor with more homogeneous phase distribution and microstructure was obtained, resulting in good nonlinear electrical characteristics. Viswanath *et al.* (1995) applied ZnO nanoparticles of 3 - 10 nm. Apart from good nonlinear characteristics, the normalized breakdown voltage was increased by a factor of 20 in comparison to coarse-grained ZnO varistors.

2.5 Conducting films

Nanometer structured, polycrystalline conducting thin films, have found potential also in the production of transparent conductive electrodes for photoconductor and solar cells applications. Polycrystalline thick films made of closely packed crystalline grains are often used for optoelectronic films. They are used for instance to conduct electrical charges in devices such as solar cells, displays and other applications where a large surface area is needed and epitaxial films are not feasible. These polycrystalline films are nowadays routinely made by spray technologies which have substantial advantages being inexpensive, using only small amounts of material and with high deposition rates (Service, 1996). However, conventional spraying techniques produce a relatively rough film surface with many gaps due to the micrometric size of the droplets. These gaps might reach from the surface of the film down to the substrate decreasing thereby the electrical conductivity of the films. By spraying a colloid of 3 nm nanoparticles on a heated substrate, Pehnt *et al.* (1995) produced very smooth conducting thin CdTe films without gaps and with a roughness smaller than 5 nm, for use in solar cells.

Thin films of wide optical band gap oxides such as SnO_2 and In_2O_3 which are transparent in the visible spectral region are applied in many areas, e.g. as electrodes and anti-reflection coatings in solar cells, photodetectors and charge-coupled imaging devices. Transparent conducting films require high transmission in the visible region and a high or even metallic-like electrical conductivity (Chopra *et al.*, 1983). For this end, inhomogeneities in the film created by the presence of large particles, causing detrimental light absorption and scattering in the visible region, can be minimized by preparing films from nanoparticles. Another advantage obtained with nanomaterials is control on the absorption characteristics by particle size variation leading to quantum confinement effects as described previously. Zhao and Pan (1994) showed that the IR absorption peaks of a film composed of ZnO nanoparticles can be changed by varying the particle size.

Another potentially applicable phenomenon is the electrical bistability of a thin

layer of Ag nanoparticles sandwiched between two layers of a conducting polymer. Up to a certain threshold voltage, no current flows while above it the conductance increases by a factor of 10^7 rendering the film conductive. These films can thus have switching applications in electronics. (Gao *et al.*, 1995)

2.6 Capacitive materials

Dielectric elements based on nanometer structures are of recent interest due to the reduction in capacitance caused by the continuing scaling down of dynamic random access memories (DRAMs). Since materials with a high dielectric constant can store more electrical charges in capacitors, materials with ever larger dielectric permittivities are sought for the shrinking DRAMs. One method for increasing the dielectric permittivity is by dispersing conductive particles in a dielectric matrix.The dissipation factor becomes, in this case however, too large. Kundu and Chakravorty (1995) showed that 2-8 nm Ag nanoparticles in a lead zirconate titanate (PZT) matrix has a high dielectric permittivity with low dissipation factor. The smaller particles led to lower dielectric permittivities but on the other hand improved the dissipation factor. Vezzoli *et al.* (1994) showed from the percolation theory of dielectrics that an optimal topology for high dielectric nanocomposites consists of ellipsoidal metal particles with a small interparticle spacing in the insulating matrix. A high dielectric constant of 5000 was obtained by embedding elongated Au nanoparticles with a length of 80 nm and a width of 30 nm in a matrix of SiO_2.

2.7 High-temperature superconductors (HTS)

Nanoparticles are currently suggested as a solution to ‘flux pinning’ improvement in HTS devices. The problem occurs if the magnetic flux entering the HTS material is not distorted or ‘pinned’ by suitable defects. Then, the material looses its superconducting properties. In general, non-superconducting particles can act as flux pinning centers in a superconductive material. Nanoparticles can be used as defects when added to the superconducting material enhancing flux pinning, and increasing thereby the critical current density. Chadda *et al.* (1991) reported that small-grained , 25-50 nm precursor particles of $YBa_2Cu_3O_{7-x}$ and CuO were necessary to obtain $YBa_2Cu_4O_8$, which upon heat treatment developed $YBa_2Cu_3O_{7-x}$ with CuO flux pinning centers. Takao *et al.* (1996) added $BaZrO_3$ nanoparticles to an HTS material, $YBa_2Cu_3O_7$, and obtained an increase of more than one order of magnitude in the critical current density.

2.8 Thermoelectric materials

Nanoparticles can be used also for producing thermoelectric materials. The thermoelectric effect creates a voltage difference between two conductor junctions kept at different temperatures. This effect is used mainly for thermocouple-type sensors. Kizaki *et al.* (1993) produced thermoelectric thin films of an nanometric-structured Fe-Si alloy. Using $FeSi_{2+x}$ ($0<x<1$) nanoparticles allowed film deposition at low temperatures. A homogeneous film of mixed Fe and SiO nanoparticles of some 10 nm showed after thermal treatment a high Seebeck coefficient of -1400 $\mu V\ K^{-1}$.

2.9 Optical materials

Inorganic pigments such as TiO_2 are used to absorb and scatter UV radiation (Parker, 1996). The particles normally used for pigments, however, impart an unfavorable whiteness to the protected surface. Since the scattered light intensity is a function of the wavelength of the incident light and the particle diameter, an optimal particle size can be found which attenuates UV but only slightly attenuates the visible light. This particle size happens to be located in the nanometer size range. Nanoparticles in a suitable dispersion are already commercially used for solar protection creames and in films which protect plastics against color degradation. Another successful development is the use of pigments as an active scattering medium in a semiconducting polymer. Hide *et al.*(1996) was able thus to obtain laser emission from a semiconducting polymer, MEH-PPV, by incorporating TiO_2 nanoparticles in the polymeric medium. The random scattering by the nanoparticles significantly increases the path length traversed by the emitted light, and lasing occurs if gain by multiple scattering exceeds loss by absorption.

Another optical phenomenon uses electrochromism in nanomaterials. In electrochromic materials the optical properties can be altered reversibly by applying an electric field. Windows made from these materials allow the control of solar energy inflow into buildings and are used also to produce mirrors with a variable reflectance and nonemissive displays with a high-contrast. Estrada *et al.* (1988) showed that the solar transmittance of a NiO_xH_y film with a grain size of about 10 nm could be changed between 29 and 74 %. Chen *et al.* (1995) showed that NiO films consisting of 5-10 nm sized grains have good electrochromic characteristics and that their performance becomes poorer with increasing grain size. The large number of grain boundaries is thought to play an important role in the transport of the alkali metal ions, which are responsible for the coloring, into the grains.

2.10 Magnetic materials

Magnetic nanoparticles approach the size of a single magnetic domain, in which the magnetic spins are aligned all to produce a magnetic moment in one direction. The particle size for single-domain formation in the ferromagnetic elements Fe, Co and Ni is typically several tens of nanometers. For applications using high density magnetic recording materials a high coercivity (representing the resistance to demagnetization) and a high magnetization are essential. It was shown that a maximum value for the coercivity is obtained for nanocrystalline magnetic materials with crystallite in size close to the single magnetic domain. Crystallite sizes smaller and larger than the magnetic domain lead to a sharp decrease in the coercivity. Fe powder with a crystallite size of 13 nm showed a coercivity of 900 Oe in comparison with 10 Oe in bulk Fe (Gangopadhyay *et al.*, 1992). Greatly enhanced values of the coercivity occur in ferromagnetic nanometer-sized metal particles embedded in an insulating oxide film. Xiao and Chien (1987) reported for a Fe-SiO_2 nanocomposite magnetic coercivities as high as 2500 Oe.

In contrast to hard magnetic materials, soft magnetic materials need the other extreme, i.e., very low coercivities. Typical examples are FeSi and FeNi alloys, ferrites and garnets. They are used in power transformers, magnetic recording heads and microwave applications. Until ten years ago, relatively coarse-grained alloys were used since smaller grain sizes caused an increase in the coercivity. It was found however that a maximum in the coercivity vs. grain size curve occurs at about 100 nm (Fig. 2.3). For smaller particles then the coercivity decreases steeply. An alloy with 10 - 20 nm nanocrystals embedded in an amorphous phase shows very low values for the coercivity. Additional useful properties of these materials are very low eddy-current losses and good high-frequency properties. (Yoshizawa *et al.*, 1988, Yamauchi and Yoshizawa, 1995).

Nanocomposites have also good potential in magnetic refrigeration technology (Zachariah *et al.*, 1995) based on the magnetocaloric effect. Bulk magnetic materials show usually a decrease in magnetization upon temperature increase and limits the temperature range in one refrigeration cycle. Superparamagnetic nanoparticles in a non-magnetic host can overcome this limitation by combining the higher magnetization of ferromagnets with the higher magnetocaloric effect of paramagnets. Zachariah *et al.* (1995) found a superparamagnetic behavior for 5-10 nm Fe_2O_3 particles embedded in much bigger SiO_2 particles.

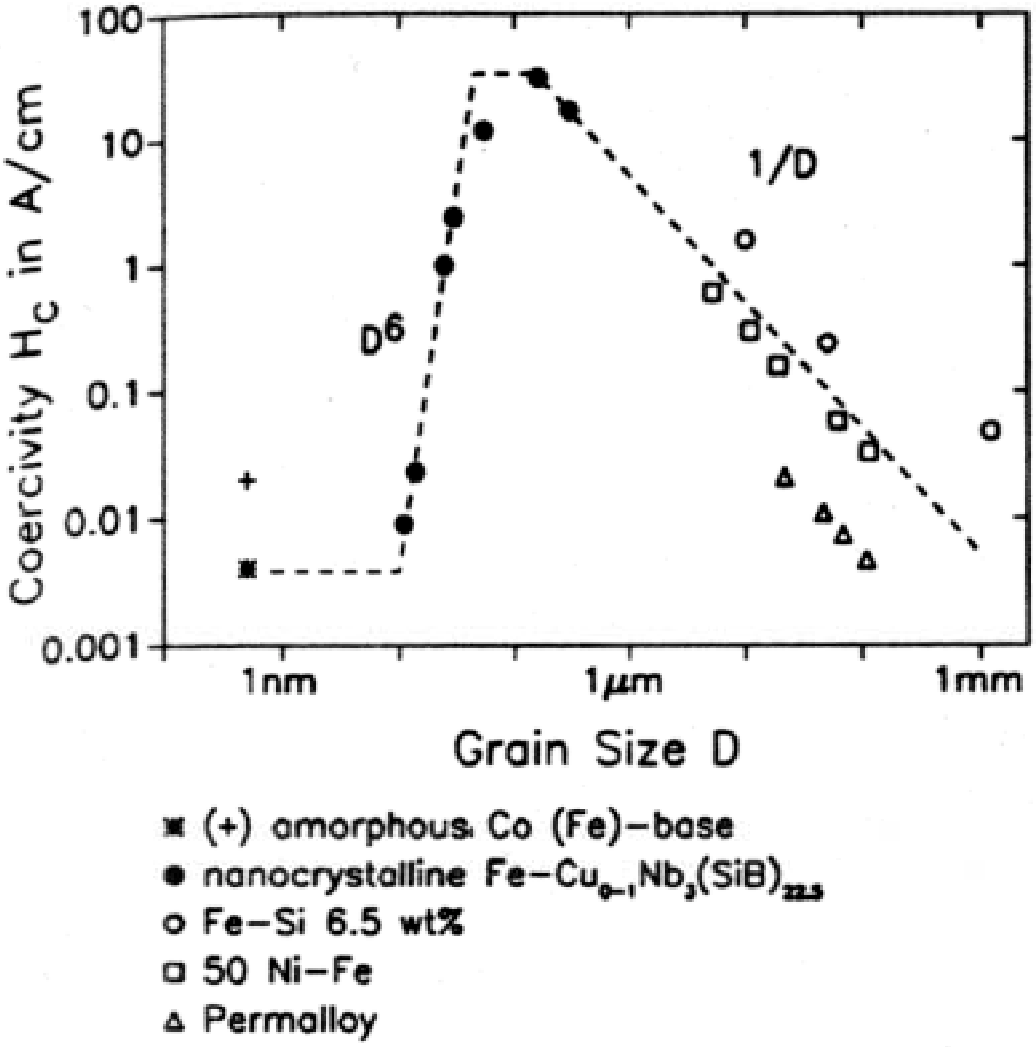

Fig. 2.3. Dependence of coercivity on crystallite size for various soft magnetic alloys (Herzer, 1990).

A novel important property found in recent years for nanocomposites is the giant magnetoresistance (GMR) effect. This is the phenomenon of a large decrease in the electrical resistivity of certain materials when exposed to a magnetic field. The resistivity-temperature change can be up to 80 % as compared to only a few percent in regular metals. Its applications are for magnetic sensors and for new storage devices with very high density. First discovered in magnetic multilayers, it was also found in the granular Co-Cu system, in which ferromagnetic Co nanocrystals are dispersed in a nonmagnetic Cu matrix (Xiao *et al.*, 1992). The magnetic field aligns the ferromagnetic domains, and reduces the scattering of electrons, thereby decreasing the electric resistivity. GMR is observed in immiscible metals, such as Co-Cu, Fe-Ag, Fe-Cu, Fe-Au and Co-Ag. The smaller the particle size, the bigger the GMR effect is. The

effect is highest near the percolation threshold (Wang and Xiao, 1994).

2.11 Conclusions: control parameters for properties of functional applications

As shown at length in this chapter, there are many parameters influencing the properties of functional applications based on nanoparticles. These are:

- Mean particle size
- Width of the particle size distribution
- Crystalline properties, such as the crystal phase and the size of the crystallites
- Chemical composition, e.g. deviation from stoichiometry
- Amount of impurities present in the nanoparticles or on the surface
- 'Packing' of the nanoparticles, e.g. intimately contacting (nanophase materials), forming a porous film or with sintered connections between them ('necks')
- Mixing with other material, e.g. imbedded in a matrix (glass, ceramic material or polymer) or in close contact with other nanoparticles (e.g. SnO_2 gas sensors doped with noble metal nanoparticles)

Depending on the application, one or more of these parameters should be controllable. It is the process which yields these properties. Gas-phase processes, although having some drawbacks, have a high level of control. The different gas-phase synthesis methods will be described in the next chapter.

3. Synthesis methods of nanoparticles in the gas phase

The synthesis methods for nanoparticles can be divided into three main groups. The first group comprises the liquid-phase methods, which apply chemical reactions in solvents. This leads to colloids, in which the nanoparticles formed can be stabilized against aggregation by surfactants or ligands. The second group consists of methods basing on surface growth under vacuum conditions. Diffusion of atoms or small clusters on suitable substrates can lead to island formation, which can be seen as nanoparticles. An important example is Stranski-Krastanow growth, which is used for growing III-V quantum dots. The last group, gas-phase synthesis, is the subject of this Chapter.

Most synthesis methods of nanoparticles in the gas phase are based on homogeneous nucleation in the gas phase and subsequent condensation and coagulation. The ablation of a solid source with a pulsed laser can also yield nanoparticles, but the formation mechanism is at present not very clear. A micron-sized aerosol droplet may also yield nanoparticles by evaporating a solute-containing droplet. Electrospray systems are often applied as droplet generators, as they produce very small droplets being quite monodisperse in comparison to other spray processes. Additionally, droplet explosion due to an electrical charge which exceeds the Rayleigh limit during evaporation may yield even smaller droplets. Finally, initiating homogeneous nucleation inside aerosol droplets can result in many nanosized nuclei in the droplet, which upon drying will yield nanoparticles. This is, in fact, not a formation mechanism in the gas phase but for sake of completeness it will be shortly discussed in this Chapter, as this so-called spray pyrolysis is a well-known aerosol synthesis route. In the following sections these methods will be described in detail. Part of this material has been published (Kruis *et al.*, 1998d). A preview of the gas-phase synthesis methods is shown in Fig. 3.1.

3.1 Processes based on homogeneous nucleation in the gas phase

Several methods with which condensable monomers are produced will be dealt with hereby. The generation of nanoparticles from the vapor phase requires the establishment of supersaturation. This is made possible by physical or chemical methods. The physical methods involve some form of cooling of the monomers, by expansion, by mixing with a cooler gas or by heat transfer to the surroundings.

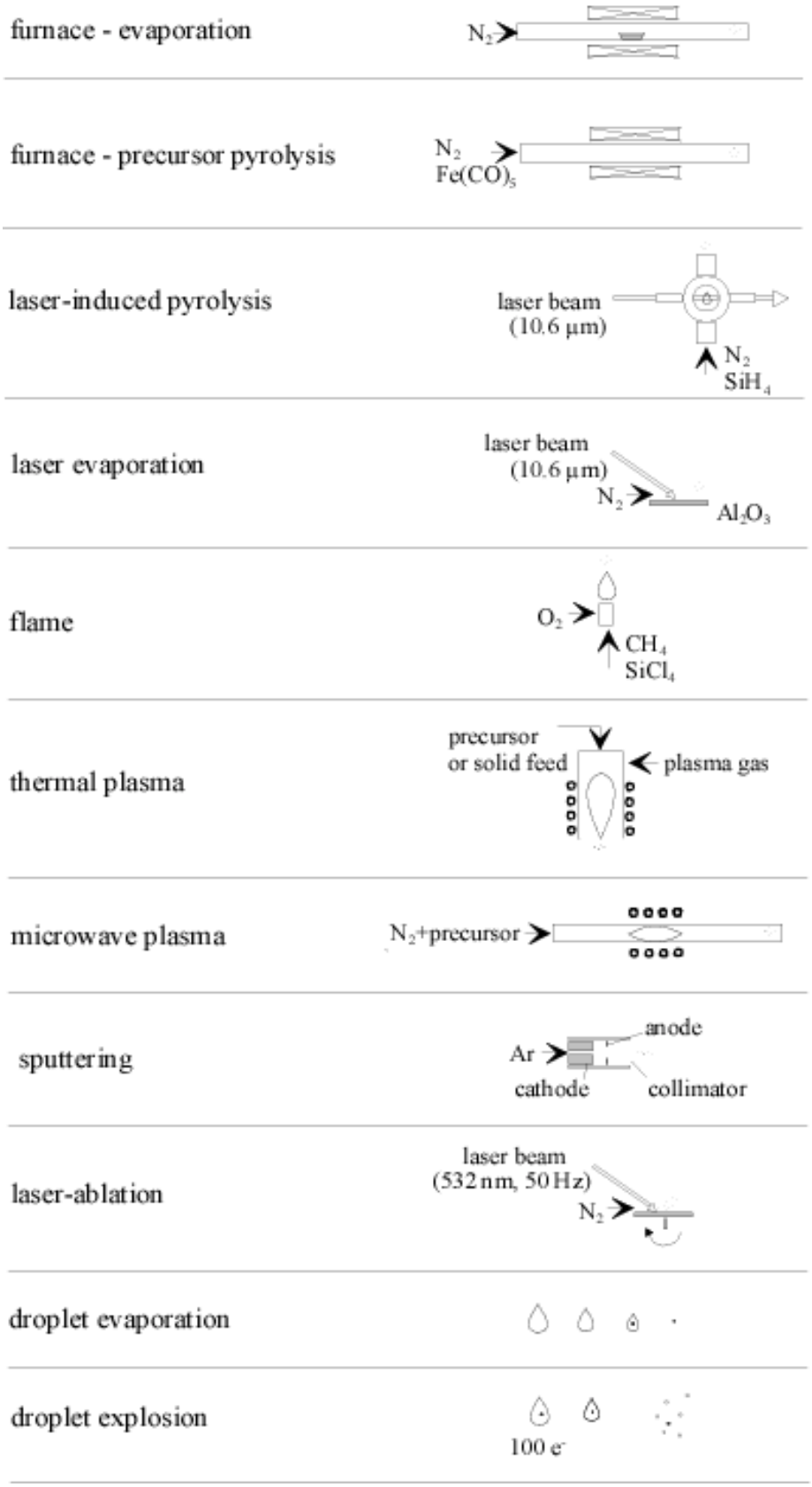

Fig. 3.1. Schematic view of different synthesis methods.

Supersaturation can be achieved also by chemical reactions which produce a nonvolatile condensable product. These reactions are usually decomposition reactions initiated by a rise in temperature and used extensively in laser and flame reactors.

Various heating and evaporation methods of interest will be dealt with in the next section. Furthermore, methods for rapidly cooling the vapor will be described because fast cooling processes are especially important when very small particles have to be synthesized and when the formation of hard agglomerates has to be avoided.

3.1.1 Furnace flow reactors

Oven sources are the simplest systems to produce a saturated vapor for substances having a large vapor pressure at intermediate temperatures up to about 1700°C. A crucible containing the source material is placed in a heated flow of inert carrier gas. This has the disadvantage that the operating temperature is limited by the choice of crucible material and that impurities from the crucible might be incorporated in the nanoparticles. Nanoparticles are formed by subsequent cooling, such as natural cooling or dilution cooling. For very small particles a rapid temperature decrease is needed which can be achieved by the free jet expansion method described later. Another method is cooling in a turbulent jet (Bartz *et al.*,1987). Materials with too low vapor pressure for obtaining appreciable particle density have to be fed in the form of suitable precursors, such as organometallics or metal carbonyls, in the furnace. These decompose in the oven to yield a condensable material. Using furnace flow reactors, elemental nanoparticles such as Ag (Scheibel and Porstendorfer, 1983) and Ga (Deppert *et al.*, 1996) and also compounds such as PbS (Kruis *et al.*, 1996) can be obtained.

3.1.2 Laser reactors

In the laser pyrolysis technique, being a special class of laser processing techniques (Peled *et al*, 1996), a flowing reactant gas is heated rapidly with an IR laser such as a cw CO_2 laser. The source molecules are heated selectively by absorption of the laser beam energy, whereas the carrier gas is only indirectly heated by collisions with the reactant molecules. A gas phase decomposition of the reactants takes place due to the temperature increase and supersaturation is created. As an example, SiH_4 pyrolysis results in Si nanoparticle formation (Kruis *et al.*, 1998b) and $Fe(CO)_5$ decomposition leads to Fe nanoparticles (Majima *et al.*, 1994). The main advantage of laser-heating in gas-flow systems is the absence of heated walls which reduces the danger of product contamination.

UV lasers can be used to obtain photochemical dissociation. Tamir and Berger (1995) showed that SiH_4 can be dissociated by a two-photon absorption of an ArF excimer laser beam with a wavelength of 193 nm, forming nanoparticles.

3.1.3 Laser vaporization of solids

This technique uses a laser which evaporates a sample target in an inert gas flow reactor (Powers *et al.*, 1982). The source material is locally heated to a high temperature enabling thus vaporization. The vapor is cooled by collisions with the inert gas molecules and the resulting supersaturation induces nanoparticle formation. Kato (1976) used a continuous-wave CO_2 laser with a power of 100 W. Nanoparticles between 6 and 100 nm of many complex refractory oxides such as Fe_3O_4, $CaTiO_3$ and Mg_2SiO_4 were synthesized under an inert gas pressure of 1 mbar to 5 bar from powders, single crystals or sintered blocks. Nanocomposites can also be produced, as shown e.g. by Chow *et al.* (1989). They evaporated simultaneously a metallic and a ceramic target by a cw CO_2 laser creating a composite film close to the target. The matrix consisted of Al and the dispersed phase consisted of amorphous SiO_2 fibers with diameters between 25 and 120 nm.

3.1.4 Flame reactors

Nanoparticles are produced by employing the flame heat to initiate chemical reactions producing condensable monomers. The flame route has the advantage of being an inexpensive method, however usually it yields agglomerated particles. An example is the oxidation of $TiCl_4$, $SiCl_4$ or $SnCl_4$ in a CH_4/O_2 flame leading to TiO_2, SiO_2 or SnO_2 particles with primary particle sizes between 10 and 100 nm (Vemury *et al.*, 1997). More complex products can be also obtained. Zachariah *et al.* (1995) added small amounts of $Fe(CO)_5$ and $SiO_2(CH_3)_6$ to a premixed CH_4/O_2 flame with temperatures at about 2000°C, forming Fe_3O_4 particles of 5-10 nm embedded in larger SiO_2 host particles. The synthesis was conducted at relatively high temperatures under oxygen-rich conditions to minimize carbon contamination.

A method to reduce the agglomeration of nanoparticles, avoiding oxidation, is to encapsulate them within a material which can be later removed. Dufoux and Axelbaum (1995) applied a Na coflow flame with a burner consisting of several concentric tubes. A $TiCl_4$ vapor was fed to the central tube while the Na vapor was fed to the concentric surrounding tube. An inert gas acts as a sheath gas between these two flows and shields the flame from ambient air. Ti particles with sizes of 10-30 nm were produced and were confined within larger NaCl particles. The NaCl can be removed by washing with water, glycerin or by sublimation.

3.1.5 Plasma reactors

A plasma can also deliver the energy necessary to cause evaporation or initiate chemical reactions. The plasma temperatures are in the order of 10^4 °C, decomposing the reactants into ions and dissociating atoms and radicals. Solid powder feeds can also be decomposed by the plasma. Nanoparticles are formed upon cooling while exiting the plasma region. Main types of the thermal plasmas are dc plasma jet, dc arc plasma and rf induction plasma (Young and Pfender, 1985). A small laboratory plasma system, the inductively coupled plasma (ICP), is often used at atmospheric pressures in combination with an aerosol spray system employing an ultrasonic atomizer. This technique is called spray-ICP (Kagawa *et al.*, 1993). As the residence time of the droplets in the plasma is very short it is important that the droplet sizes are small in order to obtain complete evaporation. Complex materials such as multicomponent oxides can be obtained by using appropriate mixtures. By using a solution of $Ba(NO_3)_2$ and $Fe(NO_3)_3$ in water, Mizoguchi *et al.* (1994) obtained by spray-ICP $BaFe_{12}O_{19}$ nanoparticles with sizes between 10 and 50 nm. In most cases, the plasma-generated vapors are quenched by mixing with a cold gas. This leads to high cooling rates, but also to nonuniform cooling which deteriorates the uniformity of the produced particles. Rao *et al.* (1995a,b) used a subsonic nozzle expansion after a dc arc plasma in order to obtain more uniform cooling rates.

Another method uses a microwave-generated plasma, in which temperatures between 300°C and 900 °C can be obtained. The plasma enhances the kinetics of the chemical reactions leading to nanoparticle formation due to ionization and dissociation of the reactive molecules. Since the lower temperature decreases the sinter rate, the formation of hard agglomerates is reduced (Vollath and Sickafus, 1992).

3.1.6 Spark source and exploding wire

A high-current spark between two solid electrodes can be used to evaporate the electrode material for creating nanoparticles. At the electrodes a plasma is formed. This technique is used for materials with a high melting point such as Si or C, which cannot be evaporated in a furnace. Saunders *et al.* (1993a) used an electric spark with an energy between 50 mJ and 150 mJ to evaporate material from crystalline Si electrodes. A continuous flow of Ar transports Si crystallites formed, of sizes 2 - 4 nm, to the collection substrate. Reactive evaporation is also possible by adding a suitable reactant gas. As an example, SiC nanoparticles were formed when an arc source generated a discharge between two Si electrodes in 500 mbar of CH_4, and Al_2O_3 was obtained from Al electrodes in a mixture of 130 mbar O_2 and 420 mbar Ar (Hayashi, 1987).

A closely related technique is the exploding wire, in which the wire material is vaporized instantaneously by a capacitor in a chamber filled with an inert gas. This method has the disadvantage of being non-repetitive. As an example, GaAs nanoparticles were synthesized by using a GaAs wire (Saunders *et al.,* 1992).

3.1.7 Sputtering

Sputtering is a method of vaporizing materials from a solid surface by bombardment with high-velocity ions of an inert gas, causing an ejection of atoms and clusters. Sputter sources such as an ion gun or an hollow-cathode plasma sputter source are normally used in vacuum systems, below 10^{-3} mbar, as a higher pressure hinders the transportation of the sputtered material. Instead of ions, electrons from an electron gun can be also used. Iwama *et al.* (1982) operated an electron gun at 10^{-5} mbar separated by a differential pumping system from a 1 mbar evaporation chamber in order to evaporate Ti and Al targets in a N_2 or NH_3 atmosphere, producing TiN and AlN nanoparticles smaller than 10 nm. Günther and Kumpmann (1992) applied an electron beam in an inert gas atmosphere with pressures up to 5 mbar in order to produce 5 nm Al_2O_3 and SiO_2 particles. Hahn and Averback (1990) showed that a DC/RF magnetron sputter source can be operated in the mbar range, ejecting nanoparticles of sizes between 5 and 20 nm. Sputtering has the advantage that it is mainly the target material which is heated and that the composition of the sputtered material is the same as that of the target.

3.1.8 Inert gas condensation

One of the earliest methods used to synthesize nanoparticles, is the evaporation of a material in a cool inert gas, usually He or Ar, at low pressures conditions, of the order of 1 mbar. It is usually called ‘inert gas evaporation’. Common vaporization methods are resistive evaporation (Tasaki *et al.*, 1965), laser evaporation (Chow *et al.*, 1989) and sputtering (Hahn and Averback, 1990). A convective flow of inert gas passes over the evaporation source and transports the nanoparticles formed above the evaporative source via thermophoresis towards a substrate with a liquid N_2 cooled surface (Granqvist and Buhrman, 1976). A modification which consists of a scraper and a collection funnel allows the production of relatively large quantities of nanoparticles, which are agglomerated but do not form hard agglomerates and which can be compacted in the apparatus itself without exposing them to air. This method was pioneered by the group of Birringer and Gleiter (Birringer *et al.*, 1984). Increased pressure or increased molecular weight of the inert gas leads to an increase in the mean particle size. This so-called Inert Gas Condensation method is already used on a

commercial scale for a wide range of materials. Also reactive condensation is possible, usually by adding O_2 to the inert gas in order to produce nanosized ceramic particles (Siegel, 1994). Another method replaces the evaporation boat by a hot-wall tubular reactor into which an organometallic precursor in a carrier gas is introduced. This process is known as Chemical Vapor Condensation referring to the chemical reactions taking place as opposed to the inert gas condensation method (Kear and Strutt, 1995). Finally, the Gas Deposition Method is also used in industry. In this method, nanoparticles are formed by evaporation in an inert gas at atmospheric pressure and transported by a special designed transfer pipe to the spray chamber at a pressure of about 0.3 mbar. By moving the nozzle at the end of the transfer pipe, the particles which have a mean velocity of 300 m/s can be deposited in required places on the substrate in the spray chamber. Using this technique writing micron-sized patterns was demonstrated. (Oda *et al.*, 1992).

3.1.9 Expansion-cooling

Expansion of a condensable gas through a nozzle leads to cooling of the gas and a subsequent homogeneous nucleation and condensation. Turner *et al.* (1988) showed by numerical simulations that by expanding an organometallic precursor in N_2 in a subsonic nozzle results in the formation of particles of about 100 nm with a relative narrow size distribution. The expansion caused the pressure to decrease from 2 bar to 0.75 bar. In order to produce nanoparticles smaller than 5 nm, supersonic free jets expanding in a vacuum chamber with pressures smaller than 10^{-4} mbar have been used. (Yamada *et al.*, 1987). In the work of Bowles *et al.* (1981) an inert gas containing a metal vapor was subjected to multiple expansions. Nuclei are formed as a result of two sonic expansions. Then a nuclei growth region in a subsonic, low-pressure reactor produced nanoparticles with mean sizes below 2.5 nm. The separation of nucleation and condensation processes results in a narrower size distribution than usually achieved by supersonic expansion. Further growth is stopped by expansion in a vacuum. Converging nozzles which create an adiabatic expansion in a low-pressure flow have also been used to produce nanoparticles (Bayazitoglu *et al.*, 1996). Although the particles sizes are larger than in a vacuum expansion, particles of the order of 100 nm were obtained with a relatively high production rate. Rao *et al.* (1995a,b) produced 4-10 nm sized nanoparticles by expanding a thermal plasma carrying vapor-phase precursors through a ceramic-lined subsonic nozzle. A special nozzle design minimizes boundary layer effects and approaches a one-dimensional temperature gradient in the flow direction. This leads to a highly uniform quench rate and thus to nanoparticles with a narrow size distribution.

3.2 Laser ablation of solids

Laser ablation is a technique in which a pulsed laser rapidly heats a very thin (< 100 nm) layer of substrate material, resulting in the formation of an energetic plasma above the substrate. This technique should be distinguished from laser vaporization, as apart from atoms and ions also fragments of solid or liquid material are ablated from the substrate surface which vary in size from sub-nanometric to micrometric. Therefore it cannot be considered as a pure homogeneous nucleation process. The pulse duration and energy determines the relative amounts of ablated atoms and particles. The nonequilibrium nature of the short-pulse (10-50 ns) laser heating enables the synthesis of nanoparticles of materials which normally would decompose when vaporized directly, such as most semiconductors and superconductive materials. Typically used lasers are the Nd:YAG (532 nm) and excimer (191, 248 and 308 nm) lasers. The material removal rate by laser ablation decreases with longer target exposure times, therefore the target is usually rotated. When used for producing films, this technique is called pulsed laser deposition (PLD). Here, the fine particles are not desired as they deteriorate the film quality and the operating conditions are chosen so as to minimize particle formation (Venkatesan and Green, 1996). Yamamoto and Mazumder (1996) showed that laser ablation of $NbAl_3$ at He pressures of 0.1 mbar did not produce any nanoparticles while an operating pressure of 1 mbar resulted in the formation of 6 nm nanoparticles with the same stoichiometry as the substrate. Typical production rates are in the order of micrograms per pulse with pulse frequencies of about 50 Hz, yielding 10-100 mg powder per hour. Reactive laser ablation in which a reaction of the ablated material with the reactor gas occurs is also used. Johnston *et al.* (1992) ablated an Al target in an O_2 atmosphere, producing Al_2O_3 nanoparticles.

3.3 Electrospray systems

A simple way to produce nanoparticles is to evaporate micron-sized droplets of a dilute solution. By choosing the appropriate solute concentration, nanosized particles consisting of the solid residue can be obtained. For instance, drying a 1 μm droplet containing a 1 ppm solution of NaCl will yield a 10 nm NaCl particle. A serious problem here is that all the impurities present in the liquid will concentrate in the solid residue (Rulison and Flagan, 1994). Furthermore, it is necessary to start from small droplet sizes which are difficult to obtain in normal spray systems.

Chen and Pui *et al.* (1995) showed that an electrospray system operated in the cone-jet mode could yield small droplets with a narrow size distribution. To avoid droplet explosion during evaporation, the highly charged aerosol is first passed through a radioactive neutralizer before the evaporation takes place. It is important

here to avoid droplet explosion since that would deteriorate the narrowness of the size distribution. Using a sucrose solution, particles as small as 4 nm were obtained. In another work (Hull *et al.*, 1997) Ag particles with a mean size of 10 nm were produced by electrospraying a dilute $AgNO_3$ solution in methanol onto a grounded substrate. A 1 mW He-Ne laser focused just below the capillary tip of the electrospray catalyzed the reduction of the Ag^+ ion. The droplets were not discharged before evaporation in this case, so Rayleigh explosion is probable.

Kim and Rye (1994) developed a special charge injection technique in order to obtain very high charge densities. It is stated that the higher the surface charge density of the electrospray jet is, the smaller is the size of the ejected droplets. The system consists of a spray capillary containing a sharp needle connected to a high voltage supply. This charge injection system stabilizes the multijet-mode, in which a large number of small droplet-emitting jets form on the wetted capillary surface. Spraying a 10 vol.-% TEOS solution in ethanol in a chamber filled with O_2 resulted in 30-100 nm sized SiO_2 particles.

3.4 Spray pyrolysis

In spray pyrolysis, a droplet containing a solute is evaporated or dissociated by a chemical reaction. During the shrinkage of the droplet, a supersaturated solution is created, as the amount of solute remains constant, and small particles may form inside the droplet Spray pyrolysis normally results in micron-sized particles which often have a hollow shape. This method is intermediate between gas-phase and liquid-phase, as the droplet are gas-carried, but the particle formation inside the droplets is in vthe liquid phase.

In some cases, nanoparticles were obtained. Lyons *et al.* (1992) obtained nanocrystalline PdO and V_2O_5 particles by spray pyrolysis. The droplets containing a precursor solution were decomposed at relatively low temperatures. This method avoids grain growth and densification, while the temperature is still high enough to fully decompose the precursors. The product consisted of 5 to 10 nm crystallites packed together in spheres, showing the form of the originating droplet and demonstrating that the droplets were not fragmented. This possibility was suggested theoretically by Leong (1987) who pointed out that formation of multiple crystals in a droplet is possible when the solubility is low, the solute mass is high or the rate of solvent evaporation is high. Kang *et al.*(1995) showed that in spray pyrolysis of ultrasonically nebulized nitrate or acetate solutions the particle size can be reduced to about 10 nm by using a low pressure system (80 mbar). The same phenomenon was observed when zinc acetate droplets of 2 µm were generated by expanding a liquid through a glass filter into a low pressure chamber and subsequently pyrolyzed,

yielding ZnO nanoparticles (<20 nm). A mechanism was proposed in which gas evolution, due to solute decomposition with increasing temperature, resulted in the fragmentation of droplet containing the nanocrystals (Kang and Park, 1996a). However, by varying the solution concentration it only changed the particle size marginally, indicating a more complex mechanism (Kang and Park, 1996b).

3.5 Conclusions: processes suitable for functional applications

In many cases the choice of the process or precursors is based on economic considerations (Kruis *et al.*, 1992). For structural applications such as production of ceramics, a process capable of producing larger quantities of nanoparticle powder is necessary, such as flame or plasma reactors. For functional applications, however, the quality more than the quantity of the nanoparticles is decisive, as most of the functional applications need only thin films. The purity of the nanoparticles is also very important, so that most processes basing on chemical reactions are not suitable due to incorporation of byproducts in or on the nanoparticles. Processes based on pure physical processes are, therefore, used more often.

One of the most simple methods is evaporation of a source material in a flowing gas, followed by condensation into nanoparticles in the cooler parts of the system. A good purity can be obtained by using a purified inert gas and high-quality source material. It is difficult, however, to avoid some contamination of the particle surface with residual gas impurities. These contaminations can be reduced by reducing the process pressure, thereby reducing the number of collisions of gas collisions with the particle surface.

The evaporation method is not always suitable for synthesizing compounds, such as compound semiconductors. We found that direct evaporation of GaAs and InP is not possible due to decomposition (Deppert *et al.*, 1998). The use of chemical reactions with synthesized metal nanoparticles is one possibility to obtain the desired stoichiometry. Another possibility is the use of laser ablation, in which the stoichiometry of the ablated material is more or less retained.

Another problem of the usual evaporation-condensation process is that the particle size distributions are relatively wide. The geometrical standard deviation is at least 1.35 due to Brownian coagulation. But the Brownian coagulation can also be made useful for obtaining composite materials. As the evaporation-condensation process is the process of choice in this work, important phenomena occurring in this process will be investigated in the next Chapter.

4. Physical phenomena in gas-phase synthesis

In synthesis in the gas phase, many phenomena play a role. The most important are:

- Homogeneous nucleation
- Condensation
- Collisions due to Brownian movement
- Coalescence due to solid state diffusion or viscous flow
- Surface reactions

These mechanisms are schematically shown in Fig. 4.1. Additionally, transport processes, e.g. due to thermophoresis or Brownian diffusion, play a role.

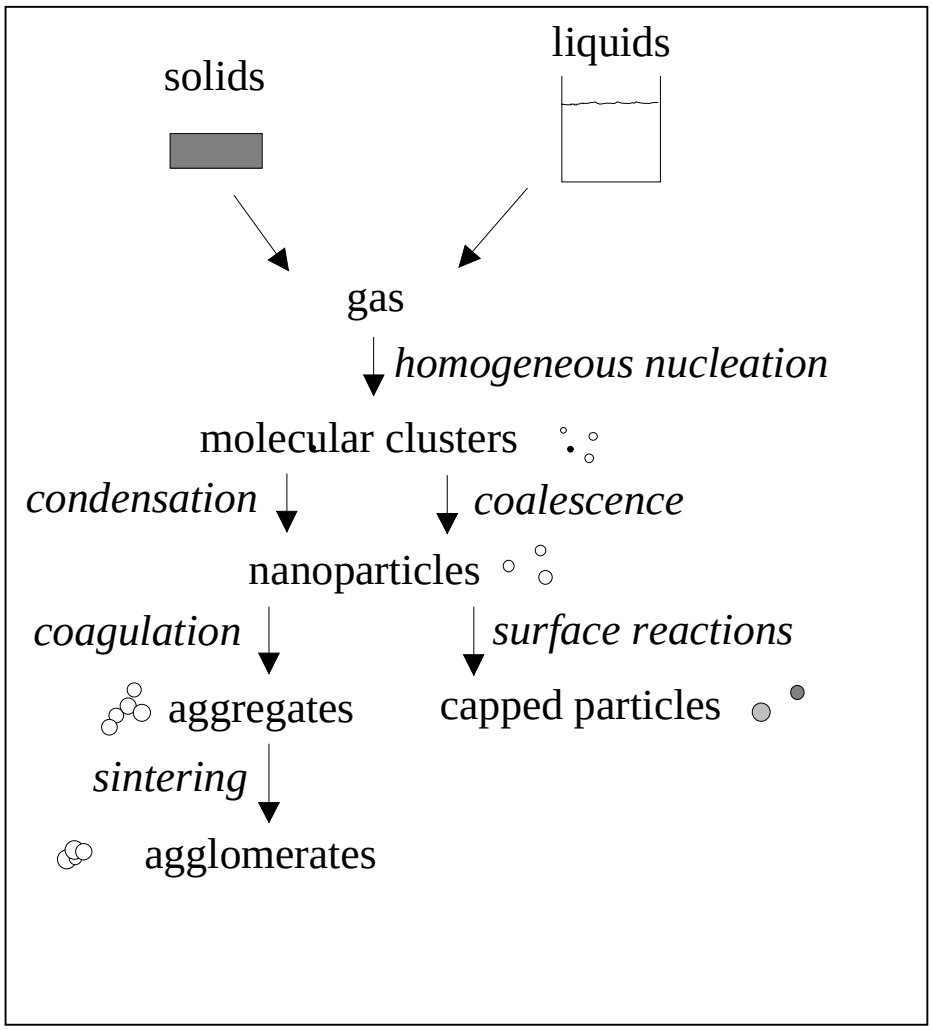

Fig. 4.1. Mechanisms in gas-phase nanoparticle synthesis

In this Chapter, several mechanisms related to relevant problems in the gas-phase synthesis of nanoparticles for functional applications are investigated. In

Chapter 4.1, the formation of nanometer-sized particles by the evaporation-condensation technique will be analyzed using a moment model describing nucleation, condensation and coagulation. This allows to predict the minimum furnace temperatures needed to form nanoparticles. The coagulation and aggregation phenomenon is modeled by a Monte Carlo simulation technique in order to be able to describe complex systems, such as multi-component or multidimensional systems with several variables, e.g. particle size and charge. The contents of Chapter 4.2 have been accepted for publication (Kruis *et al.*, 2000a). The method is useful for describing the mixing of charged nanoparticles for the synthesis of composite nanoparticles (Chapter 4.3).

4.1 Particle formation by nucleation, condensation and coagulation: application to synthesis in tube furnaces

Most of synthesis methods for gas phase nanoparticle synthesis are formation are still in the laboratory stage, and process design and product development rely heavily on experience. Aerosol science provides a theoretical framework for understanding particle formation processes in the gas phase, which can be used to understand experimental results or to find favorable process conditions. Modeling of most aerosol reactors is very complex due to the interplay of many physicochemical phenomena and due to the problematic description of complex phenomena such as exploding wires and laser evaporation of solid material. Therefore, a gas which is heated and subsequently rapidly cooled down is chosen here as a model system. In this so-called evaporation-condensation process (Scheibel and Porstendörfer, 1983), a saturated vapor is cooled resulting in a supersaturation, thereby producing nanosized particles. The same basic phenomena occur in the more complex systems as laser ablation and inert-gas condensation but there the process conditions are not so easily defined.

Several approaches for modeling particle formation in tube furnaces have been described in the literature. Panda and Pratsinis (1995) assume a monodisperse size distribution to describe the formation of aluminium particles in a furnace. A more detailed model describes the changes in the first three moments of the particle size distribution due to nucleation and condensation (Friedlander, 1983). This allows to assume a lognormal particle size distribution. In order to close these three moments, Pratsinis (1988) assumed a lognormal size distribution and added the coagulation mechanism. More advanced modeling techniques do not assume a shape of the particle size distribution but require longer computation times and more complexe numerical methods.

In this subchapter, particle formation in tube furnaces is analyzed using a moment model, based on Pratsinis (1988) but modified for the non-isothermal conditions of tube furnaces. After validation of the model, most of the chemical elements have been screened in order to find conditions necessary for nanoparticle synthesis using the evaporation-condensation mechanism in tube furnaces.

4.1.1 Theory

In the evaporation-condensation process, a vapor is generated by slow evaporation or sublimation of a powder material in an evaporation boat and can form particles by homogeneous nucleation when cooling down. In order to calculate the supersaturation the saturation vapor pressure is described in terms of the general equation:

$$\log p_s = \frac{A}{T} + B \log T + C\,T + D\,T^2 + E \tag{4.1.1}$$

This expression is fitted to the experimental data (Honig and Kramer, 1969) for most of the elements. The expression proposed by Girshick and Chiu (1990) for the homogeneous nucleation rate is used here:

$$I = v_1 \sqrt{\frac{2\gamma}{\pi m_1}}\, n_s^2\, S \exp\left(\theta - \frac{4\theta^3}{27(\ln S)^2}\right) \tag{4.1.2}$$

using the dimensionless surface tension group θ:

$$\theta = \frac{\gamma s_1}{k_B T} \tag{4.1.3}$$

A linearly temperature-dependent surface tension (Mezey and Giber, 1982) is used in this work. The supersaturation S is found using:

$$S = \frac{\hat{n}_1 \rho_g}{n_s} \tag{4.1.4}$$

the number of monomers in the particles formed by homogeneous nucleation is:

$$k^* = \left(\frac{2\theta}{3\ln S}\right)^3 \tag{4.1.5}$$

The particle dynamics can be described in terms of the three leading moments of the size distribution, approximating the form of the distribution as lognormal:

$$n(v,t) = \frac{1}{3\sqrt{2}\ln\sigma}\exp\left(-\frac{\ln^2\left(v/v_g\right)}{18\ln^2\sigma}\right)\cdot\frac{1}{v} \qquad (4.1.6)$$

The moments M_0, M_1 and M_2 are related to the geometric average particle volume v_g and the standard deviation σ by:

$$M_k = M_0 v_g^k \exp\left(\frac{9}{2}k^2\ln^2\sigma\right) \qquad (4.1.7)$$

Following Pandas and Pratsinis (1995) the moments and the monomer concentration are expressed per unit mass of carrier gas instead of using concentrations per unit volume of carrier gas. This is done in order to cope with the non-isothermal conditions in the system. We define:

$$\hat{M}_k = \frac{M_k}{\rho_g} \qquad (4.1.8)$$

this transforms the moment equation into:

$$\frac{\mathrm{d}\hat{M}_0}{\mathrm{d}t} = \frac{I}{\rho_g} + \left(\frac{\mathrm{d}\hat{M}_0}{\mathrm{d}t}\right)_{coag} \qquad (4.1.9)$$

$$\frac{\mathrm{d}\hat{M}_1}{\mathrm{d}t} = \frac{I\,k^* v_1}{\rho_g} + \left(\frac{\mathrm{d}\hat{M}_1}{\mathrm{d}t}\right)_{cond} \qquad (4.1.10)$$

$$\frac{\mathrm{d}\hat{M}_2}{\mathrm{d}t} = \frac{I\left(k^* v_1\right)^2}{\rho_g} + \left(\frac{\mathrm{d}\hat{M}_2}{\mathrm{d}t}\right)_{coag} + \left(\frac{\mathrm{d}\hat{M}_2}{\mathrm{d}t}\right)_{cond} \qquad (4.1.11)$$

in which the change of the moments due to a specific mechanism (nucl=nucleation, cond=condensation, coag=coagulation) is a function of the moments themselves, derived by Pratsinis (1986). Harmonic averaging is being applied in order to cope with the different coagulation and condensation rates in the free-molecular and continuum regime. The monomer mass balance, also expressed per unit mass carrier gas, is:

$$\frac{\mathrm{d}\hat{n}_1}{\mathrm{d}t} = -\frac{Ik^*}{\rho_g} + \left(\frac{\mathrm{d}\hat{n}_1}{\mathrm{d}t}\right)_{cond} \qquad (4.1.12)$$

The gas density, gas viscosity and mean free path of the gas are described using temperature-dependent functions.

4.1.2 Results and discussion

Until now, no systematic study of the nucleation behaviour of the elements has been carried out. It is, however, very useful to know which temperatures are needed to induce particle formation. Applying the homogeneous nucleation formula, the following screening procedure is used. At a certain maximum temperature, which can be thought of as the furnace temperature for instance, a monomer concentration is generated in accordance with the saturation pressure. Then the gas is cooled and supersaturation is created. The nucleation rate has to be screened over the whole range between maximum temperature and room temperature, as it is possible that a system shows no nucleus formation (here defined where the nucleation rate is smaller than 1 cm^{-3}/s, which is an often encountered criterion for particle formation) at room temperature but it does at intermediate temperatures. B, C, W, Cr, Ge and Si e.g. show this behaviour. This can be seen in Fig. 4.1.1 which shows the nucleation rate of several elements when initially a temperature of 60 % of the melting point is established and then cooled down to the indicated temperature. This maximum in the nucleation rate is however an exception, usually a continuously increasing nucleation rate is found when going to lower temperatures.

The moment method was applied to follow the complete particle formation process with nucleation, condensation and coagulation. In order to validate the model, experimental results for silver nanoparticles (Scheibel and Porstendörfer, 1983) are modeled. In these experiments, silver powder in a boat is heated in a tube furnace, forming nanoparticles during the cooling down. The temperature and cooling rate was determined experimentally and the particle size distribution was measured using a DMA. The temperature at the center of the tube was found to be 70 K lower than the furnace temperature. In Fig. 4.1.2 it can be seen that the model describes the experiments (which apply a cooling rate of 3300 K/s) satisfactorily, in view of the incertainties in the surface tension and the nucleation model. The influence of the cooling rate is also shown: the higher the cooling rate, the smaller the resulting particle size at a given temperature. This can be explained from the competition between nucleation at the one hand and condensation and coagulation at the other hand. A slow cooling down results in a lower nucleation rate, so that the particles formed have more time for interaction which each other and with condensing molecules.

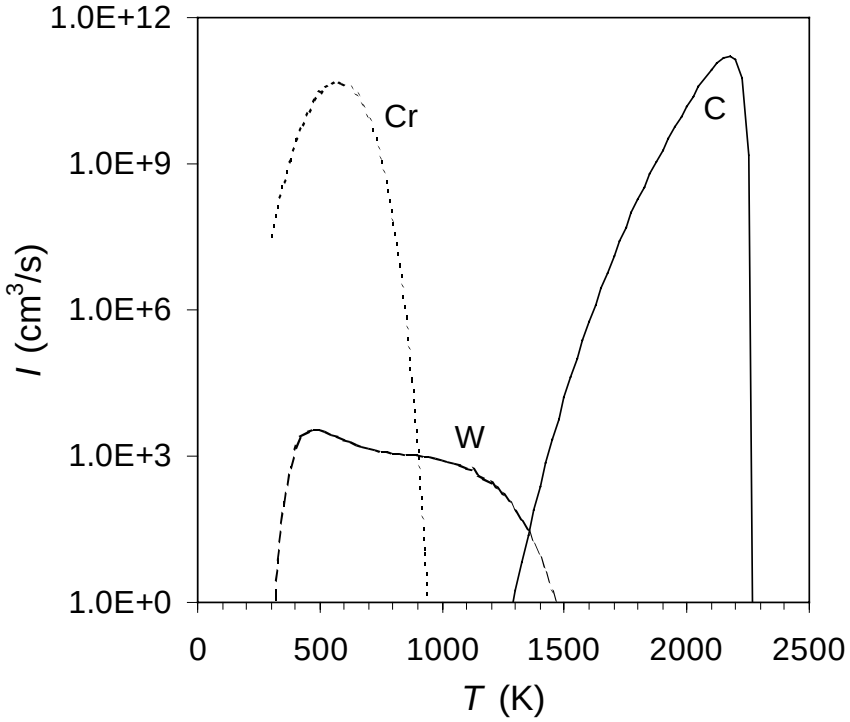

Fig. 4.1.1. Nucleation rate of different elements in N_2 at 1 bar as function of temperature, after creating saturation at T=0.6 T_m (2294 K for C, 2210 K for W, 1278 K for Cr)

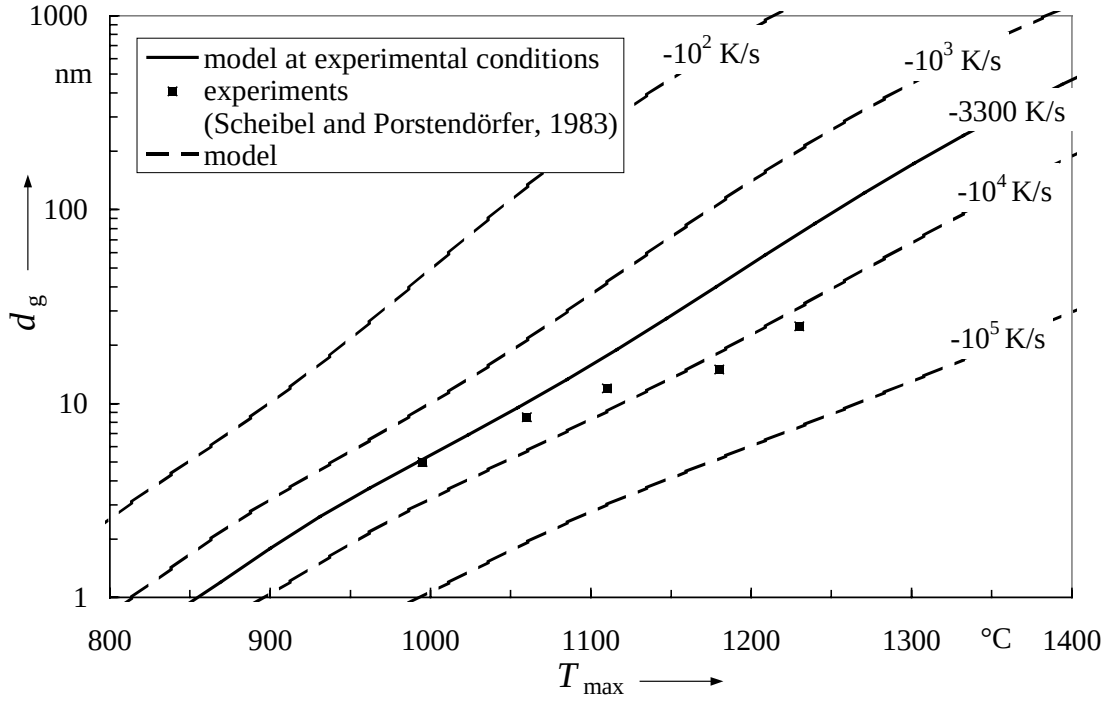

Fig. 4.1.2. Geometric mean particle diameter of Ag particles when cooling down from T_{max} to room temperature with different cooling rates indicated. Lines are based on the moment model, experimental data is shown as points.

The nucleation model and the moment model are now used to screen the different elements on their ability to form nanoparticles. Here we distinguish nucleation ability and particle formation ability. In table 1 it can be seen to what temperatures a material has to be heated to initiate nucleus formation, indicated by T_n. As can be seen, almost all elements show initial particle formation when heated up to the melting point. The results are independent of system pressure or carrier gas, as the saturation pressure is pressure-independent. It has to be pointed out that the surface tension is a very critical parameter in calculating the nucleation rate. Small changes in the surface tension lead to dramatic changes in the nucleation rate. Therefore the table should be viewed with some care. The other way around, nucleation experiments could be used to check the correctness of the applied surface tension.

The next question is to what particle size the nuclei will grow when nucleation occurs. Using the standard submicron particle detection techniques such as condensation nucleus counters particles as small as 3 nm can be detected. For the elements shown in Table 4.1, the moment model was applied in order to find the maximum temperature needed resulting in a geometric particle diameter of 3 nm. This temperature is indicated in the table by T_p. A cooling rate of 10^3 K/s was chosen which is a normal cooling rate to be expected in tube furnaces. Rates in the order of 10^5 K/s are more characteristic for plasma- and laser-driven syntheses. The calculation has been performed until the temperature reaches room temperature.

As can be seen from the table, is this temperature T_p in most cases hundreds degrees Kelvin higher than the maximum temperature where the nucleation starts. Thus it seems that this ‘nucleation’ criterion expressed by T_n is not a practical criterion in order to predict the start of detectable particle formation. The table can be used in order to get an idea of the minimum furnace temperatures needed for nanoparticle formation of the different elements.

From this table, also the limitations of the evaporation-condensation method using tube furnaces become clear: the temperature needed for nanoparticle formation is for many elements above 2000 K, so that the use of tube furnaces becomes questionable due to material problems and too elevated costs. An example of such an element is Pt, which is potentially interesting as dopant in gas sensing applications. For these elements, alternative methods have to be applied which are crucible-free, such as laser ablation.

Table 4.1. Melting temperature T_m, maximum temperatures necessary for nucleus formation T_n ($I > 1$ cm^{-3}/s) and maximum temperature T_p needed for reaching a geometric particle diameter of 3 nm. For the calculation of T_p, a cooling rate of 10^3 K/s until room temperature was used with N_2 at atmospheric pressure as carrier gas.

	T_m/K	T_n/K	T_p/K		T_m/K	T_n/K	T_p/K		T_m/K	T_n/K	T_p/K
Ag	1235	740	1190	K	337	380	430	Ru	2583	1550	2330
Al	934	840	1310	La	1193	1120	1740	S	386	310	360
As	1267	480	560	Li	454	450	690	Sb	904	490	720
Au	1338	960	1530	Mg	922	610	660	Sc	1812	940	1410
B	2573	1440	2110	Mo	2890	1620	2490	Se	490	320	460
Be	1551	840	1300	Mn	1517	730	1120	Si	1683	1080	1620
Bi	545	530	840	Na	371	390	490	Sr	1042	480	690
C	3823	1760	2450	Nb	2741	1810	2630	Ta	3269	1900	2940
Ca	1112	530	760	Ni	1726	1210	1590	Tc	2445	1610	2450
Co	1768	1130	1660	Os	3318	1860	2850	Te	723	390	580
Cr	2130	980	1530	P	317	310	420	Ti	1933	1120	1740
Cu	1357	790	1250	Pb	601	550	870	Tl	577	590	800
Fe	1808	1010	1590	Pd	1825	950	1530	U	1406	1180	1740
Ga	303	720	1150	Po	527	360	530	V	2163	1210	1860
Ge	1211	820	1260	Pt	2045	1350	2130	W	3683	1990	3020
Hf	2500	1950	2950	Rb	312	360	390	Y	1796	1040	1620
In	430	450	560	Re	3453	1865	2900	Zn	693	570	600
Ir	2638	1790	2480	Rh	2239	1300	2060	Zr	2125	1450	2340

4.2 Coagulation and aggregation: a Monte Carlo simulation

Once particles are formed and are solid, coalescence will not any more be rapid and aggregates consisting of primary particles develop. When the collision takes place at room temperature, in general the primary particles will conserve their original shape. At higher temperatures, solid state diffusion or viscous flow between the primary particles can lead to complicated structures.

The classical way of dealing with coagulation (here defined as describing colliding droplets) and aggregation (describing colliding solid particles) is the Smoluchowski equation (Smoluchowski, 1917). An analytical solution to this equation is only possible in the case of simple collision kernels, which are not relevant for the

systems of interest discussed above. In the case of complex coagulation kernels however, the problem has to be solved by numerical means.

This population balance problem is traditionally solved by discrete population balances, moment methods or sectional methods. Solving the discrete particle (or ’cluster ‘) dynamic equation based on the Smoluchowski equation for the whole submicron size spectrum implies that more than 10^9 differential equations have to be solved simultaneously in order to describe the particle size distribution $n(v,t)$ between 1 nm and 1 µm. This is computational too expensive at the moment. It has been done, however, for only a small part of the particle size spectrum, e.g. up to 20 basic units in a particle whereas the larger particles are described by the sectional representation (Landgrebe and Pratsinis, 1990). Another way of numerical simulation assumes some form of the particle size distribution, e.g. a log-normal one, which results in a few relatively easy to solve equations for the moments of the distribution (Pratsinis, 1988, Otto and Fissan, 1999). Finally, the particle size distribution can be cut into sections for which differential equations can be derived (Litster *et al.*, 1995). It provides the solution accurately when the number of sections is high enough with a reasonable computational time.

All these methods have the following drawbacks:

- There is no information about the history of each particle. The particles are described by means of their volume. It cannot be traced back which particles collided to form a bigger particle and the information about the internal structure is lost. Especially in case of aggregates this is a problem, as sometimes the size distribution of the primary particles composing an aggregate has to be known. Such cases are e.g. the mixing of solid particles with different composition and the coating of large particles with smaller ones.
- When more-dimensional systems have to be dealt with, the sectional representation results in very complex algorithms. Examples are additional information about the agglomerate form (Xiong and Pratsinis, 1993) using a particle size distribution $n(v,a,t)$ describing the particle volume and area or about the charge distribution (Vemury *et al.*, 1997) which requires the solution of $n(v,q,t)$ describing volume and charge level.

A classical method to overcome such drawbacks is to use Monte Carlo simulation methods. A well-known example of this method is the simulation of the Brownian movement by stochastic processes. When a sufficient number of particles is taken, collisions will result from the random Brownian motions and a change in the particle size distribution can be recorded. With the help of such trajectory methods based on the Langevin equation Brownian coagulation of droplets (Pearson *et al.*, 1984) and agglomerate formation by Brownian coagulation (Gutsch *et al.*, 1995) have been described. Such methods can deliver a priori coagulation rates, but are time-consuming

and are not suited for simulating large number of particles. The number of simulated particles is here usually between 500 and 1000.

When the collision rates are known, a much simpler method can be used. This method bases on choosing collision partners by a stochastic game and is known as the Direct Simulation Monte Carlo method (DSMC, Bird, 1976). It was originally developed for describing gas dynamics and is essentially the simulation of molecular collisions without regarding their spatial positions. As the number of particles in real systems is too large for the present computer memories, the simulation volume is chosen such that a reasonable amount (10^4 – 10^5) of simulation particles results. Advantageous is that information about the history and internal structure of the particles is available, and that multi-dimensional systems such as charged and multicomponent aerosols, requiring the solution of $n(v,q,c,t)$ describing particle volume, charge level and composition, can be simulated. Monte Carlo (MC) simulations are computationally expensive, computer power has reached however a level where simulations with up to 10^5 particles are now possible on fast PCs. Furthermore, more care has to be taken to ascertain that the numerical solutions, which vary due to the use of random numbers, are representative ones. The MC algorithms for solving particle dynamics are however easily programmed, and it can be said that in comparison to sectional models the time spent on solving a problem is shifted from the programmer to the computer.

The DSMC method has been used before to solve complex problems which involved particle collisions (e.g. Shah *et al.*, 1977, Bapat *et al.*, 1983). There are however few studies in which different DSMC methods for solving the coagulation and aggregation problem are investigated and tested more in detail. In this subchapter, these methods are briefly described and then a related method is proposed which is computationally more efficient. The accuracy of the solutions is tested by comparing them with (I) analytical solutions and (II) numerical results from a sectional model. Two examples of industrial relevance are given to show the suitability of the DSMC method for describing complex multi-dimensional particle dynamics.

4.2.1 Direct Simulation Monte Carlo methods

It is assumed that the *N* colliding particles with an initial distribution $n_0(v)$ are contained in a fluid of volume *V*. This volume is chosen such that *N* is a reasonable number, with the present personal computer power not more than 10^5. It is further assumed that all collisions are binary, i.e. we are not dealing with concentrated dispersions or slurries, and that the sticking coefficient is unity. The collision rate β is a known function which depends on the properties of the medium and on the properties of the colliding particles.

The particulate system considered here is usually described by the Smoluchowski equation:

$$\frac{\partial n_k}{\partial t} = \frac{1}{2}\sum_{i=1}^{k-1} \beta_{i,k-i} n_i n_{k-i} - n_k \sum_{i=1}^{\infty} \beta_{i,k} n_i \qquad (4.2.1)$$

where t is the time, n_k is the number concentration of the k-fraction and $\beta_{i,k}$ is the collision rate of the particle pair (i,k) which defines the kinetics of the process. In the DSMC method, particle pairs are selected by stochastic methods based on the transformation of collisions rates into collision probabilities.

Garcia *et al.* (1987) describes two stochastic methods based on the simulation procedure for a Markov process. The methods were not tested by these authors, however. The mean time between two collisions events is τ, which can be calculated by:

$$\tau = \frac{1}{\sum_{i=1}^{N}\sum_{j=i+1}^{N} \beta_{i,j}^{V}} \qquad (4.2.2)$$

in which β^V is the collision rate in a volume V. It is assumed that τ is an exponentially distributed random variable. This time is therefore selected by means of a random number generator. The coagulation pair (i,j) is chosen on the basis of the probability $Pr_{i,j}$ which is calculated by:

$$Pr_{i,j} = \frac{\beta_{i,j}^{V}}{\sum_{k=1}^{N}\sum_{l=k+1}^{N} \beta_{k,l}^{V}} \qquad (4.2.3)$$

As it is in this method necessary to calculate the collision rates of all possible particle pairs (inverse method) which is time-consuming, Garcia *et al.* (1987) proposed a second method based on the acceptance-rejection procedure (Bird, 1976). Here, a particle pair (i,j) is selected entirely at random independent of the collision probability. Then this pair is accepted as a collision pair if

$$R < \frac{\beta_{i,j}^{V}}{\max\left\{\beta_{k,l}^{V}\right\}} \qquad (4.2.4)$$

where R is a random number uniformly distributed between 0 and 1. When the pair is rejected, a new random number is selected, and so on, until the condition is fulfilled. This method is only practical when the maximum of the collision rate can easily be

determined and might introduce an error according to Garcia *et al.* (1987). In order to investigate this error, simulations are compared based on this method with the analytical solution for the simple collision kernel $\beta = A(i + j)$ (described further in this subchapter). The results are shown in Fig. 4.2.1. Even with 10^5 simulation particles, the error in the total particle number is rather large as in comparison with the results which will be shown further on. Furthermore, when the range of particle sizes increases the ratio of the randomly generated collision rate and the maximum collision rate becomes very small, the large number of rejections slows down the program considerably. As an example, in an aerosol system with wide range of particle classes undergoing Brownian coagulation $\beta(d_1 = 1\,\text{nm}, d_2 = 1\,\text{nm}) / \beta(d_1 = 1\,\text{nm}, d_2 = 100\,\text{nm})$ at standard conditions is in the order of 10^{-3}.

A third method is proposed by Liffman (1992) who uses a two-step method. The mean time which particle *i* experiences between two collision events is:

$$\tau_i = \frac{1}{\sum_{j=1}^{N} \beta_{i,j}^{V}} \qquad (4.2.5)$$

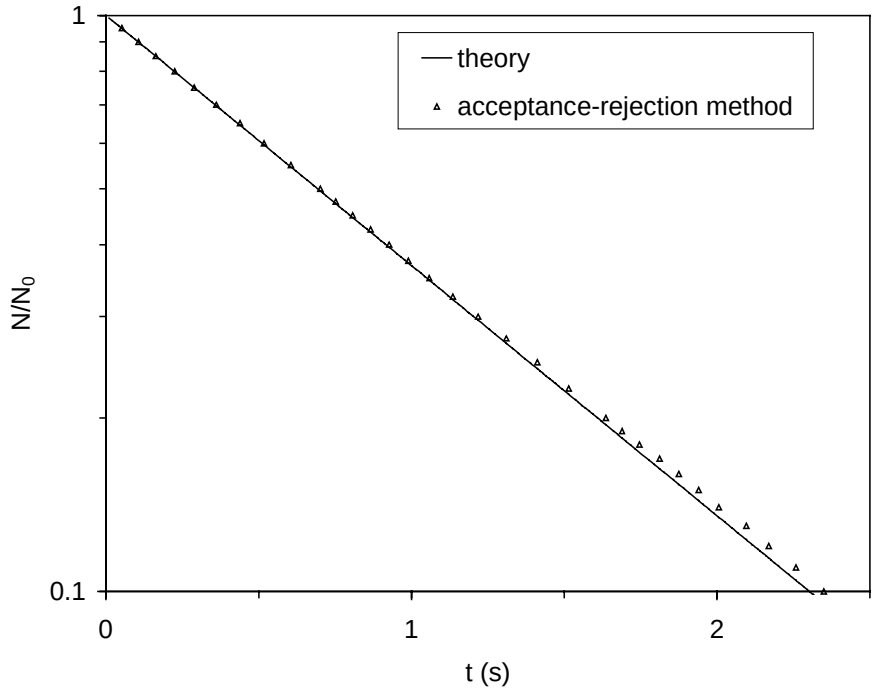

Fig 4.2.1. Decrease in relative total number concentration N / N_0: comparison between theory (Case 2 , $\beta_{i,j}$=A(i+j)) and the acceptance-rejection Monte Carlo simulation procedure of Garcia et al. (1987). Number of simulation particles: 10.000

It is assumed that this time is an exponentially distributed function. A time step is chosen which should be much smaller than the smallest value of all possible τ_i's. Then, the particle *i* is accepted if

$$R < 1 - e^{\left(-\frac{\Delta t}{2\tau_i}\right)} \tag{4.2.6}$$

When *i* has been found, the collision partner *j* is found by computing first all collision probabilities between the chosen particle *i* and any other particle *j*:

$$Pr_j = \frac{\beta_{i,j}^V}{\sum_{k=1}^{N} \beta_{i,k}^V} \tag{4.2.7}$$

and then selecting *j* by means of:

$$\sum_{k=1}^{j-1} Pr_k \le R \le \sum_{k=1}^{j} Pr_k \tag{4.2.8}$$

As in the acceptance-rejection method of Garcia *et al.* (1987), selecting one particle pair might take a large number of random numbers which is computationally expensive. A further problem is that it is no clear criterion to select the time step. Nevertheless, the simulation results were extensively compared with analytical solutions and found to be correct.

4.2.2 A Fast DSMC method

A new method is proposed which is related to the inverse method. As the collision kernel represents the probability of a binary collision in unit time, the sum over all collision kernels will be the probability that one collision takes place in the particle ensemble in unit time. So the mean time $\langle\tau\rangle$ needed for one collision taking place in the particle ensemble is the inverse of the sum of all collision kernels:

$$\langle\tau\rangle = \frac{2}{\sum_{i=1}^{N} \sum_{i=1, i\neq j}^{N} \beta_{i,j}^V} \tag{4.2.9}$$

The factor 2 is added in order to account for the double counting of the particle pairs. A collision pair is chosen by making a list of all pairs and accumulate the collision rate until the sum surpasses a random number. If a random number *R* is

uniformly distributed in (0,1], $R\sum\sum\beta_{i,j}^{V}$ is uniformly distributed in (0, $\sum\sum\beta_{i,j}^{V}$]. We can put the selection criterion as follows:

$$\sum_{k=1}^{i}\sum_{l=1}^{j}\beta_{k,l}^{V} \le R\sum_{k=1}^{N}\sum_{l=1}^{N}\beta_{k,l}^{V} \le \sum_{k=1}^{i}\sum_{l=1}^{j+1}\beta_{k,l}^{V} \quad \text{with } k \neq l \tag{4.2.10}$$

which causes the particle pair *(i,j)* to form a new particle with volume $v_i + v_j$ (see Fig. 4.2.2). Only one random number is used for the selection of a particle pair and no acceptance-rejection procedure takes place. If *m* steps are completed, the total time can be simply calculated from:

$$t = \sum_{i=1}^{m}\langle\tau\rangle_i \tag{4.2.11}$$

When an initial size distribution has to be modeled, it is generated by means of a random generation method (Rubinstein, 1981). The DSMC method can be applied in a aggregation mode, in which each aggregate is assigned an array indicating which primary particles compose the aggregate, or in an coagulation mode, in which after each collision the new (droplet) properties such as volume and density are stored.

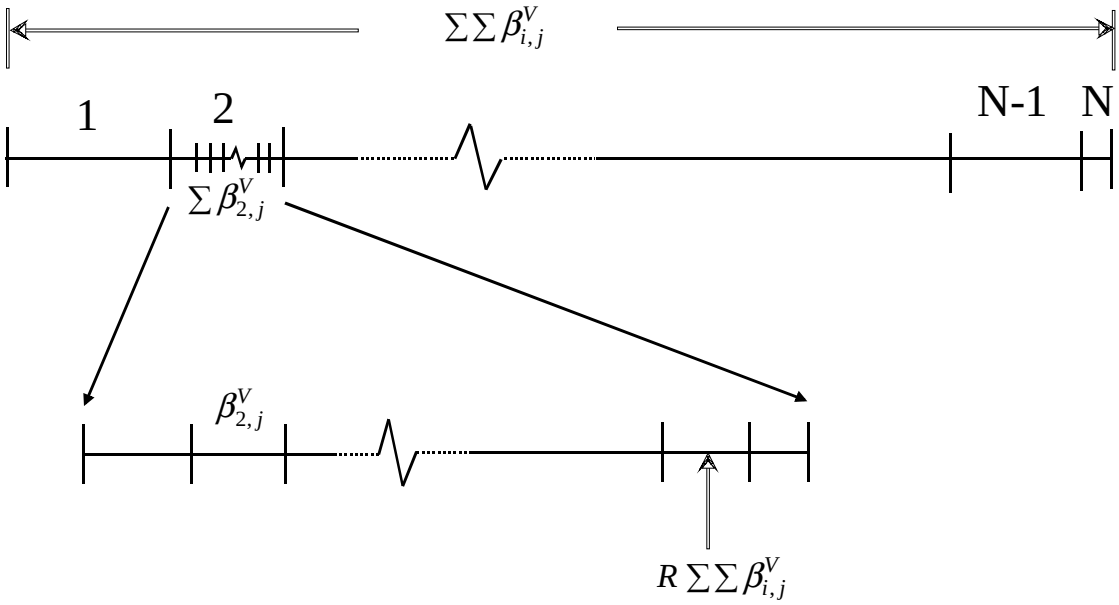

Fig. 4.2.2. Illustration of the MC technique used to choose pairs of colliding particles (i,j) by means of a random number R. In this procedure the collision rates of all possible particle pairs are weighted.

During the simulation the number of simulation particles N drops, which means that the error increases as the sample error is in the order of $\sigma/\sqrt{N}$. In order to encounter this, the simulation volume V and the number of particles N are doubled when the concentration has dropped by half. The properties of each 'old' particle are of course copied to the 'new' particles in the additional volume in order to conserve the statistical properties. This procedure is discussed by Liffman (1996).

It should be pointed out that this method necessitates the calculation of the collision rates of all possible particle pairs. If N is large, the storage of N^2 collision rates becomes prohibitive: 10^5 simulation particles would mean the storage of 10^{10} collision rates. In order to overcome this, for each particle only the sum of possible collision rates is stored and by means of the random number it is determined which particle i is selected. Then the collision rates of i with the other particles is calculated and summated until the condition 10 is met. This method implies the storage of only N values. After each pair selection, a simple correction can be made in the summated collision rate values to account for the change in particle properties and, consequently, in the collision rates. The large number of calculations of the collision rate, which are independent of each other, makes the simulation very suitable for parallel computing.

The method described here is similar to the inverse method of Garcia *et al.* (1987). However, exponentially distributed time steps between collisions which would necessitate a random number and a correction of all collision rates as in the work of Garcia are not used, instead a calculated deterministic mean time is used. This is possible due to the large number of simulated particles and greatly accelerates the simulation procedure.

4.2.3 Comparison with theoretical solutions for aggregation

Obviously, the fast DSMC must be compared to known theoretical solutions to determine if it is a valid method of analysis and to become an idea of the accuracy. There exist only a few forms of the collision kernel for which an analytical solution of the Smoluchovski equation exists (Spouge, 1983). $\beta_{i,j}=A$, $\beta_{i,j}=A(i+j)$, $\beta_{i,j}=Aij$. Here A is a constant, i,j are the section numbers. The fast DSMC method is examined using these collision kernels. The initial particle size distribution is monodisperse.

Case 1. $\beta_{i,j}=A$. If we define N_0 as the initial number of primary particles at $t=0$, the total number of particles N at time t is

$$N=\frac{N_0}{1+N_0At/2} \qquad (4.2.12)$$

The probability of obtaining a particle, containing k primary particles is:

$$P_k = \frac{(N_0 At/2)^{k-1}}{(1+N_0 At/2)^k} \tag{4.2.13}$$

Case 2. $\beta_{i,j}=A(i+j)$. In this case the decrease of particle number can be expressed as:

$$N = N_0 e^{-N_0 At} \tag{4.2.14}$$

with the probability of obtaining a k-aggregate

$$P_k = \frac{k^{k-1}}{k!}(1-e^{-N_0 At})^{k-1} e^{-k(1-e^{-N_0 At})} \tag{4.2.15}$$

Case 3. $\beta_{i,j}=Aij$. In this case there exists only an analytical solution for times shorter than a finite time $t=1/N_0A$,

$$N = N_0(1-N_0 At/2), \quad 0 \le t < \frac{1}{N_0 A} \tag{4.2.16}$$

$$P_k = \frac{k^{k-2}}{k!}\frac{(N_0 At)^{k-1}}{(1-N_0 At/2)} e^{-kN_0 At}, \quad 0 \le t < \frac{1}{N_0 A} \tag{4.2.17}$$

The results of the simulations for $N_0=10^{12}$ m^{-3} and $A=1/N_0$ are shown in Figs. 4.2.3 and 4.2.4. Fig. 4.2.3 demonstrates the high degree of accuracy of the DSMC method in simulating the decrease in relative total number concentration. Here, using even only 1000 simulation particles results in very accurate results for the total number concentration. The doubling procedure is a necessity, as can be seen in Fig. 4.2.3a where the total number concentration drops with a factor of 10^3. This results in some 8 doubling procedures, clearly resulting in an accurate description. Fig. 4.2.b,c show the two other test cases. The probability distribution of aggregates with k primary particles for the above mentioned test cases is however a more sensitive function of the number of simulation particles. The statistical nature of Monte Carlo simulations become evident when there are only few aggregates in the simulation volume. This can be seen in Fig. 4.2.4a,c. where the scatter increases at large k-numbers. Fig. 4.2.4b shows clearly the decrease of the statistical scattering when increasing the number of simulation particles from 10.000 to 100.000.

a)

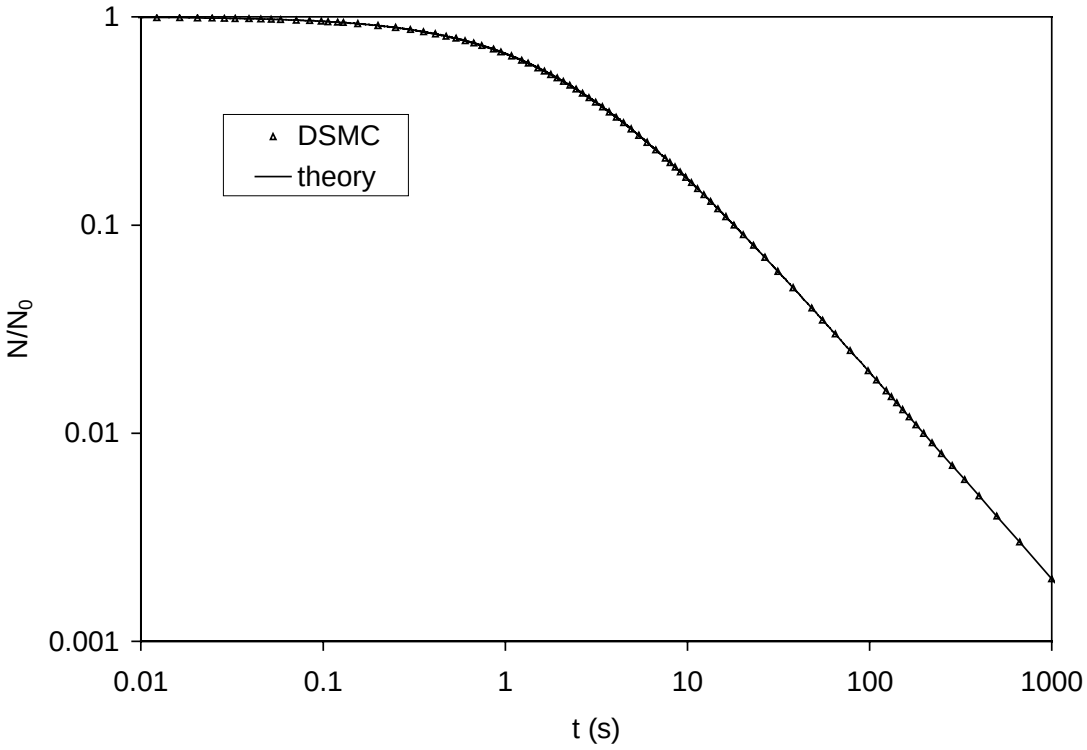
1
0.1
0.01
0.001
N/N0
DSMC
theory
0.01
0.1
1
10
100
1000
t (s)

b)

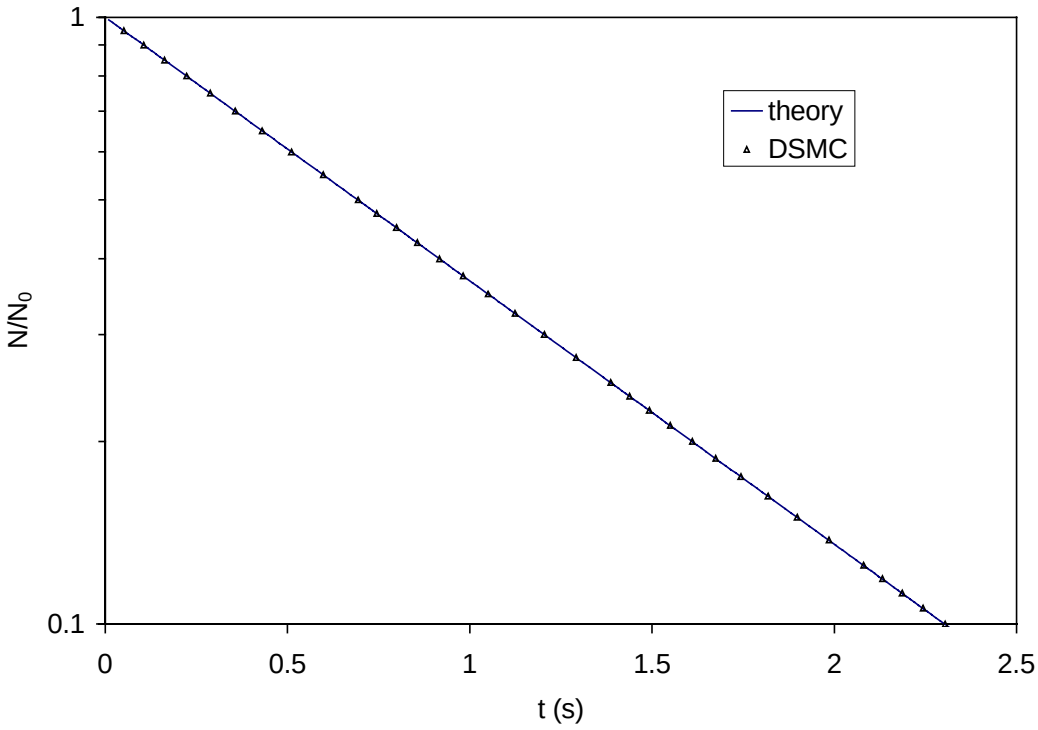
1
0.1
N/N0
theory
DSMC
0
0.5
1
1.5
2
2.5
t (s)

c)

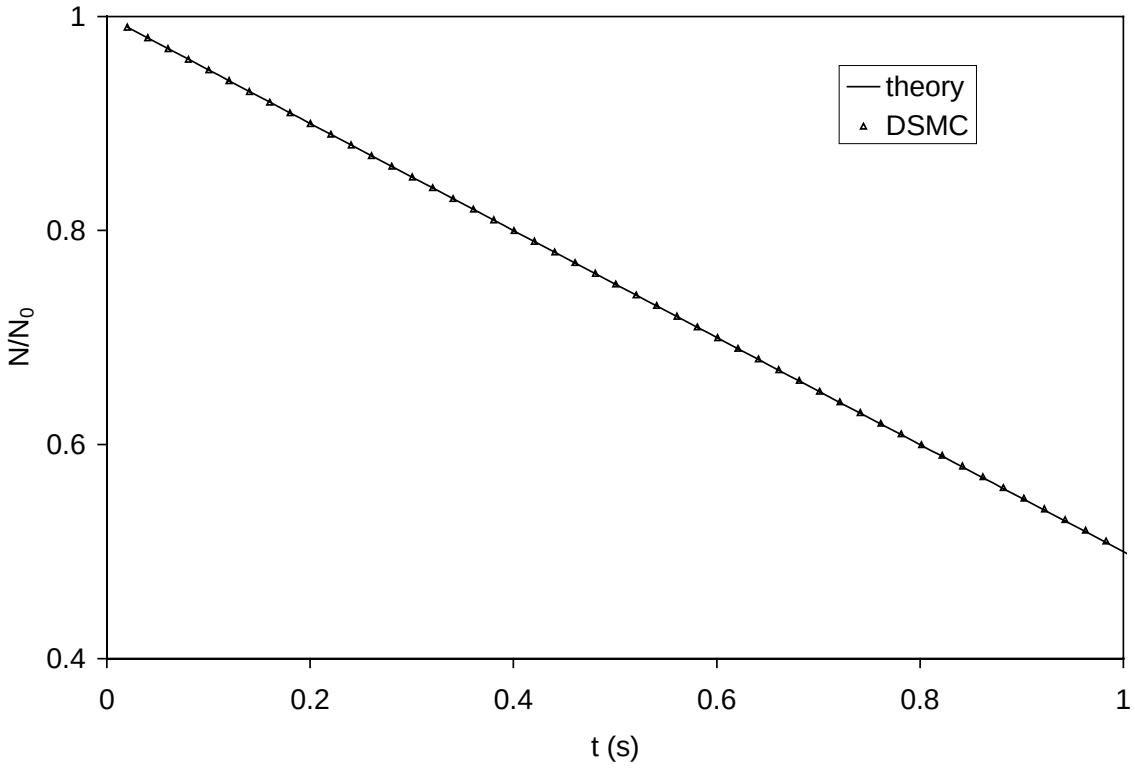

Fig. 4.2.3. Decrease in relative total number concentration N/N_0: comparison between theory and the Direct Simulation Monte Carlo method for (a) Case 1, $\beta_{i,j}=A$ (b) Case 2, $\beta_{i,j}=A(i+j)$. and (c) Case 3, $\beta_{i,j}=Aij$. Number of simulation particles: 1000.

a)

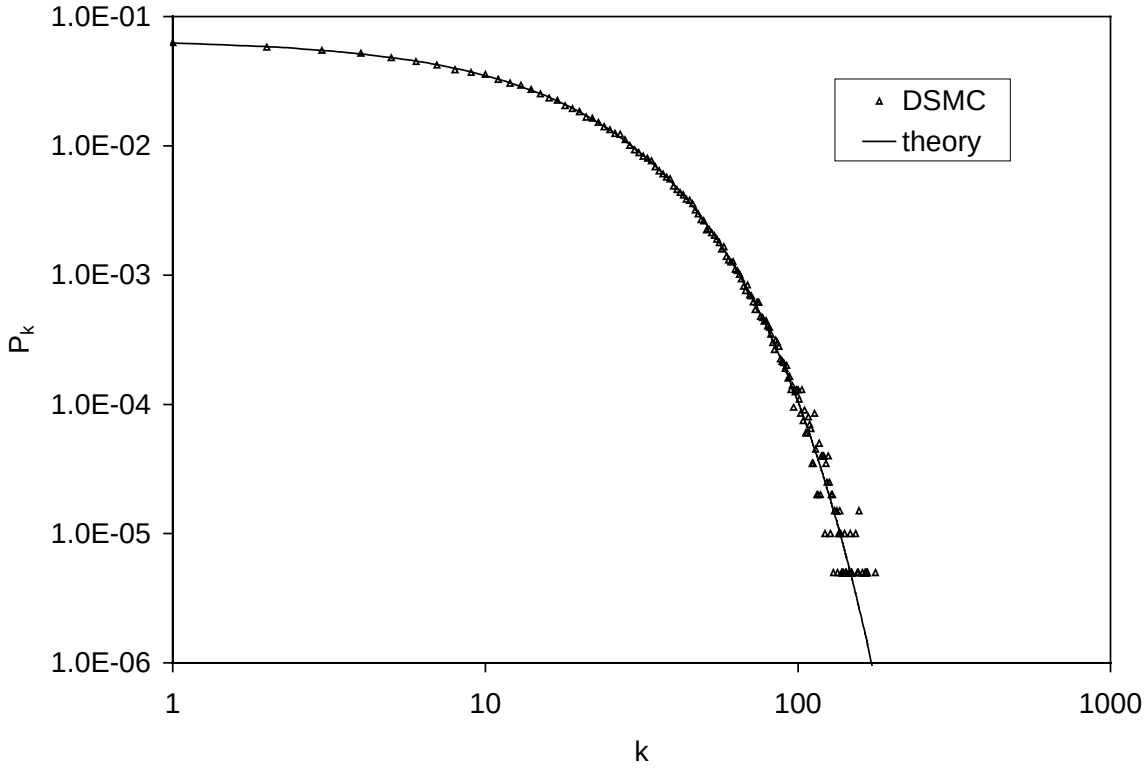
1.0E-01
1.0E-02
1.0E-03
1.0E-04
1.0E-05
1.0E-06
P_k
1
10
100
1000
k
DSMC
theory

b)

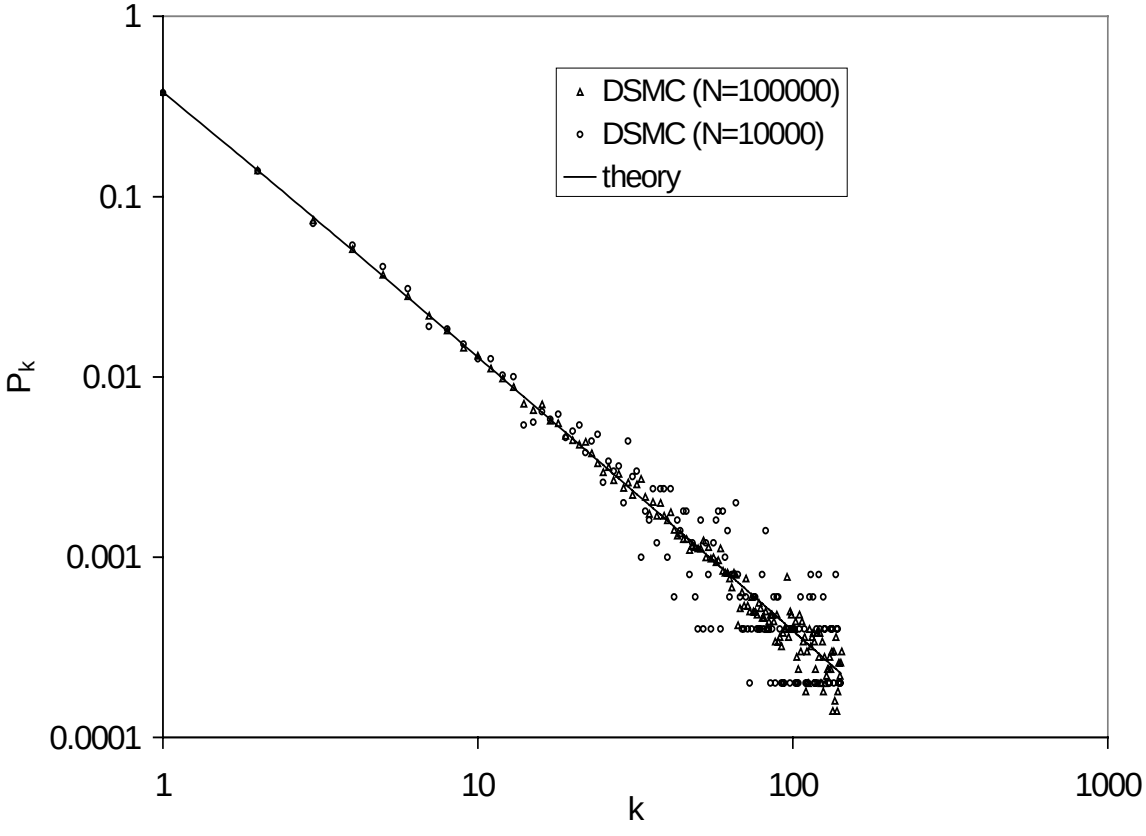
1
0.1
0.01
0.001
0.0001
P_k
1
10
100
1000
k
DSMC (N=100000)
DSMC (N=10000)
theory

c)

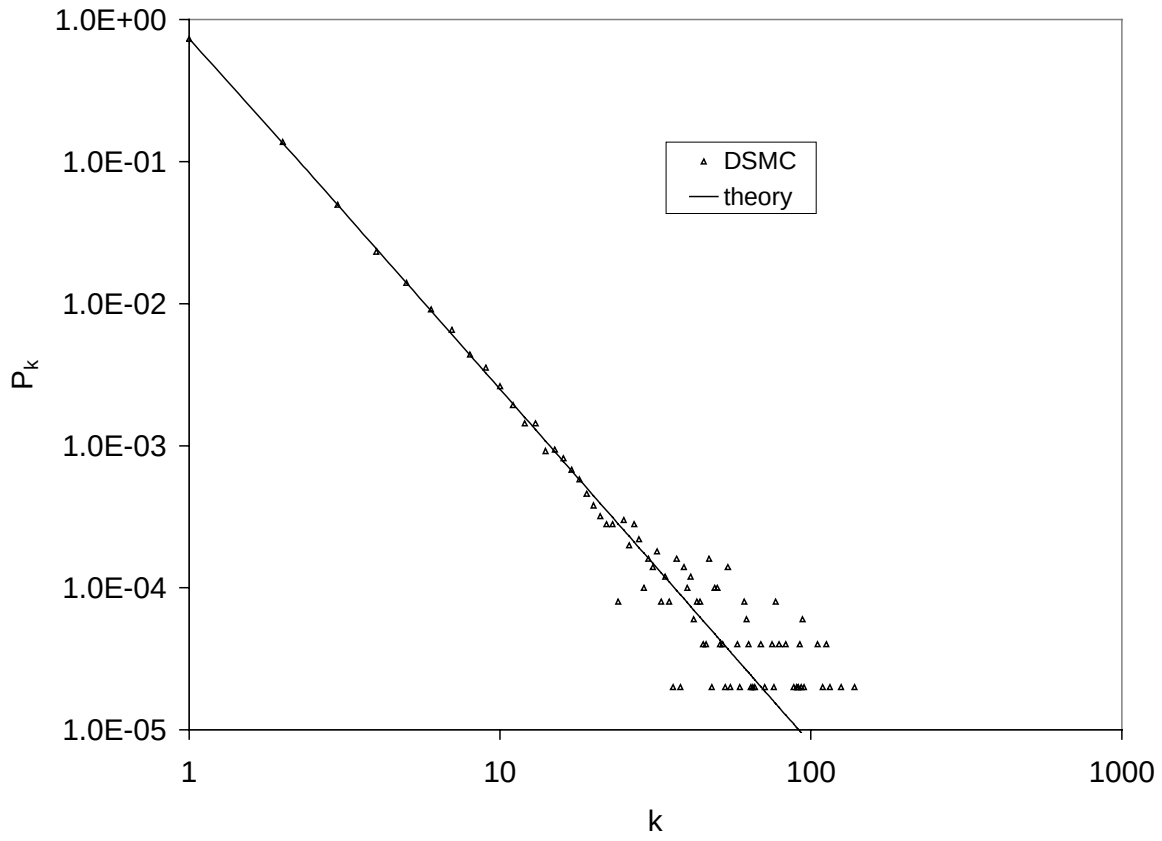

Fig. 4.2.4. The probability P_k of obtaining an aggregate containing k primary particles versus the size of the particles: comparison between theory and the DSMC method for (a) Case 1, $\beta_{i,j}=A$ at t=7.5 s (b) Case 2, $\beta_{i,j}=A(i+j)$ at t= 3.5 s and (c) Case 3, $\beta_{i,j}=Aij$ at t= 1 s. Number of simulation particles: 100.000 (a), 10.000 and 100.000 (b) and 100.000 (c).

4.2.4 Comparison with numerical solutions for coagulation

The form of the particle size distribution is an important issue in particle synthesis. In order to check the validity of the DSMC method in a more realistic system than cluster aggregation, a coagulating aerosol is simulated. In Fig. 4.2.5 the development of the geometric standard deviation σ_g in an initially polydisperse aerosol is shown. As reference a sectional model (Landgrebe and Pratsinis, 1990) is used with a section spacing of 1.08. It can be seen that two simulations with the same number of simulation particles can give different results due to the stochastic nature of the modeling. It is seen that when a sufficient number of particles is taken, the deviations to the sectional model are in the order of 1 %. As both methods are numerical it is difficult to say which one is the more correct one. The stochastic effect can be reduced by repeating the simulation with different random numbers. This is

shown in Fig. 4.2.5 for the case of 40.000 simulation particles, where the simulation now shows a smooth curve after taking the mean of 3 different simulations.

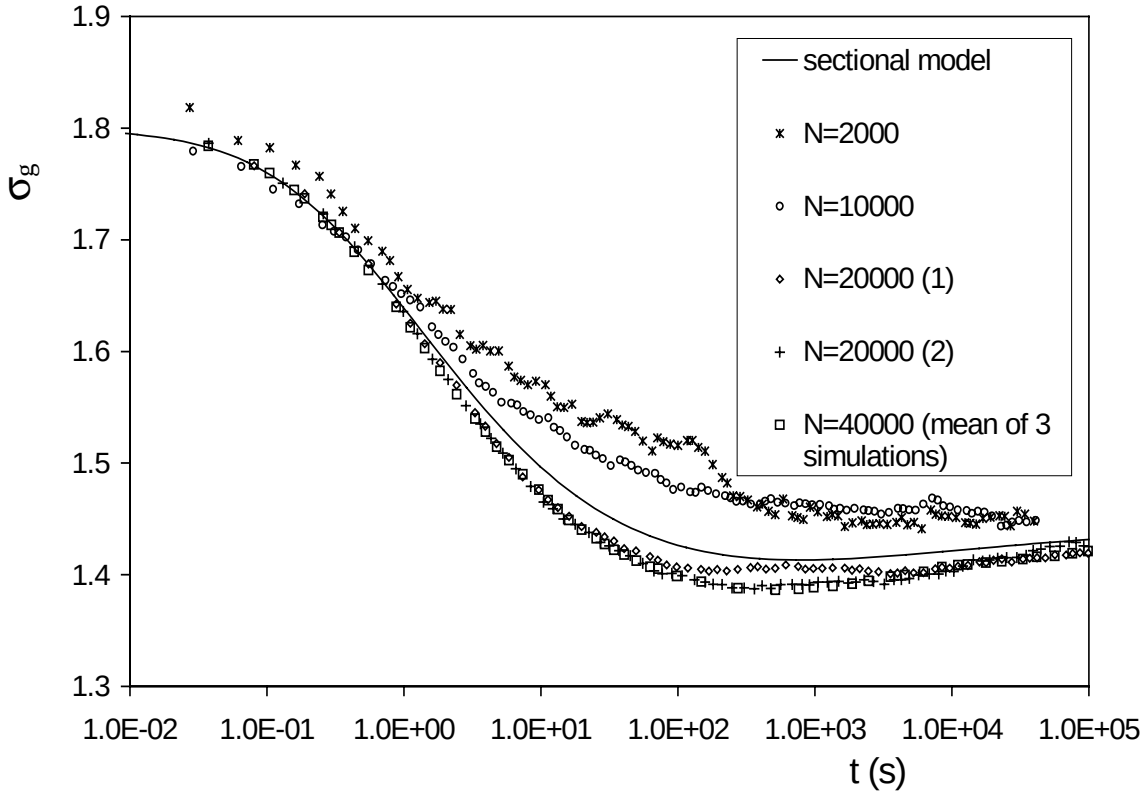

Fig. 4.2.5. The geometric standard deviation σ_g of a coagulating aerosol system (initially $d_g = 53.5$ nm, $N = 10^9\, cm^{-3}$ and $\sigma_g = 1.8$) as a function of time t: comparison between a sectional model and the DSMC method. The collision kernel used is from Dahneke (1983) and the sectional model used is by Landgrebe and Pratsinis (1990). The number of simulation particles N is indicated in the legend.

The statistic errors can be quantified by calculating the standard deviation from different simulations. This procedure is illustrated in Fig. 4.2.6, where the so-called self-preserving particle size distribution (Friedlander, 1977) for the collision kernel $\beta(v_i, v_j) = \left(v_i^{1/3} + v_j^{1/3}\right)\left(v_i^{-1/3} + v_j^{-1/3}\right)$ is shown. Ten DSMC simulations were made so that an estimation of the statistical errors could be obtained by the standard σ method (corresponding to a probability of 67 %). As can be seen from the figure, the form of the distribution is correctly described by the DSMC method and the standard σ method generally overestimates the error in the simulations. The statistical errors can be further reduced by increasing the number of simulations and/or the number of simulation particles. This was not further pursued here. Curve-fitting can also be

applied here. The most striking feature in the figure is that the left-hand side of the curve shows much larger statistical deviations than the right-hand side. This is due to the fact that the method is particle number-based: to the left of the maximum less simulation particles are available for one data point due to the logarithmic axis.

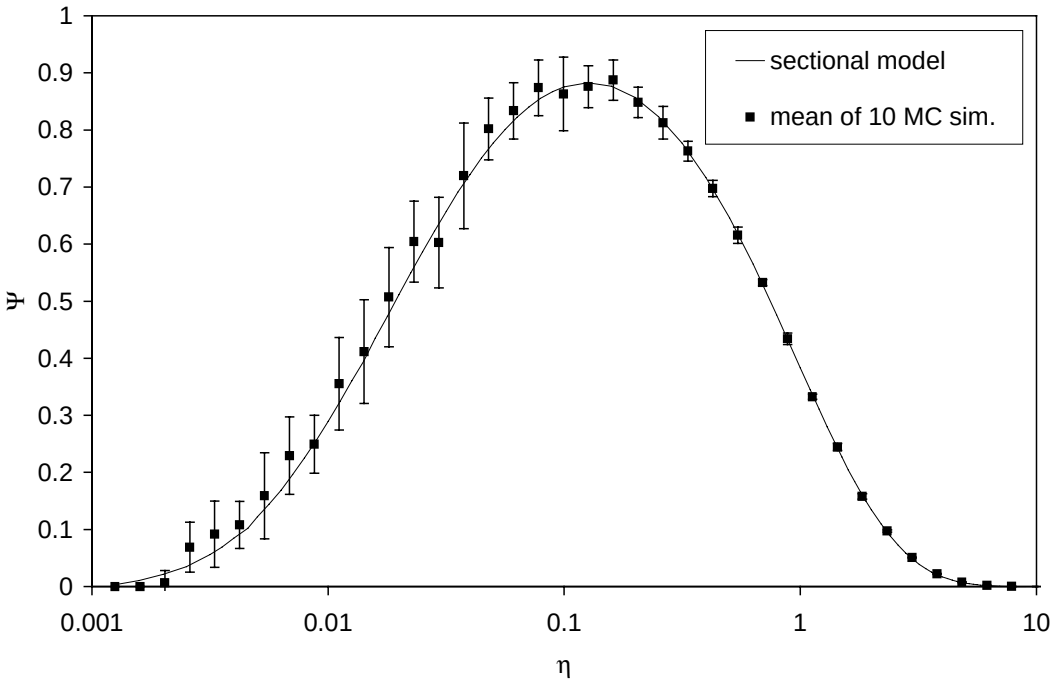

Fig. 4.2.6. Self-preserving particle size distribution for the collision kernel $\beta(v_i, v_j) = (v_i^{1/3} + v_j^{1/3})(v_i^{-1/3} + v_j^{-1/3})$*, in which the dimensionless particle density function* Ψ *(defined as* $Vn(v,t)/N^2$ *where V and N are the total particle volume and number) is a function of a dimensionless particle volume* η *(defined as* Nv/V*). The DSMC results are compared with results from Vemury et al. (1994) who use a sectional model. A confidence range of* $\pm\sigma$ *is calculated from 10 simulations.*

4.2.5 Case study 1: Chemical reaction in coagulating droplets (microreactors)

The standard numerical solution schemes, e.g. sectional models, for solving coagulating particle systems are more computer time-efficient than the DSMC simulation. They are however not very well suited for solving more complex systems such a reacting microdroplets. In order to show the applicability of the DSMC simulations, the reactive mixing of two sprays containing two different solutions is chosen. A chemical reaction takes place when droplets with solution A coagulate with droplets containing solution B, producing a new droplet acting as ‘microreactor’ in

which the product C is formed. This kind of mixing is used to mix two liquid reactants very fast. The chemical kinetics is given by:

$$\frac{\mathrm{d}[\mathrm{C}]}{\mathrm{d}t} = k\,[\mathrm{A}][\mathrm{B}] \qquad (5.2.18)$$

where $[A]$ denotes the concentration of A and k is a reaction constant. The problem is analogous with that of a chemical reaction in a liquid-liquid dispersion described by Shah *et al.* (1977). However, a polydisperse initial size distributions is used here. The chemical reaction is closely related to the droplet dynamics as a collision event changes the concentrations of the reactants and product, depending on the relative volume of the colliding droplets. The coagulation version of the DSMC code is very easily adapted for calculating the change in concentrations due to the chemical reaction between two collisions by adding only a few additional program lines.

The results of the simulation are plotted in Fig. 4.2.7. As collision kernel the collision frequency for the continuum regime (Friedlander, 1977) is taken. The results for the volume fraction of droplets *v/V* having the indicated product concentration [C] are shown in a histogram-fashion, with the values of the concentration located at the midpoint of a section. Here also several simulations were made to get an idea of the accuracy of the results by using the standard σ method. It is seen that only a few simulations are necessary to get a relative accurate result. The DSMC is an easily programmed method to calculate complicated multi-dimensional size distributions, in this case $n(v,[A],[B],[C],t)$.

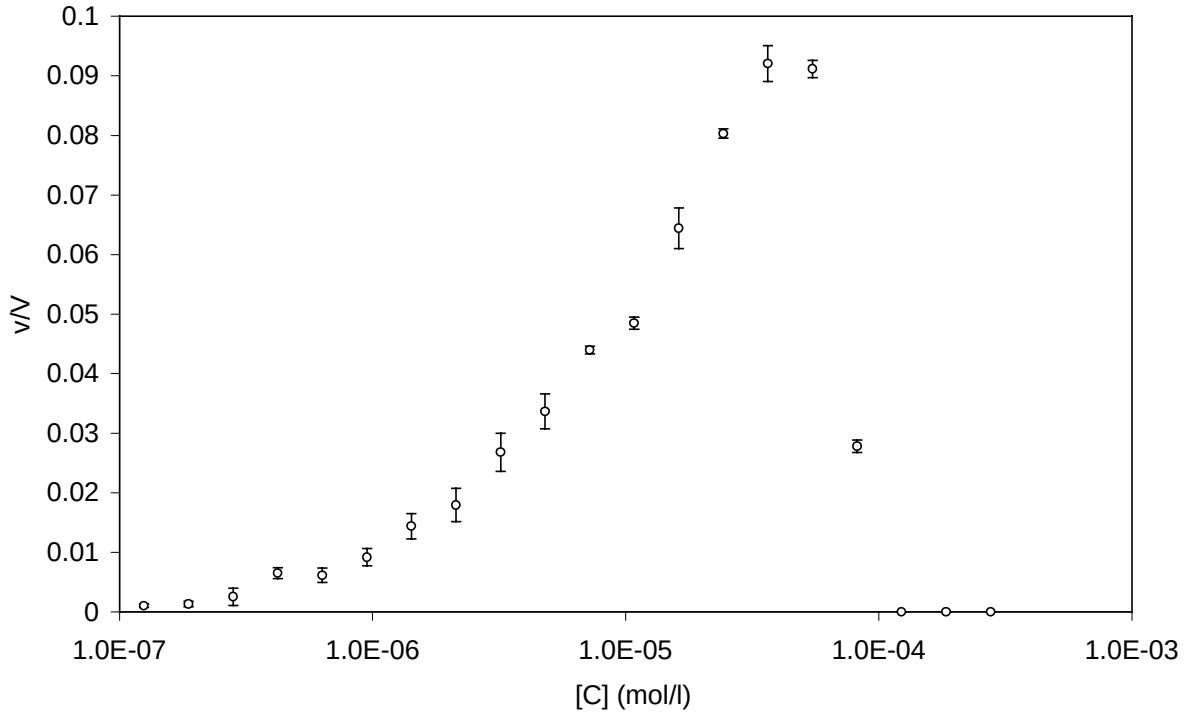

Fig. 4.2.7. Distribution of product concentration [C] resulting from the chemical reaction $A+B \rightarrow C$ with a reaction rate k=2.067 10^{-3} l/(mol s) between an A-containing spray (initially $[A]=10^{-3}$ mol/l, $d_g = 1$ µm, $N = 5\ 10^2$ cm^{-3} and $\sigma_g = 1.5$) and a B-containing spray (initially $[B]=10^{-3}$ mol/l, $d_g = 1$ µm, $N = 5\ 10^2$ cm^{-3} and $\sigma_g = 1.6$). v/V is the volume fraction of droplets having a concentration [C]. The time elapsed is 4.37 10^5 s. The initial number of simulation particles is 30.000 particles for each spray. The error bars ($\pm\sigma$) result from repeating the simulation 4 times.

4.2.6 Case study 2: Coating of particles with smaller particles by aggregation

A second example of a problem which is very difficult to solve with standard particle dynamical models is the coating of solid particles with nanoparticles with both particle fractions having an initially polydisperse size distribution. Particle coating is applied in industry to apply a functional, protective or wear-resistive layer and is often carried out in a fluidized bed reactor (Li and Hua, 1997). The problem is to determine how much of the surface of the larger particles (1 µm) is covered with the smaller particles (100 nm). This is expressed in the surface coverage, which is defined as the ratio of the sum of the area of all nanoparticles deposited on a large particle and the surface area of the large particle. Due to the polydisperse size distribution and the

random nature of the collision process, the surface coverage of the large solid particles will be a distributed variable.

For the DSMC simulation, it means that the aggregation mode has to be used where information on the primary particles composing an aggregate is stored. As an approximation, the collision kernel for the continuum regime (Friedlander, 1977) is used. The results are shown in Fig. 4.2.8 as a cumulative distribution of the surface coverage for different coating times indicated in the legend. As can be seen from the slopes of the curve, there is a rather broad distribution of surface coverage of the large particles. The results of the DSMC method are in fact a solution of the multi-dimensional size distribution $n(v_1, v_2, ..., v_{n_p}, t)$ in which n_p is the number of particles in the aggregate.

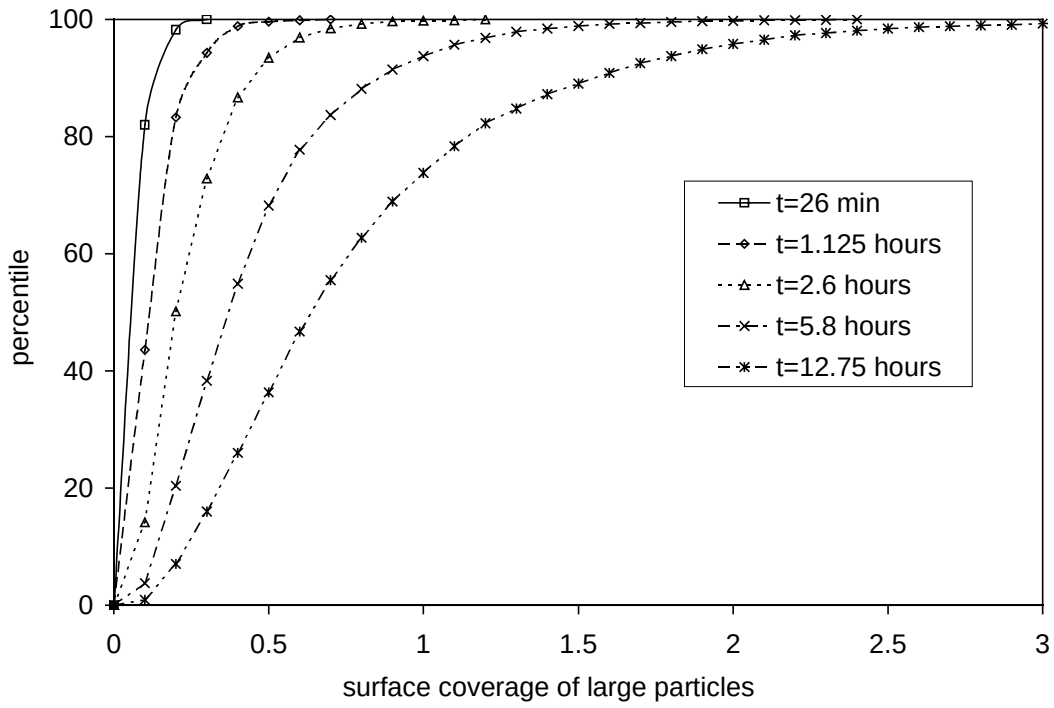

Fig. 4.2.8. Cumulative distribution of the surface coverage as a result of coating large particles ($d_g = 1$ μm, $N = 10^3 cm^{-3}$ and $\sigma_g = 1.2$) with nanoparticles ($d_g = 100$ nm, $N = 10^6 cm^{-3}$ and $\sigma_g = 1.5$) for different coating times indicated in the legend. The initial number of simulation particles is 20.000 for the nanoparticles, the simulation was repeated 5 times.

4.3 Mixing by means of aggregation of charged particles

A special case of nanomaterials is formed by composite particles, here defined as aggregates composed of two different particle classes. The technological use of such particles is manyfold, e.g.:

- improve the functional properties of semiconductor nanoparticles by adding a second semiconductor particle which provides a charge transfer, thereby improving the quantum yield,
- improve the functional properties of nanoparticles by adding another nanoparticle which has catalytic properties, such as Pt or Pd which enhances the sensitivity of SnO_2 nanoparticles used for gas sensors,
- improve the superconductive properties of YBCO particles by adding smaller particle which act as flux pinning enhancement (Takao *et al*., 1997),
- improve the mixing characteristics when two ultrafine powders have to be mixed: when the powders are mixed in aerosol form, the occurance of large aggregates of one component, which is detrimental for the mixing, can be suppressed.

When mixing of primary particles of different chemical composition (e.g., component A and B) takes place by Brownian coagulation, the mixing is a stochastic process in which as many aggregates composed of two A particles will occur as composite particles A-B when both particle components have the same size. The mixing quality can be enhanced by applying electrical forces. When the two particle components are oppositely charged, it is clear that more well-mixed A-B composite particles will be obtained than unmixed doublets of A or B (Fig. 4.3.1).

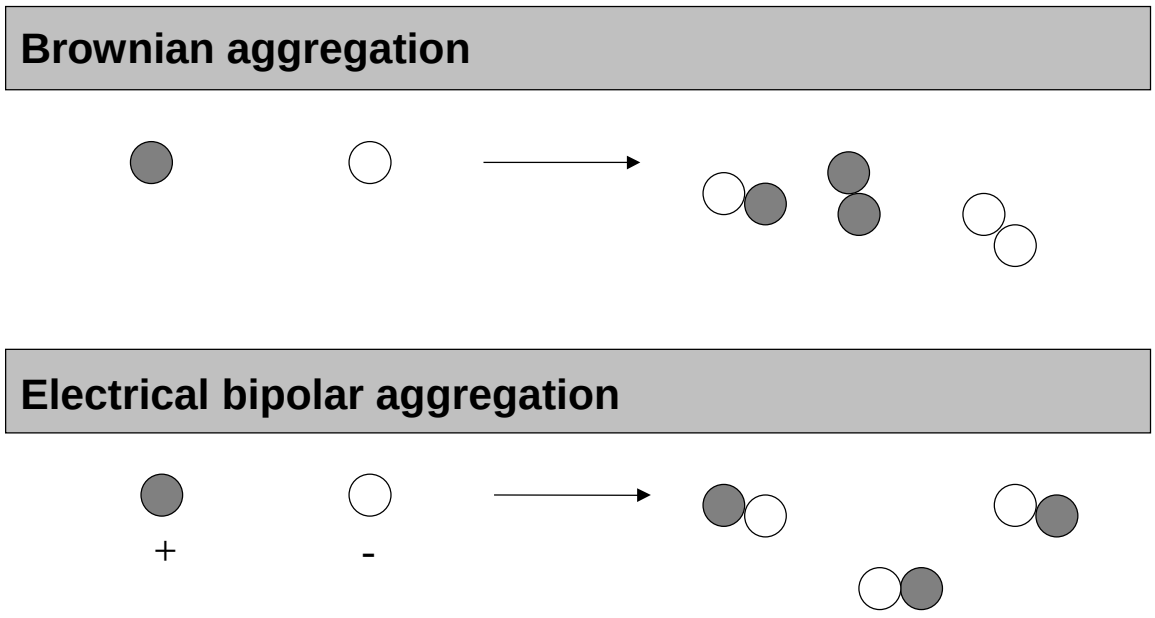

Fig. 4.3.1. Principle of influencing aggregate formation by charges on particles.

The dynamic behavior of such systems is complicated, because the aggregates formed may consist of particles dissimilar with respect to size, electrical charge and composition. Numerical techniques have to be applied in order to simulate the dynamical behavior when no assumptions about the form of the particle size distribution are made. These techniques, such as the sectional model (Gelbard *et al*., 1980), require complicated programs. The addition of charges further complicates these models. Oron and Seinfeld (1989) developed a detailed but very elaborate sectional model for the dynamics of charged particles, necessitating the solution of the two-dimensional distribution $n(v,q)$ as a function of time. Vemury *et al.* (1997) used the simpler sectionalization technique developed by Litster *et al.* (1995). Even when simplifying assumptions such as a log-normal shape of the size distribution and a fixed charge distribution are made (Otto, 1997), the mathematical description remains very cumbersome. Models involving charge and size have mainly been applied for describing the charging of particles by ions and the increase in mean particle size by bipolarly charging an aerosol which has to be precipitated (Otto *et. al*., 1996).

Several studies considered the coagulation of two- or multi-component aerosols. Lushnikov (1976) was the first to consider the coagulation of two-component mixtures, deriving an analytical solution for a size-independent coagulation kernel. Gelbard and Seinfeld (1980) developed a sectional technique for dynamic behavior of particle size and chemical composition. However, both the setting up of the kinetic equations and their numerical solution are very time-consuming. Another numerical technique for dealing with two-component coagulation was independently developed by Piskunov *et al.* (1997). These models have mainly been applied to atmospheric aerosols, e.g. to account for chemical reactions in water droplets or to describe accidental release of radioactive species and their deposition onto aerosols. At present, however, no models exist for simultaneously solving the size, electrical charge and composition of an aerosol.

In this subchapter, we investigate what are optimal conditions for obtaining composite particles containing the same number of primary particles of the different components. When a large fraction of such agglomerates is present, the primary particles can be considered as well mixed. We consider several possible methods: the mixing of bipolarly charged aerosols, the mixing of unipolarly charged aerosols and the laboratory method of mixing size-selected and oppositely charged nanoparticles. The use of the newly developed DSMC technique (Chapter 4.2.) allows us to obtain insight in the behavior of these complicated processes, in which the formed particles are in the form $A_i B_j$ (with $i,j \geq 0$) and where the primary particles have a size and charge distribution.

4.3.1 Theory of bipolar aggregation

For the case of spherical uncharged particles, Fuchs (1964) proposed an interpolation formula for the coagulation coefficient valid in the whole particle size range:

$$\beta_{i,k} = 2\pi D_{i,j}(d_i + d_j)\left(\frac{d_i + d_j}{d_i + d_j + 2\delta_{i,j}} + \frac{8D_{i,j}}{\bar{v}_{i,j}(d_i + d_j)}\right)^{-1} \qquad (4.3.1)$$

with

$$\delta_{i,j} = \sqrt{\delta_i^2 + \delta_j^2}\ ,\ \delta_i = \left(\frac{1}{3d_i\lambda_i}\right)\left((d_i + \lambda_i)^3 - (d_i^2 + \lambda_i^2)^{\frac{3}{2}}\right) - d_i \qquad (4.3.1a)$$

$$\lambda_i = \frac{8D_i}{\pi\bar{v}_i} \qquad (4.3.1b)$$

$$\bar{v}_i = \sqrt{\frac{8k_BT}{\pi m_i}} \qquad (4.3.1c)$$

$$\bar{v}_{i,j} = \sqrt{\bar{v}_i^2 + \bar{v}_j^2} \qquad (4.3.1d)$$

$$D_i = \frac{Ck_BT}{3\pi\eta d_i} \qquad (4.3.1e)$$

$$D_{i,j} = D_i + D_j \qquad (4.3.1f)$$

where m is the particle mass, k_B is the Boltzmann constant, T is the fluid temperature, η is the dynamic gas viscosity, d is the particle diameter, C is the slip correction factor, and the indexes i and j refer to the colliding particles. Different particle densities of the colliding particles are taken into account by this formula. If the particles are charged, the Coulomb forces have to be considered and the coagulation coefficient has to be corrected into:

$$\beta_{i,j;el} = \frac{\beta_{i,j}}{W_{i,j}^{p,q}}\ , \qquad (4.3.2)$$

where $W_{i,j}^{p,q}$ is the Fuchs stability function (Fuchs, 1964):

$$W_{i,j}^{p,q} = -\frac{1-\exp(\kappa)}{\kappa} \qquad (4.3.2a)$$

$$\kappa = \frac{2pqe^2}{4\pi\varepsilon\varepsilon_0(d_i + d_j)k_B T} \qquad (4.3.2b)$$

where p and q are the numbers of elementary charges on particles i and j, respectively. This correction factor $1/W_{1,2}^{p,q}$ is shown in Fig. 4.3.2 for singly charged nanoparticles. It can be seen that this correction becomes important for smaller particles.

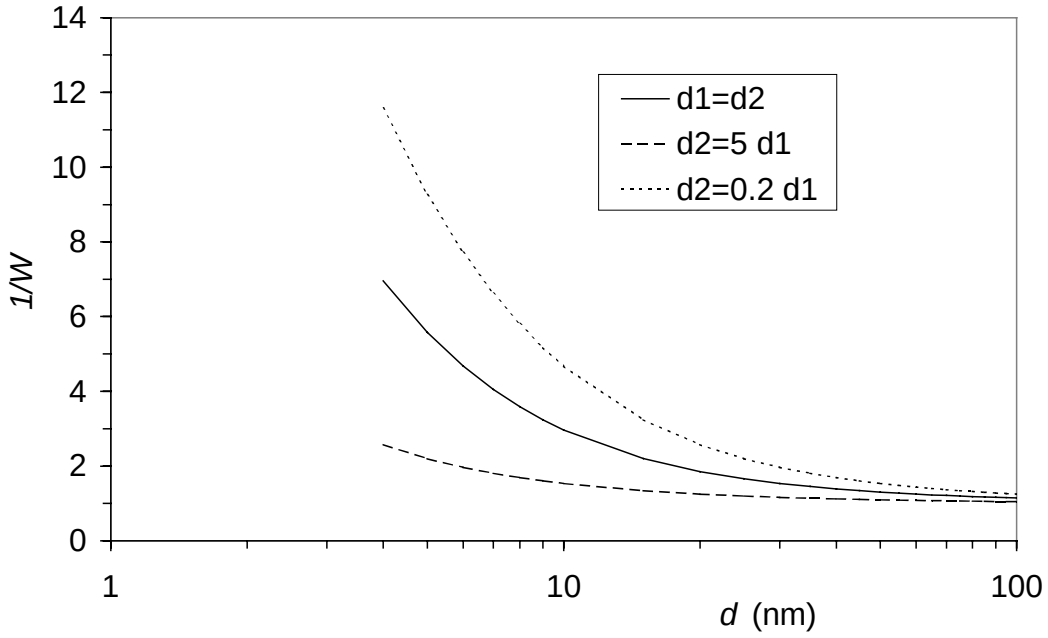

Fig. 4.3.2. Correction factor $1/W_{1,2}^{p,q}$ *for the influence of opposite charges (p= -1, q= 1) on two coagulating particles*

Furthermore, it is important to take into account in the calculation of the coagulation coefficient that the aggregates formed are not any more spherical, in contrast to the primary particles. This leads to a higher coagulation coefficient in comparison to the case when the new particle has again a spherical shape (Katzer *et. al.*, 1998). A commonly used correction method is to describe the effective aggregate diameter d by means of a fractal dimension D_f (Matsoukas and Friedlander, 1991):

$$\left(\frac{d}{d_0}\right)^{D_f} = N_p, \qquad (4.3.3)$$

in which N_p is the number of primary particles with diameter d_0. This method is, however, only applicable for equal-sized primary particles. To overcome this problem the effective diameter of an aggregate composed of primary particles of any size is estimated by calculating the projected outer diameter and taking the mean over all possible orientations. By comparing the results with the expression of Matsoukas and Friedlander for the effective aggregate diameter *d* (1991), eq. (5.3.3), the methods are found to be equivalent for D_f =1.43. Smaller fractal dimensions are encountered only for magnetic particles which tend to align. In order to be able to describe the aggregation process for higher fractal dimensions, we simply interpolate between this lower boundary and the densest possible aggregate with a D_f =3.

4.3.2 Simulation of aggregation of charged aerosols for mixing purposes

With the coagulation coefficient for charged particles and aggregates composed of unequal-sized primary particles now being known, the dynamics of the aggregation process can be studied by means of the DSMC method described in Chapter 4.2. . The simulations are performed for a bicomponent mixture with equal number concentrations of both components ($N_A = N_B$). The number of simulation particles is 20000. Each simulation was repeated five times with different random numbers to reduce the influence of the stochastic nature of the simulation process. Mean values were computed from these five simulations. Each component has an initial lognormal size distribution, which is also generated by means of random numbers (Rubinstein, 1981). The initial charge distribution can be based on any formula for the charging method used, such as bipolar charging or unipolar charging. The bipolar charge equilibrium for particles larger than 50 nm can be described by the Boltzmann charge distribution, where the concentration ratio of particles carrying *q* elementary charges is (Fuchs, 1964):

$$\frac{N^q}{N^0} = \exp\left(-\frac{q^2}{2\sigma^2}\right) \tag{4.3.4}$$

where N_0 is the total particle number and with

$$\sigma = \sqrt{\frac{dk_B T}{2e^2}} \tag{4.3.5}$$

As the Boltzmann theory underestimates the number of charged particles with diameters smaller as 50 nm, the following approximation formula is used (Wiedensohler, 1988):

$$F(q) = 10^{\sum_{i=0}^{5} a_i(q) \log \frac{d}{nm}} \qquad (4.3.6)$$

where *F(q)* is the distribution function and $a_i(q)$ are coefficients as determined by Wiedensohler.

The aerosols investigated have initial geometric mean diameters d_g in the 10 to 100 nm range. For smaller nanoparticles it is more difficult to reach sufficiently high charge levels for influencing the aggregation process, and they were therefore not considered. The aggregates which were formed were assumed to have a fractal dimension D_f =1.43. The same initial number concentrations are used in all the cases, $N_{A,\,t=0} = N_{B,\,t=0} = 5 \times 10^5$ cm^{-3} in order to be able to compare the results for different cases. Higher or lower values of these values only influence the kinetics of the mixing process, not its qualitative behavior. Particle densities were taken to be 7500 kg/m^3 and 9600 kg/m^3 for aerosols A and B, respectively. As carrier gas N_2 at 20°C was taken.

The simulation results in a complex mixture which consist of the number concentrations of $A_i B_j$ aggregates containing primary particles with different sizes and charges. The mixing quality can be shown by means of the distribution function. The distribution function of primary particles $N_{i/(i+j)}/N$ is based on the ratio of the number of primary particles of one component to the total number of primary particles in the aggregate, $i/(i+j)$. Here, *i* corresponds to the number of primary particles of component A and *j* refers to the primary particles of component B. In Fig. 4.3.3 an example is given of the time evolution of the distribution function of primary particles in the case of two bipolarly charged aerosols with mean particle diameters of 10 nm.

The initial unmixed situation shows two peaks, indicating the unaggregated primary particles. At the half time $t_{0.5}$ (689 s) maximum values at $i/(i+j)$ = 33, 50 and 66 % develop, representative for $A_{2n}B_n$, A_nB_n and A_nB_{2n} aggregates. At longer times larger and more complex aggregates develop, but there is still a maximum around symmetric aggregates.

In order to simplify the representation of the results, another definition is used here. The number fraction of symmetric aggregates N_{sym}/N represents the fraction of symmetric $A_i B_{j=i}$ aggregates, which corresponds to perfectly mixed aggregates. In some way N_{sym}/N is an indication of the mixing selectivity.

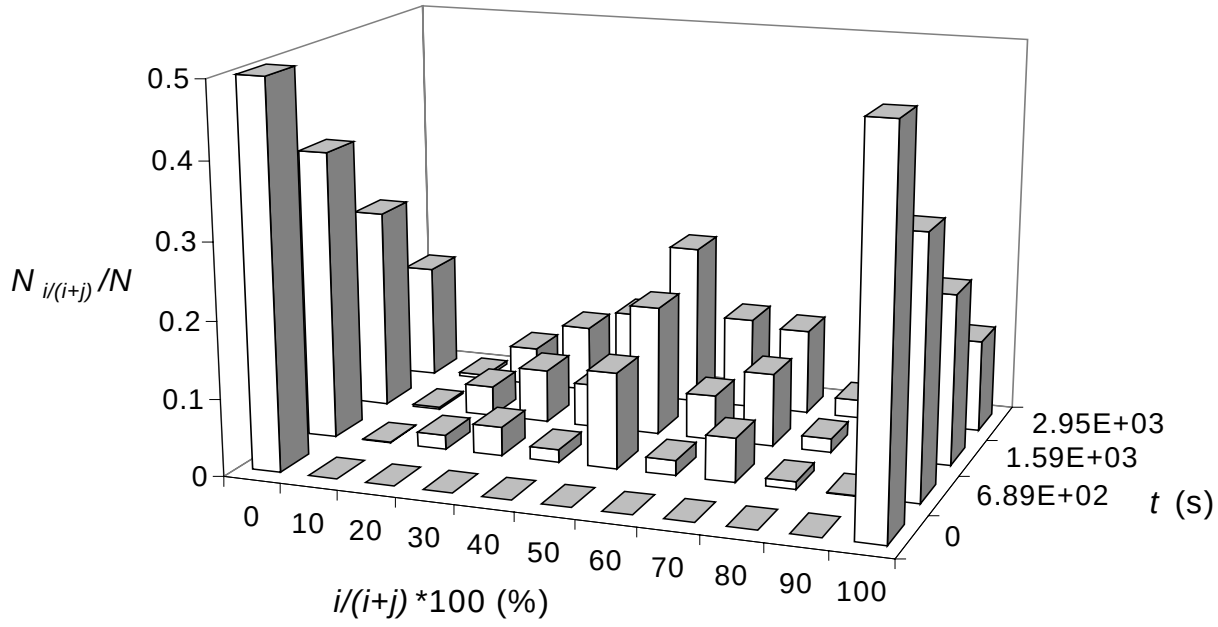

Fig. 4.3.3. Time-dependent distribution function of primary particles in aggregates. Initial conditions are $d_{g,A}$ *= 10 nm,* $d_{g,B}$ *= 10 nm,* $\sigma_{g,A}$*=1.8 and* $\sigma_{g,B}$*=1.6. Both aerosols are initially bipolarly charged*

4.3.3 Results

In order to assess different methods which can be used to obtain composite particles, we investigated three cases. These are: the mixing of bipolarly charged aerosols, the mixing of unipolarly charged aerosols and the laboratory method of mixing size-selected and oppositely charged nanoparticles.

The mixing of bipolarly charged particles is representative of the mixing of aerosols which are in charge equilibrium. The charge equilibrium is obtained after conducting the aerosol through a radioactive source, often used to obtain a known charge distribution or to minimize the charge level of charged aerosols. Consequently, both aerosols contain neutral particles and charged particles of both polarities. Aerosols with broad size distributions were used in the simulation, with σ_g=1.8 and σ_g=1.6 for the aerosol with component A and B, respectively. The time evolution of the number fraction of symmetric aggregates N_{sym}/N is important to find the optimal conditions for such mixing processes. From Fig. 4.3.4a it becomes clear that N_{sym}/N becomes larger with increasing particle size difference, but does not exceed 0.25. The decrease after some longer time can be explained by the formation of a wide range of aggregate which are not exactly symmetric.

Charging of aerosols in radioactive neutralizers has some drawbacks: the charging efficiency is relatively low and the bipolar nature of the charge distribution

decreases the selectivity of the aggregation process. Unipolar chargers applying an alternating electric field (Büscher *et al.*, 1994, Kruis *et al.*, 1998) allow to solve these problems. They possess a higher charging efficiency than radioactive neutralizers as they are not limited by the bipolar charge equilibrium, and all charges are of one sign. Therefore, mixing unipolar aerosols can be more suitable for industrial application. For our simulations, aerosols with the same particle size distribution function as for bipolar charged particles ($\sigma_{g,A}$=1.8, $\sigma_{g,B}$=1.6) were used, but this time one of them contains only positively charged particles (A), and the other (B) contains only negative charges with some amount of uncharged particles in both aerosols. Charging efficiencies in both aerosols are taken similar to those described by Büscher *et al*. (1994) for positively charged particles. The increased fraction of charged particles as compared to the bipolar case and the fact that particles of different kinds carry only charges of opposite signs have a positive influence on the fraction of symmetric aggregates, as can be seen from Fig. 4.3.4b. Remarkable is not only an increase of N_{sym}/N of roughly a factor 2 with respect to bipolarly charged aerosols, but also different conditions leading to a maximum of selectivity. It was found that the maximum of N_{sym}/N is for both aerosols having the largest diameters. This is due to the competition of two effects: on the one hand the coagulation coefficient increases with increasing difference in particle sizes, on the other hand for larger particles the correction factor due to electric charge strongly increases due to the multiple charges. Clearly, the first effect dominates in case of bipolarly charged aerosols due to a low fraction of multiple charged particles while in case of unipolarly charged aerosols the second effect prevails.

Comparison of the results for the bipolar and unipolar cases leads to recognition of the importance of the number and sign of charges on particles for the aggregation process. For further study a bicomponent mixture of particles with a narrow size distribution (σ_g=1.1) carrying an equal charge number but of opposite sign (q_A=-q_B) was taken. These aerosols can be obtained using the standard equipment for particle fractionation consisting of an aerosol charger and a Differential Mobility Analyzer. For applications, however, it has one main disadvantage: the maximum particle number concentration which can be obtained is relatively low. The evolution of N_{sym}/N, representing the selectivity, is presented in Fig.4.3.4c for $d_{g,A} = d_{g,B}$= 30 nm. The maximum charge level is taken to be three elementary charges, as this is the limit for the diffusion charging for 30 nm sized particles according to Fuchs (1963). It can be seen that only multiply charged particles result in high selectivity, over 80 % for triply charged particles. It was found in simulations not shown here that the highest selectivity is obtained for the smallest particle sizes and the highest charge levels taken. This is due to the fact that all particles are charged and to the higher mobility of smaller particles.

a)

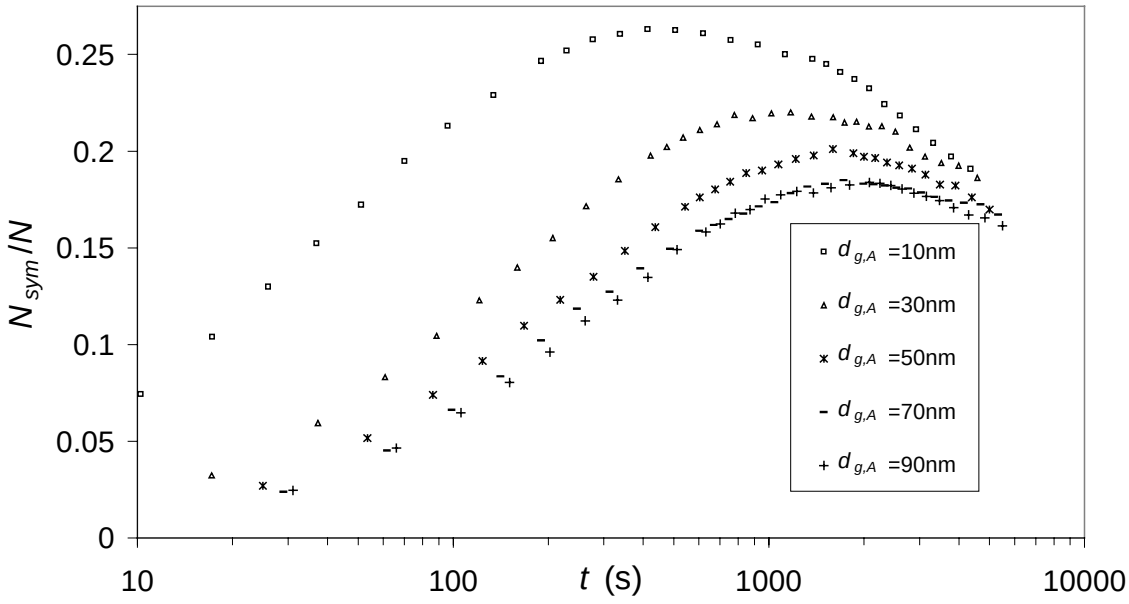
0.25
0.2
0.15
0.1
0.05
0
N_{sym}/N
10
100
1000
10000
t (s)
$d_{g,A}$ =10nm
$d_{g,A}$ =30nm
$d_{g,A}$ =50nm
$d_{g,A}$ =70nm
$d_{g,A}$ =90nm

b)

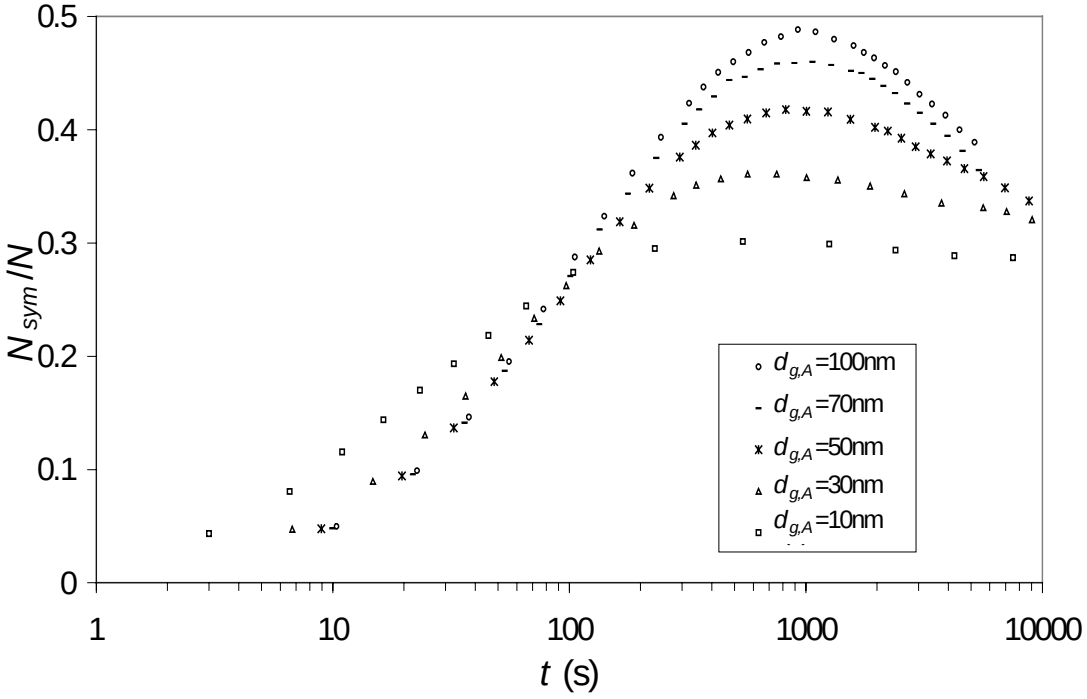
0.5
0.4
0.3
0.2
0.1
0
N_{sym}/N
1
10
100
1000
10000
t (s)
$d_{g,A}$=100nm
$d_{g,A}$=70nm
$d_{g,A}$=50nm
$d_{g,A}$=30nm
$d_{g,A}$=10nm

c)

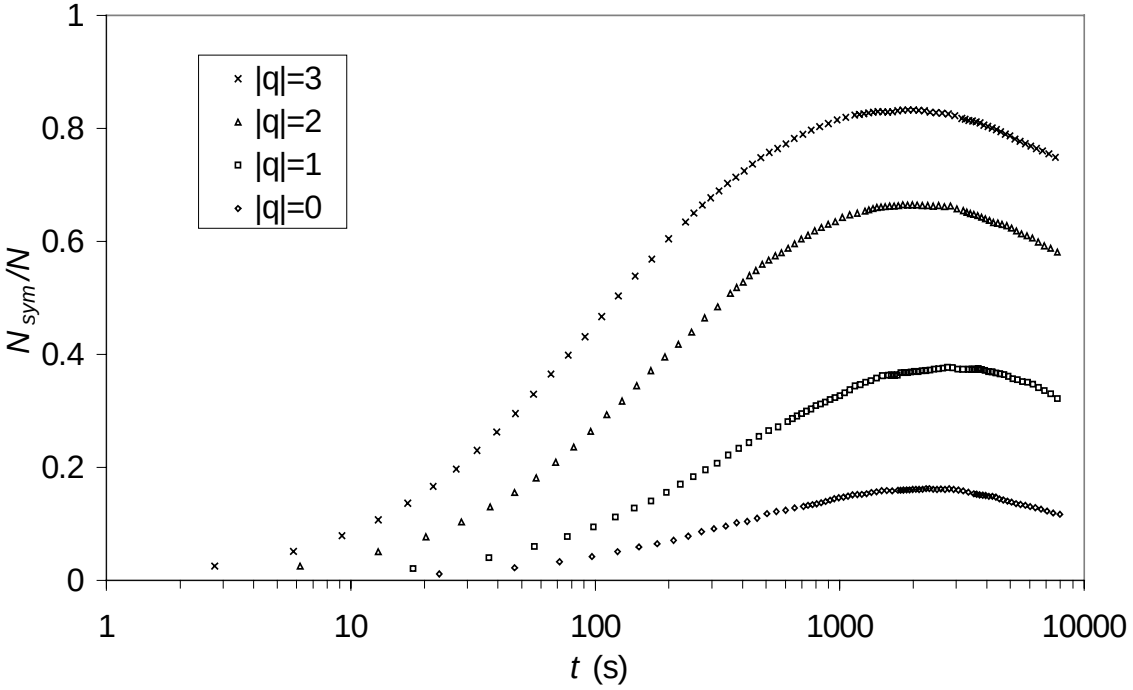

Figure 4.3.4. Fraction of "symmetric" aggregates as function of time: a) in the case of initially polydisperse bipolarly charged (according to Wiedensohler, 1988) primary particles for different mean geometric diameters of component A with $d_{g,B}$=90 nm, b) in the case of initially polydisperse unipolarly charged (according to Büscher et al., 1994) primary particles for different mean geometric diameters of component A with $d_{g,B}$=90 and c) in the case of initially quasi monodisperse ($d_{g,B}$=$d_{g,A}$=30 nm) oppositely charged (q_A=-q_B) primary particles for different charge levels.

4.4 Conclusions: mechanisms relevant for gas-phase synthesis

The formation of nanoparticles by the evaporation-condensation technique was analyzed using a moment model describing nucleation, condensation and coagulation. Using the model, it was shown that the temperature in the evaporation furnace and the cooling rate determines the mean particle size and that an aerosoldynamical model allows the prediction of the temperatures needed for nanoparticle formation. For obtaining particle in the nanometer size-range, a temperature range of some 200-300 K can be found for each element. In the Chapters 7.1 and 7.2 the evaporation-condensation technique is experimentally applied.

For more complicated systems having more degrees of freedom, such as distribution of particle sizes, different chemical compositions, distribution of charges and distribution of number of primary in an aggregate, a newly developed Direct Simulation Monte Carlo method showed to be suitable. Two examples of practical relevance containing multi-dimensional particle dynamics were given: coagulation with chemical reaction in droplets (microreactors) and the coating of solid particles with nanoparticles.

Aggregation of mixtures of charged nanoparticles is useful for obtaining composites. This was studied by means of the Direct Simulation Monte Carlo method. The selectivity of mixing is characterized by means of the fraction of symmetric aggregates. It was shown that for each charge distribution different conditions lead to a highest possible selectivity. Chapter 7.4 will describe an experiment designed for obtaining very well-defined composite nanoparticles, based on charges on nanoparticles.

5. A review of synthesis of nanoparticles in the gas phase for electronic, optical and magnetic applications

In the preceding chapters the applications of nanoparticles, the synthesis methods and the relevant mechanisms were described. In this chapter most of the relevant works are described which are done using gas-phase methods to obtain nanoparticles or nanoparticle-based films and powders for electronic, optical and magnetic applications. Parts of this review have been published (Kruis *et al.*, 1998d). This background allows to choose two interesting functional applications. The requirements for a process suitable for complying with the requirements for these applications will be discussed, finally leading to the selection of a synthesis process.

5.1. Synthesis for microelectronic and optoelectronic applications of zero-dimensional structures (quantum dots)

Synthesis of semiconducting nanoparticles was pioneered by Kaito *et al.* (1976), who evaporated CdS powder from a boat heated at 1100°C in a low-pressure inert gas. The particles, ranging from 10 to 100 nm, were collected on TEM grids at various positions in the produced aerosol. The same procedure was also applied by Kaito *et al.* (1983) to CdTe. Agata *et al.* (1990) synthesized CdS nanoparticles of 20-150 nm by evaporating CdS powder in low-pressure Ar. However, quantum effects were not detected in the photoluminescent spectra due to the relatively large size of the particles. Nevertheless the photoluminescence intensities increased with decreasing particle size, probably related to the appearance of new electronic states on the free surface. Hayashi *et al.* (1989) detected quantum effects in gas-evaporated ZnTe nanoparticles with sizes between 20 and 80 nm by measuring the Raman spectrum. The change in the relative intensities of the different Raman lines indicated a blue shift of the ground-state energy. In order to avoid problems due to incongruent evaporation, Kaito and Saito (1990) co-evaporated the metals (Zn, Cd) and the chalcogenides (S, Se, Te) from two boats kept at different temperatures. Thus the vapor pressures of both elements could be matched and several II-VI semiconductor nanoparticles compounds were obtained.

Saunders *et al.* (1992) synthesized semiconductor nanoparticles from the gas phase in order to obtain quantum confinement effects. GaAs nanoparticles in the 5-10

nm size range were formed from the nonequilibrium vapor created by the exploding wire method. Optical extinction measurements of the nanoparticles when collected in a liquid were suggestive of quantum size effects, especially due to the fact that a distinct absorption edge at the bulk material band gap was absent. Sercel *et al.* (1992) obtained GaAs nanoparticles by using an organometallic precursor. $(CH_3)_3Ga$ was mixed in a furnace flow reactor with AsH_3 gas yielding crystalline GaAs particles with sizes between 10 and 20 nm. Saunders *et al*. (1993b) showed that when $(CH_3)_3Ga$ was pyrolyzed to form Ga nanoparticles, the GaAs nanoparticles obtained after the addition of AsH_3 had a different morphology as compared to the case where $(CH_3)_3Ga$ and AsH_3 were premixed. In the premixed case, homogeneous nucleation of GaAs clusters was probably the dominant mechanism. The optical absorption spectrum showed in this case quantum confinement effects.

As the quantum confinement effect is a sensitive function of particle size (Yoffe, 1993), a narrow size distribution is required to observe it experimentally otherwise the size effect will be averaged out. To this end, a differential mobility analyzer (DMA) can be used to 'size-select' an aerosol at atmospheric pressure (Fissan *et al.*, 1996). An indirect way to obtain quantum dot structures is by depositing size-selected metallic aerosol particles onto InP wafers. After etching away the uncovered surface of the wafer, free-standing columns of semiconducting material result (Wiedensohler *et al.*, 1992; Stratmann *et al.*, 1993; Deppert *et al.*, 1994). The diameter of these columns, between 20 and 50 nm, was defined by the size of the masking aerosol particles. The height of these columns, typically 150 nm, is dependent on the etching time. Maximov *et al.* (1993) measured cathodoluminesence of the created quantum dot structures and obtained a blue shift in the luminescence peak, although this effect could not be explained by confinement effects alone. A similar etching method was used by Kim and Rye (1994) to obtain GaAs quantum dots by reactive ion etching of a GaAs wafer covered with SiO_2 nanoparticles. These particles were synthesized by electrospraying a TEOS solution in ethanol in an O_2 atmosphere.

Size-selected quantum dots can also be produced directly. Deppert *et al.* (1996) evaporated Ga in a furnace flow reactor and then size-selected the formed Ga nanoparticles. Finally, by adding AsH_3 gas in a second furnace, the Ga nanoparticles were reacted to obtain GaAs nanoparticles. This complicated route was used because GaAs does not evaporate stoichiometrically. Kruis *et al.* (1996) on the other hand showed that PbS, which belongs to the group of IV-VI semiconductors, can be directly sublimated in a furnace flow reactor without decomposition. This yielded amorphous PbS nanoparticles which were then size-selected. Control over particle deposition was obtained by creating a lateral electric field between the electrodes, resulting in the particles depositing preferentially on one electrode. Another method uses photoresist

patterns on the substrate. The particles deposit preferentially on the areas without photoresist, probably due to charging of the photoresist. The photoresist is removed afterwards without visible loss of particles. As a first device application metal-semiconductor-metal photodetectors with multifinger interdigitated electrodes were produced. After nanoparticles deposition the detectors show a higher sensitivity, 4x on a GaAs substrate and 60x on a Si substrate (Prost *et al.*, 1998).

Koyama *et al.* (1992) used laser ablation to obtain CdS and CdTe nanoparticles with stoichiometric composition. Substrates placed in a low-pressure chamber were ablated using a pulsed Nd:YAG laser. The nanoparticles formed were transported through a pipe into a vacuum collection chamber where they deposited onto a cold finger and were covered with frozen methanol. The nanoparticle diameter could be controlled between 4 and 10 nm by changing the laser power and the inert gas pressure. Absorption spectra indicated quantum size effects. Using the same experimental setup, a glass doped with CdTe microcrystallites was produced by ablating alternatively a CdTe target and a SiO target in an O_2 atmosphere (Ohtsuka *et al.*, 1992). In this case, nanoparticles with nonlinear optical properties were obtained.

Danek *et al.* (1994) prepared quantum dot nanocomposites consisting of CdSe nanoparticles embedded in ZnSe thin films, which is a larger band gap semiconductor. The semiconductor matrix was expected to stabilize the quantum dots and protect them against oxidation. The CdSe nanoparticles were brought in the aerosol phase by using the electrospray method. The aerosol was transported into an organometallic CVD reactor where the ZnSe film was being deposited. It was observed that the optical properties of these quantum dots were preserved during this process. Another kind of nanocomposite quantum dot was synthesized by Salata *et al.* (1994a), who imbedded PbS nanoparticles in a polymer film. An aerosol of a liquid containing $Pb(NO_3)_2$ and a polymer precursor was obtained by an electrospray system and then reacted with H_2S from the gas phase producing PbS nanoparticles. The PbS nanoparticles covered with a polymer layer were then driven by the electrical field towards the substrate. The optical absorption spectrum showed a large blue shift, corresponding to a theoretical mean particle diameter of 4.6 nm. Using a $Cd(NO_3)_2$ solution, CdS nanoparticles were also obtained with an average diameter smaller than 5 nm claimed to have a narrow size distribution (Salata *et al.*, 1994b).

5.2 Synthesis of luminescent nanocrystalline silicon

Littau *et al.* (1993) synthesized Si nanoparticles with sizes between 3 and 8 nm by pyrolysis of 3-30 ppm Si_2H_6 at 865 °C in a furnace flow reactor operated at 1.4 bar He. The aerosol was then diluted with He and reacted with O_2 in a second furnace at

700°C, yielding a passivating layer of SiO_2. The shell thickness of the nanoparticles was 1.2 nm. The aerosol was collected as colloid in ethylene glycol and size-selected using a liquid phase method. The luminescence of the colloid obtained was weak but could be improved through chemical treatment to reach a quantum yield of 5 % at room temperature and 50 % quantum yield below 50 K (Wilson *et al*., 1993). The luminescence shifted to higher energy with decreasing particle size, indicating thereby quantum confinement effects (Brus *et al*., 1995).

Both Kanemitsu *et al.* (1993) and Kawaguchi and Miyazima (1993) decomposited SiH_4 with a Nd:YAG laser at 10-20 mbar and obtained Si nanoparticles with sizes between 3 and 20 nm. The samples were oxidized at room temperatures for several weeks in a clean air box, resulting in a thin amorphous SiO_2 layer around the particles. These particles exhibited a strong visible photoluminescence at room temperature, the maximum-intensity wavelength being however independent of the Si core size. Takagi *et al.* (1990) applied a microwave plasma to decompose SiH_4. The diameter of the Si nanocrystals could be varied in this case from 2.5 to 20 nm. They were blown through a transfer pipe onto a substrate in a vacuum chamber and oxidized. Here, the luminescence peak showed a weak dependence on the particle diameter. Saunders *et al.* (1993) produced 2 - 4 nm sized Si crystallites by a spark source. Immediately after synthesis, the sample consisting of a 10 nm thick particulate film showed little or no visible photoluminescence. After exposure to air however, the luminescence increased dramatically. Werwa *et al.* (1994) used pulsed laser ablation combined with supersonic expansion and obtained 2-3 nm Si nanoparticles, which then showed visible photoluminescence after surface passivation by chemical means. More detailed studies (Seraphin *et al*., 1996) showed that the maximum-intensity wavelength is determined by the particle size, while the luminescence intensity is determined by the degree of surface passivation.

The first report on size classification in the gas phase originates from Camata *et al.* (1996). They obtained Si nanoparticles with a high-voltage electric spark discharge in an inert gas at atmospheric pressure and then size-selected them by a DMA. The nanoparticles, with sizes selected between 2.8 and 11 nm, were collected on a substrate by an electrostatic precipitator or hypersonic impactor. The standard deviation of the classified aerosol was 1.2 - 1.3. The size distribution of the smallest particles selected, i.e., 2.8 nm, showed however also the presence of a significant amount of larger particles. This was due to the omission of the neutralizer at this size resulting in multiply charged particles.

5.3 Fabrication of gas sensors

Ogawa *et al*. (1981a, b) produced a thick film consisting of SnO_2 nanoparticles with mean sizes between 3 and 15 nm. A heated boat containing Sn was placed underneath an RF-induced plasma in a low-pressure O_2 gas. The SnO_2 nanoparticles were deposited on a substrate placed above the O_2 plasma. The macrostructure of the films, which ranged from porous columnar to spongy, was found to be dependent on the O_2 pressure. The porous columnar structure had the highest selectivities, and was used to detect water, ethanol and isobutane vapor. A similar reactive plasma system was used by Zhu *et al.* (1993), who replaced the RF coil by the more economic d.c. gas discharge ring electrode. The nanoparticles in the film had a mean size of 40 nm and exhibited a good sensitivity to ethanol vapor.

The results obtained by Ogawa will be analyzed here more in detail, as they provide a good insight in the mechanisms of gas sensing. A 10 -50 µm thick porous film composed of 15 nm SnO_2 particles showed a high gas sensitivity and an improved gas selectivity in comparison to sensors consisting of micron-size grains (Ogawa *et al.*, 1981b). From mobility measurement results it was postulated that due to the small dimensions of the conduction channels in the nanoparticles the depletion layer has a large influence on the conductivity (Ogawa *et al.*, 1982).

Gas sensors based on semiconducting metaloxides are applied for the detection of explosive or toxic gases. The measurement signal bases on the conductivity, σ, of the material. In the temperature range normally used (400-700 K) the chemical sensing mechanism is a result of a surface reaction between chemically adsorbed oxygen and reducing gases. The oxygen is chemically adsorbed in the form of O_2^-, O^- or O^{2-} and induces a depletion zone at the surface which has a lower conductivity in comparison with the bulk because electrons are bounded to the adsorbed oxygen. A reducing gas will reduce the concentration of chemically adsorbed oxygen so that the conductivity increases. Chemical reactions at the surface were investigated by means of mass-spectrometric measurements of the desorption products when the film is heated (Kohl, 1989). The following reaction was found when ethanol reacts with O^- at the surface of SnO_2:

$$C_2H_5OH + O^- \leftrightarrow CH_3CHO + H_2O + e \qquad (5.1)$$

The adsorbed C_2H_5OH molecules oxidize at 250°C to CH_3CHO. The electron which is freed by this reaction effectively increases the conductivity of the SnO_2.

Gas sensors based on ultrafine thin films of metal oxides are known since several decades. A porous film composed of particles with diameters between 6 and 20

nm showed an improved sensitivity and a high gas selectivity due to the increased surface area to volume ratio (Ogawa *et al.*, 1981b). The increased sensitivity was investigated by means of Hall measurements (Ogawa *et al.*, 1982). Contrary to the simple measurement of the conductivity σ , which is equal to the product $qn\mu_H$, allow these to measure separately the concentration of carriers, n, and the mobility, μ_H. The charge number on the carrier is indicated by q.

The carrier concentration n was found to change with gas concentration. It was shown that for normal thin films the mobility μ_H was independent of the gas concentration but that the thin films composed of nanoparticles showed a strong dependence of the gas concentration (Fig. 5.1). This is the reason for the increased sensitivity of these films.

The largest effects were found for the films with the smallest particles. The changed mobility can be understood by the following schematic model visualized in Fig.5.2. Fig 5.2a shows several SnO_2 nanoparticles before C_2H_5OH is adsorbed. The O^- species which are chemisorbed at the surface act as scattering centers and hinder the movement of the charge carriers. The area where this hindering occurs is given by the Debye length L_D:

$$L_D = \left(\frac{\varepsilon k_B T}{q^2 n} \right)^{1/2} \qquad (5.2)$$

where ε is the dielectric constant, k_B is Boltzmann constant T is the absolute temperature. When the size of the particles approaches that of the Debye length, a clear decrease in the mobility of the charge carriers results. The adsorption of ethanol results in the decrease or elimination of these scattering centers, as can be seen in Fig 5.2b. This effective increase in the size of the conduction channel leads to an increase in the mobility. The Debye length for the ultrafine particle films was found to be around 3 nm. Other investigations showed also a large increase in sensitivity when the particle size drops below 10 nm (Xu *et al.*, 1991). But also film thickness, stoichiometry and morphology of the film have influence on the electrical properties of the film (Sanjines *et al.*, 1990).

The combined effects of particle size distribution, the nature of the contacts between the particles and the chemical composition of the surface are so complex that the production of semiconducting oxide gas sensors is at present mainly an empirical technology. Grain size control and size homogeneity remain hence a fundamental issue of investigation (Dieguez *et al.*, 1996).

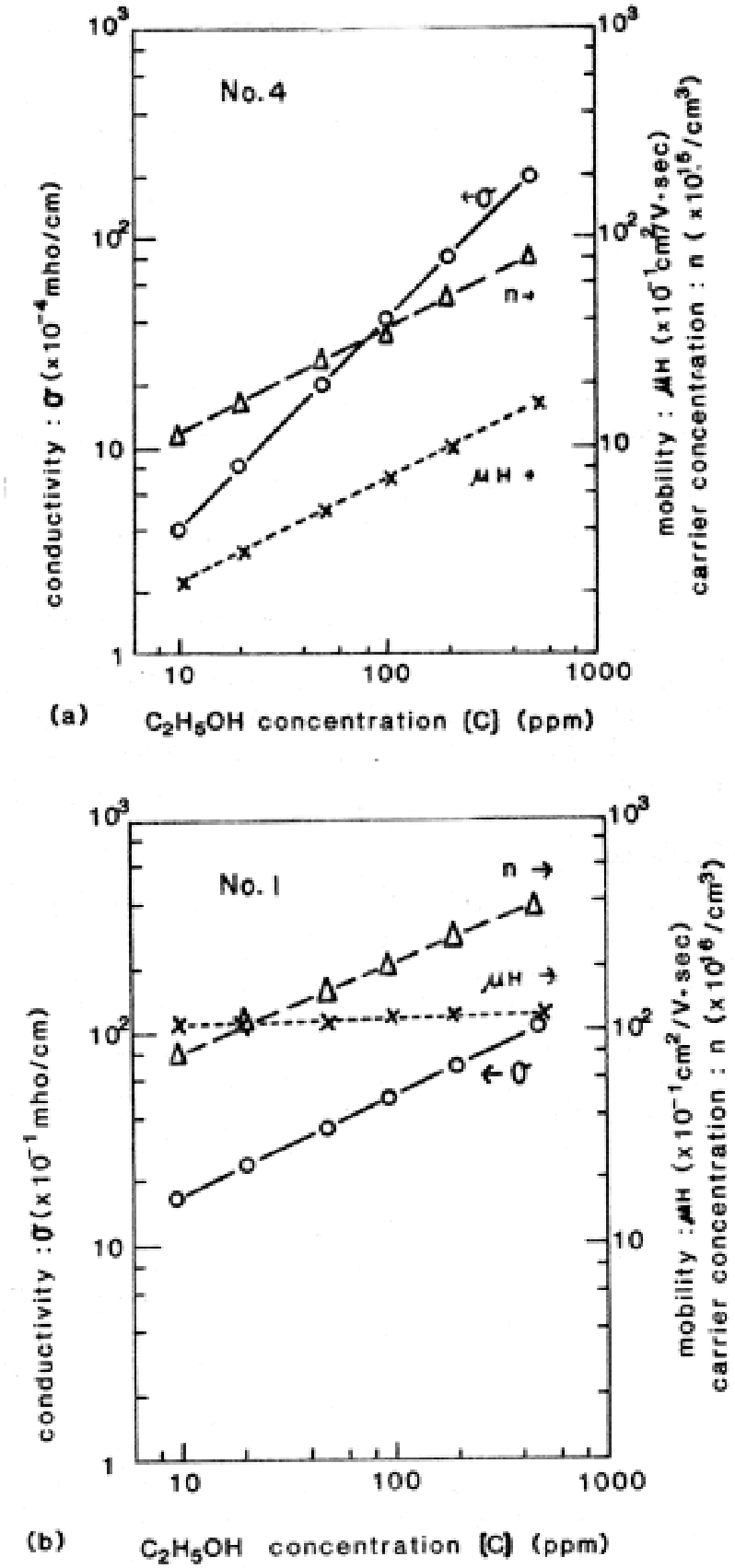

Fig. 5.1. Hall measurements for nanoparticle film (a) and thin film (b) (from Ogawa et al., 1982)

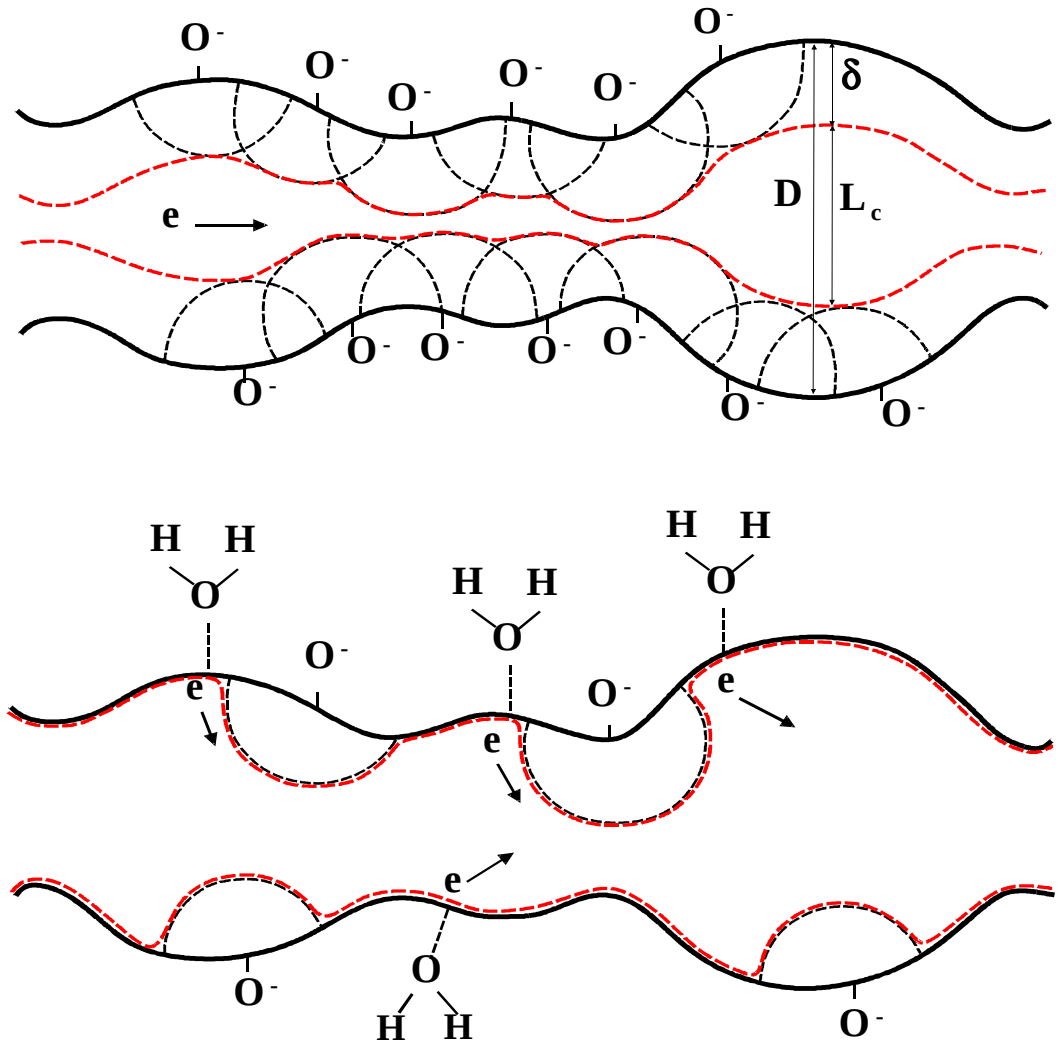

Fig. 5.2. Schematic model for the modification of the conductivity channel by gas adsorption a) before gas adsorption and b) after gas adsorption (from Ogawa et al, 1982)

Adachi *et al.* (1988) applied an evaporation-reaction type aerosol generator to produce SnO_2 particles. Sn was vaporized in a furnace and reacted with O_2, yielding upon cooling SnO_2 particles with mean sizes between 10 and 100 nm. The particle size distribution was measured using a DMA-CNC combination. Thin nanoparticle films on a glass substrate were produced by accelerating the particles through a critical orifice into a low-pressure chamber. The electrical properties of the films were sensitive to H_2 especially at room temperature.

Spray pyrolysis of a $SnSO_4$ solution yielded a SnO_2 powder consisting of 1 µm sized agglomerates composed from nanocrystals of 9 nm mean size. This is a result of multiple nucleation in the drying aerosol droplet. The powder was sintered at several temperatures, which led to a slight increase in the size of the nanocrystals. The resulting sensor characteristics for ethanol and CO vapor were measured. It appears that the electrical resistance was mainly due to the contacts between the agglomerates (Schmatz *et al*., 1994). A Sn-precursor, dibutyltindiacetate, in a solution was spray-pyrolysed unto a heated substrate by using a ultra-high frequency nebulizer. This led to a polycrystalline SnO_2 film with crystallite sizes between 8 and 25 nm. When a Pt-precursor, platinumacetylacetonate, was added to the solution, 3-5 nm sized Pt nanoparticles were dispersed on the SnO_2 grains (Labeau *et al.*, 1993). A similar procedure was adopted to produce SnO_2 sensors doped up to 10 vol% with Pd nanoparticles, showing an increased sensitivity for CO and ethanol vapor (Gautheron *et al.*, 1993).

The inert gas condensation method has also been used for synthesis of gas-sensing materials. Volkening *et al.* (1995) produced Pd nanoparticles with a size of 10 - 15 nm using inert gas condensation with a DC/RF magnetron sputter source. The gas-sensing properties of the compacted powder for H_2 gas were analyzed using a contactless method. Lin *et al.* (1995) produced a thin film gas sensor by depositing TiO_2 nanoparticles on a thin film of TiO_2 to obtain good adherence. The nanoparticles were synthesized by evaporation of Ti in a low-pressure mixture of O_2 and He. By carefully heating the film, a porous structure was obtained showing a good sensitivity for H_2S gas. In order to increase the sensitivity further, a dopant in the form of Pt nanoparticles with sizes less than 10 nm was added on top of the nanocrystalline film. This increased the sensitivity and decreased the operating temperature by some 200°C below that of a regular TiO_2-based gas sensor.

Hu *et al.* (1997) applied reactive laser ablation in order to produce very thin granular SnO_2 films. An excimer laser with a wavelength of 248 nm and pulse width of 20-30 ns at 3 Hz repetition rate ablated a rotating Sn target. Nanoparticles were deposited on a substrate heated above the melting point of Sn and placed several centimeters below the target. Although the ablation was carried out at a pressure of 1 mbar O_2, the oxidation of Sn nanoparticles took place mainly on the substrate. TEM micrographs and X-ray diffraction showed grain sizes of 10-30 nm. The thinnest films produced were 24 nm and showed a high sensitivity to ethanol vapor.

5.4 Fabrication of conducting films

Lee *et al.* (1996) applied a RF plasma reactor operating at atmospheric pressure to produce thin ITO films based on nanoparticles. A precursor solution containing $SnCl_4$ and $In(NO_3)_3$ was ultrasonically nebulized and introduced into the plasma region. The film on the substrate located underneath the plasma consisted of particles with sizes between 50 and 150 nm and was optically transparent. The resistivity was found too high for practical applications except for using these films in transparent electrical heaters. Zhao and Pan (1994) obtained ZnO nanoparticle films by evaporating Zn in a dc arc jet using O_2 as the plasma forming gas in a low pressure environment (0.1-10 mbar). The optical properties of the films which were composed of particles with mean sizes between 20 and 80 nm showed a transmission between 20 and 80 % in the visible spectrum. The IR spectra showed size effects and the electrical properties were found to depend on the amount of O_2 absorption.

5.5 Synthesis of high-temperature superconductors (HTS)

Aerosols have been used extensively in the preparation of HTS films, but mainly as a means of transport of the precursors to the reaction zone where they evaporate (Wang *et al.*, 1990, Salazar *et al.*, 1992). The HTS material can also be produced as a powder, which can be sintered into larger HTS units. This has been done mainly by spray pyrolysis yielding particles in the size range of 0.1-5 µm. Okuyama *et al.* (1993) obtained particles of about 50 nm of a bismuth oxide superconductor ($Bi_2CaSr_2Cu_2O_x$) by evaporating volatile organometallic precursors and reacting the gas mixture of the different precursors with O_2 in a furnace reactor. The particles were then collected with an electrostatic precipitator. The presence of the 80 K phase was found by X-ray diffraction, and it was shown that a precise control of the reactor temperature and residence time could avoid the undesirable formation of the 10 K phase.

Chadda *et al.* (1991) obtained an $YBa_2Cu_3O_{7-y}$ /CuO composite powder consisting of 25-50 nm crystallites by spray pyrolysis of a nitrate solution. This powder could be converted into $YBa_2Cu_4O_8$ by heating it in an O_2 atmosphere. However, this conversion was not successful when using a larger grained powder of 100-250 nm. $YBa_2Cu_4O_8$ has certain advantages over $YBa_2Cu_3O_{7-y}$ with respect to the flux pinning requirement, see section 2.7. Takao *et al.* (1996) used an electrostatic aerosol mixing process to produce composite $BaZrO_3/YBa_2Cu_3O_{7-y}$ particles. Here, after a separate synthesis of the two compounds the $BaZrO_3$ aerosol particles smaller than 100 nm were electropositively charged while the $YBa_2Cu_3O_{7-y}$ particles with a

size of 500 nm were electronegatively charged. By imparting a multiple charge to the superconducting particles and singly charging the nanoparticles, a coating of $BaZrO_3$ nanoparticles on the $YBa_2Cu_3O_{7-y}$ particles resulted after mixing. After sintering the powder to a superconducting composite body, the critical current density increased by a factor of ten as compared to the same superconducting material without $BaZrO_3$ nanoparticles.

5.6 Synthesis of magnetic materials

Inert gas evaporation using a low-pressure, between 1 and 10 mbar, is used routinely to produce magnetic nanoparticles for research purposes. It stems from the pioneering work in the group of Uyeda who produced Fe, Co and Ni particles from 8 to 200 nm by evaporating the metal in low-pressure Ar (Tasaki *et al.* ,1965). As an example of a more recent work, Gangopadhyay *et al.* (1992) evaporated Fe from a heated crucible and obtained nanoparticles on a cooled substrate by thermophoresis. The Fe nanoparticles with sizes between 5 and 20 nm were subjected to a slow oxidation in a Ar-air mixture to passivate the surface. The resulting Fe-oxides layers were 1-2 nm thick. The highest coercivity at room temperature was 1050 Oe for nanoparticles with a diameter of 13 nm. Particles smaller than 9 nm were superparamagnetic.

Alloy nanoparticles have also been obtained using inert gas evaporation. They have magnetic properties of technological importance when composed of a magnetic material imbedded in a nonmagnetic material. Li *et al.* (1994) obtained by evaporating the alloy in Ar gas FeCr particles having mean sizes between 8 and 36 nm. Some Fe and Fe-oxide was also detected in the particles, making the interpretation of the magnetic properties difficult.

A method better suited for large scale synthesis is inert gas condensation. Balachandran *et al.* (1995) evaporated Cr in low pressure He and collected the Cr nanoparticles on a cold finger. The powder could be compacted in-situ after an oxidation step with O_2 to form Cr_2O_3. The nanophase powder with a mean particle size of 10 nm exhibited superparamagnetic behavior. Sintering led to an increase in particle size, up to 80 nm at the highest sintering temperature, with the superparamagnetic properties partly retained.

Pyrolysis in a oxyhydrogen flame of $Fe(CO)_5$ or iron acetylacetonate dissolved in toluene led to γ-Fe_2O_3 powders with particle sizes as small as 5 nm (Grimm *et al.*, 1997). Laser pyrolysis of $Fe(CO)_5$ using a pulsed CO_2 laser has been applied by Majima *et al.* (1994), who obtained nanoparticles with a mean size of 13 nm. The particles contained a large percentage of γ-Fe which is normally stable at high

temperatures and which is paramagnetic up to room temperatures. Vollath *et al.* (1995) synthesized γ-Fe_2O_3 particles in the size range 4-5 nm by heating $FeCl_3$ in a microwave plasma. The particles were found to be superparamagnetic. A superparamagnetic nanocomposite was synthesized by Zachariah *et al.* (1995), who used a CH_4/O_2 flame as the reaction environment to which Fe and Si-bearing precursors such as $Fe(CO)_5$ and $SiO_2(CH_3)_6$, were added. The magnetic Fe_2O_3 nanoparticles of 5-10 nm were encapsulated in SiO_2 particles ranging from 30 to 100 nm. The samples showed evidence for superparamagnetism over a wide temperature range. Hwang *et al.* (1997) synthesized 18 nm Ni nanoparticles encapsulated by a graphite layer several nanometers thick, to protect them against oxidation. This was done by an arc discharge plasma in a He environment with Ni contained in a graphite anode. The encapsulated Ni nanocrystals showed a significant lowering of the magnetic coercivity and saturation magnetization , as compared with bulk Ni.

Spray pyrolysis has been used to produce nanoparticles of magnetic materials such as ferrites and garnets. Tang *et al.* (1989) atomized a solution of $Fe(NO_3)_3$ and $Ba(NO_3)_2$ in water, and obtained after pyrolysis in a furnace spherical particles of $BaFe_{12}O_{19}$ with sizes between 40 and 80 nm. Post-annealing was necessary to obtain a crystalline phase and achieve high coercivity values, up to 5360 Oe at room temperature.

Mizuguchi *et al.* (1994) introduced aqueous metal nitrate solutions in aerosol form into an ICP and obtained $BaFe_{12}O_{19}$ nanoparticles with sizes between 10 and 50 nm. Film formation, obtained by an electrostatic precipitator at elevated temperatures using a H_2-O_2 flame, proved problematic due to deviations from stoichiometry. De Marco *et al.*(1993) used a R.F. plasma suited for large scale nanoparticle production. $Ni_{0.5}Zn_{0.5}Fe_2O_4$ and $NiFe_2O_4$ nanoparticles with a mean size of about 55 nm were produced, containing Fe_3O_4 as an impurity. The nanoparticle powders had higher coercivities than the bulk material.

5.7 Conclusions: special process requirements for selected functional applications

Two chemical compounds are selected for the remaining of this work. One component is selected for its potential quantum confinement effects. PbS is a narrow-gap IV-VI semiconductor with a cubic rock salt structure and is an attractive candidate for the study of quantum confinement effects as its hole Bohr radius is 9 nm. This results in strong confinement effects as compared to the II-VI semiconductors such as CdS and CdSe with Bohr radii of about 1 nm (Machol *et al.,* 1994). The confinement results in a blue shift in the optical absorption spectrum (Brus, 1984). The other

material, SnO_2, is selected for its gas-sensing properties, which were described extensively in Chapter 5.3.

A size uniformity is important in order to study or make use of quantum size effects, as a distribution of particle sizes will decrease or smear out these effects. In view of the high specific surface and activity of SnO_2 nanoparticles, considerable improvement in sensing properties is expected. In order to understand the relationship between gas-sensing behaviour and particle size better it is necessary to generate monodisperse nanoparticles, because a distribution of particle sizes will decrease the special properties and complicates the interpretation of the experimental results. This was also emphasized by Göpel and Schierbaum (1995) in their review article on future prospects of SnO_2 gas sensors: 'Particular emphasis is put on preparing thin films of SnO_2 with homogeneous particle sizes in the nanometre range'. At the moment no gas sensors based on almost equal-sized nanoparticles are available. As shown in the preceding chapter, Brownian coagulation rules out the synthesis of monosized particles by gas-phase synthesis. Therefore, a size-fractionation technique will be applied in this work in which a narrow fraction is taken from the original wide distribution.

Apart from the size homogeneity, the chemical composition is important. In case of PbS, it should be investigated if it is possible to retain the stoichiometry when sublimating the source material directly. Furthermore, the particles should be crystalline as amorphous material does not show semiconducting properties. In case of the SnO_2, some deviation of stoichiometry is desirable, as in substoichiometric SnO_2, denoted by SnO_x, the electrical transport properties are more suitable for gas sensing applications. Furthermore, some special handling techniques are necessary. The nanoparticles have to be brought onto a suitable substrate for use in functional applications. For some applications, e.g. doped gas sensors, a control over the mixing of two different nanoparticle flows is needed. It will be shown in the next chapter that the use of electrical effects allows size-fractionation, nanoparticle deposition and controlled mixing.

6. Controlling nanoparticle behaviour by use of electrical effects

A control of gas-phase nanoparticle synthesis is possible on the basis of the movement of charged particles in an electric field. This allows size fractionation, direct particle size measurement, deposition of nanoparticles onto suitable substrates and controlled mixing.

This requires nanoparticles which are charged. Therefore, a charger especially suited for nanoparticles is needed. In the newly developed twin Hewitt charger two corona discharge zones are connected by a charging zone where the nanoparticle aerosol flows. Ions move into the charging zone alternating from each corona discharging zone by means of a square-wave voltage. The operation parameters of the device are experimentally characterized and described in Chapter 6.1 with the goal to optimize the charging efficiency in N_2 carrier gas. The contents of this subchapter has been published (Kruis and Fissan, 2001).

Most nanoparticle formation paths in the gas phase involve particle growth induced by particle collision due to the Brownian motion. This leads to a minimum geometric standard deviation of 1.4 (see Fig. 4.2.5), which is further increased by turbulence and variations in residence time. Narrowing the size distribution is possible by use of a DMA at the cost of decreased particle number concentration. The standard DMA design is, however, not suitable for use at sub-atmospheric pressures. Lower pressures are desirable for the synthesis because it will lead to a smaller mean particle size and to a reduction of gas-phase impurities. Therefore, a new DMA has been designed to operate at lower pressures. Theoretical and practical considerations for the design will be shown in Chapter 6.2.

The application of the so-called electrical mobility analysis allows the direct measurement of particle size distributions. For this goal, a DMA is connected to a particle counter such as a condensation nucleus counter or an electrometer. An inversion technique combined with the transfer function of the DMA and the charging efficiency of the charging device allows to calculate the particle size distribution. This technique will also benefit from an increased charging efficiency, as this increases the sensitivity in the nanoparticle size range. Furthermore, a DMA capable for operating at lower processes enables size measurements in low pressure reactors, which are used in industry for TiO_2 , SiO_2 and soot particle synthesis.

The characterization of the electrical properties of thin nanoparticle films was hampered by problems of contamination of the samples by air as the sample was transported from the reactor to measurement set-up. A nanoparticle film formation

device, basing on electrostatic deposition, which enables measurement under clean conditions will be described in Chapter 6.3.

6.1 Nanoparticle charging using a twin Hewitt charger

One important way of obtaining control over their movement is manipulation of charged nanoparticles in an electric field. This can be used for the generation of monodisperse particles by means of a Differential Mobility Analyzer at atmospheric conditions, as will be shown in chapter 7, or by means of a time of flight Mass Spectrometer in a high vacuum (Ehbrecht *et al.,* 1997). It is also essential when using electrostatic deposition.

Nanoparticle charging at standard temperature and pressure is possible by means of unipolar or bipolar diffusion charging. Unipolar ions are commonly generated by means of a corona discharge whereas bipolar ions are generated by means of radioactive sources, either α or β sources such as ^{85}Kr or ^{241}Am. Bipolar charging leads to a charge equilibrium which has however low charging efficiencies, e.g. 3.3 % for positively charged 10 nm particles and 5.7 % for negatively charged particles (Wiedensohler, 1988). Unipolar diffusion charging has advantages over bipolar diffusion charging as it does not reach an equilibrium charge distribution, therefore potentially enabling the attainment of a higher charging efficiency. However, considerable difficulties arise because of large losses due to electrostatic effects as soon as the particles are charged.

In unipolar chargers using a corona discharge the particle-laden carrier gas is passed along a wire mesh around a corona wire, either over some part of it (Hewitt, 1957) or over the whole circumference (Büscher *et al* , 1994). Already in the first unipolar charging device described in 1957 by Hewitt a square wave voltage was applied between the wire mesh and the other side of the charging zone in order to reduce particle losses of charged particles in the electric field. A steady electric field would lead to large losses of charged particles. However, during only 50 % of the time ions fill the charging zone, during the other period they are expelled by the reversed field. In another diffusion charger (Wiedensohler *et al.,* 1994) in which ions are produced by a radioactive source, the charging zone is filled from two sides with ions, in each square-wave period from a different side. The most recent developed nanoparticle charger (Chen and Pui, 1999) uses a radioactive source, a charging zone with a longitudinal electric field and a large sheath gas flow in order to minimize losses to the walls.

Here, the advantages of the different chargers are combined into one new charger, which might be called a twin Hewitt charger. In this device, two corona discharge zones are connected by a charging zone. The particle-carrying gas flow is

parallel to the corona wires and the wire mesh. Ions move into the charging zone alternating from each corona discharging zone by means of a square-wave voltage between the two wire meshes.

6.1.1 Experimental setup

6.1.1.1 The twin Hewitt charger

Fig. 6.1.1 shows the schematic diagram of the newly developed twin Hewitt charger. The particle-laden gas is introduced via a short inlet section into a square charging zone with a width of 16 mm and a height of 10 mm. The charging zone is separated from the two ion production zones by means of metal wire meshes, and the bottom and top are composed of isolating material. The wire screens are connected to two square-wave generators with opposite phase and a maximal voltage difference ΔV of 600 V. The use of the square wave with a frequency f allows the use of a relatively large potential between both grids which results in a high ion concentration in the charging zone. The use of a non-alternating field would lead to a continuous movement of the charged particles toward the wire mesh.

Positive ions are produced by corona discharge of a 25 µm thick Au wire placed in the center of in a metal cylinder, which has at one side a slit of a length 15 cm and a height 1 cm. This slit is placed towards the charging zone and is covered with the wire mesh. The careful handling of the thin Au wire is critical for obtaining a long life time of the wire. The wire attached by glue to a needle is inserted through the openings at the end of the cylinder, and immobilized by means of a isolation strip and a drop of glue. Its' electrical contact is made by means of a drop of silver paste.

The length of the charging zone L with a maximum length of 15 cm can be adjusted by covering part of the wire meshes with thin Al sheets. The exposed wire meshes are always as close to the exit as possible.

Initial measurements using a constant high voltage connected to the coronas showed problems with stability and reproducibility. This problem was solved by using two different high voltage sources which were so regulated that a constant current in the range 10 to 100 µA was obtained. The largest part of this current will flow via the cylinder and the square-wave generators, which are electrically connected, towards ground potential. This did not affect the functioning of the square-wave generators, which was checked by means of an oscilloscope.

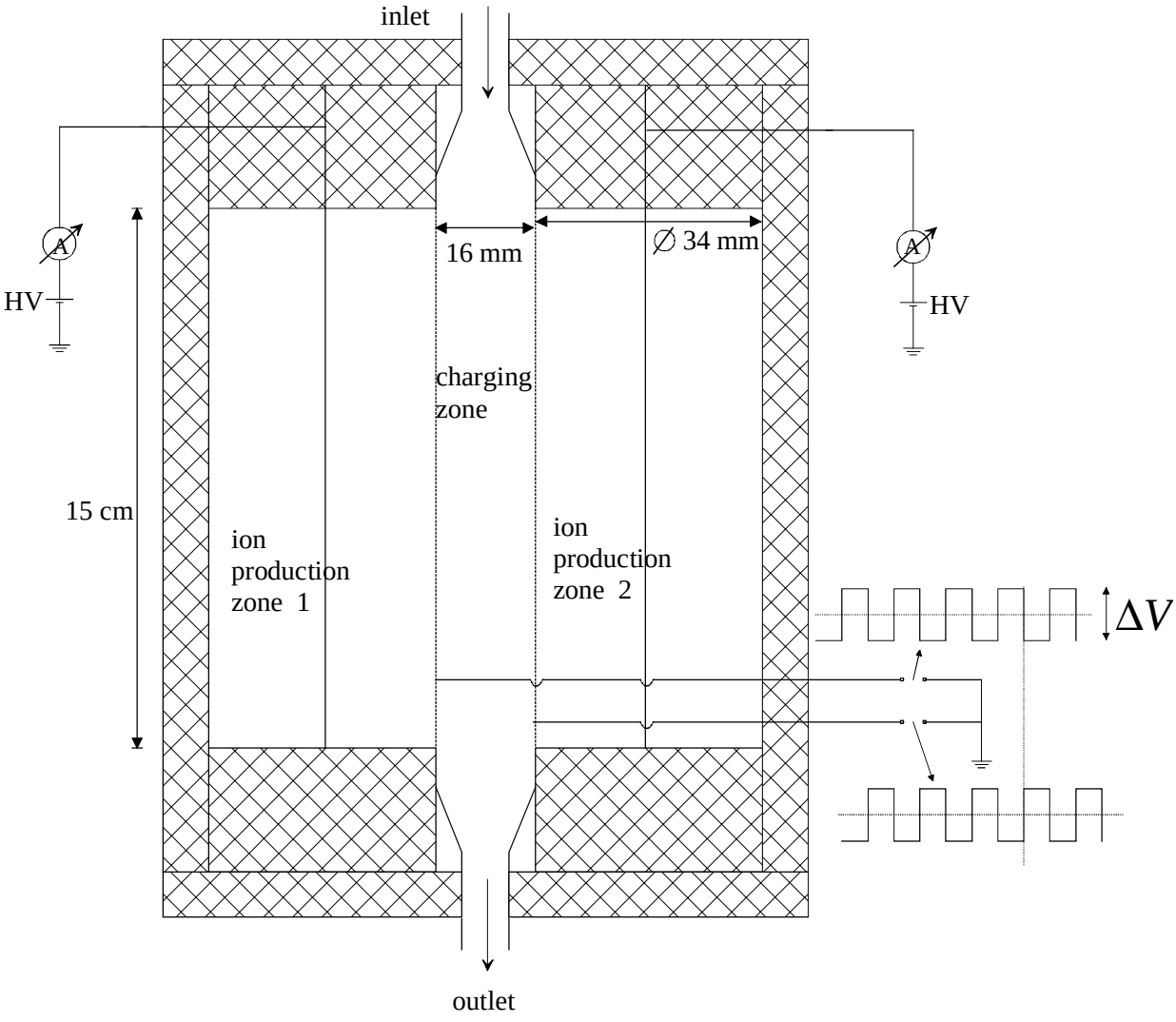

Fig. 6.1.1. Schematic diagram of the twin Hewitt charger. Ions are produced in two cylindrical sections with a central Au wire with a diameter of 25 µm and move through a slit covered with wire mesh into the charging zone. A square wave electric potential is established between both wire meshes.

6.1.1.2 Setup for measuring charging efficiencies

Fig. 6.1.2 shows the schematic diagram of the experimental setup used in measuring the charging efficiency. It consists of four parts: a generator of monodisperse particles, a device used for discharging the particles, the twin Hewitt charger and the measurement section for distinguishing charged and uncharged particles.

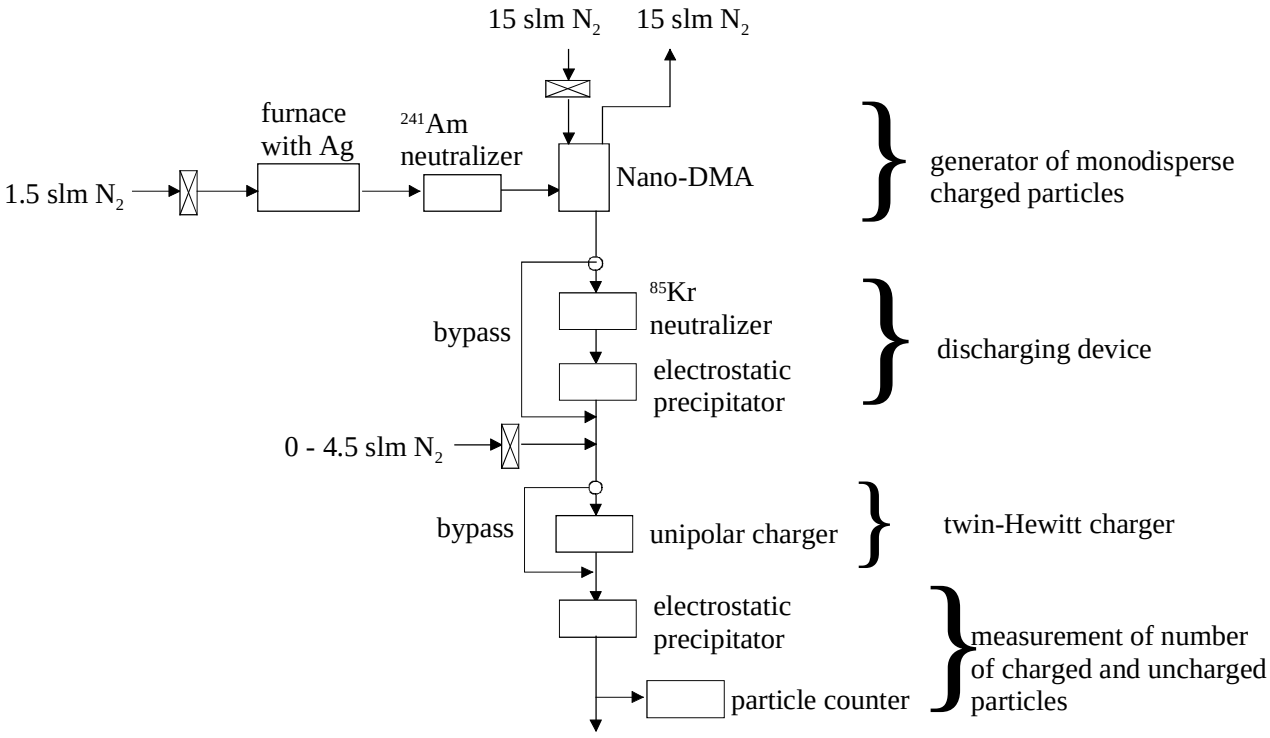

Fig. 6.1.2. Experimental setup for measuring the charging efficiency of a unipolar charger. A nanoparticle aerosol is generated by means of evaporation-condensation, size-classified by means of a Differential Mobility Analyzer (DMA) and subsequently discharged. After being charged in the twin-Hewitt charger, the particles pass an electrostatic precipitator after which the number concentration is monitored by means of a particle counter.

The aerosol generator consists of a furnace in which Ag is evaporated, followed by condensation in the cooler parts of the tube. The nanoparticles thus formed are partially charged using a radioactive source and are then classified according to their electric mobility by means of a Nano-DMA (Chen *et al.*, 1998) to obtain a well-defined test aerosol. When using a carrier gas flow of 1.5 slm (standard liters per minute) and an additional flow of 15 slm through the Nano-DMA (TSI, Minneapolis, USA), a theoretical GSD of 1.1 is attained for the classified aerosol and can therefore be called monodisperse. The experiments are performed with N_2 as carrier gas at standard conditions (1 bar, 293 K). The flow through the tube furnace and DMA was fixed at 1.5 slm. The use of dilution gas allowed the gas flow rate through the charger to be adjusted between 1.5 slm and 6 slm.

The particles leaving the DMA are charged which is undesirable for the charging measurements. Therefore, they are led through a radioactive neutralizer which partially neutralizes the particles. The fraction which is still charged is removed in an electrostatic precipitator, which consists of a annular tube with a high electric

field intensity (2 kV/cm). The discharging section can also be bypassed in order to produce monodisperse charged particles for the measurement of electric losses in the charger.
After being charged in the twin-Hewitt charger, the particles pass a second electrostatic precipitator before being counted in a particle counter (UCPC 3025, TSI, Minneapolis, USA) which has a detection threshold of about 3 nm. The number concentration of charged particles n_+ is determined by taking the difference between particles counted without an electric field (giving $n_+ + n_0$) applied in the electrostatic precipitator and particles counted with an electric field applied field (giving the number concentration of uncharged particles n_0) applied. The extrinsic charging efficiency can be calculated by the following equation:

$$E_e = \frac{n_+}{n_{in}} \tag{6.1.1}$$

where n_{in} is the number concentration of particle entering the charger. The charging thus defined is called extrinsic because the charging efficiency is actually higher, but charged particles are lost more easily than uncharged particles. In the remainder of this article, when referring to charging efficiency the extrinsic charging efficiency is meant. The intrinsic charging efficiency E_i is defined as the fraction of particles which are charged inside the charger, but which also can be lost there.

6.1.2 Ion concentration in the charging zone

In this section, the ion concentration in the charging section is estimated. The charging zone is in between $x = 0$ and $x = a$, a is the width of the charging channel. We calculate the electrical field $E(x)$ and the ion concentration $n(x)$ for the case of constant grid voltage. On the basis of Maxwell's theory, the electrical field between the two grids can described by:

$$\text{div}\,\vec{E} = \frac{\rho(x)}{\varepsilon_0} \tag{6.1.2}$$

where $\rho(x)$ is the space charge density and ε_0 the dielectric constant of vacuum. As the upper and lower end of the charging channel is an isolator, we assume that the field lines do only have a component in x-direction:

$$\frac{dE(x)}{dx} = \frac{\rho(x)}{\varepsilon_0} \tag{6.1.3}$$

The ion current density $\vec{j}$ is given by:

$$\vec{j} = \rho \vec{v} \tag{6.1.4}$$

The ion velocity v_{ion} is determined by:

$$v_{ion}(x) = Z_{ion}\ E(x) \tag{6.1.5}$$

where Z_{ion} is the electric mobility of the ions. The current density can be expressed on the basis of the ion current I through the grid, which has an effective area of wL, as:

$$\rho(x)\ Z_{ion}\ E(x) = \frac{I}{wL} \tag{6.1.6}$$

The space charge defines the ion concentration:

$$\rho = n_{ion} e \tag{6.1.7}$$

so that the space charge can be eliminated, leading to a differential equation for $E(x)$:

$$E(x) = \sqrt{\frac{2Ix}{wLZ_{ion}\varepsilon_0} + c} \tag{6.1.8}$$

In order to determine I and n_{ion} from experiments, we have to solve:

$$\int_0^a E(x)dx = \Delta V \tag{6.1.9}$$

leading to

$$\frac{wLZ_{ion}\varepsilon_0}{3I}\left\{\left(\frac{2Ia}{wLZ_{ion}\varepsilon_0} + c\right)^{3/2} - c^{3/2}\right\} = \Delta V \tag{6.1.10}$$

For each pair $(\Delta V, I)$ we can determine c by solving this equation iteratively and determine the ion concentration in the charging zone:

The ion current per unit area of wire mesh I / wL, measured with constant electric field applied over the charging zone, showed little dependence on the length of the charging zone, as expected. Using the model the ion concentration can be calculated based on the experimental values of the ion current. The product of ion concentration and time $n_{ion}t$, an important parameter in the charging process, is shown in Fig. 6.1.3. The ion concentration varies over the width of the charging zone, therefore the ion concentration in the middle of the charging zone is taken. Increasing L or decreasing the flow rate for ϕ yield a higher value of $n_{ion}t$. The nonlinear increase of $n_{ion}t$ indicates that the ion concentration is not constant at various L. A possible explanation is that the electric field will extend beyond the charging zone into the aerosol in- and outlet, leading to a higher effective length. This boundary effect is obviously less important at higher L.

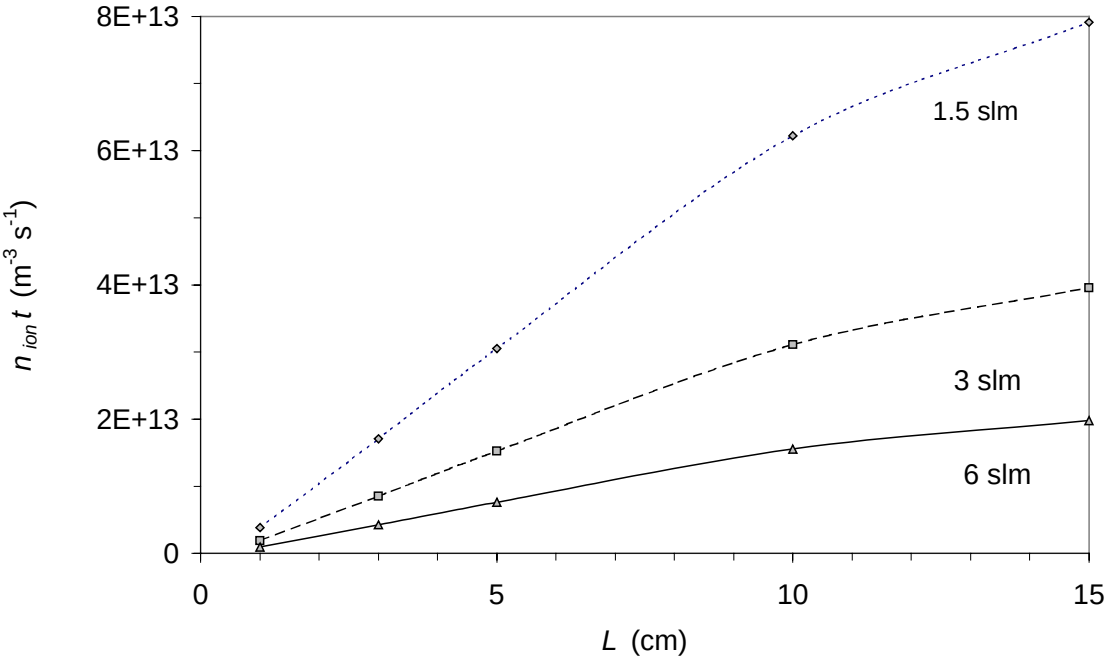

Fig. 6.1.3. The product of ion concentration and time $n_{ion}t$ *as function of the length of the charging zone L for different flow rates as indicated in the figure.* n_{ion} *is calculated at* $x = \frac{1}{2}a$.

6.1.3 Charging efficiency

6.1.3.1 Effects of frequency and electrical potential

The charging efficiency was measured as function of the square wave frequency and the voltage difference applied between the two meshes in order to find the best operating conditions. The extrinsic charging efficiency as function of the frequency is shown in Fig. 6.1.4 for different particle sizes. At frequencies above 100 Hz, the extrinsic charging efficiency decreases but is almost constant below 100 Hz. Frequencies below 10 Hz result in undesirable fluctuations of the high voltage of the corona wires, as the voltage supply is used in the constant current mode. In the remainder of the experiments a frequency of 50 Hz was used.

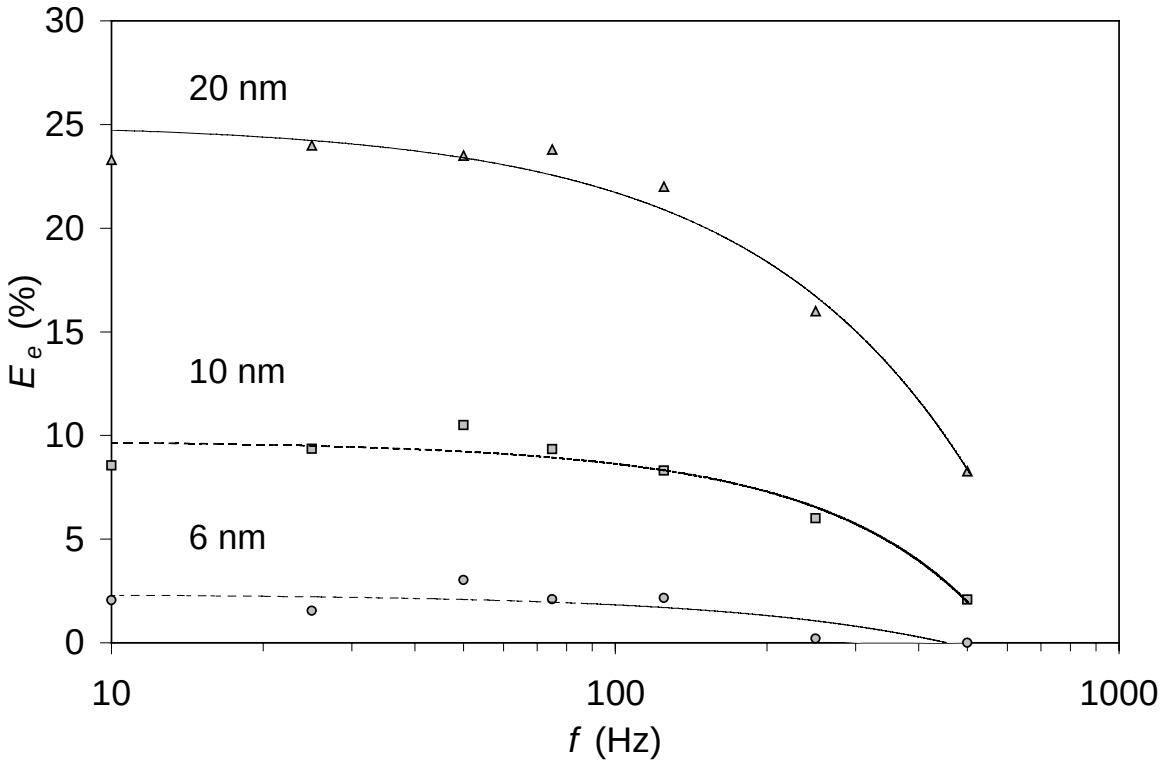

Fig. 6.1.4. Extrinsic charging efficiency as function of the frequency of the square wave generator for different particle sizes. Further conditions were I_c = 50 μA, ΔV = 400 V, ϕ = 1.5 slm , L = 15 cm.

Fig. 6.1.5 shows the extrinsic charging efficiency as function of the voltage difference ΔV using the whole length of the charging zone, L = 15 cm. After an initial increase, the charging efficiency E_e is not affected by the value of ΔV when ΔV >300V. Using a very short charging zone, L = 1 cm, E_e steadily increases with ΔV . The increase seems to level off around 600 V. Higher voltage differences could not be applied as the current through the square wave generators became too high. Therefore, ΔV = 600 V seemed to be optimal for obtaining a high charging efficiency for all lengths of charging zones.

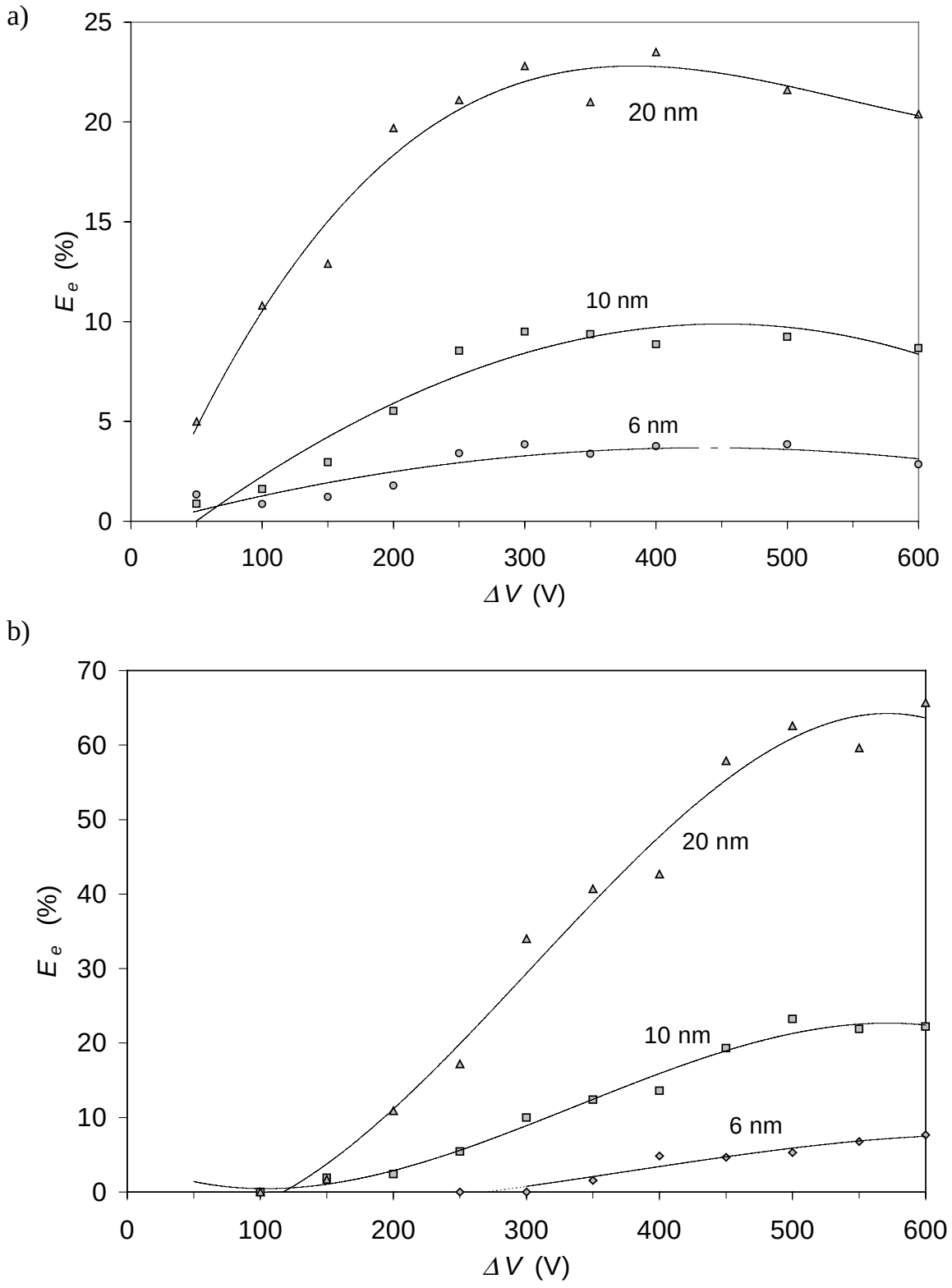

Fig. 6.1.5. Extrinsic charging efficiency as function of the voltage difference ΔV between the wire meshes for (a) L = 15 cm and (b) L = 1 cm. Further conditions were I_c = 50 µA, f = 50 Hz, ϕ = 1.5 slm.

6.1.3.2 Effects of length of charging zone and residence time

After obtaining a lower charging efficiency than we expected with L = 15 cm, we decided to perform a systematic study into the effect of the length of the charging zone. The method described earlier for obtaining a variable length is not ideal because the shorter charging zones have a relatively long entrance zone which causes some diffusion losses. This will be discussed later on. Building differently sized chargers is however unpractical and uneconomical. The lowest flow rate through the charger ϕ was 1.5 slm, a common flow rate when operating DMAs. For material synthesis applications, higher flow rates are desirable so this flow rate was increased to 3 and 6 slm in order to investigate the effect of having a shorter residence time in the charger. The residence times in the charging zone with L = 15 cm are τ = 0.96, 0.46 and 0.23 s for 1.5, 3 and 6 slm, resp.

Fig. 6.1.6 shows the effect of varying L and ϕ for particles with diameter 6 nm (Fig. 6.1.6a), 10 nm (Fig 6.1.6b) and 20 nm (Fig 6.1.6c). For each particle size and ϕ there exists a length where E_e is maximal. This length is L = 3-5 cm for ϕ = 1.5 slm and around L = 10 cm for ϕ = 6 slm, independent of particle size. For larger flow rates clearly a longer charging zone is needed. Furthermore, when the particles become smaller it seems to become increasingly difficult at higher flow rates to reach the same charging efficiencies as with ϕ = 1.5 slm by changing L.

a)

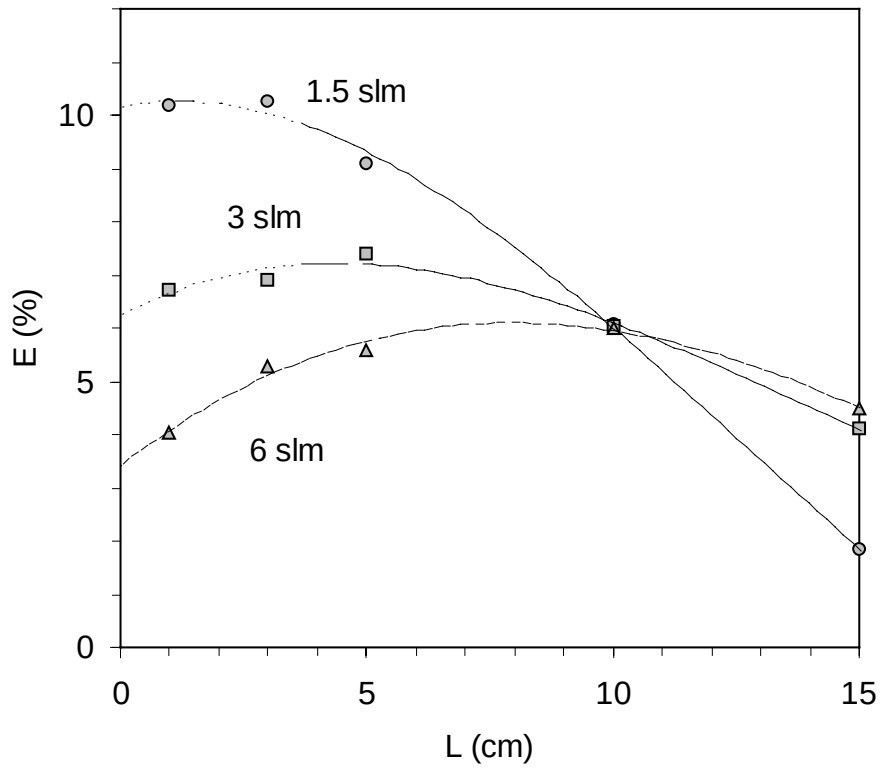

b)

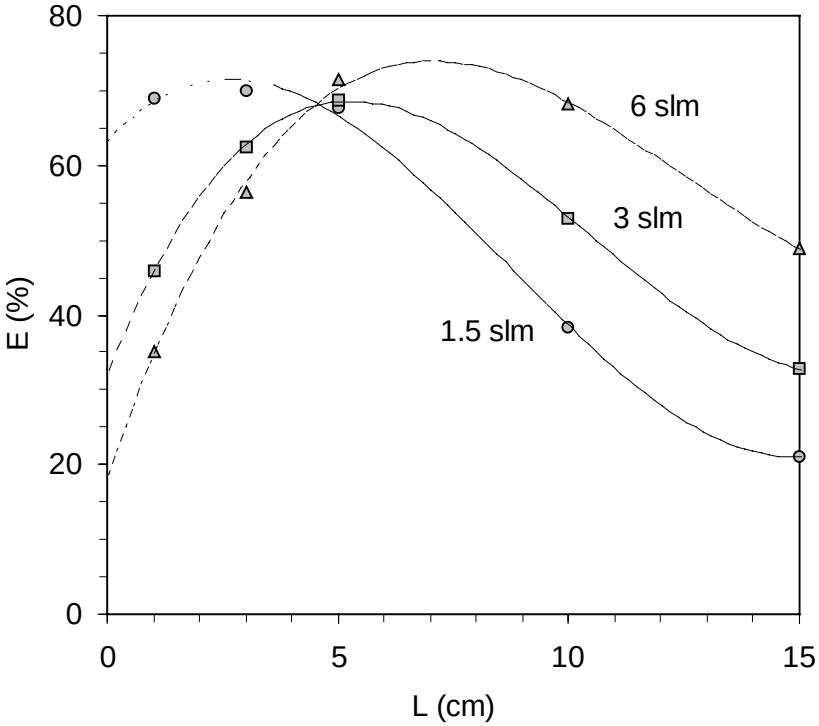

c)

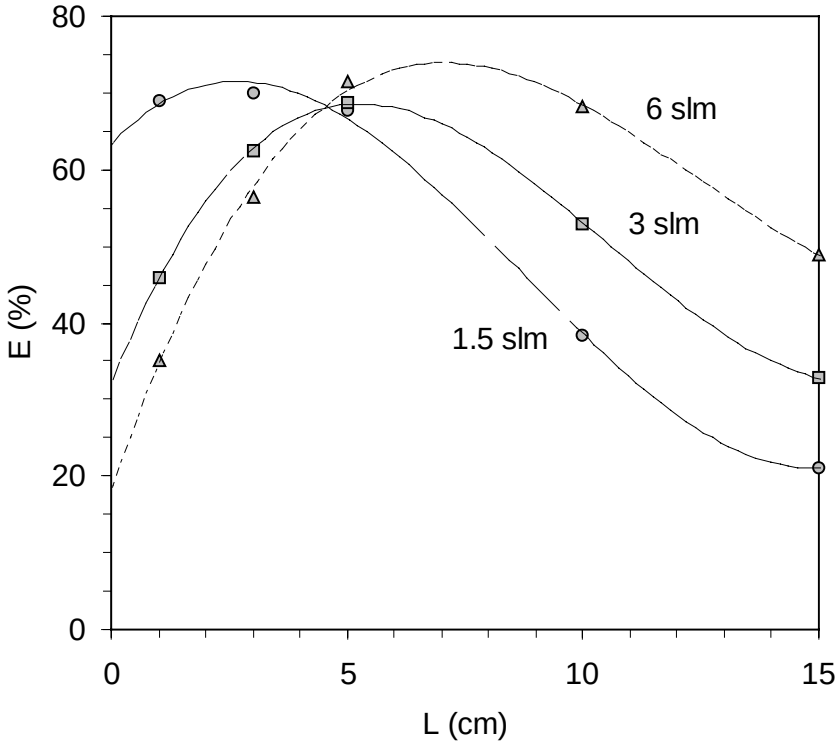

Fig. 6.1.6. Extrinsic charging efficiency as function of the length of the charging zone, for particles with a diameter of (a) 6 nm, (b) 10 nm and (c) 20 nm. The gas flow rates ϕ were varied as indicated in the figures. Operating conditions were I_c = 50 µA, ΔV = 600 V and f= 50 Hz.

Fig. 6.1.7 shows the charging efficiency E_e as function of the particle size up to 50 nm, for ϕ =1.5 slm (Fig 6.1.7a) and 6 slm (Fig 6.1.7b). Decreasing the particle size also decreases E_e, below 6 nm the efficiency becomes too low for accurate measurement and for practical application.

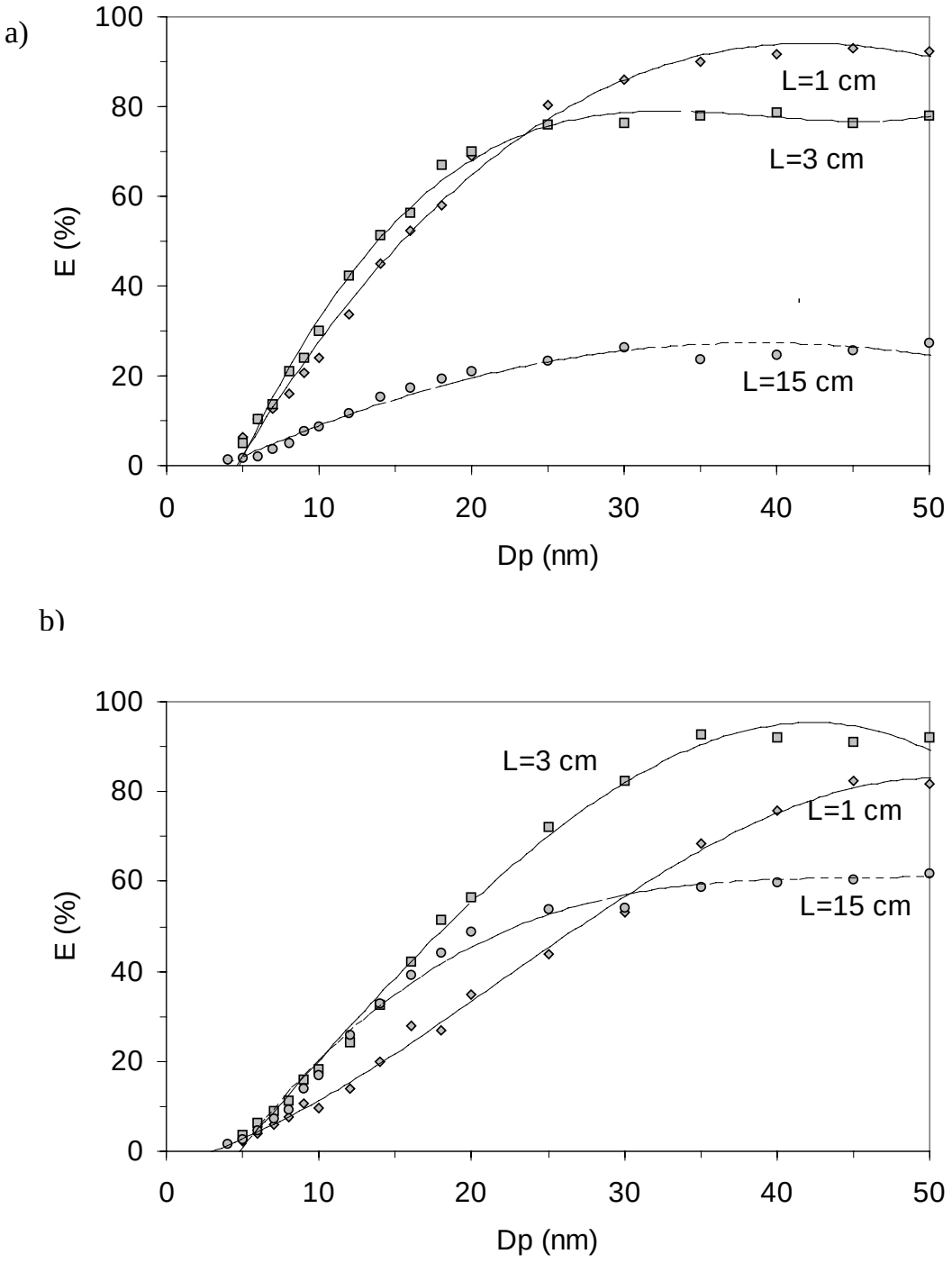

Fig. 6.1.7. Extrinsic charging efficiency as function of particle diameter for a flow rate of (a) 1.5 slm and (b) 6 slm. Curves for different lengths of the charging zone L are shown. Operating conditions as in Fig. 6.1.5.

6.1.4 Particle losses in the charging zone

A key in understanding the performance of a nanoparticle charger lies in understanding by what mechanisms the particles are lost. There are several mechanisms which might be responsible for the particle losses:

(i) The Brownian diffusion losses affects both charged and uncharged particles.

(ii) The oscillation of charged particles due to the alternating electrical field will lead to particles moving toward the wire mesh, so that particles relatively close to the wire mesh will be lost there.

(iii) The space charge due to the unipolar ions in the charging zone will drive charged particles toward the walls, which are the wire meshes and the upper and lower isolated parts of the channel. This is difficult to describe by a model, because the system is two-dimensional and periodically changing.

(iv) Electrostatic effects which will be especially important for the aerosol in the vicinity of the isolating material at the top and bottom of the charging channel. The material can become charged due to static electricity or deposition of charged particles.

Especially the last two effect are very difficult to model, so a series of experiments were done to investigate the importance of particle losses. The experiments were performed with charged particles, as diffusion losses of uncharged particles were found to be small in magnitude compared to the losses of charged particles. The results are shown in Fig. 6.1.8. Most experiments were performed with the longest charging section (L=15 cm), because this is the system with the largest losses.

First consider the case (a) with ϕ=6 slm and ΔV=0 V, so without applied field. The fraction of charged particles lost increases with decreasing particle sizes, because smaller particles have a higher electrical mobility, so that they are more ‘sensitive’ to electrical fields and electrostatic effects. Applying now the square wave potential over the charging channel, case (b), no significant change in the particle loss is observed. This means that effect (ii), losses due to the oscillation of the particles, is probably not very important and that the effects (iii) and (iv) are dominant. When the gas flow rate ϕ is decreased to 1.5 slm, case (c), the losses are seen to increase, except for particles below some 10 nm. It is probable that a kind of layer exists next to the walls and wire meshes of the charging channel, where particles have a high probability of being lost by mechanism (ii) or (iv). The width of this layer will be larger for smaller particles. A longer residence time increases the probability that charged particles enter this layer by Brownian diffusion or space charge effects, and furthermore the longer the particles remain in this layer next to the wall, the higher the probability they will get lost. This is clearly illustrated by comparison of case (c) for L=15 cm and (d) for L=3 cm. The losses for L=3 cm are a factor of 5-8 smaller than for L=15 at this low gas flow rate.

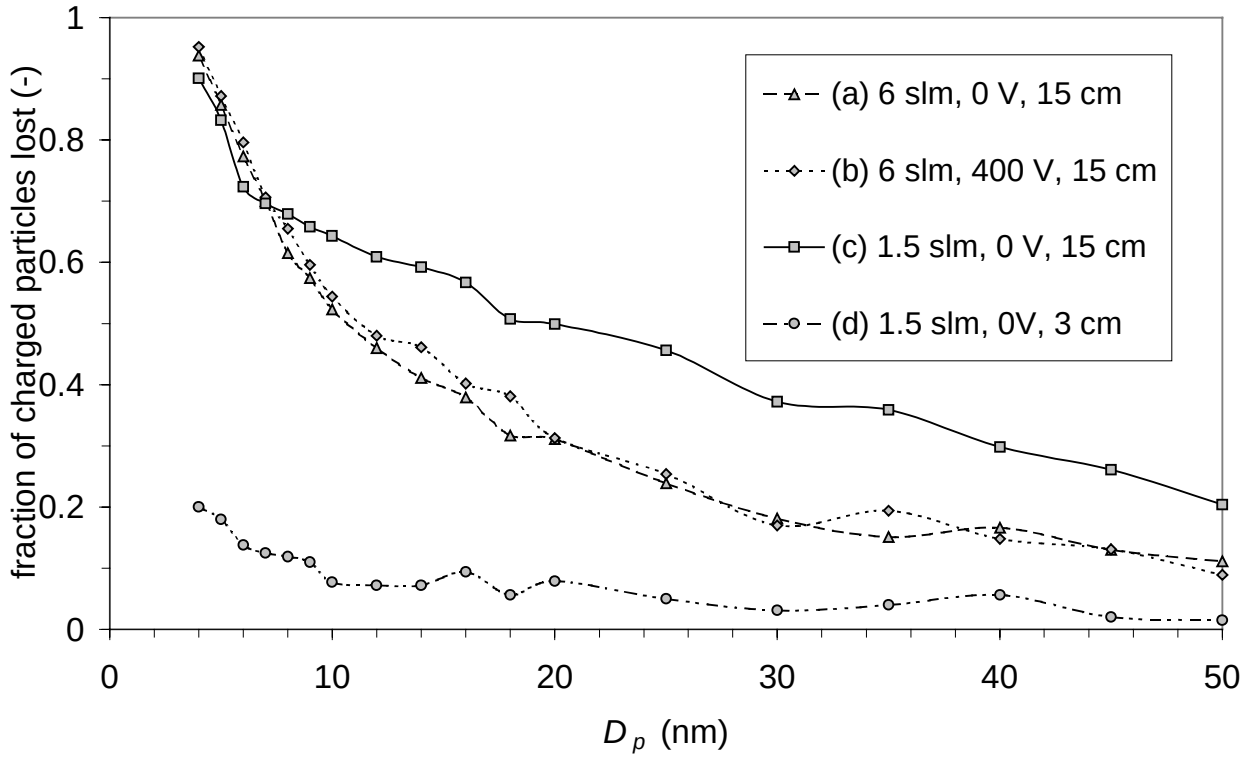

Fig. 6.1.8. Fraction of charged particles lost as function of particle diameter. The insert shows the values of the gas flow rate ϕ, voltage difference ΔV and length of the charging zone L, respectively.

In an attempt to reduce the electrostatic losses, the isolating material (DELRIN^{TM}) which composes the top and bottom of the charging channel was replaced by an antistatic material which allows charges to dissipate due to a moderate resistivity in the range of GΩ cm. The losses of charged particles were clearly reduced but the charging efficiency dropped dramatically. The electrical field lines will probably not any more be connecting the two wire meshes, but will lead from the wire meshes toward the bottom and top of the charging material. This leads to a loss of ions and a decrease in the $n_{ion}t$-product. The use of isolating material might be advantageous due to the fact that the material becomes slightly charged due to deposition of ions and charged particles, which can repel charged particles from the walls. Therefore, care was taken to run the charger in the charging mode before making measurements.

6.1.5 Discussion

The decreasing charging efficiency with increasing frequency of the square wave (Fig. 6.1.4) is due to the finite time it takes to fill the charging channel with ions in a new period. At a too high frequency, the ion concentration in the channel is not yet at

its' maximum. The mean ion concentration will therefore drop above a certain frequency, thereby lowering the charging efficiency. Increasing the voltage difference ΔV over the charging channel (Fig. 6.1.5) also increases the ion concentration. Above ΔV =500 V the increase in charging efficiency starts to level off, probably because the particle loss mechanisms (ii) and (iii) which are dependent on the applied field become more dominant.

The maximum in the charging efficiency as function of the length L of the charging channel (Fig. 6.1.6) is more complicated to understand. From the measurements of the losses of charged particles (Fig. 6.1.8), it is clear that a smaller value of L leads to a significant decrease in charged particle losses. At the same time, however, the $n_{ion}t$ -product which influences directly the intrinsic charging efficiency drops with lower L. From Fig. 6.1.3 it can be seen that the decrease in the $n_{ion}t$ -product is more pronounced at lower values of L, probably due to non-uniformity of the electric field, as the length of the charging channel L is shorter than its' width at the smallest value of L. Therefore, the maximum in the charging efficiency occurs there where the $n_{ion}t$ -product is sufficiently high for obtaining a high intrinsic charging efficiency, but where L is not too high in order to minimize the losses of charged particles. A higher value of the gas flow rate ϕ leads to a lower $n_{ion}t$ -product at constant L (Fig. 6.1.3), so that a longer charging channel is necessary.

The present charger does not use a sheath gas flow along the walls or wire meshes. A sheath flow have been used in order to decrease the losses of charged particles. Chen and Pui (1999) report reaching an extrinsic charging efficiency of 65 % (with a definition based on absolute particle number, not on particle concentration) for particles with a diameter of 10 nm. However, a large sheath gas flow is applied which results in a dilution of the aerosol by a factor of four. This dilution is usually not desired. Using our definition of extrinsic charging efficiency (eq. 6.2.1), an extrinsic charging efficiency of 16 % would result.

6.2 A Differential Mobility Analyzer design for low pressures

The differential mobility analyzer (DMA) is the predominant instrument for measuring the size distribution of submicron aerosols. Additionally, the instrument is more and more being used as a source for delivering particles with a narrow size distribution. In a DMA, charged particles are separated according to their electrical mobility. In a cylindrical DMA, the median value of the electrical mobility of the classified particles is given by (Knutson and Whitby, 1975):

$$Z_p = Q_c \frac{\ln(R_2 / R_1)}{2\pi L V} \qquad (6.2.1)$$

in which L is the effective electrode length, R_1 and R_2 the inner and outer radii, V the applied voltage and Q_c the flow rate of the sheath gas. In another DMA design, the radial DMA originating from Pourprix and tested by Fissan *et al.* (1998) the electrical mobility is given by:

$$Z_p = \frac{Q_c h}{\pi\left(R_2^2 - R_1^2\right)V} \tag{6.2.2}$$

in which h is the distance between the electrodes. Both DMA types are available in several design types, and their performance was tested by Fissan *et al.* (1996). In Fig. 6.2.1 both types are shown.

The mobility Z_p can be related to a mobility-equivalent diameter:

$$Z_p = \frac{neC_c}{3\pi\mu d_p} \tag{6.2.3}$$

where n, e, C_c, μ and d_p are the number of elementary charges, the elementary electrical charge, the Cunningham correction factor, and the gas viscosity, respectively. For charged nanoparticles, the number of elementary charges is usually one.

The performance and suitability of a DMA for a certain application, i.e a given flow rate and pressure, is a function of the following instrument characteristics:

- Deviation from the ideal transfer function, e.g. by diffusional broadening effects. Diffusional broadening is caused by the Brownian movement of the nanoparticles between inlet and outlet slits, and increases with decreasing particle size.
- Particle losses inside the instrument, e.g. by diffusional or electrostatic losses.
- The maximal voltage before sparking between the two electrodes occurs.
- The maximal flows allowed in the instrument before turbulence occurs.
- Pressure drop inside the instrument.

The dynamic range of the instrument is usually limited to smaller particle sizes by the allowed value of the diffusional broadening , and to larger sizes the limitation is given by the voltage at which sparking occurs.

DMA's are designed to operate at atmospheric pressure. However, many nanoparticle synthesis systems operate in the mbar-range. There has been only one report on a DMA capable to operate under lower pressure conditions, 70-760 Torr (Seto *et al.,* 1997). The instrument is of the cylindrical type.

There are several considerations for low-pressure operation. When decreasing the pressure, the diffusion coefficient of particles increases as it is a linear function of the mean free path. This can be offset by increasing the velocity inside the instrument. Seto *et al.* (1997) found out that the performance could be kept on an acceptable level

when keeping the mass flow rate of the gas constant. A constant mass flow rate implies a higher gas velocity, as the product of velocity and density is constant.

In this work, a radial DMA is taken as geometry. The main reason is that the instrument is easily constructed in comparison to cylindrical DMA's. This can clearly be seen in Fig. 6.2.1. The performance of radial DMA's at atmospheric pressure has been experimentally found to be equal or even surpass that of a cylindrical geometry.

The tendency of a flow to become turbulent is determined by the Reynolds number. For a simple tube flow, it is given by:

$$\mathrm{Re} = \frac{\rho v D_{tube}}{\mu} \tag{6.2.4}$$

with ρ as gas density, v as gas velocity and D_{tube} as tube diameter. When decreasing the pressure by a factor C, the gas velocity v is not affected. The gas density changes with a factor $1/C$ and the gas velocity is multiplied with a factor C. This means that the Reynolds number is not affected by changing the pressure. For geometries other than a tube, the hydraulic diameter D_h has to be used in eq. 6.2.4. The conclusion that the Reynolds number is independent of system pressure is also valid for other DMA geometries, as the pressure does not change the hydraulic diameter. For the cylindrical DMA geometry, the hydraulic diameter can be derived to be:

$$D_h = \frac{2\left(r_2^2 - r_1^2\right)}{r_1 + r_2} \tag{6.2.5}$$

For a radial DMA, the hydraulic diameter is:

$$D_h = 2h \tag{6.2.6}$$

The standard conditions for DMA operation are an aerosol flow of 1.45 slm, sheath flow of 15 slm and N_2 carrier gas at STP. It can be shown that most cylindrical DMA's operate with Reynolds numbers below 1000. However, for the radial DMA the velocity is highest close to the central exit. When calculating for r=1.5 mm the Reynolds number, a value of 3890 is found which is in the turbulent range. Interestingly, the existing instrument does not show signs of turbulence which would have been detected by an increase in the transfer function. This can be understood by the practical experience that it takes some time for turbulences to develop. Because the flow is initially laminar and the actual position where the flow becomes turbulent is close to the exit, it looks like turbulence did not develop. The system is, however, sensitive to small disturbances.

a)

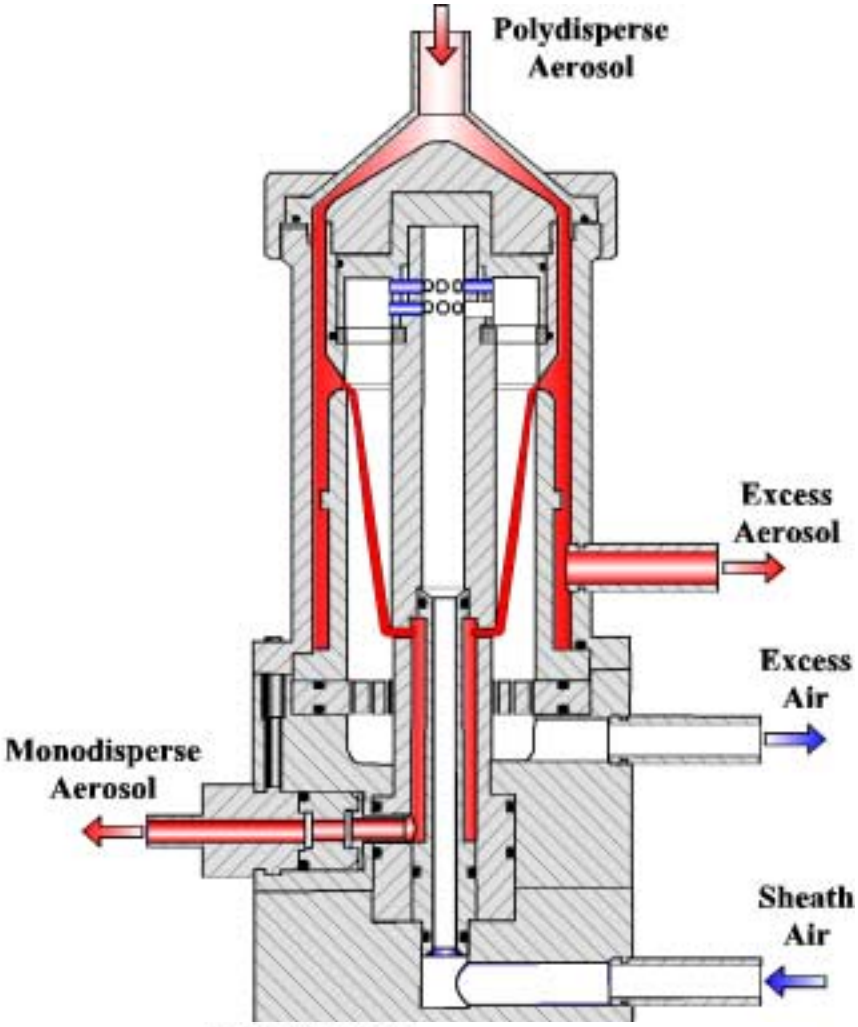

b)

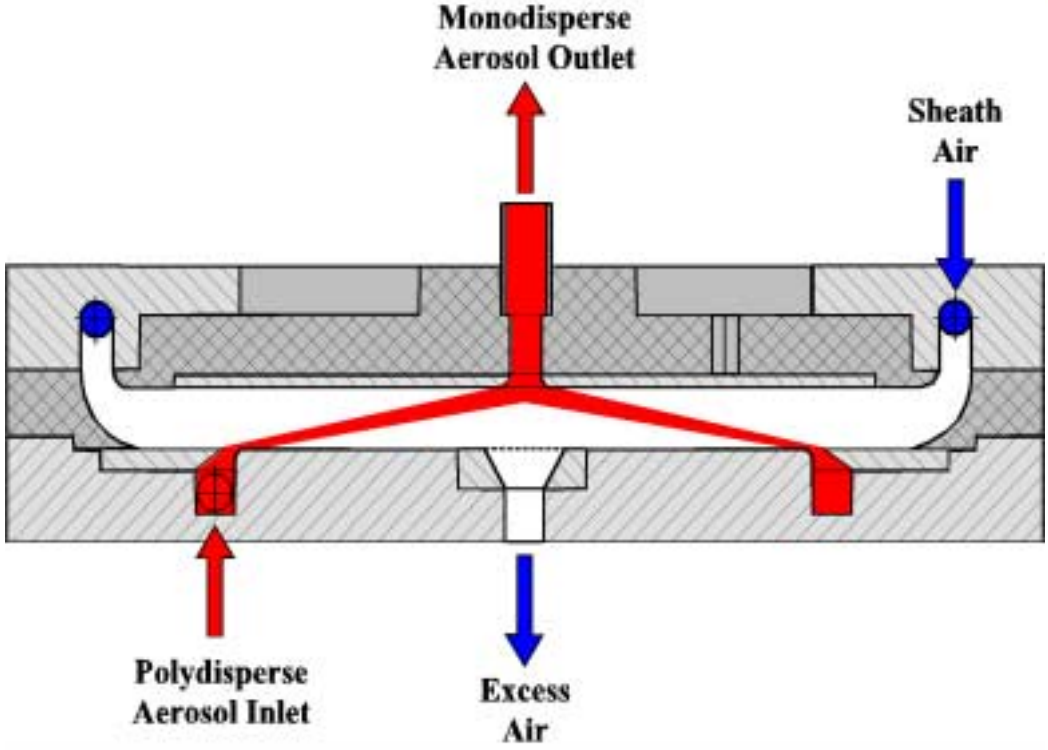

Fig. 6.2.1. a) Cylindrical (Chen et al., 1998) and (b) radial (Fissan et al., 1998) DMA design.

We can now derive the ratio of the Reynolds numbers of the two geometries:

$$\frac{\mathrm{Re}_{rad}}{\mathrm{Re}_{cyl}} = \frac{A_{cyl} D_{h,rad}}{A_{rad} D_{h,cyl}} = \frac{r_{1,cyl} + r_{2,cyl}}{2 r_{rad}} \tag{6.2.7}$$

Because the typical radial dimensions of a cylindrical DMA are in the cm-range and in the mm-range for a radial DMA, the radial DMA with a central outlet shows a higher tendency for turbulence. One solution to decrease the Reynolds number for the radial DMA which is adopted here, is not to use a central outlet but a slit at some distance to the central axis. This increases the value of r_{rad} and decreases thus the value of the Reynolds number.

When designing a DMA, an important performance criterion is the diffusional broadening at the lowest particle diameter to be classified. This broadening might be estimated by means of the Péclet number, which is the ratio of the particle convective to diffusive transport. For the radial DMA, the Péclet number is given by:

$$Pe_{rad} = \frac{h Q_c}{\pi \left(R_2^2 - R_1^2 \right) D} \tag{6.2.8}$$

in which D is the particle diffusion coefficient. Fissan *et al.* (1997) showed that the half-width of the transfer function increases with decreasing Péclet number, based on the mean velocity. This can be seen in Fig 6.2.2. This diagram shows that the difference from the ideal value of 0.1 becomes more than 50 % when the Péclet number becomes below smaller than 1000. This result can be used in order to estimate for given geometry and experimental conditions the smallest particle diameter which can be fractionated with reasonable accuracy.

Practical experience showed that a DMA configuration usually allows a particle size range between one and two decades. Therefore it was decided to design two DMA's, so that by combining the two instruments a larger measurement range is obtained. In table 6.2.1. the chosen geometry parameters are shown. Two slits, a larger one for the aerosol entrance and a smaller one for the monodisperse aerosol outlet are used. The Reynolds number at the aerosol outlet is now in the laminar range. For the calculations which assume a slit with zero width, the middle of the slit is used as the radial position of the slit.

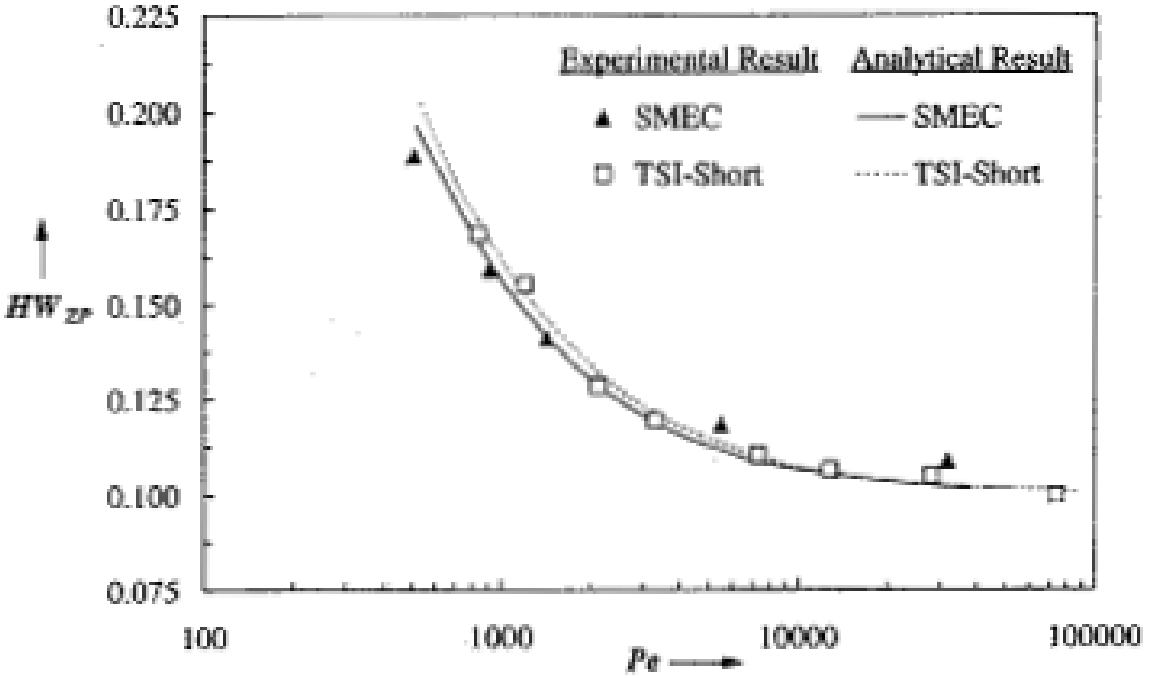

Fig 6.2.2. Experimental and analytical half-width HW of a radial DMA (SMEC) and a cylindrical DMA (TSI-short) as a function of the Péclet number. The sheath flow rate is 10 slm and 15 slm, respectively (Fissan et al., 1997).

Table 6.2.1. Geometry parameters (in mm) of the proposed low-pressure radial DMA's.

type	$R_{1,\ inner}$	$R_{1,\ outer}$	$R_{2,\ inner}$	$R_{2,\ inner}$	h
LP-RDMA1	4.6086	6.6517	21	21.9876	10
LP-RDMA2	4.6086	6.6517	82	82.9876	15

For predicting the measurement range of the instruments at a lower pressure, the following procedure is followed. For each particle size, the Péclet number is calculated for the usual operation at 1 bar and also at 100 mbar. This is shown in Fig. 6.2.3 for both DMA geometries. The smaller one (LP-RDMA1) is usually operated with higher flow rates (15 slm) in order to reduce the diffusional losses, whereas the larger one (LP-RDMA2) is operated with a lower flow rate in order to enable size fractionation of larger particles.

a)

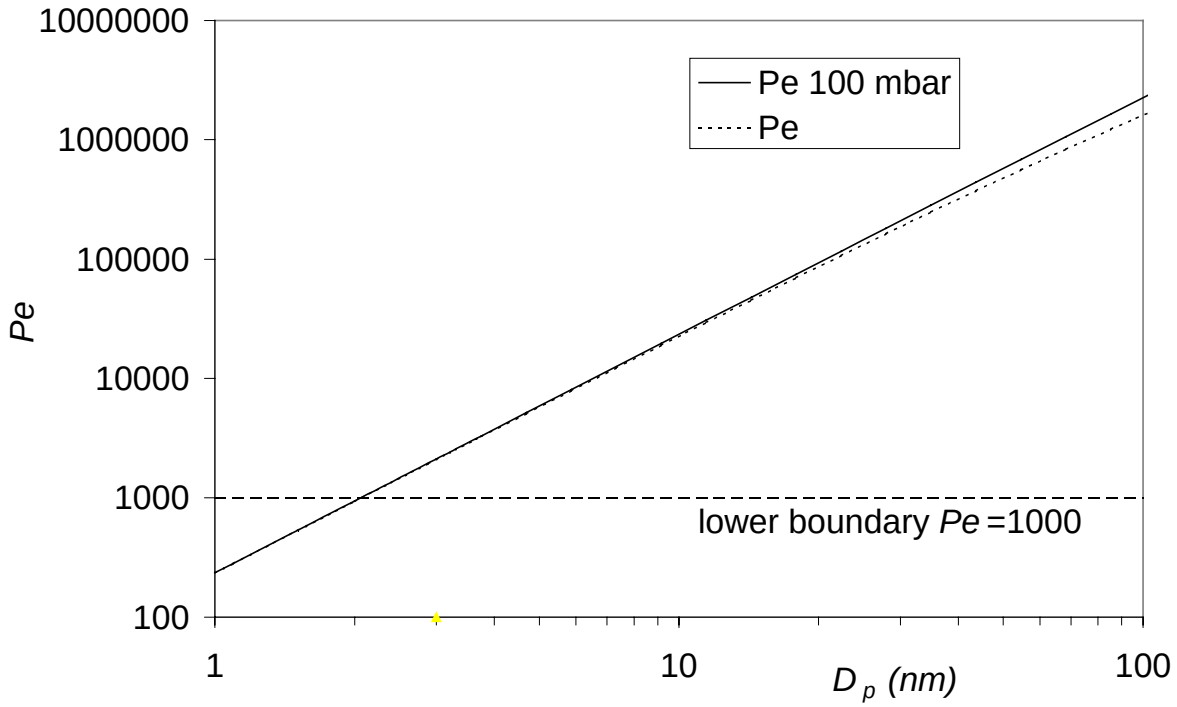

b)

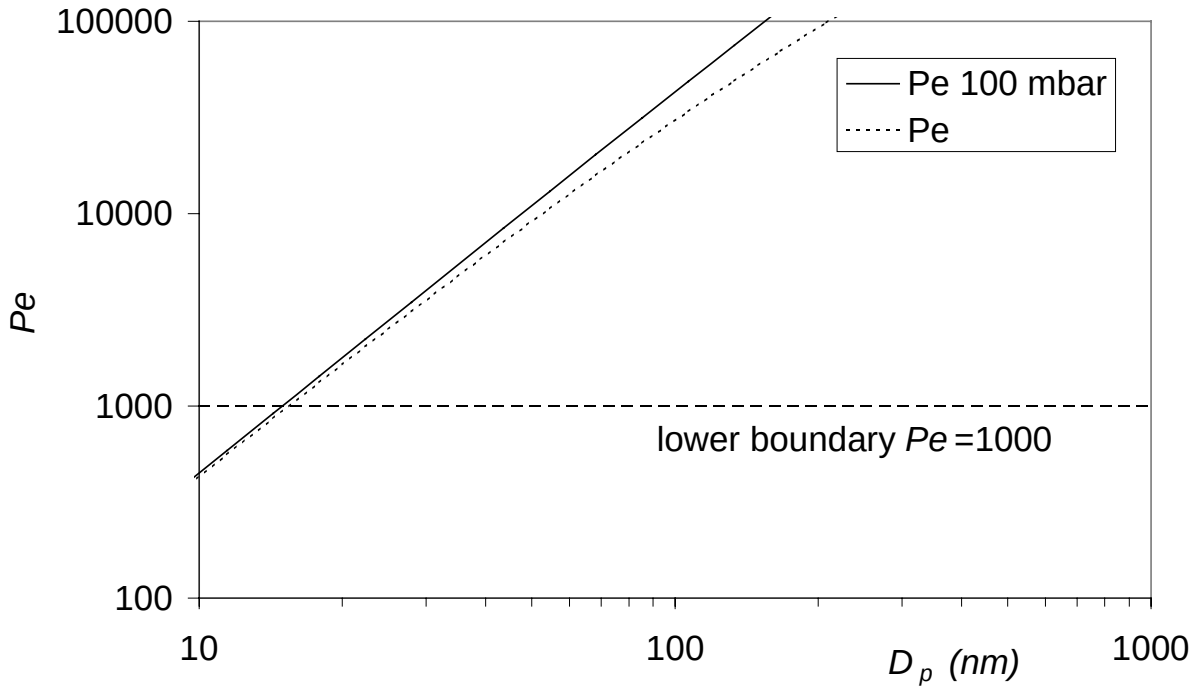

Fig. 6.2.3. Péclet numbers as function of particle diameter for a) LP-RDMA1 with 15 slm sheath gas and for b) LP-RDMA2 with 3 slm sheath gas.

It is interesting to see that the Péclet number is not changing substantially when operating at lower pressures as compared to standard conditions. This is due to the mass flow rate being constant, so that the actual velocity increases. The increased diffusion coefficient of particles at lower pressures is compensated by the higher flow rate at lower pressures. Because the ratio of volumetric flow rate and diffusion coefficient is used in the Péclet number, it does not change. For larger particles the deviation is due to the fact that the particles are not any more in the free-molecular regime for which the diffusion coefficient is inversely proportional to pressure. From the figures it becomes clear that, when taking Pe=1000 as lower limit where adequate fractionation is still possible, the LP-RDMA1 has a lower particle diameter limit of 2 nm and the LP-RDMA2 of about 15 nm.

The upper limit for the particle size is determined by the voltage which can be applied before sparking occurs. The maximal field strength is, however, a pressure-dependent function and decreases when the pressure decreases, until some point in the sub-mbar range where it increases again which is not of interest here. In Fig. 6.2.4 the voltage which has to be applied is shown as function of particle diameter. As indicated in the figure, the maximum voltage which can be applied is lower in case of the lower pressure. The upper particle limit with the given sheath flow rates is 30 nm for the small type and 250 nm for the large type. These are of course estimations and will have to be experimentally determined.

The preceding engineering estimations result in a particle size range of 2-30 nm and 15-250 nm at 100 mbar for the small and large type, respectively. It can be concluded that the lower particle limit is not affected essentially by pressure decrease but that the reduced maximal field strength results in a lower maximum particle size than in case of standard conditions. Each particle size decade probably requires an appropriate DMA.

After these quantitative estimations of the operation range of the two proposed radial DMA's, construction designs were made. The design is shown schematically in Fig. 6.2.5. Important features are:

- The aerosol outlet is a slit.
- The excess gas flow is directed toward the outlet by means of a protrusion in the middle of the central electrode.
- The electric field is almost perfectly homogeneous inside the fractionation channel.
- Stainless steel is used for all metal parts and delrin is used as isolation material.
- There are no holes for screws at the outside of the instrument, as this is not compliant with the requirement for vacuum tightness. Much care was taken to put the screws inside the vacuum chamber, but outside the main fractionation channel. The design requires the upper and lower parts to be assembled before final assemblage.

a)

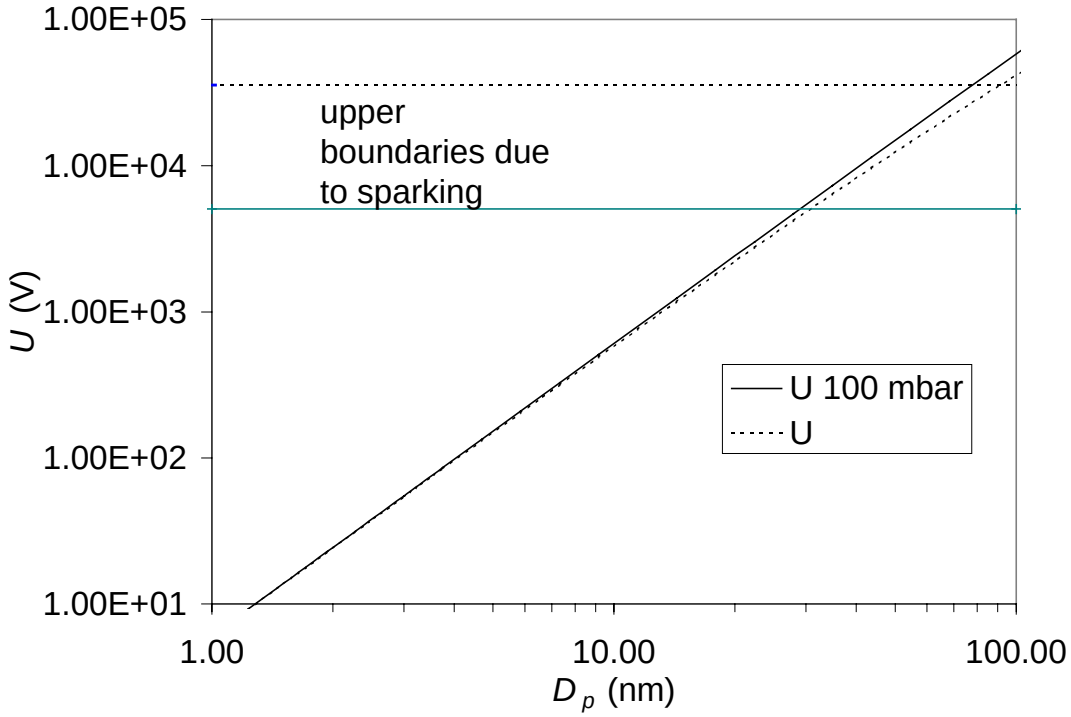

b)

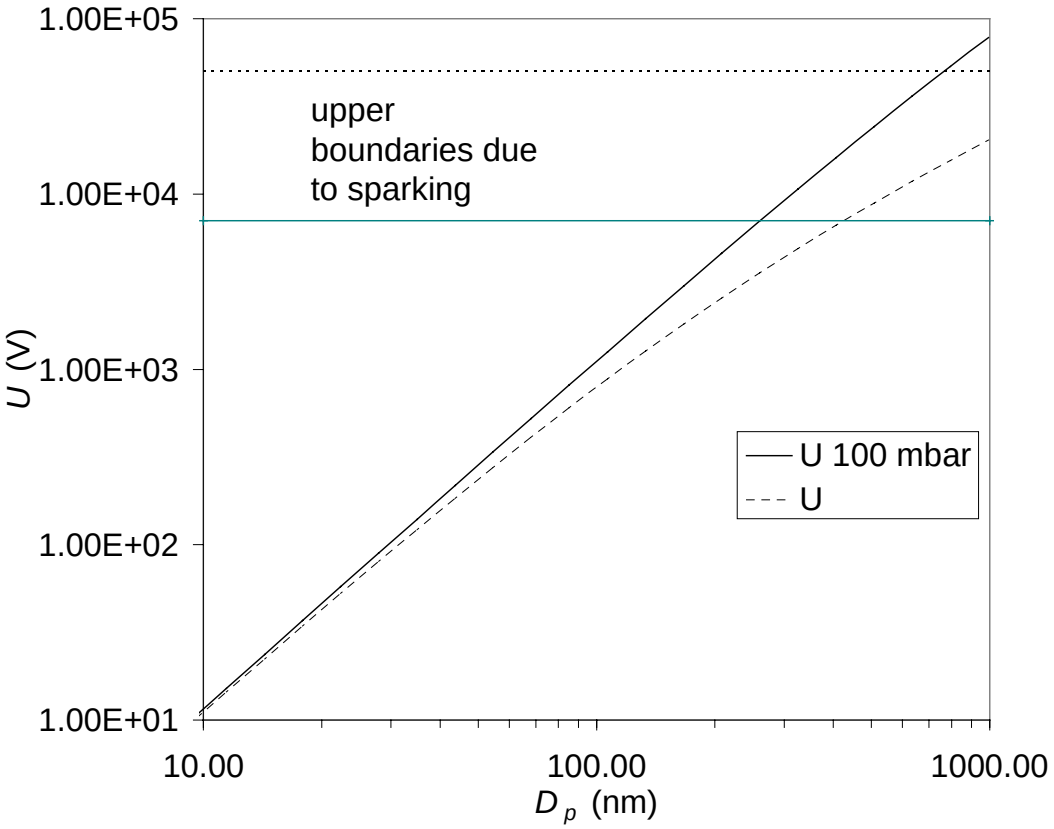

Fig. 6.2.4. Voltage to be applied as function of particle diameter for a) LP-RDMA1 with 15 slm sheath gas and for b) LP-RDMA2 with 3 slm sheath gas.

- Standard KF16 vacuum connections are used as gas and aerosol in- and outlets.
- The sheath gas is introduced through four large inlet ports. A porous inset (not shown in the figure) will be used as flow laminarisator. The excess gas outlet has only one outlet port.
- The DMA can very quickly be opened and cleaned, which is important for materials synthesis applications.
- Both aerosol in- and outlet are positioned at the axis of the instrument.
- The aerosol inlet does not have a swirling velocity compound in tangential direction
- The design is such that the main components can easily be replaced. Several other delrin isolation inserts allow the distance between the electrodes to be easily modified.
- The internal tightness of the different flow channels is obtained by means of O-rings.

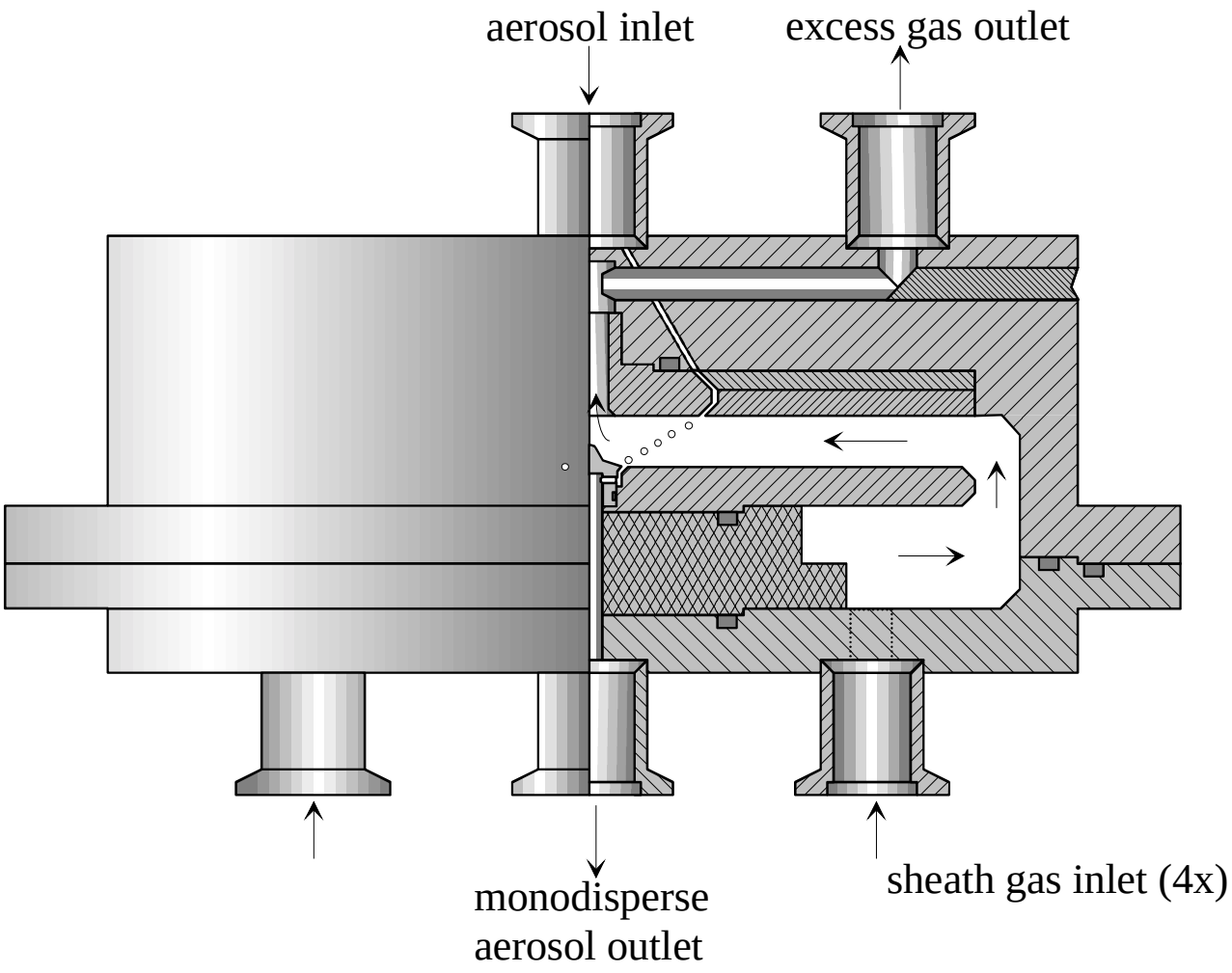

Fig. 6.2.5. Schematic design of the new LP-RDMA.

The main uncertainties concern the pressure drop in the instrument and the distribution of the aerosol flow inside the inlet slit. These will have to be resolved experimentally.

6.3 An electrostatic precipitator for measurements under clean conditions

A nanoparticle aerosol will be of no practical use when the particles are not in some way deposited on a substrate or imbedded in some matrix. In the method applied in this work to produce well-defined nanoparticles, the particles leaving the process are unipolarly charged. A simple method to deposit them onto a substrate is to use an electrostatic precipitator (ESP). Here, a central electrode connected to a high voltage (5-15 kV) with the opposite polarity as that of the particles extracts the nanoparticles from the flow. When a substrate is placed on the central electrode, a thin layer of nanoparticles develops in form of a circular deposit with a diameter of 5-10 mm, depending on particle size, electrode diameter and voltage. The ESP is schematically shown in Fig. 6.3.1.

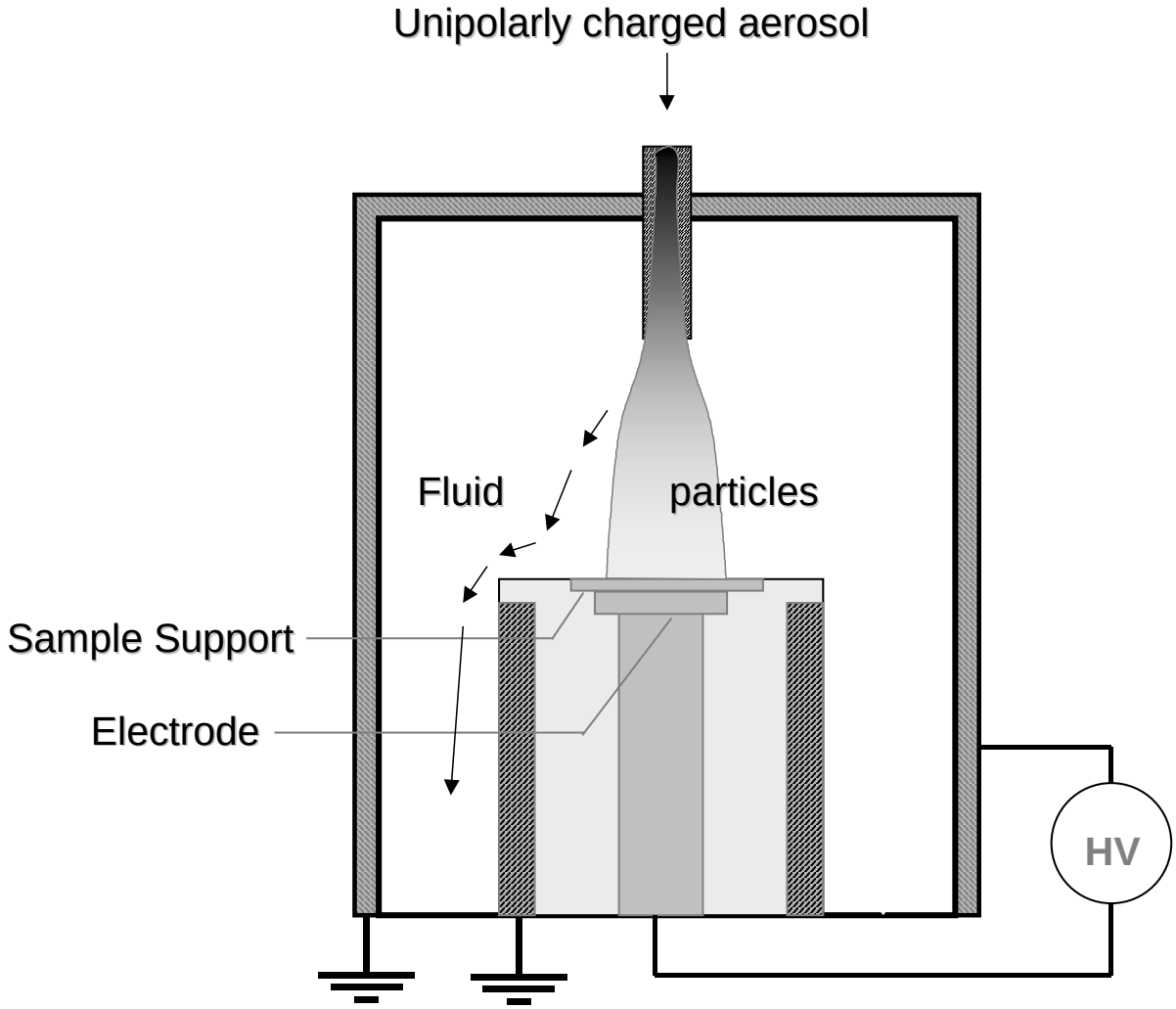

Fig. 6.3.1. Schematic view of the electrostatic precipitator (ESP).

The first version of the ESP was developed by Dixkens and Fissan (1997) and was subsequently adopted for our goals. The modifications include construction from stainless steel, an easily exchangable central electrode with the goal to change its diameter and the possibility to insert a small inlet tube which extends closer to the electrode. Over a critical orifice in the central inlet the apparatus can be used as a low-pressure impactor when a pump is connected to the gas outlet. This second mechanism for particle deposition onto a substrate allows the deposition of uncharged particles and increases the deposition velocity so that particle adhesion can be improved. Furthermore, it is expected that films formed by uncharged particles are more homogeneous than those formed by charged particles, as charged particles can lead to the formation of dendrites, long particle chains pointing away from the surface. The present version allows to apply both deposition mechanisms and even a combination of them.

During preliminary measurements of electrical properties of thin films of PbS nanoparticles, it was found that measurements in ambient air were not particularly reproducable. The substrates with deposited nanoparticles had to be taken from the ESP toward a probe station, so that surface contamination occurred. An measurement of the electrical properties without air exposure is preferable and thus a special ESP has been constructed. It consists of a deposition chamber, where the ESP itself is situated, and a chamber which can be evacuated in which the deposition electrode can be placed after particle deposition. The electrical contact is obtained over micromanipulators with meaurement tips. The substrate is in its measurement position placed close to an observation window for accurate observation of the contacting process by means of a macroscope. Fig. 6.3.2 shows the schematics of the M-ESP.

The advantage of the system is that immediately after particle deposition, the electrode can be brought in measurement position and evacuated. A pressure of 10^{-3} mbar was obtained, which was limited by the characteristics of the pump. The instrument is constructed such that the substrate can easily be connected to a liquid N_2-cooling system.

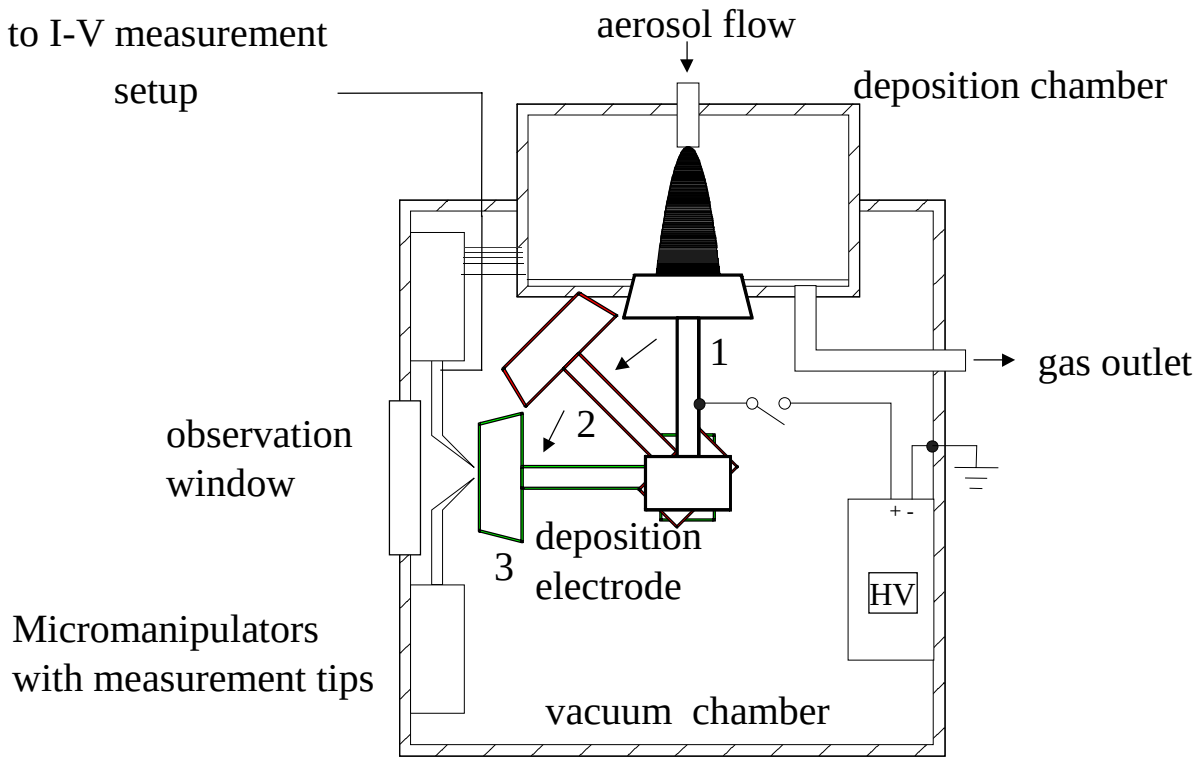

Fig. 6.3.2. Schematics of the measurement-ESP (M-ESP).

6.4 Conclusions: Instrumentation for controlling nanoparticle behavior

In this Chapter, newly developed instrumentation for controlling nanoparticle behavior 'in-flight' is described which allow to obtain more control over processes which are essential for the synthesis and handling methods chosen in this work. These processes are nanoparticle charging, nanoparticle size fractionation and nanoparticle deposition.

A newly developed nanoparticle charger, the twin-Hewitt charger, allows a larger fraction of the nanoparticles to be charged, which is important to get a higher yield. A higher yield would result in a shorter deposition time, which is important because the deposition of thin nanoparticle layers takes at present still too long. The instrument has been extensively investigated experimentally in order to find the optimal charging conditions.

Differential Mobility Analysis at lower pressures than atmospheric pressure has been investigated theoretically. It was found that the lower particle limit is not changed fundamentally with lower pressures when keeping the mass flow rate constant, but that the higher particle limit is decreased due to decrease of the maximum allowed field strength. A Differential Mobility Analyzer design for low pressure has been presented. It is important to perform size fractionation at pressures lower than atmopsheric

pressure, as usually the system pressure is decreased in order to get a higher yield of smaller nanoparticles.

An Electrostatic Precipitator has been developed which allows the investigation of electrical properties of nanoparticle films under clean conditions direct after deposition. This is especially important for semiconductor nanoparticles, where the surface influences the optical and electronic properties.

7. Synthesis of PbS and SnO_x nanoparticles for functional applications

The synthesis of semiconducting material (PbS) via the evaporation-condensation route is undertaken in combination with the control techniques described in the preceding chapter such as size fractionation and on-line particle size measurements. By means of an on-line measurement of the agglomerate diameter the evaporation and sintering characteristics of PbS nanoparticles are investigated and reported in Chapter 7.1. The measurements allow to obtain a theoretical description of the evaporation and sintering process. Strictly speaking, the particles are sublimating but generally the term evaporation is used. These experiments have partly been published in Kruis *et al.* (1998c) and the evaluation of the sintering appeared in Kruis *et al.* (2000b). Similar synthesis experiments for obtaining SnO_x nanoparticles for gas-sensing applications will be reported in Chapter 7.2.

Quantum confinement effects in semiconducting nanocrystals have been widely studied since Brus in 1983 focussed the attention of the scientific community on this phenomenon (Brus, 1983). Almost all investigations have been done for colloid systems, i.e. in the liquid phase. For most practical applications, these particles will, however, have to be supported on a substrate. The gas-phase techniques described in this Habilitation Thesis are ideally suited for this, as both synthesis and deposition are done in the gas phase. For the system chosen in this work, PbS, the confinement effects have until now only been reported for PbS nanoparticles synthesized in the liquid phase. In Chapter 7.3 optical absorption spectra indicative for quantum confinement effects in size-fractionated PbS nanoparticles from the gas phase will be shown.

Finally, an experimental method to obtain well-defined composite aggregates of size-selected nanoparticles in the gas phase is proposed. Such composite aggregates are interesting for applications in which the properties of semiconducting nanoparticles are modified by addition of another nanoparticle material. A well-known example is the addition of Pt nanoparticles to SnO_2 nanostructured material, which increases the sensitivity of the gas sensor, presumably due to catalytic surface reactions on the Pt. As a model for the composite system semiconductor-metal, PbS-Ag is chosen here, as for both materials exists experience with the synthesis. Both materials are synthesized separately by nucleation and aggregation processes in a furnace reactor. The two oppositely charged aerosols which have been size-selected on the basis of their

electrical mobility are mixed. The fact that nanoaggregates which contain the two different materials are uncharged is used in order to separate them from unaggregated particles and aggregates containing only one component. A paper dedicated to this subject has been published (Maisels *et al.*, 2000).

7.1 Preparation of size-classified PbS nanoparticles in the gas phase

Nanocrystals of semiconducting materials can exhibit quantum-size effects when the particle size becomes comparable to or smaller than the spatial extent of the wavefunctions of electrons or holes. This results in a blue shift in the optical absorption spectrum (Brus, 1984). A size uniformity is important in order to study or make use of quantum size effects, as a distribution of particle sizes will decrease these effects.

The synthesis of nanocrystals in the vapor phase has several advantages over other methods such as controlled chemical purity and the generation of clusters with free surfaces (Saunders *et al.*, 1992). Size-selection has been proven to be also possible in the gas phase and was applied to produce Si (Camata *et al.*, 1996) and GaAs (Deppert *et al.*, 1996) nanocrystals. However, the lower atomic mobilities in the solid phase can inhibit crystallization of the particles and the stoichiometry of the material is in some systems difficult to maintain (Saunders *et al.*, 1992).

The generation of nearly monodisperse PbS nanocrystals in the gas phase is demonstrated in this subchapter. PbS is a narrow-gap IV-VI semiconductor with a cubic rock salt structure. PbS is an attractive candidate for the study of quantum confinement effects as its hole Bohr radius is 9 nm. This results in strong confinement effects as compared to the II-VI semiconductors such as CdS and CdSe with Bohr radii of about 1 nm (Machol *et al.*, 1994).

Previously reported syntheses of PbS nanocrystals with sizes below 20 nm are all performed in a liquid phase. They include controlled precipitation in polyvinylalcohol (Nenadovic *et al.*, 1990), sol-gel synthesis (Gacoin *et al.*, 1995) , synthesis on Langmuir monolayers (Zhao and McCormick, 1992) and electrostatically spraying a $PbNO_3$ solution in a H_2S atmosphere (Salata *et al.*, 1994a). Earlier studies on gas-phase synthesis reported loss of stoichiometry due to dissociation when directly evaporating PbS in Ar (Kaito *et al.*, 1987). On the other hand, it is known that the IV-VI semiconductors evaporate essentially in a molecular form (El-Rahaiby and Rao, 1982), and that film formation of stoichiometric IV-VI compounds is possible by direct evaporation (Lopez-Otero,

1987). Hereby, the tendency to dissociate is smaller the lower the evaporation temperature and the higher the pressure.

7.1.1 Experiments

In the present work a gas-phase synthesis method is used at normal pressure for the preparation of sub-20 nm, crystalline, quasi-spherical, monodisperse PbS particles. Heating a furnace containing the PbS powder at temperatures between 600°C and 700°C resulted in appreciable particle formation as measured with a condensation nucleus counter. These particles are formed by homogeneous nucleation and subsequent aggregation by Brownian motion. Transmission electron micrographs showed amorphous and partially sintered particles with a standard deviation between 1.4 and 1.6, typical for gas-phase synthesis.

In order to obtain crystalline and spherical particles, the aerosol flow was passed initially through a second furnace. Electron micrographs showed crystalline particles, which were however mostly present in aggregates consisting of several quasi-spherical particles bonded together by amorphous material. Therefore, it can be concluded that the particle number concentration is too high when the aerosol enters the second furnace, causing aggregation at the same time crystallization and sintering are taking place.

The experimental setup was then changed to that depicted in Fig. 7.1.1. It contains six elements: a nanocrystal source, an aerosol charger, a size classifier, a tube furnace, an electrostatic precipitator and a particle size measurement system consisting of a Differential Mobility Analyzer (DMA) and a condensation nucleus counter. Fig. 7.1.1 shows a schematic diagram of the setup, which is similar to that used by Deppert *et al.* (1994). A PbS aerosol is formed by sublimating a PbS powder in a tube furnace and after dilution (1:2) charged by a radioactive β–source (Kr^{85}). Nitrogen obtained from evaporating liquid nitrogen is used as carrier gas. The total gas flow was kept at 1.5 l/min by means of mass flow controllers (MFC), and the system is operated at atmospheric pressure. In a Differential Mobility Analyzer the charged particles are size-selected on the basis of their electric mobility, which is a function of their charge level, mass and shape. The mobility equivalent diameter based hereon is defined as the diameter D_m related to the Stokes-Cunningham formula (Hinds, 1982) and is equal to the geometric diameter when the particles are singly charged and spherical. The DMA (NANO-DMA, TSI, Minneapolis, USA) is capable of delivering monodisperse aerosols with sizes adjustable between 2 and 50 nm and standard deviations between 1.05 and 1.20, depending on the flow conditions in the apparatus (Chen *et al.*, 1998) .

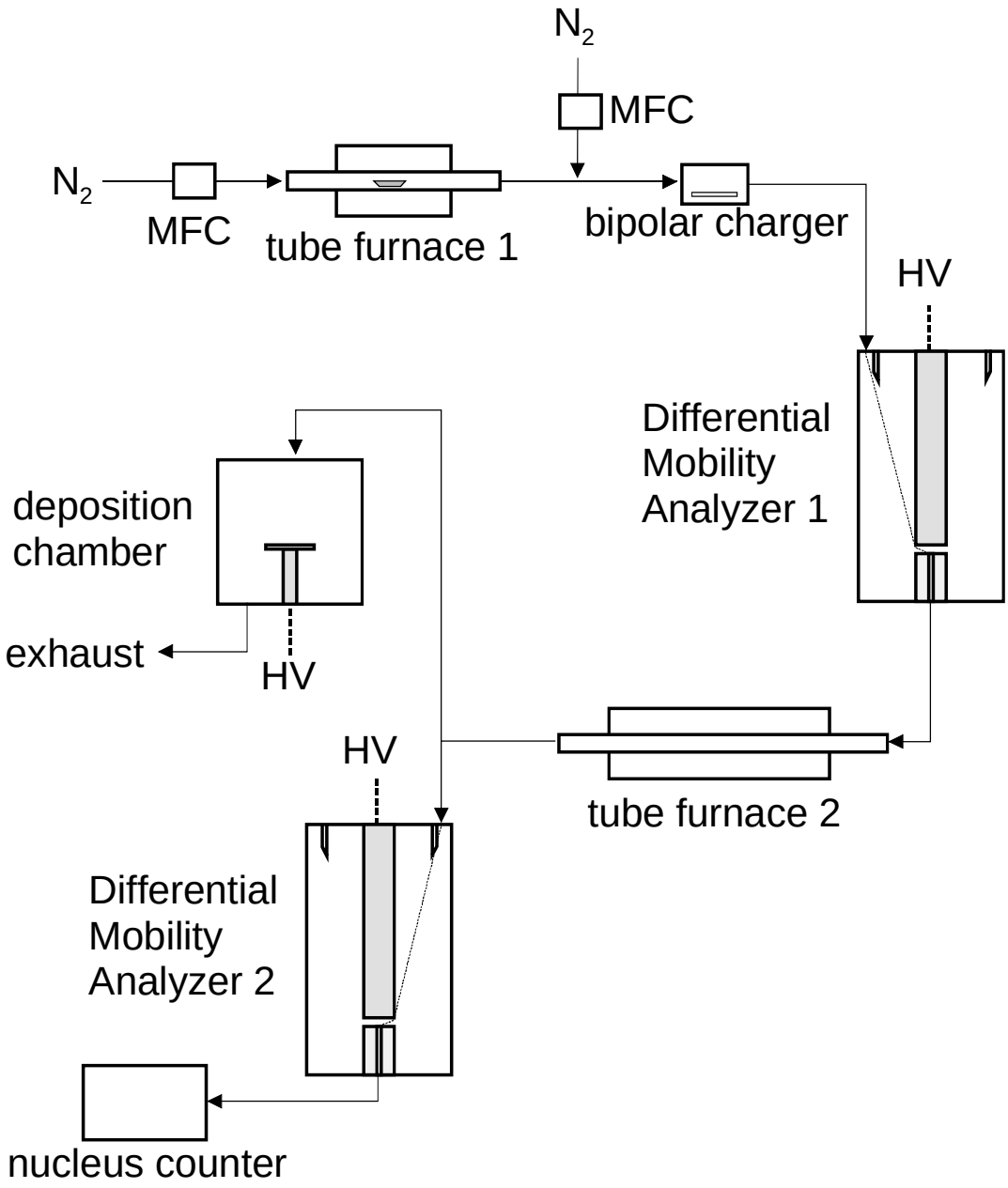

Fig. 7.1.1. Schematic drawing of the experimental setup for gas-phase synthesis and size fractionation of PbS nanocrystals. Particles are generated in tube furnace 1, charged by means of a bipolar charger, size-fractionated utilizing a first Differential Mobility Analyzer (DMA), sintered in tube furnace 2 and deposited onto a substrate within a deposition chamber. A second DMA, in combination with a nucleus counter, is used to measure the particle size distribution. The N_2 gas flow is controlled by mass flow controllers (MFCs).

In our studies, the flow ratio was chosen to get a theoretical distribution in diameter of $\pm 0.1\ D_m$.

An electrostatic precipitator enables the aerosol to be deposited with nearly 100 % efficiency on a substrate placed in a high-voltage field. A condensation nucleus counter (3025, TSI, Minneapolis, USA) with a lower detection limit of 3 nm enables the monitoring of the aerosol number concentration. By means of a second DMA after the second furnace it is possible to detect on-line the change in mobility diameter due to the passage through the second furnace.

As the sintering step now takes place after the size fractionation, the particle number concentration in the second furnace is roughly two decades smaller, thus decreasing the rate of aggregation during the crystallization and sintering step. The smaller number concentration has two causes: the charging efficiency in the radioactive charger, which is only 5 % for particle with diameter of 10 nm, and the size fractionation, which takes out part of the size spectrum. The final production rates of sintered particles with initial mobility diameters $D_m^{unsintered}$ =15 nm (sintered at 400°C) and $D_m^{unsintered}$ =50 nm (sintered at 500°C) are 3 10^4/cm^3 and 10^5/cm^3, respectively. Typical electron micrographs now showed single crystalline particles.

The second furnace proved to be necessary to obtain monocrystalline particles. Above 350°C, crystalline particles were detected by XRD, with the crystallite size increasing with sintering temperature. In Fig.7.1.2 a HRTEM micrograph of a monocrystalline PbS nanoparticle is shown, as obtained after sintering a particle fraction with an initial mobility diameter of 50 nm.

However, at too high temperatures the particles evaporated. This can be seen in Fig. 7.1.3, which shows a size distribution for particles having initially a mobility diameter of 15 nm. Strictly speaking, the word size distribution is not correct as the curves are not corrected for the transfer function of the DMA and the charging efficiency. For our purposes, however, the exact form of the size distribution before the charger and DMA is not of interest, what is important is the yield of particles after the size fractionation, as the DMA is an integral part of our synthesis setup. The amorphous nature of the particles makes sintering however necessary. It can be seen that the mean mobility diameter shifts to smaller sizes. This is due to the compaction process caused by restructuring, sintering and crystallization. Restructuring and sintering processes are known to lead to a smaller mobility equivalent diameter with increasing temperature (Schmidt-Ott, 1988). This is due to increased solid state diffusion coefficients which result in more compact particles. The total number concentration of particles decreases at increasing sintering temperatures because of increased thermophoretic losses when exiting the furnace, and at the highest temperature also because of evaporation.

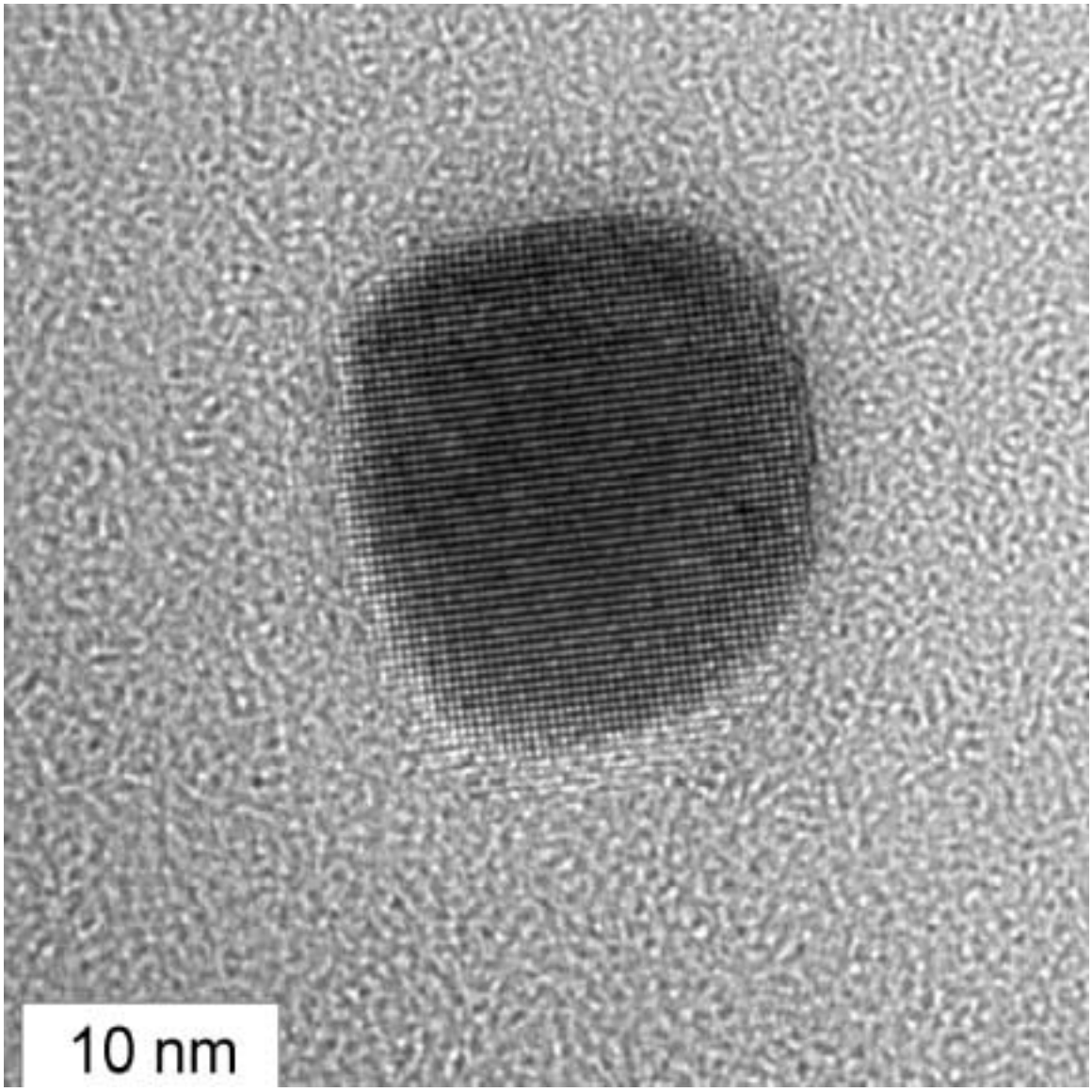

Fig.7.1.2. HRTEM micrograph of a monocrystalline PbS nanoparticle.

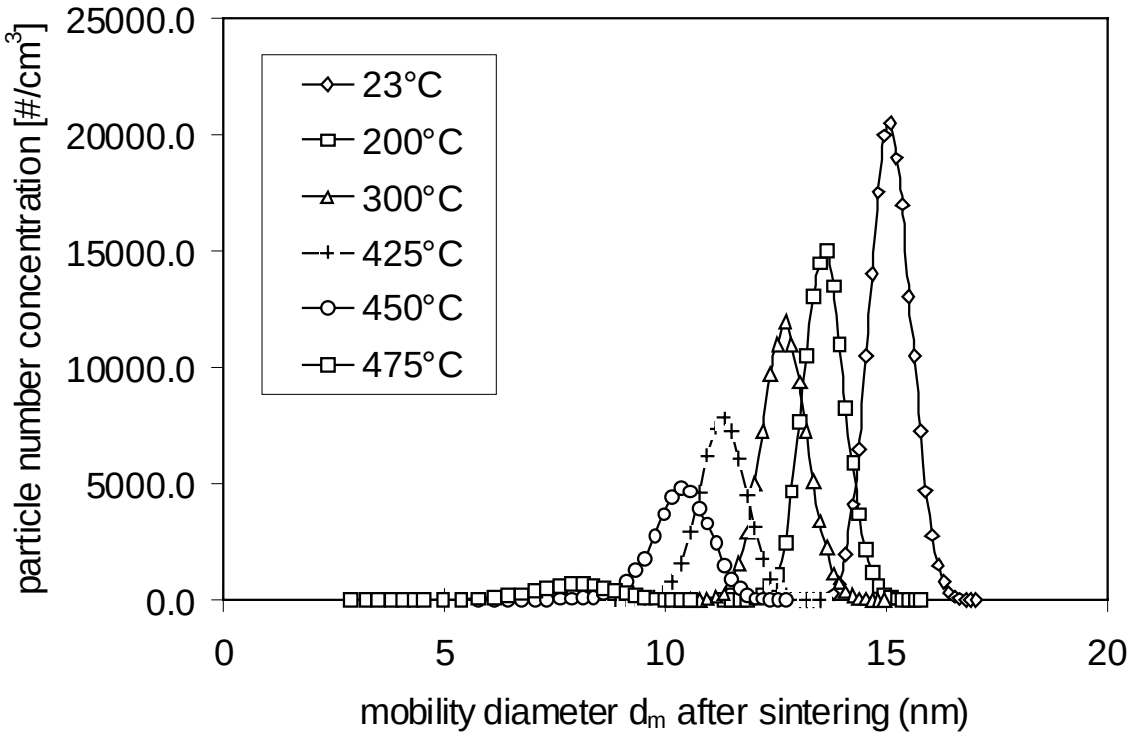

Fig. 7.1.3. Size distribution of size-selected PbS nanoparticles (d_m=15 nm) as a function of sintering temperature.

The mean mobility diameter as a function of sinter temperature is shown in Fig. 7.1.4 for PbS particles having different initial mobility diameters. It can be seen that initially larger particles show a higher decrease in mobility diameter, indicating an increased compaction rate. This is confirmed by TEM microscopy, from which we observe a more porous and open structure containing tens of primary particles for the larger unsintered aggregates, which can be stronger compacted due to sintering. Smaller particles contain however few primary particles and are therefore more compact, which means that they can be less easily compacted. At the highest temperature used, the particle size decreases rapidly.

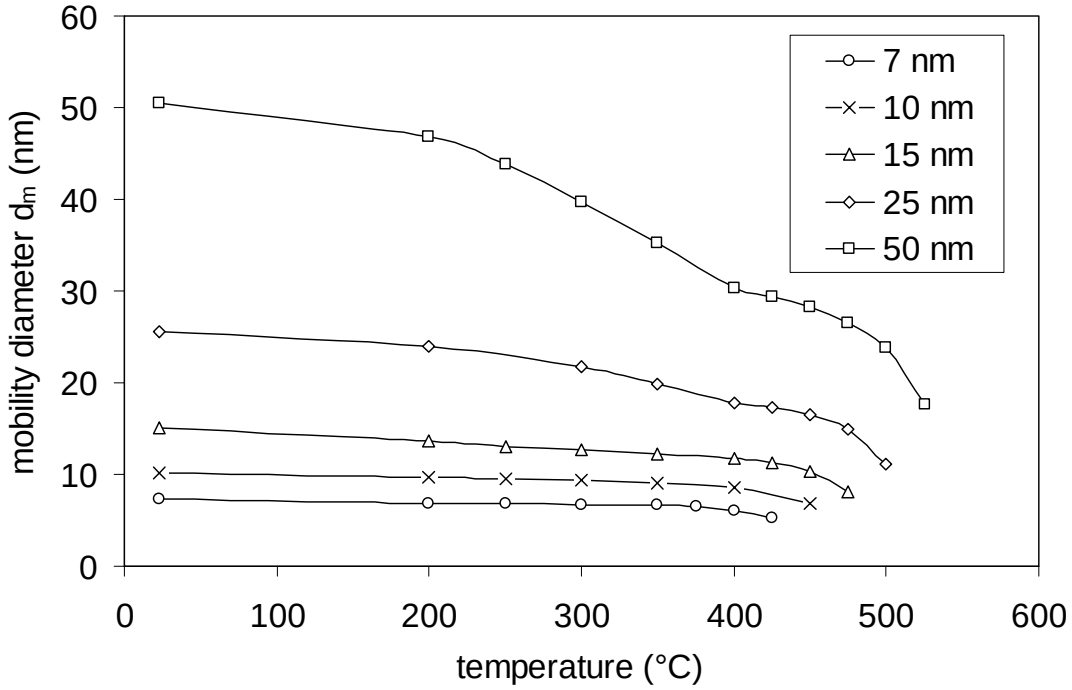

Fig. 7.1.4. Mobility diameter of PbS nanoparticles with different initial mobility diameters as function of the sintering temperature.

This is accompanied by a rapid increase in the half-width of the size distribution, Fig. 7.1.5. The width of the size distribution increases above a certain threshold temperature which is a function of the initially selected mobility diameter. We attribute this to evaporation, which destroys the original size distribution and can also lead to new particle formation. The origin of the local maximum in the curves for mobility diameters of 25 and 50 nm is not quite clear, but might be due to coagulation in the sinter furnace as large porous particles have an increased coagulation probability at higher temperatures.

The necessity of sintering to obtain spherical particles is clearly seen in Fig. 7.1.6, where electron micrographs of particles with $D_m^{unsintered}$ =50 nm, sintered at 300°C (A) and at 500°C (B), are shown. The larger 'volume' of the agglomerates in Fig. 7.1.6A as compared to the spherical particles in Fig. 7.1.6B supports our suggestion that evaporation takes place. From the electron micrographs of quasi-spherical sintered particles (comparable to those in Fig. 7.1.6B), we have determined size distributions of the particles (Fig. 7.1.7). Although the agglomerates shown in Fig. 7.1.6A exhibit a very irregular morphology, we obtain a rather narrow size distribution with a standard deviation of 1.13 for the quasi-

spherical particles. The smallest particles obtained with the procedure described above have a diameter of some 3 nm.

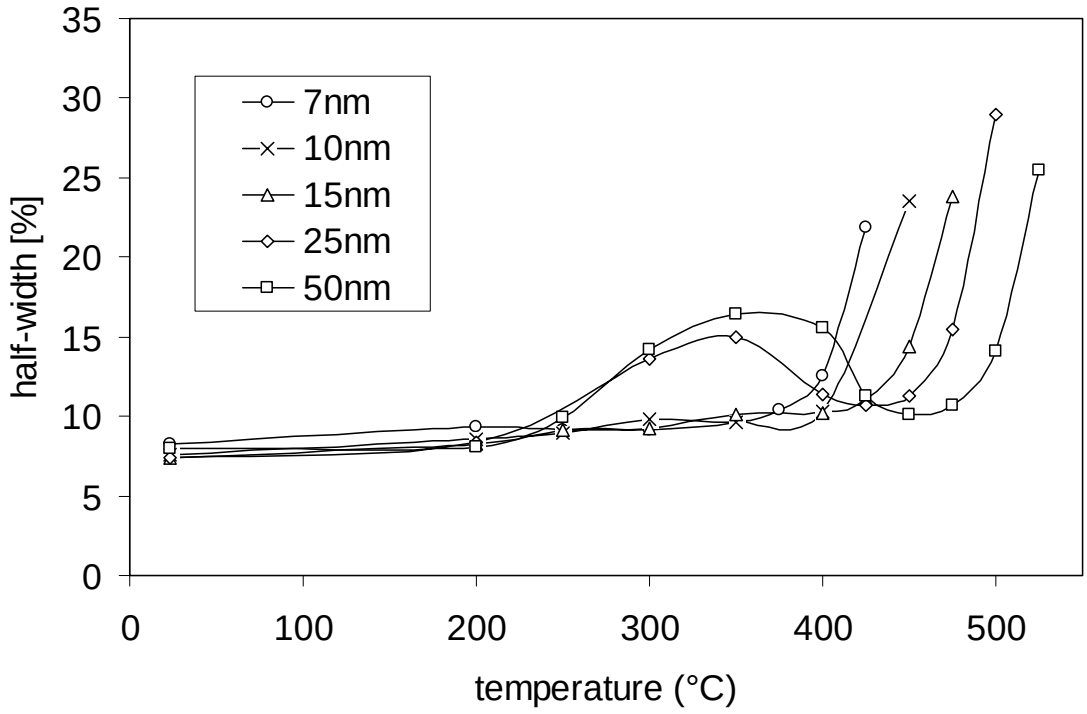

Fig. 7.1.5. Half-width of the size-fractionated distribution after sintering.

Electron diffraction and X-ray diffraction (XRD) were used to confirm the crystallinity of the PbS samples. A lattice constant of 5.945±0.005 Å was determined using X-ray diffraction, being within 0.15 % of the bulk value for PbS (Pearson, 1967). No Pb nor Pb-S-O compounds were detected. Line broadening of the diffraction pattern was used to determine the grain size. Since the grain size as determined from XRD is in good agreement with the particle size as taken from the TEM investigations, the PbS nanoparticles are to be considered monocrystalline. This is furthermore supported by the observation that the particles show facetting.

From the experimental results, it becomes clear that the sublimation and sintering temperatures have to meet the following conditions:

$$T_{high\ nucleation\ rate} < T_{furnace\ for\ sublimation} < T_{stoichiometric\ evaporation}$$

and

$$T_{appreciable\ sintering} < T_{furnace\ for\ sintering} < T_{appreciable\ evaporation}$$

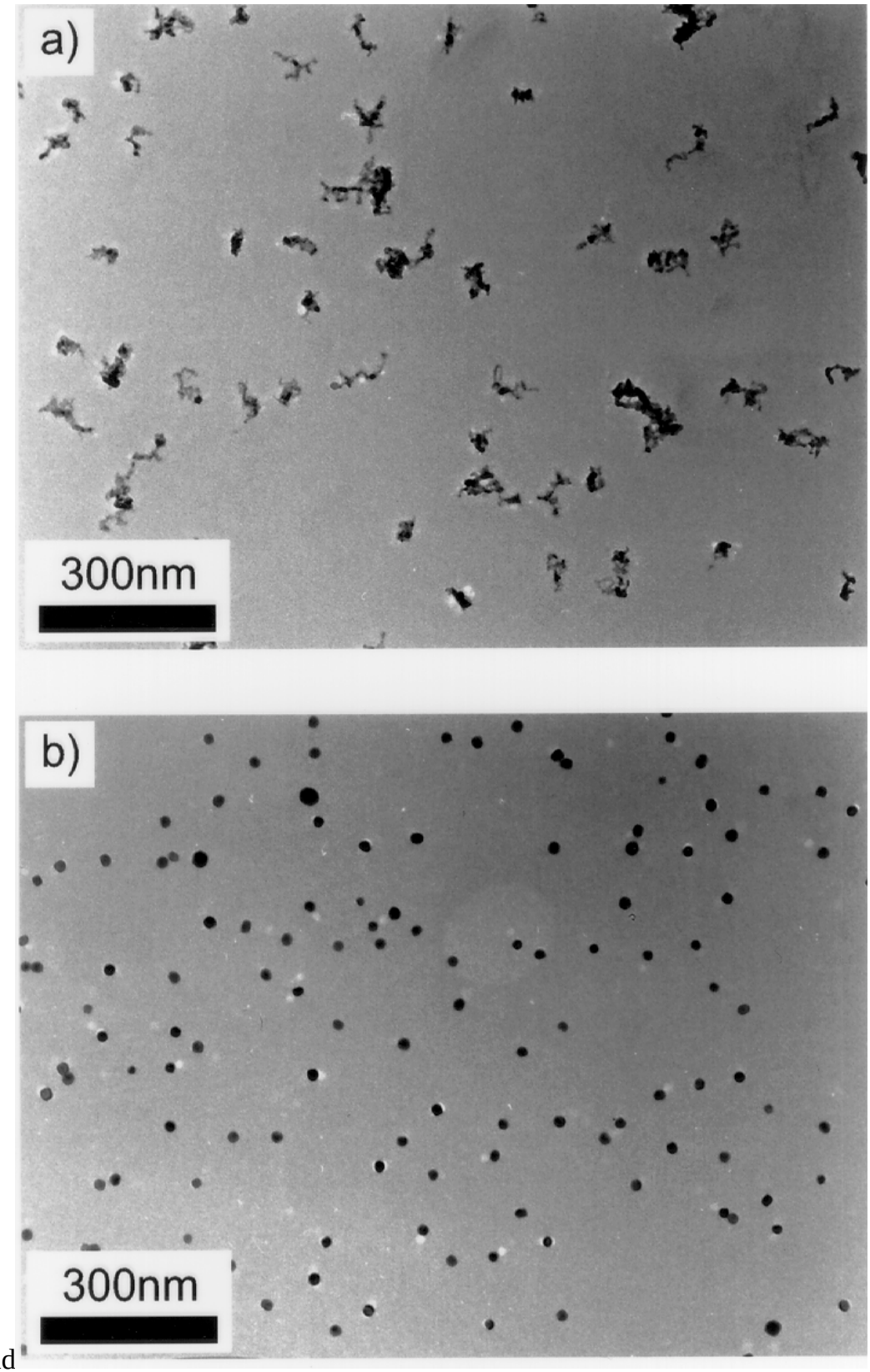

and

Fig. 7.1.6. Electron micrographs of PbS particles with $D_m^{unsintered}$ *=50 nm sintered at (a) 300°C and (b) 500°C.*

Fulfilling the first condition ensures that a sufficient number of particles is formed by homogeneous nucleation at temperatures lower than the temperature where off-stoichiometric evaporation starts. For InP and GaAs e.g., this relation is not fulfilled (Deppert *et al.,* 1998) . The second relation is clear from the earlier description of the experiments: crystalline and quasi-spherical particles have to be obtained by sintering at temperatures which do not cause extensive evaporation. For PbS, there is for each particle size a temperature range of some 50 K where the sintering rate is appreciable while at the same time the evaporation rate is such that the particles shrink but do not disappear. The optimum sintering temperature turns out to be 400°C for particles having a mobility equivalent diameter of 15 nm and 500°C for particles having a mobility equivalent diameter of 50 nm.

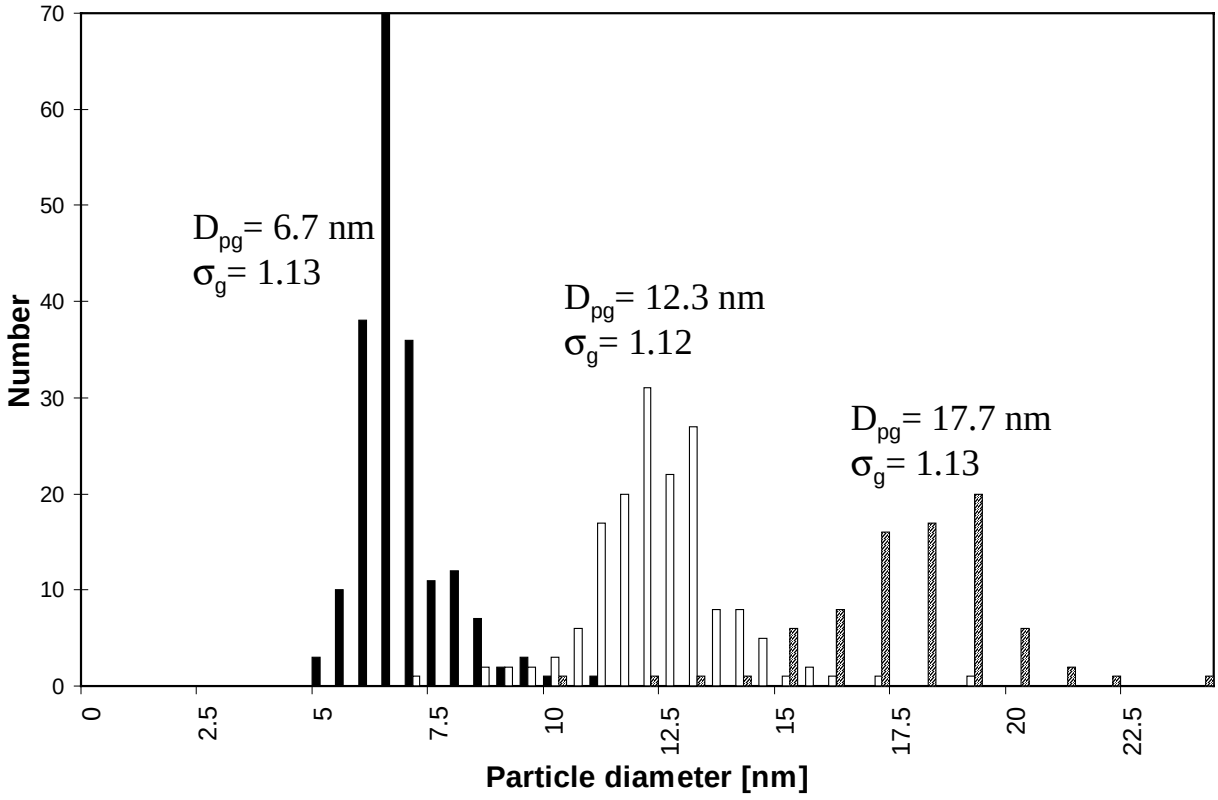

Fig. 7.1.7. Size distributions determined from electron micrographs for particles synthesized under optimized conditions ($D_m^{unsintered}$ =15 nm sintered at 400°C, $D_m^{unsintered}$ =25 nm sintered at 475°C and $D_m^{unsintered}$ =50 nm sintered at 500°C). Residual agglomerates (~5% of all particles) were not taken into account.

7.1.2 Analysis of evaporation and sintering mechanisms of PbS

In order to assess the evaporation mechanism, the evaporation rate of a PbS particle is calculated using the following formula (Hinds, 1982):

$$\frac{\mathrm{d}d_p}{\mathrm{d}t} = \frac{4D_v M}{R\rho_p d_p}\left(\frac{p_\infty}{T_\infty} - \frac{p_s}{T_s}\right)\frac{2\lambda + d_p}{d_p + 5.33\frac{\lambda^2}{d_p} + 3.42\,\lambda} \qquad (7.1.1)$$

where D_v is the diffusion coefficient of the vapor, M is the molecular weight of the particle, R is the gas constant, ρ_p is the particle density, d_p is the particle size, p_∞ and p_s refer to the partial pressure in the background gas and at the particle surface, T is the temperature and λ is the mean free path of the gas. p_∞ is assumed to be negligible in comparison to p_s, for which we use the vapor pressure of PbS, fitted from data in the range 755–1108°C (Gmelin, 1979):

$$\log p(\mathrm{Torr}) = -1.126\ 10^5 \frac{1}{T(\mathrm{K})} + 5.80910^{-4}\ T(\mathrm{K}) + 9.3531 \qquad (7.1.2)$$

The resulting evaporation rates are shown in table 7.1.1. As can be seen from the table, the evaporation rate is only a slight function of the particle size. With a residence time of 6 s in the second furnace, the calculations on the evaporation rate of the PbS nanoparticles predict a decrease in particle diameter of 2.2 nm (@450°C), 7.2 nm (@475°C), 23 nm (@500°C) and 65 nm (@525°C). This corresponds well with the experimental observation, e.g. particles with an initial mobility diameter of 15 nm have completely disappeared with a furnace temperature of 500°C.

Table 7.1.1. Evaporation rates $\frac{\mathrm{d}d_p}{\mathrm{d}t}$ *(nm/s) of PbS nanoparticles.*

Evaporation rate (nm/s)	***Temperature (°C)***				
Diameter (nm)	***425***	***450***	***475***	***500***	***525***
7	**0.09**	**0.34**	**1.1**	**3.6**	**10.3**
50	**0.1**	**0.36**	**1.2**	**3.8**	**10.9**

It is clear that at temperatures below 450°C evaporation will not play an important role according to this calculation and that the change in mobility equivalent diameter will be almost exclusively due to restructuring and sintering. Therefore, a sintering model can be applied in order to obtain information about the characteristic sintering time. According to Koch and Friedlander (1990) the following expression can be used to account for the reduction of surface area of an aerosol particle being an agglomerate of primary particles:

$$\frac{\mathrm{d}a}{\mathrm{d}t} = -\frac{1}{\tau}(a - a_{sph}) \tag{7.1.3}$$

where a is the surface area of the agglomerate and a_{sph} is the surface area of the equivalent sphere. The characteristic sinter time τ can be written in the following form, in which the dependencies on the temperature and the primary particle size are separated:

$$\tau = c_1 T\, d_p^{\,n}\, e^{c_2/T} = \tau'\, d_p^{\,n} \tag{7.1.4}$$

where c_1 and c_2 are constants, T is the temperature, τ' is some temperature-dependent sintering function, which is however independent of the primary particle diameter, n is a coefficient which varies with the sinter mechanism which is still unknown for PbS nanoparticles (n=3 for volume sintering, n=4 for grain boundary or surface sintering) and d_p is the diameter of the primary particles composing the agglomerate:

$$d_p = \frac{6 v_{sph}}{a} \tag{7.1.5}$$

in which v_{sph} is the volume of the equivalent sphere. The reason for separating the dependencies of the characteristic sinter time on the primary particle diameter and the temperature is that both parameters are varying in the experiments. For substances with well-known properties, the constants c_1 and c_2 can be calculated (see e.g. Kruis *et al.* (1993) for Si), but for PbS these parameters are not available. Therefore, they are determined on the basis of the experimental data.

According to Seto *et al.* (1995), the diameter of primary particles can be determined from experiments using:

$$d_p = \frac{d_{sph}^3}{d_m^2} \qquad (7.1.6)$$

This bases on eq. (7.1.5) with the assumption that the mobility diameter for nonspherical particles is related to its surface area. Using the measurements of d_m from Fig. 7.1.4, we still need to know the diameter of the particle when sintering is completed, i.e. d_{sph}, for which the mobility diameter at the temperature before evaporation starts is taken. It is estimated that the sintering is complete at 450°C for particles having an initial mobility equivalent diameter of 50 nm, at 425°C for 25 nm, at 400°C for 15 nm, at 375°C for 10 nm and at 350°C for 7 nm. This is based on the experimental observations of the sudden increase of the half-width of the size distribution above these temperatures (Fig. 7.1.5), which are consistent with TEM observations of particle morphology at different sintering temperatures and initial mobility diameter. This enables us to calculate the primary particle size d_p (Fig. 7.1.8a) and consequently the number of primary particles in an aggregate (Fig. 7.1.8b).

The initial primary particle diameter of 5 to 10 nm is in agreement with TEM observations. The larger number of primary particles in an agglomerate for particles with larger initial mobility diameters in the case without sintering (at a temperature of 20°C) has also been observed by means of TEM investigations. It has often been observed in gas-phase processes that agglomerates of different sizes differ mainly in the number of primary particles, not so much in primary particle diameter. This is due to strong dependence of the characteristic sinter time τ on the primary particle size d_p according to eq. (7.1.4), so that during the initial agglomerate formation just after the first furnace the sintering stops when the primary particle size reaches a certain size. It is also possible to simulate numerically the sintering by solving the equations (7.1.3) – (7.1.5) for the given residence time in the second furnace, using the initial conditions obtained from the experiments and using a given value of the sintering function τ' which is constant at a given temperature. It is possible to obtain information about the values of τ' by means of a comparison of the primary particle diameter obtained from the experiments (Fig.7.1.8a) and from the simulations as a function of temperature. The results are shown in Fig. 7.1.9 for two different values of the coefficient *n*.

a)

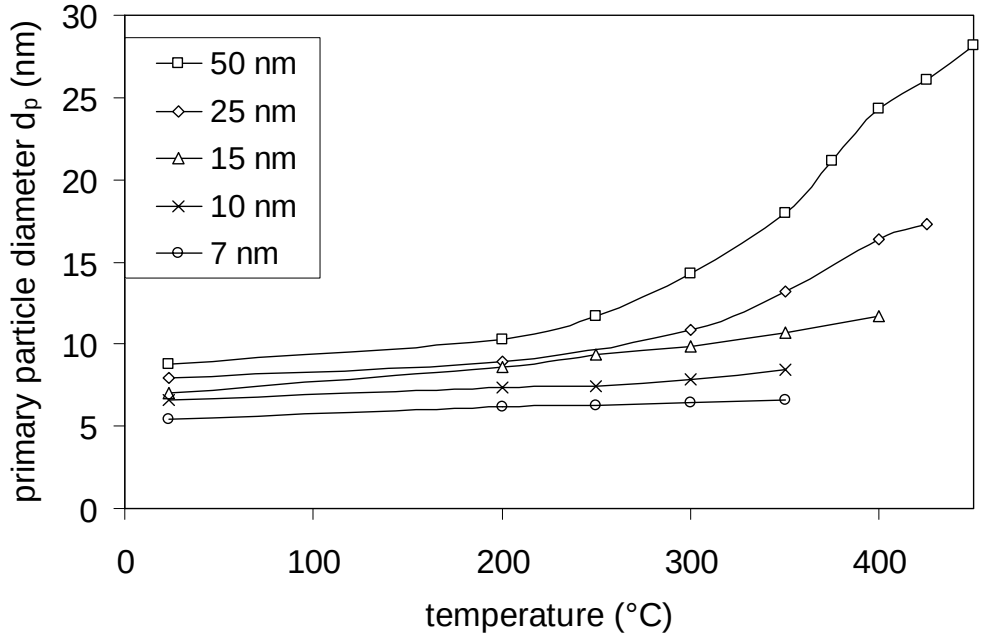

b)

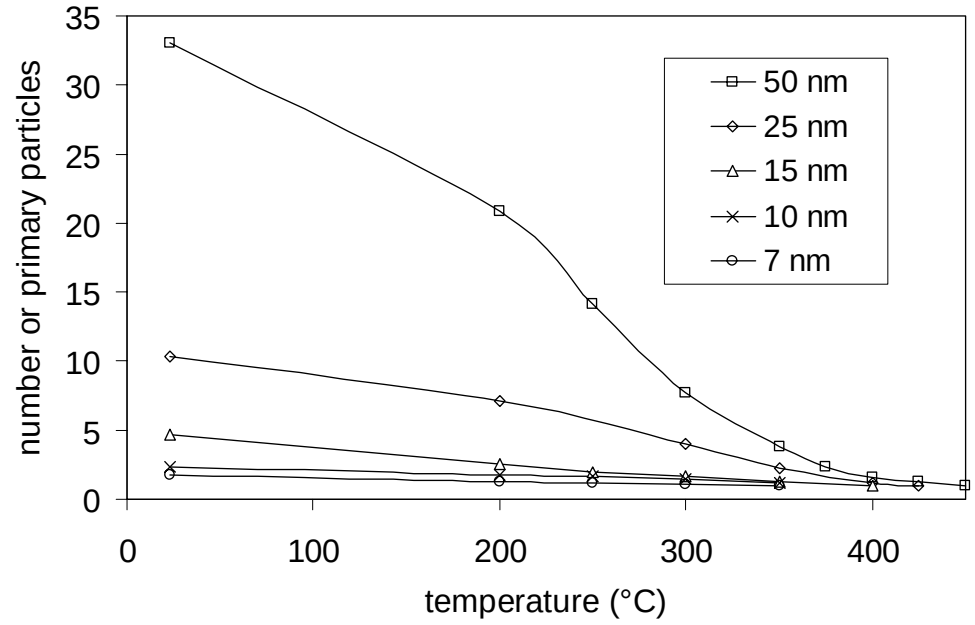

Fig. 7.1.8. (a) Primary particle diameter d_p calculated from experiments on the basis of eq. (7.1.6) as function of the sintering temperature and initial mobility equivalent diameter of the corresponding agglomerate and (b) the corresponding number of primary particles in an agglomerate.

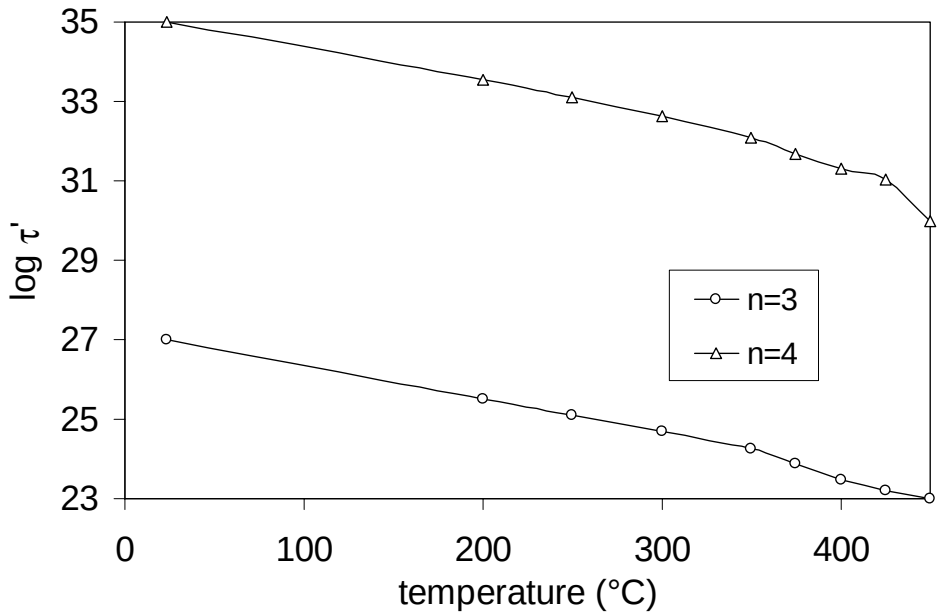

Fig. 7.1.9. Temperature-dependent sintering function τ' determined by comparison of the primary particle diameter extracted from experiments (eq. 7.1.5) and from numerical simulations (eq. 7.1.3). Curves fitted according to eq. (7.1.4) are also shown.

Also shown in Fig. 7.1.9 are the functions fitted to the data according to eq. (7.1.4): $\tau' = 6.068\,10^{17} T \exp(4898/T)$ for $n=3$ and $\tau' = 5.787\,10^{22} T \exp(9065/T)$ for $n=4$, with T expressed in K. A slight change in the slope of the data based on the experiments occurs for both coefficients above 350°C, which might be indicative for two different sintering regimes. This change is, however, too small to enable a clear division between two regimes. It is not possible either to assign clearly a sinter mechanism to this system, as there is not a clearly better fit for one of the coefficients. Both combinations of coefficient and temperature-dependent sintering function τ' might be used in predicting the sintering of PbS.

7.2 Preparation of size-classified SnO_x nanoparticles in the gas phase for gas-sensing appllications

Tin oxide is one of the most important semiconducting materials for gas sensors. Its electrical properties change as a result of the adsorption of gases onto the surface, as described in Chapter 5.3. In view of the high specific surface and activity of tin oxide nanoparticles, considerable improvement in sensing properties

is expected. In order to understand the relationship between gas-sensing behaviour and particle size better it is necessary to generate monodisperse nanoparticles, because a distribution of particle sizes will decrease the special properties and complicates the interpretation of the experimental results. This was also emphasized by Göpel and Schierbaum (1995) in their review article on future prospects of SnO_2 gas sensors: 'Particular emphasis is put on preparing thin films of SnO_2 with homogeneous particle sizes in the nanometre range'. At the moment no gas sensors based on almost single sized particles are available. A similar technique as described in the preceding section is applied here to synthesize monodisperse SnO_x nanoparticles. The subscript 'x' is used in order to stress that stoichiometry is here not necessarily obtained, in fact some oxygen deficiency is desirable.

7.2.1 Experimental set-up

The experimental set-up is similar to the PbS synthesis set-up, the difference is however that in the second tube furnace a combined oxidation-sintering step is performed. Sn (99.999 %, Aldrich, Germany) is evaporated to form a Sn aerosol in the tube furnace 1. In a second experiment SnO powder (>99 %, Aldrich, Germany) is used. Nitrogen obtained from evaporating liquid nitrogen is used as carrier gas. The system is operated at atmospheric pressure. The gas flow through the furnace was kept at 1.5 l/min.

In the second tube furnace the size-fractionated Sn and SnO nanoparticles can be sintered at different temperatures in order to obtain quasi-spherical particles, as the as-formed particles are agglomerates. The oxidation rate of the nanoparticles can be adjusted in the second tube furnace by means of an oxygen flow, controlled by a MFC. A second DMA allows on-line monitoring of the change in the particle size distribution due to the sintering and/or oxidation in the second furnace.

7.2.2 Results of structural and electrical characterization

The DMA monitoring technique allows fast optimization of the process conditions. For each desired particle size, the evaporation temperature in the first tube furnace has to be tuned for getting the maximal particle number concentration, whereas the final particle morphology and composition depends on the temperature of the second furnace. It was found for Sn as evaporation material that the maximum particle amount shifts to larger particle sizes and that the total quantity of the particles increases with increasing evaporation temperature. When the temperature of the second tube furnace was increased up to 750°C, the curves

shifted to smaller particle sizes and the maximum particle number concentration decreased with increasing temperature. Two mechanisms can be responsible for this phenomenon: the first is a compaction process caused by restructuring, sintering and crystallisation. The second mechanism is evaporating of the particles. In this system, increasing the temperature from 600 °C to 750 °C did not change the mean particle diameter any more, which decreased from 10 nm to 6 nm due to restructuring and sintering.

The evaporation of Sn was not a stable process, however. This can be attributed to contamination of the carrier gas with oxygen. Therefore the evaporating material was changed to SnO, resulting in stable particle concentrations over several days. In Fig. 7.2.1 the particle size distributions are shown when changing the evaporation temperature. The sintering of the size-fractionated aerosol (Fig. 7.2.2) shows the compaction and sintering behavior already encountered for PbS. However, with temperatures above 670 °C a bimodal particle size distribution appears if SnO is evaporated due to a evaporation-recondensation mechanism (Fig. 7.2.3). Here, the SnO vapour from the evaporating particles condenses after leaving the sintering furnace, leading to a new particle fraction with smaller diameter together with the fraction of partly evaporated particles.

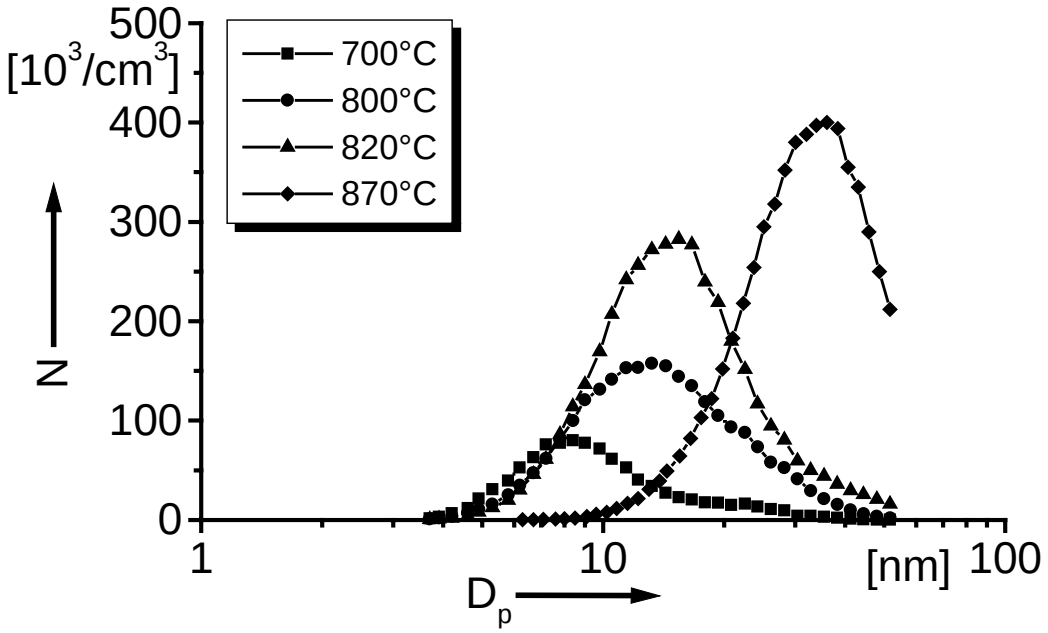

Fig. 7.2.1. Particle size distribution when using SnO as evaporation material at different evaporation temperatures in the first furnace.

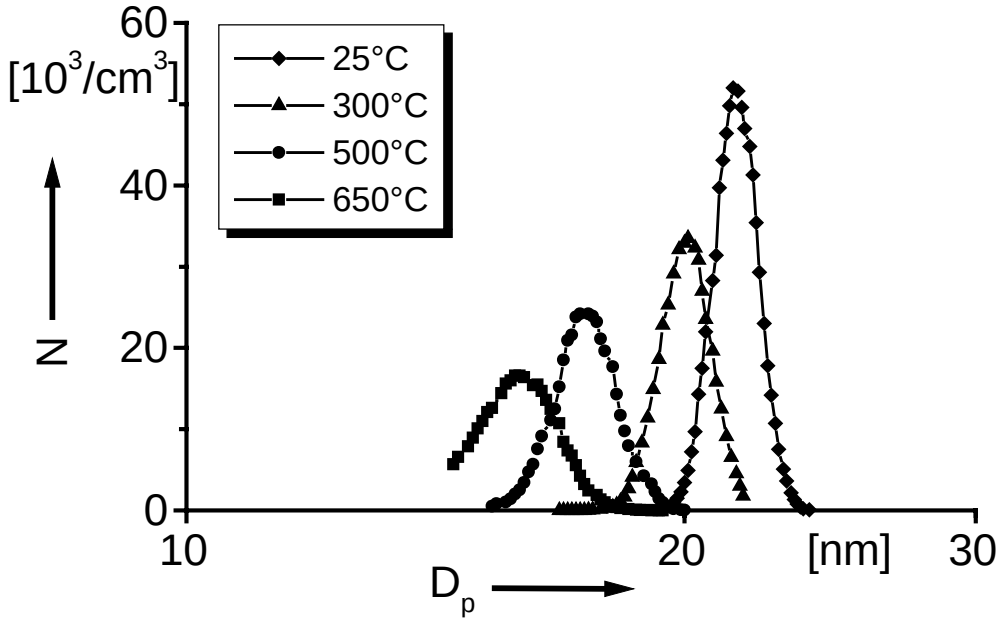

Fig. 7.2.2. Particle size distribution of a size fractionated SnO aerosol (Dp=15 nm) at different sintering temperatures in the second furnace (evaporation temperature 800 °C).

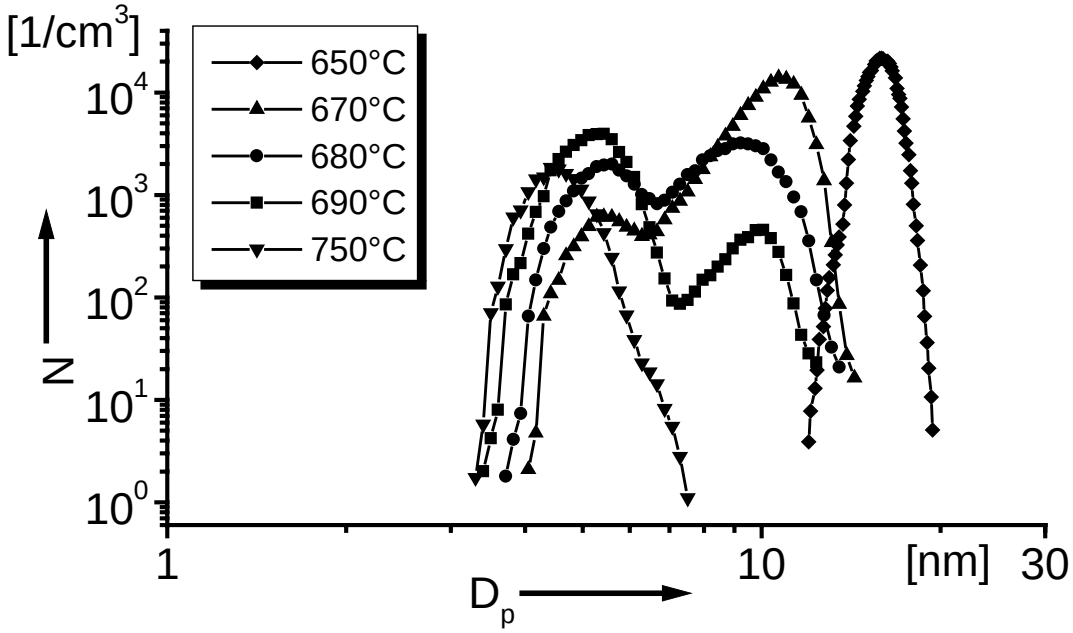

Fig. 7.2.3. Similar to Fig. 7.2.2, with the insert as sintering temperature, now showing a bimodal distribution at a sintering temperature above 670 °C.

It is remarkable that after a running time of several days, the evaporation behaviour of Sn and SnO becomes similar. This can be understood on the basis of the vapour pressures of these materials. The vapour pressure of SnO is much higher compared to Sn at the same temperature, leading to more condensable material in the gas phase. This explains the higher particle concentrations measured in the SnO system. If the carrier gas contains a small amount of O_2, it is assumed that Sn will be oxidized and will evaporate due to the high vapour pressure of the SnO. Another possibility would be to use SnO_2 as starting material, but SnO_2 decomposes into SnO and O_2 upon heating so that this is not a stable evaporating system.

In order to investigate the morphology of the synthesized nanoparticles, TEM micrographs were made. In Fig. 7.2.4 a TEM micrograph is shown of SnO_x nanoparticles coming from the first furnace, i.e., without size-fractionation and sintering/oxidation. The particles are clearly not monocrystalline and monodisperse, they show however appreciable necking due to sintering, which took place during the cooling down after the first furnace. The TEM micrographs of size-fractionated and sintered nanoparticles (Fig. 7.2.5) show much more homogeneous particles. Electron diffraction was used to identify the crystalline structure.

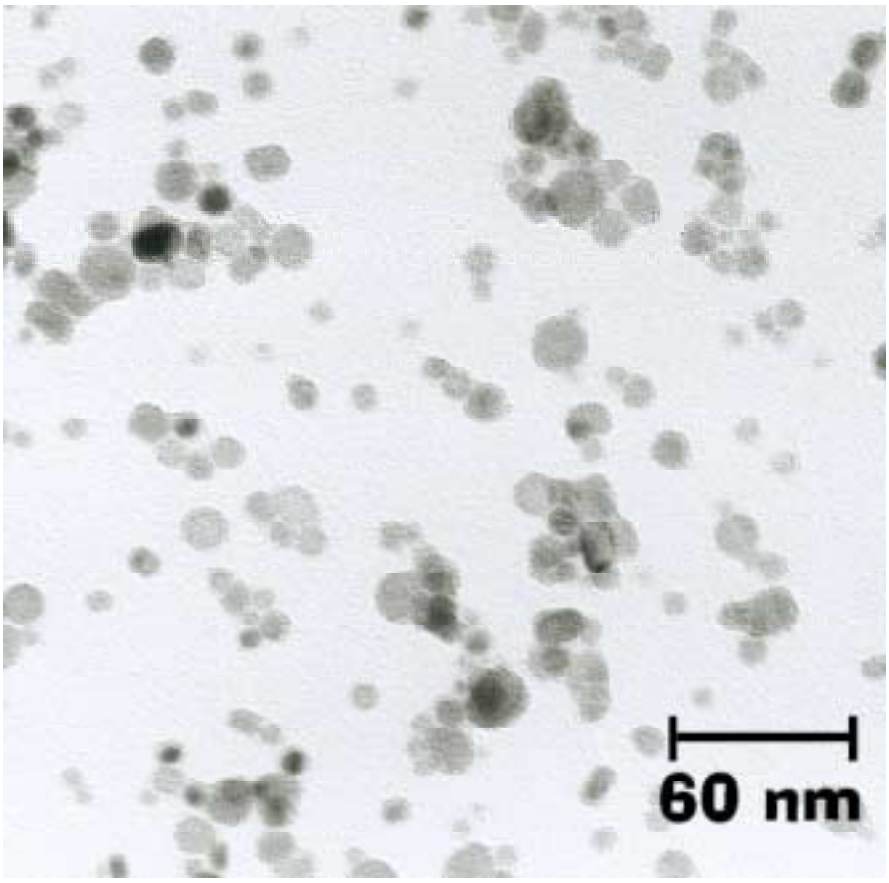

Fig. 7.2.4. TEM micrograph of unfractionated SnO_x nanoparticles coming from the first tube furnace (T=870°C).

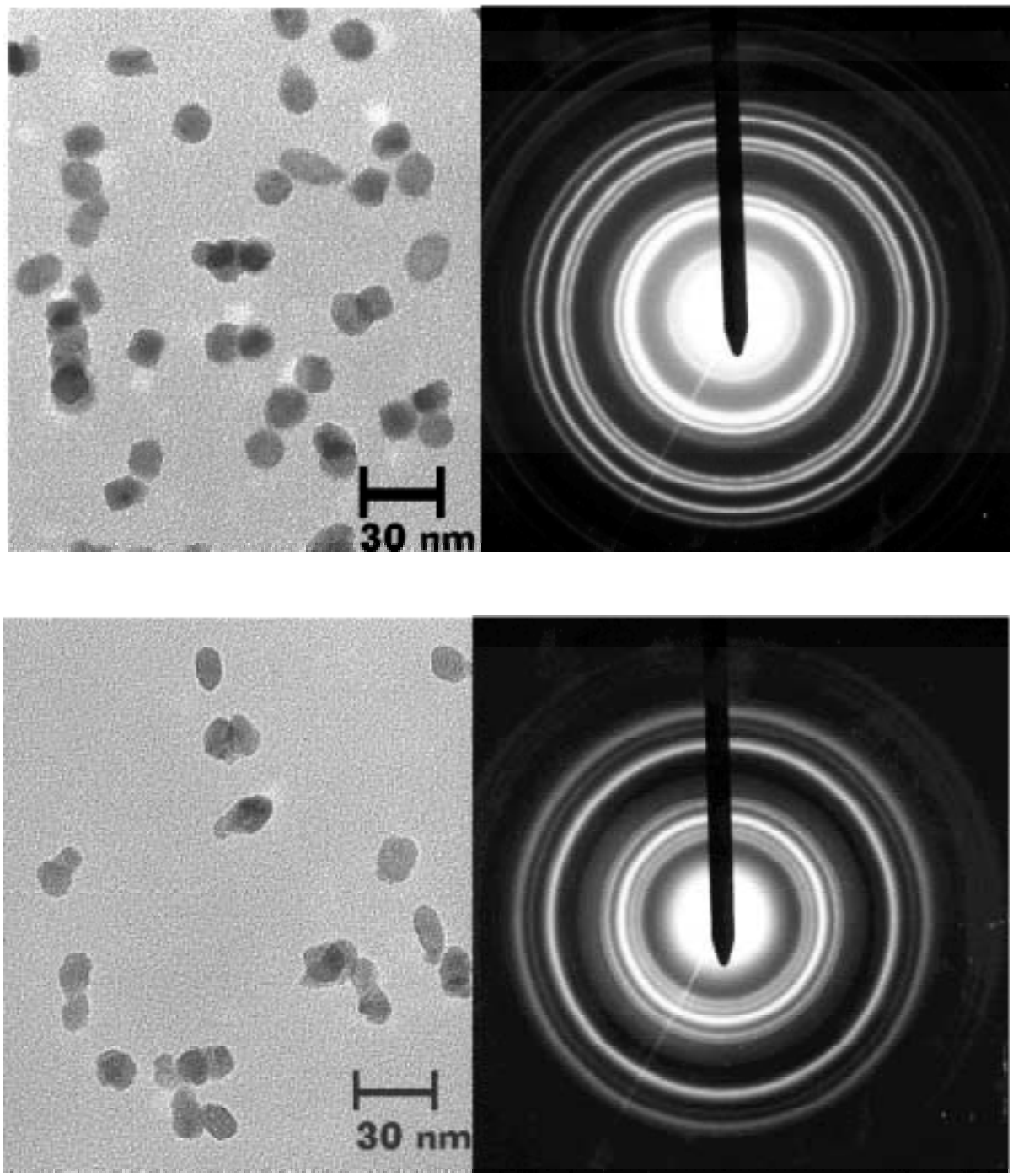

Fig. 7.2.5. TEM micrographs of fractionated SnO_x nanoparticles a) without addition of O_2 in the sinter furnace and b) with addition of O_2 (evaporation temperature 820°C, sintering temperature 650°C, D_p=20 nm). The electron diffraction patterns are characteristic of romarchite (a) and casserite (b).

The crystal structure of the nanoparticles which were sintered without addition of oxygen shows a tetragonal crystal structure, romarchite, characteristic for SnO. When a flow of O_2 was added to the SnO aerosol flow in the sintering furnace, so that the O_2 percentage was approximately 50 vol%, the crystal structure found was a tetragonal phase, casserite, characteristic for SnO_2. Although the exact stoichiometry could not directly be determined, the presence of different crystal structures induced by O_2 addition indicates that it will be possible to vary the stoichiometry by changing the concentration of O_2 in the second furnace.

In order to get a first impression of the feasibility of the synthesized SnO_2 nanoparticles for use in gas-sensing investigations, an electrical characterization was carried out. To this end, an approximately 0.2 µm thick film of nanoparticles with a diameter of 35 nm after size-fractionation was deposited on a glass substrate. The film was electrically contacted by means of silver paste and the *I-V* characteristic was measured (Fig. 7.2.6). The addition of 0.5 vol% CO, which is a reducing gas, increases the current at constant voltage. Thus, the resistance decreases, which is expected according to the qualitative model described in Chapter 5.3, which states that a reducing gas decreases the concentration of chemically absorbed oxygen so that the conductivity increases.

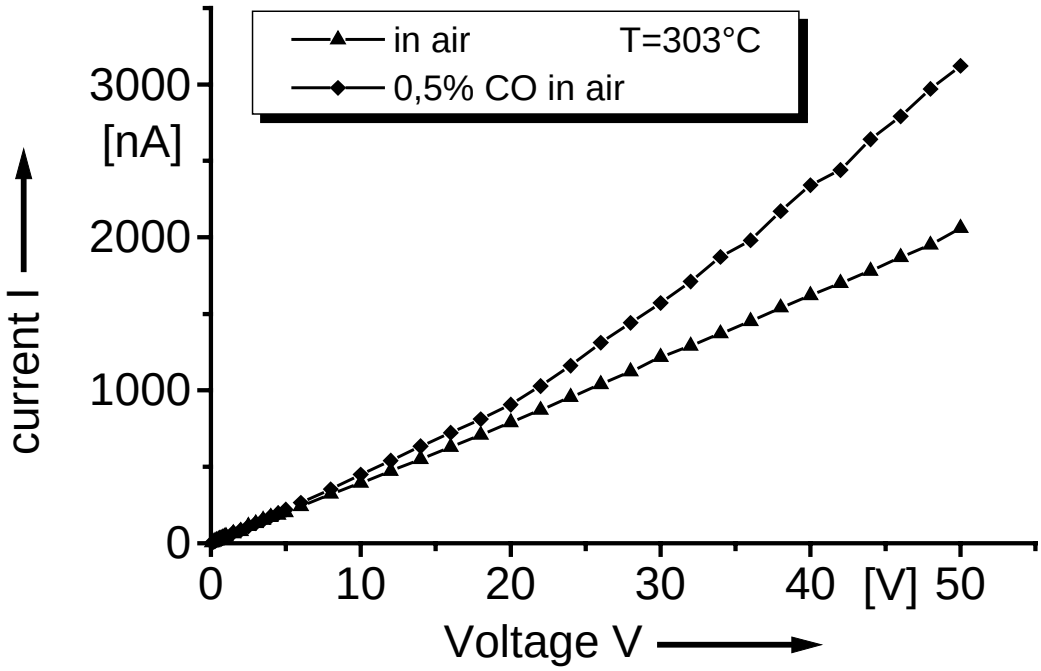

Fig. 7.2.6. I-V characteristics of a thin film (~0.2 µm) of SnO_2 nanoparticles which were 35 nm in diameter after sintering at 650°C. The film itself has not been sintered.

Gas sensors detect changes in the gas concentrations by measuring changes of the resistance of the sensor in a certain gas atmosphere, R_g, when compared with its resistance in pure air, R_a. Therefore, the sensitivity, defined here as R_a / R_g, is shown in Fig. 7.2.7 and shows the expected increase with temperature, most probably due to the changes in surface chemistry with temperature. This increased sensitivity is the reason why gas sensors are operated at higher temperatures, usually between 200 and 400°C.

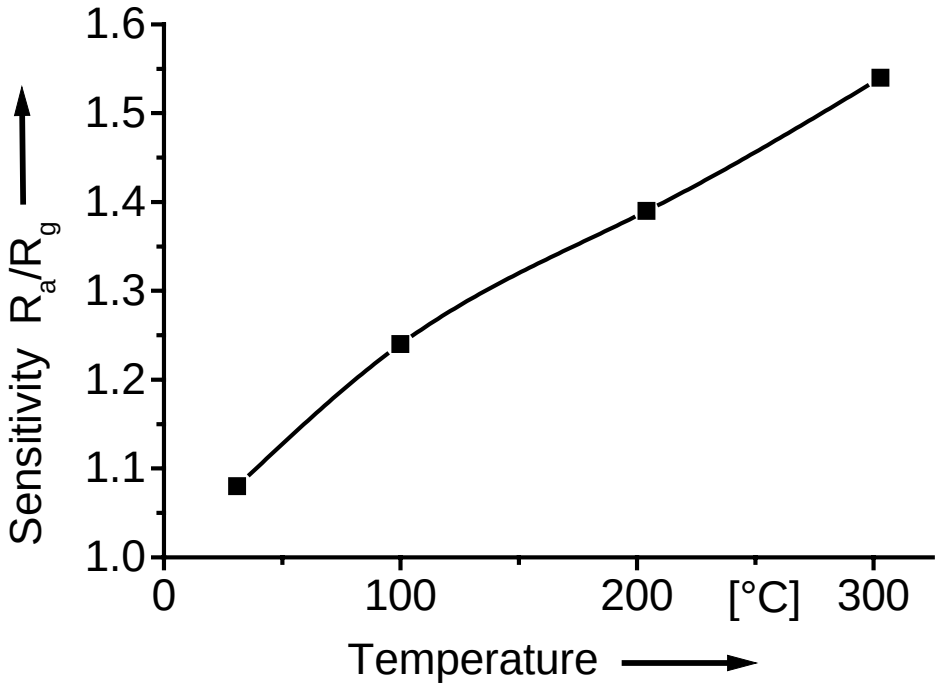

Fig. 7.2.7. The sensitivity R_a / R_g of a thin SnO_2 film (described in Fig. 7.2.5) in 0.5 vol% CO as a function of the temperature in the measurement cell.

Another important characteristic of a gas sensor is its response time. This is tested by changing rapidly the gas atmosphere, in Fig. 7.2.8 from a CO atmosphere to air and back to CO. Due to the use of a flow system and a small volume of the measurement cell, it takes some 5 s to exchange the gas atmosphere. It can be seen from the figure that the change on adding CO is relatively rapid, in the order of 2 minutes, while it takes longer to recover when the CO is not any more present. It is clear that the process is not completely reversible, presumable due to the complicated relationship between chemistry and material properties.

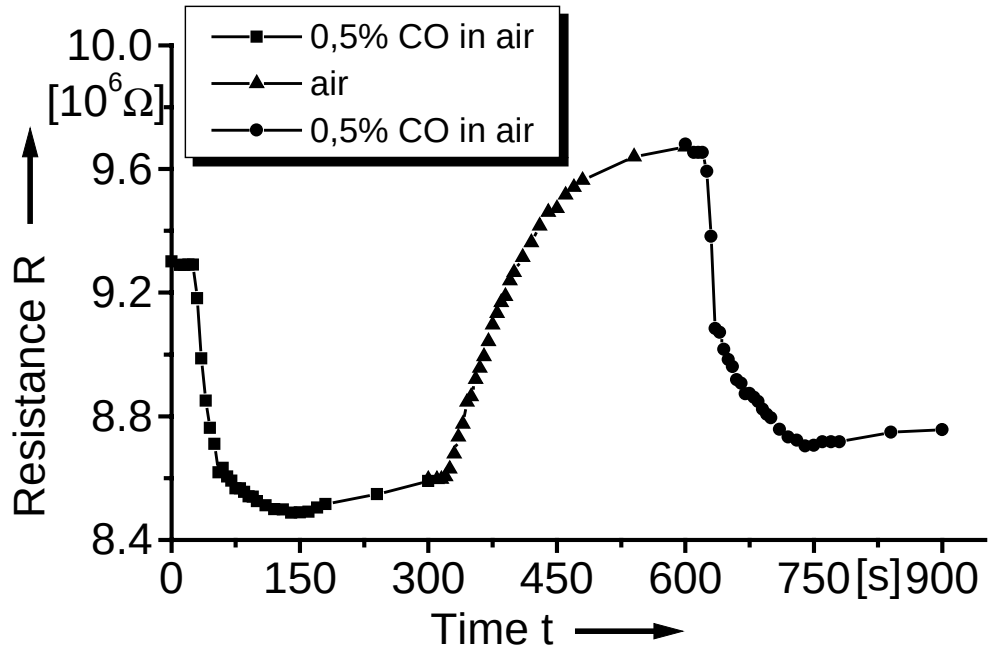

Fig. 7.2.8. The time-dependence of the resistance of the thin SnO_2 layer (described in Fig. 7.2.6) when changing the gas atmosphere from 0.5 vol% CO to air and back to 0.5 vol% CO (T=303°C)

The measurements shown were done for thin films which were not yet sintered, so that the interparticle contacts, which are essential for the gas-sensing mechanism, were probably not yet fully established. These preliminary measurements show that it is possible to create thin gas-sensitive layers composed of equal-sized SnO_2 nanoparticles. The experimental procedure allows to produce thin films, in which the properties of the nanoparticles can be independently controlled by size-fractionation and in-flight sintering and oxidation. In the usual thin film synthesis techniques, such as sputtering and vacuum-evaporation, the particle formation and film formation take place in one step, so that the control over the final morphology of the nanostructured film is not as good as in the method described here.

7.3 Quantum confinement in size-classified PbS nanoparticles

As already discussed in Chapter 2.1, it well known that semiconductor nanocrystals exhibit quantum confinement effects when the particle size is of the order of the Bohr exciton. This is indicated by a blue shift in the optical absorption spectra. PbS is an attractive candidate for the study of quantum confinement effects as the Bohr radius is 9 nm and the effect in PbS nanoparticles synthesized by different chemical routes are well studied (Wang *et al.*, 1987, Zhao and McCormick, 1992, Salata *et al.*, 1994a). Quantum confinement effects have also been observed in evaporated composite films of PbS nanoparticles (Thielsch *et al.*, 1998). In this subchapter, quantum confinement effects in PbS nanoparticles synthesized in the gas phase are reported. Advantages of the gas-phase synthesis method described earlier in this chapter over liquid-phase synthesis methods for investigating quantum confinement effects are the possibility of size-fractionation and the absence of ligands and other impurities. Furthermore, the sintering process involved in the synthesis allows control over crystallinity and shape.

7.3.1 Experimental methods

Single crystalline PbS nanoparticles with different crystalline sizes are synthesized by the gas phase technique described earlier in this chapter. For the optical absorption studies, different crystalline sizes are sintered at different temperature. The name of the samples are given according to the initial mobility diameter. In this context it is worth pointing out that the size and shape of the particles depend on the sintering temperature. The sintering temperatures are well below the respective evaporation temperatures. Several monolayers of nanoparticles were deposited by means of the electrostatic precipitator onto a glass substrate.

The optical absorption spectra at room temperature were recorded using a Beckman-spectrophotometer (Model UV-5240) which is able of recording spectra between 300 and 3000 nm. For this, a bare glass plate was put in front of the reference beam while the glass substrate with PbS films was placed in front of the sample beam. The thickness of the PbS layers was estimated by knowing the area of deposition, the rate of deposition and the size of the particles deposited with the assumption that the particles are spherical. The absorption spectra were normalized with respect to the thickness of the film thus estimated.

7.3.2 Results and discussion

The optical absorption spectra for PbS nanoparticles with different sizes are shown in Fig. 7.3.1. As PbS is a direct band gap semiconductor, the band gap can be determined from the plot $(\alpha h\nu)^2$ vs $h\nu$ by extrapolating $(\alpha h\nu)^2$ to zero value, where α is the absorption coefficient and $h\nu$ is the photon energy. The band gap is the value of $h\nu$ for which $(\alpha h\nu)^2$ is zero. The large blue shift in the absorption spectra with respect to the bulk band gap of 0.4 eV is indicative of the quantum confinement effect.

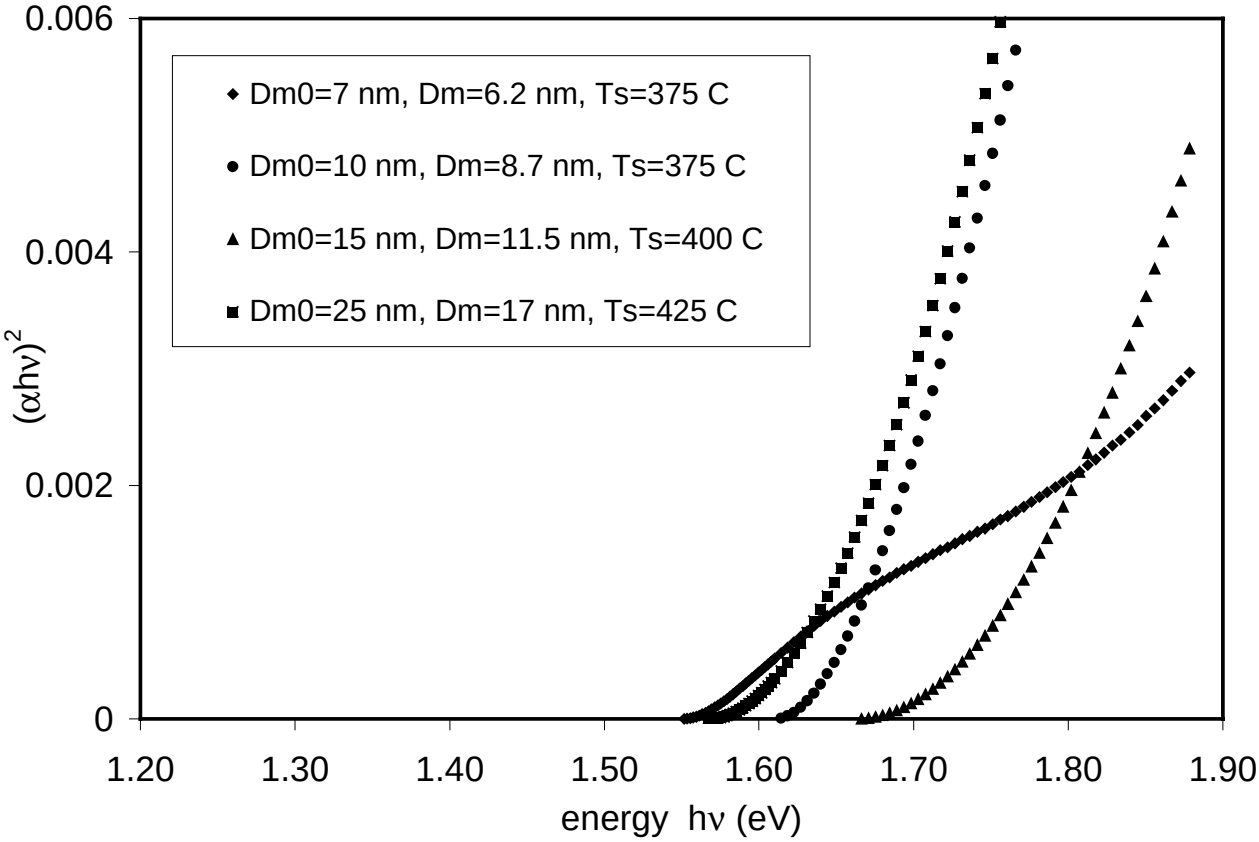

Fig. 7.3.1. The optical absorption spectrum (normalized with respect to film thickness) of PbS nanoparticles of different sizes (D_{m0} is the initial mobility diameter and D_m is the mobility diameter after in-flight sintering at T_s)

It can be seen from the figure that the band gaps of the particles with mobility diameters between 6 and 17 nm are all between 1.5 and 1.8 eV, whereas this band gap range was found for PbS nanoparticles synthesized in a liquid between 3 and 4 nm, as can be seen from Fig. 2.1. Several explanations are possible. The mobility diameter is not related in any way to the crystallite size. A particle might be polycrystalline and be composed of several smaller crystallites, so

that a larger bandgap would result. Another possibility is that the particle are composed of a crystalline core with an amorphous shell or even an oxide layer, which would reduce the effective crystallite diameter. Furthermore, the literature data (as shown in Fig 2.1) are for particles suspended in a liquid and protected against aggregation by means of organic ligands, which might influence their electronic properties. The compact PbS nanoparticle films investigated here do not have such ligands, but the nanoparticles have no or very small interparticle distances, which also might influence their properties. Finally, the possibility exists that the particles are non-spherical. When they are in the form of platelets, this is difficult to detect using TEM, and the smallest particle dimension tends to have the largest influence on the quantum confinement (Zhao and McCormick, 1992).

The comparison between the samples with different diameters is difficult due to the fact that both the initial mobility diameter and the sintering temperature play a role. An attempt to elucidate the effect of sintering temperature is shown in Fig. 7.3.2.

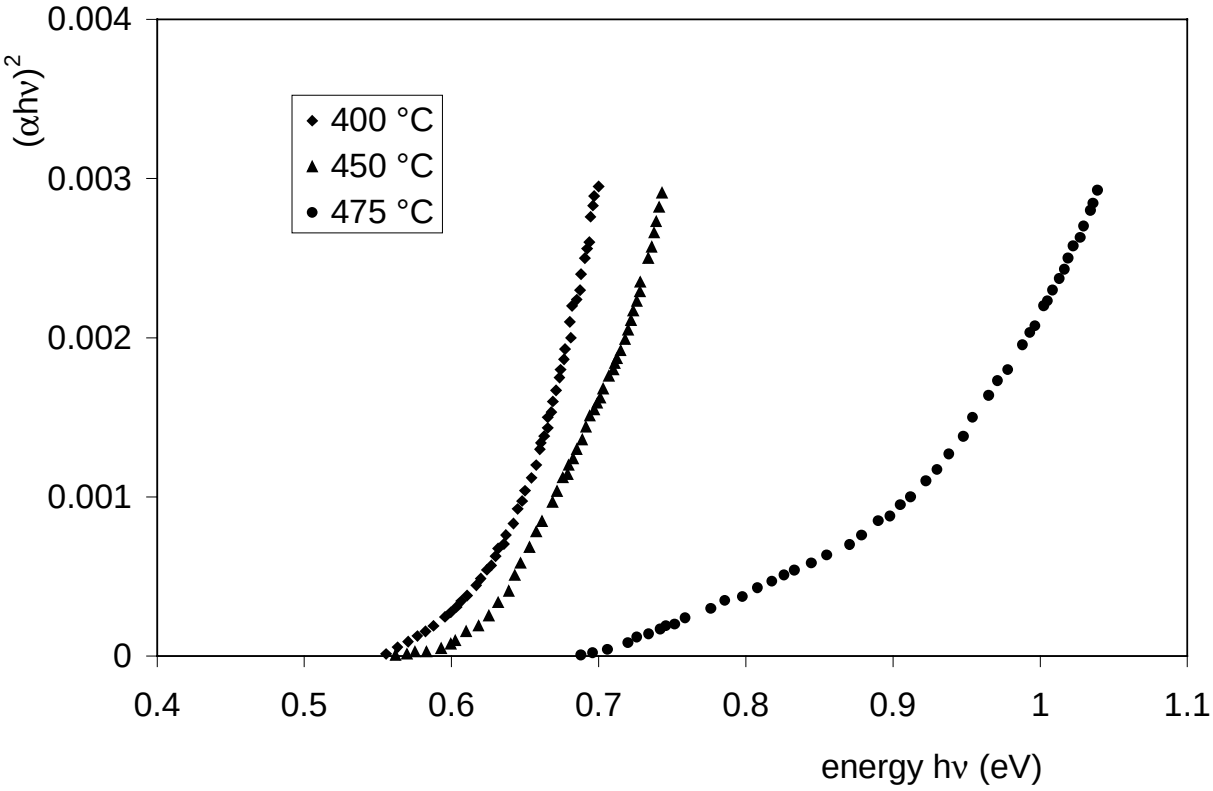

Fig. 7.3.2. The optical absorption spectrum (normalized with respect to film thickness) of PbS nanoparticles with an initial mobility diameter of 50 nm and sintered at the temperature indicated.

As discussed in subchapter 7.1., the geometry of the particles depends on the sintering temperature. When the sintering temperature is increased, the mobility equivalent diameter is found to decrease - a consequence of the restructuring, sintering and crystallisation. Furthermore, evaporation can play a role above a certain temperature which is particle size-dependent. For the particles sintered at 400°C and 450°C, there is little difference observed in the absorption and the band gap does not change clearly. At 475°C however, the bandgap is shifted toward the blue which is an indication for smaller particles. This agrees very well with the results from subchapter 7.1. – evaporation which reduces particle size is negligible at 450°C and starts taking place at 475°C.

Another effect which was found to influence the experimental results, is the time between film deposition and measurement of the optical absorption spectrum. As can be seen in Fig. 7.3.3, the band gap shifts to a higher value one month after deposition, but then seems to be stable. The change in the band gap might be due to oxidation of the nanoparticles, as they were stored in air, or due to morphological changes, as in TEM observations sintering at room temperature has been observed.

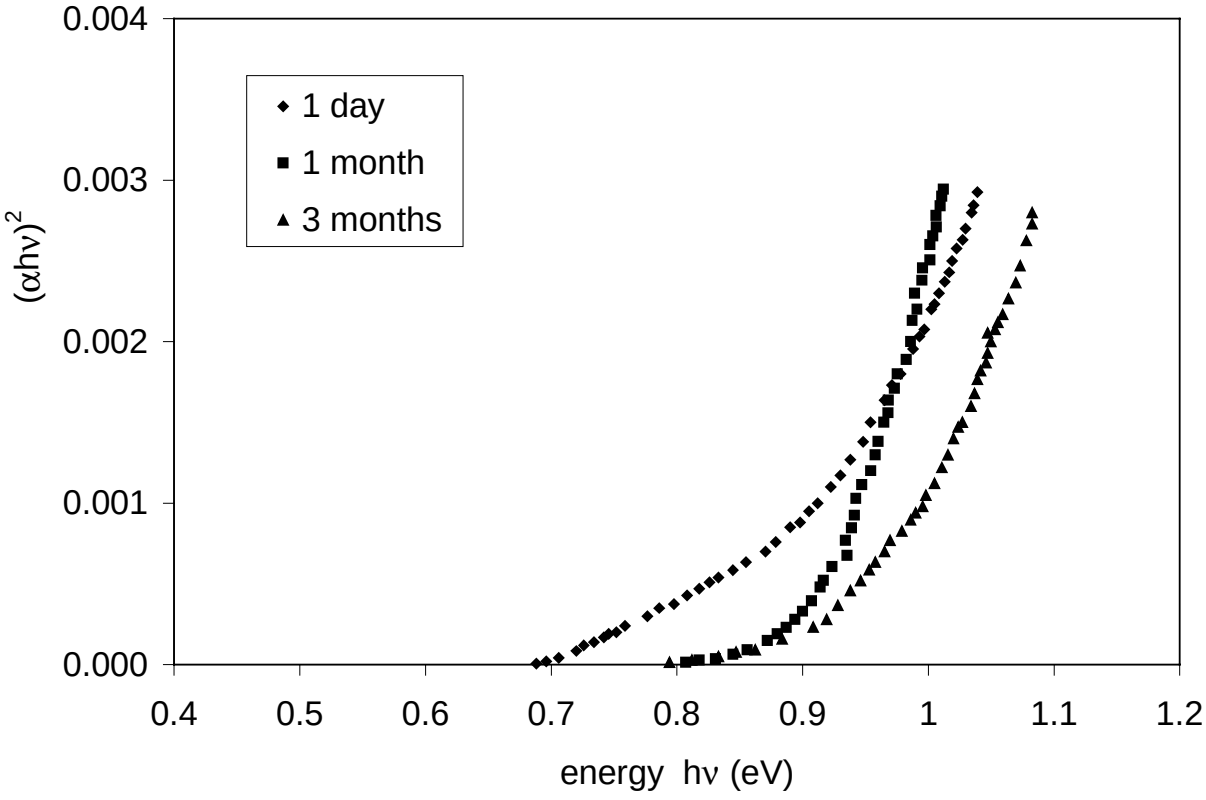

Fig. 7.3.3. The optical absorption spectrum (normalized with respect to film thickness) of PbS nanoparticles with an initial mobility diameter of 50 nm and sintered at 475 °C at different times after deposition.

When comparing the band gaps for the samples having initially a mobility diameter of 50 nm, in the range 0.6-0.7 eV, and for the samples having a mobility diameter of 25 nm or smaller, in the range 1.5-1.8 eV, it is interesting to see that the range of 0.7-1.5 eV is not yet covered. This range contains the commercially interesting range around 1.3 eV, used for very fast optical data transfer by means of GaAs solid state lasers. By choosing initial mobility diameters in between 25 and 50 nm, it should be possible to attain this band gap. Further investigations should be accompanied by careful observations of the actual particle diameter and crystallinity after sintering at different temperatures, preferably by means of high-resolution transmission microscopy.

7.4 Experimental investigation of synthesis of tailored composite nanoparticles in the gas phase

A special case of nanostructured materials is formed by composite particles, here defined as aggregates composed of two different particle classes. Three different basic classes of such composite particles can be distinguished (Fig. 7.4.1):

- a single particle containing two compounds mixed on an atomic scale,
- a ‘core-shell’ particle, in which the core and the shell are composed of different compounds,
- a ‘nanoaggregate’, which is a compound particle consisting of two particles of different chemical composition

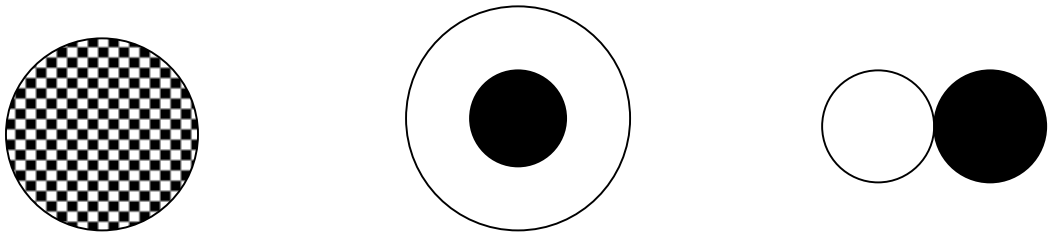

Fig. 7.4.1. Basic classes of composite nanoparticles: a composite nanoparticle, a core-shell nanoparticle and a nanoaggregate.

The technological use of such particles is manyfold, e.g.:

- improve the mixing characteristics when two ultrafine powders have to be mixed: when the powders are mixed in aerosol form, the occurance of large aggregates of one component, which is detrimental for the mixing, can be suppressed,

- improve the functional properties of semiconductor nanoparticles by adding a second semiconductor particle which provides a charge transfer, thereby improving the quantum yield,
- improve the functional properties of nanoparticles by adding another nanoparticle which has catalytic properties, such as Pt or Pd which enhances the sensitivity of SnO_2 nanoparticles used for gas sensors,
- improve the superconductive properties of YBCO particles by adding smaller particle which act as flux pinning enhancement (Takao *et al.*, 1997)

Most methods rely on Brownian aggregation between two different aerosols, which is however difficult to control. Here an experimental procedure is proposed for the controlled synthesis of composite nanoparticles in the gas phase. The theoretical background is already given in Chapter 4.3. Two oppositely charged aerosol flows with different nanoparticles are mixed and the ensuing aggregation will lead to formation of a fraction of composite nanoparticles.

7.4.1 Experimental methods

Nanoparticles of two different substances, PbS and Ag, were generated separately in the gas phase by means of the DMA fractionation technique. and mixed bipolarly. The experimental set up is presented in Fig. 7.4.2.

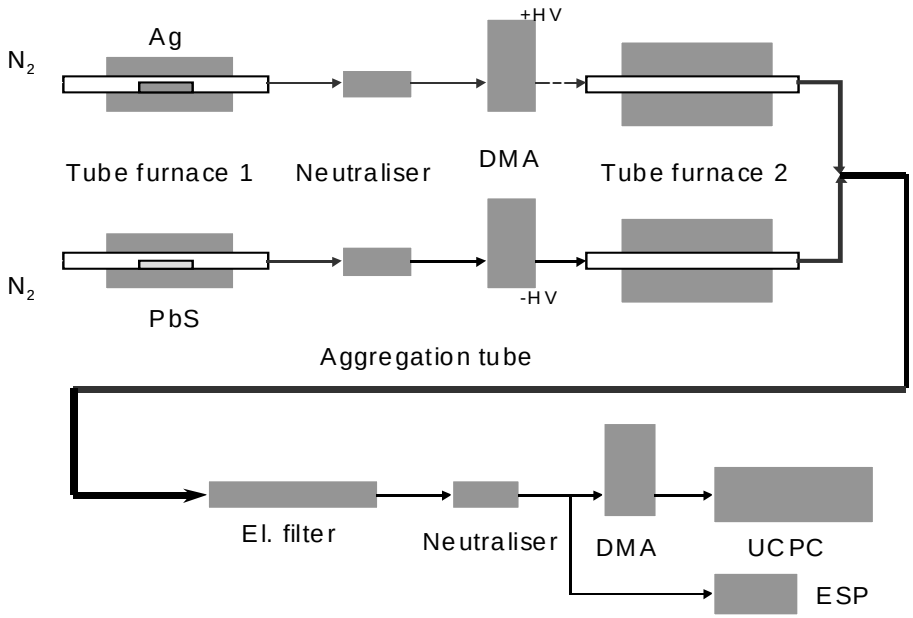

Fig. 7.4.2. Experimental set up for synthesis of composite particle pairs, here PbS and Ag.

The experimental setup contains five main elements: two synthesis units which deliver monosized quasi-spherical nanoparticles of PbS and Ag, an aggregation tube, an electrostatic precipitator and a particle size measurement system. The entire process took place in purified N_2 at 1 bar. The synthesis unit for PbS has been described earlier. Briefly, powders of PbS or Ag are heated at 680°C and 1150°C, respectively, in a tube furnace under flowing N_2 and form particles by homogeneous nucleation in the cooling vapor and subsequent aggregation by Brownian motion. It results in relative broad size distribution. The aerosols are charged bipolarly by a radioactive β–source (Kr^{85}) and size-selected by means of a Differential Mobility Analyzer (NANO-DMA, TSI, Minneapolis, USA and VIE06-3/150, HAUKE GmbH, Austria). The DMA selects particles on the basis on their electrical mobility and is operated such that geometric standard deviations of about 1.1 are obtained. Applying voltages of opposite polarities inside the DMA's one can obtain oppositely singly charged aerosols. The irregularly–formed aerosol particles are then sintered in-flight ($t_{\text{sinter, Ag}} = 400°C$, $t_{\text{sinter, PbS}} = 475°C$) in order to obtain quasi-spherical nanoparticles, which facilitates their identification. The values of particle number concentrations for both components were approximately matched (between 7.0×10^4 cm^{-3} and 9.5×10^4 cm^{-3}), measured by means of a condensation nucleus counter (UCPC, TSI, Minneapolis, USA).

Both the PbS and Ag aerosols with quasi-spherical, monosized and oppositely charged nanoparticles were lead to the aggregation tube, which consisted of copper tubes with a length of 5 or 10 m and a diameter of 20 or 32 mm. The resulting size distribution was measured by a measurement setup consisting of a bipolar charger, a DMA and a condensation nucleus counter. To remove the remaining charged particles, the aerosol flow could be passed through an electrostatic filter so that only electrically neutral particles came through. An electrostatic precipitator (ESP) was used to deposit these selected composite nanoparticles on a TEM grid after recharging them by means of an excimer lamp (λ=172 nm) or a radioactive source.

7.4.2 Results and discussion

The resulting particle size scans after mixing oppositely charged Ag and PbS nanoparticles with diameters of about 20 and 24 nm, respectively, are shown in Fig. 7.4.3 for different residence times in the aggregation tube. Again, these scans have not been corrected for charging efficiency of the radioactive source and transmission efficiency of the DMA, and are strictly speaking no size distributions. The curves show three features: the first two corresponding to primary,

unaggregated nanoparticles and the third corresponding to nanoaggregates. When applying electrostatic filtering, only the uncharged nanoaggregates with an effective mobility diameter of 30 nm are left. It can be seen that doubling the residence time in the aggregation tube increases the number of nanoaggregates approximately by a factor of two, which is in accordance with aggregation kinetics.

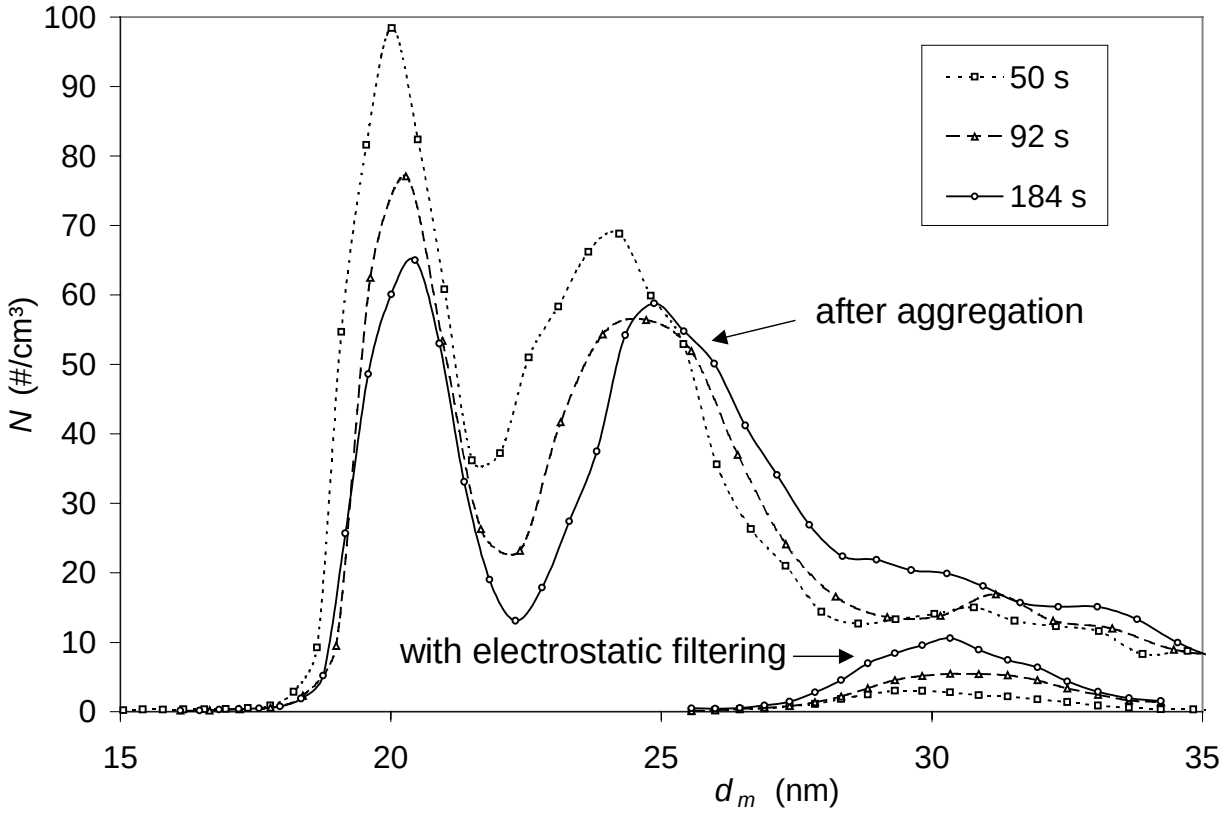

Fig. 7.4.3. Scan over the particle mobility diameter of the resulting aerosol after different residence times in an aggregation tube when Ag and PbS nanoparticle aerosols with diameters of about 20 and 24 nm and a one negatively and positively elementary charge, respectively, are mixed. Also shown are the corresponding scans after applying electrostatic filtering, so that only uncharged particles which are Ag-PbS nanoaggregates are left.

The relative low value of the primary particle concentrations N_{Ag} and N_{PbS} due to the size-selection results in low values of composite particle concentration $N_{\mathrm{Ag\text{-}PbS}}$, which can be estimated from $\mathrm{d}N_{12}/\mathrm{d}t = \beta_{12} N_1 N_2$, so that long residence times are necessary. As particle diffusion losses to the walls of the aggregation tube do not depend on the diameter of the tube for a given volumetric flow but increase

with the tube length, increasing the diameter of the aggregation tube seems to be the best way to obtain a larger residence time and thus a higher concentration of composite nanoparticles. With the largest residence time some 7% of the primary particles are aggregated in form of composite nanoparticles, so that after electrostatic filtering a concentration of 7 10^3 cm^{-3} of composite nanoparticles is obtained.

An additional information contained in Fig. 7.4.3 is the direct experimental determination of the mobility diameter for aggregates consisting of two well-defined primary particles. The aggregate mobility diameter can be estimated using the concept of fractal dimension. In this approach, the value of the mobility diameter d_m depends on the primary particle diameter d_0, number of primary particles in the aggregate n and the fractal dimension D_f as follows:

$$d_m = d_0 n^{D_f} \qquad (7.4.1)$$

This equation was shown to be valid for small aggregates ($n < 20$) in the free molecular regime, for which a fractal dimension of 2.18 was experimentally found (Cai and Sorensen, 1994). Using eq. (7.4.1) yields a mobility diameter of 30.6 nm with the primary particle diameter taken here as the volumetric mean value of the two diameters (20 and 24 nm). This value agrees well with the experimentally found mobility diameter, being about 30 nm.

On transmission electron micrographs of the deposited composite nanoparticles (Fig. 7.4.4) one can clearly see nanoaggregates composed of two primary particles to prevail. Also some nanoaggregates composed of four primary particles were observed, which results from the electrostatic filtering allowing to pass only uncharged aggregates. Uncharged aggregates can be composed of equal numbers of PbS and Ag primary particles. In the TEM micrograph, also some particles look like single primary particles. This might be due to a discharging of primary particles in the aggregation tube or due to one particle being shielded from view by another one.

Electron diffraction shows the presence of both silver and lead sulfide in crystalline form. An EDX line-scan over a single nanoaggregate along a line between the particle centers is shown in Fig. 7.4.5. Both Ag and PbS were detected, the maxima of the distributions being some 13 nm apart which is approximately the distance between primary particle centers as determined from TEM (the insert in the figure). The relatively broad distribution of the components is due to the finite width of the electron beam, here about 10 nm.

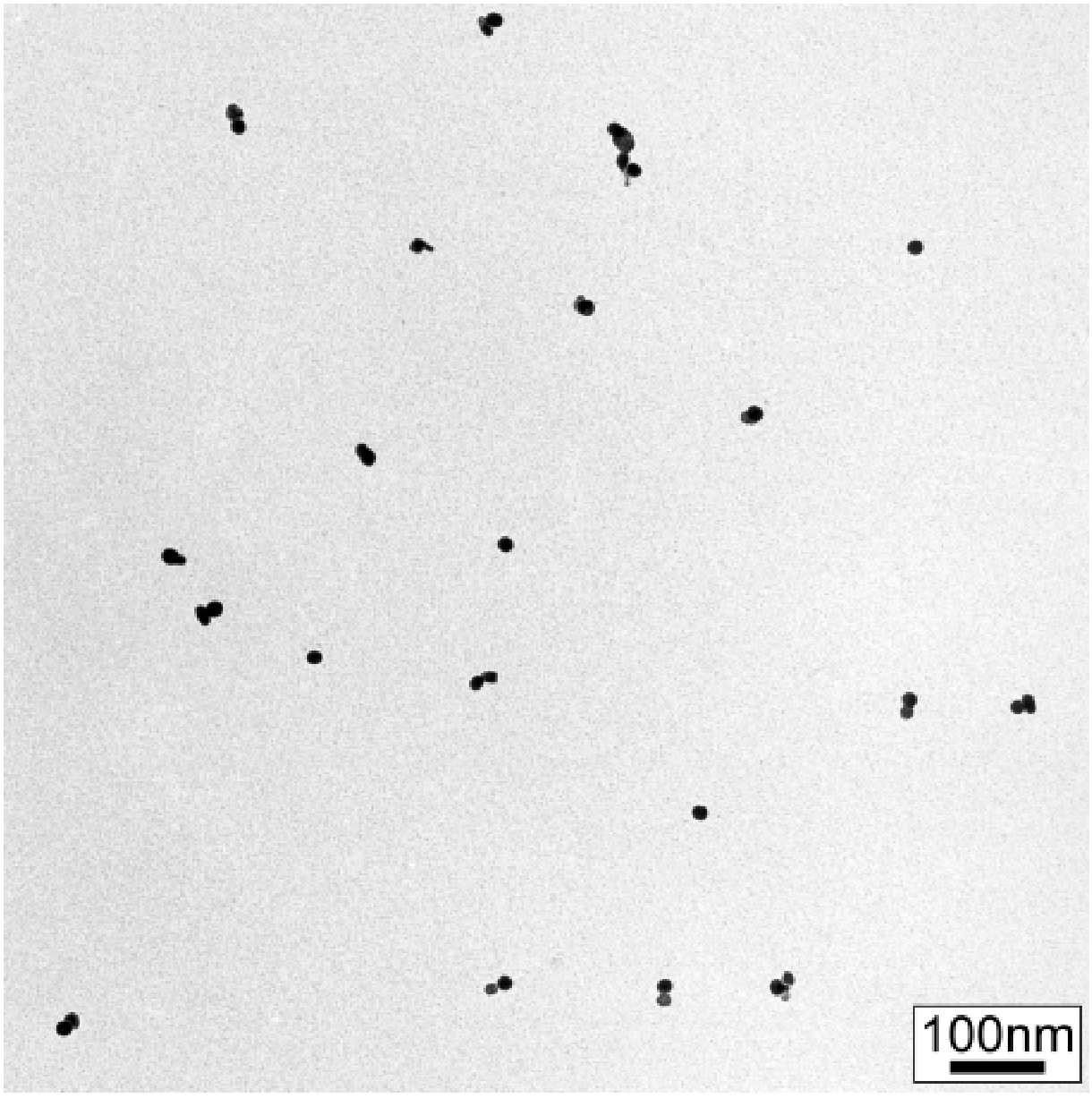

Fig. 7.4.4. Transmission electron micrograph of Ag-PbS nanoaggregates, composed of PbS nanoparticles with a mobility diameter of 17.5 nm and Ag nanoparticles with a mobility diameter of 21.5 nm.

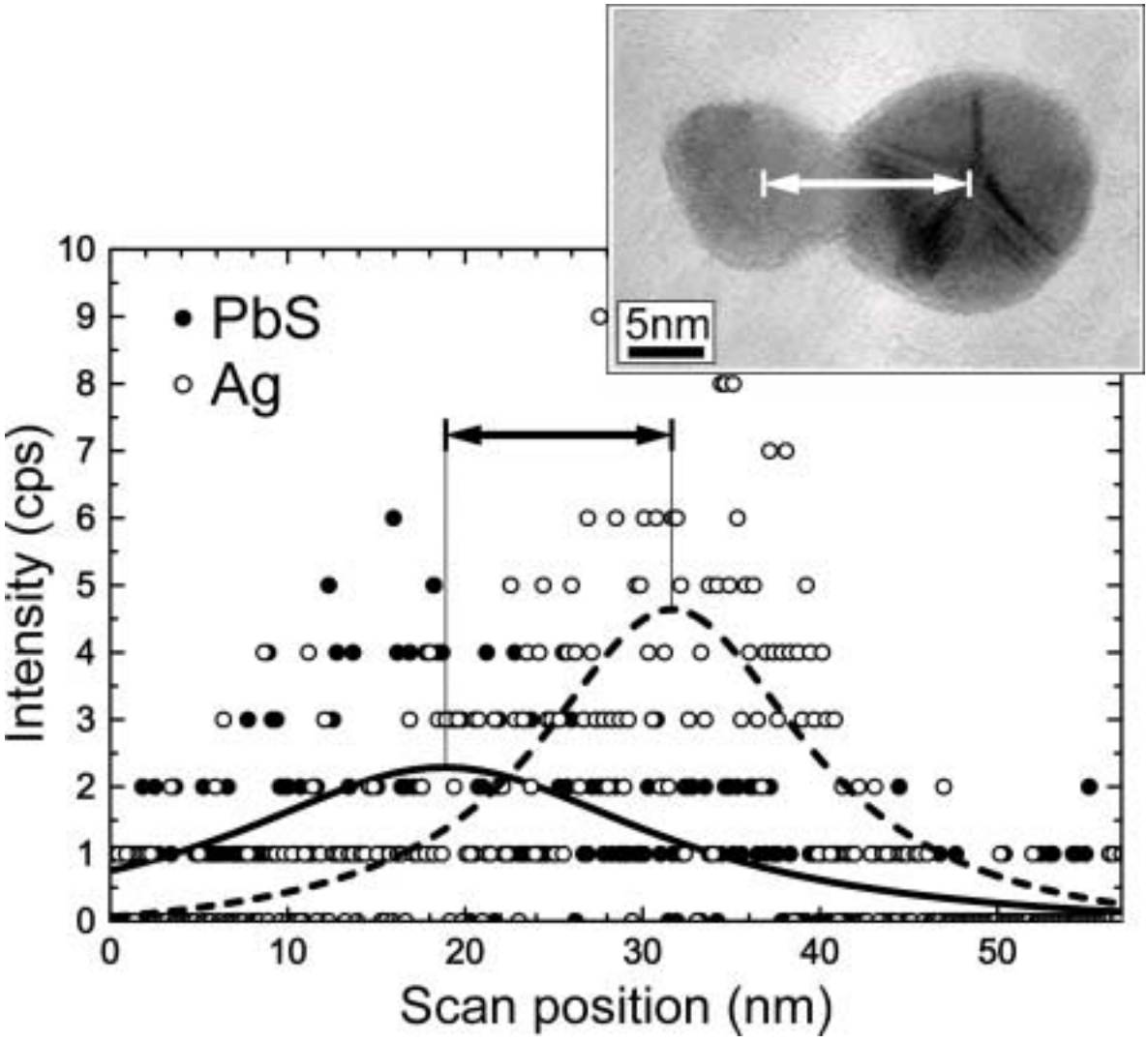

Fig. 7.4.5. EDX line-scan over a nanoaggregate, composed of size-fractionated Ag and PbS primary particles, as described in the caption of Fig. 7.4.4. The insert shows the TEM micrograph of the corresponding nanoaggregate.

Due to the low concentrations of the nanoparticle pairs formed (some 10^3 cm^{-3}), the applications of the method are at present limited to fundamental investigations of the properties of the formed particle pairs, e.g. in optical materials, sensors, solar cells and catalyst and to applications where only very thin layers are needed. Higher concentrations can be reached when the size fractionation step is deleted and two aerosols are mixed after having been charged unipolarly and oppositely, but at expense of the high degree of control in the present process

7.5 Conclusions: Synthesis of PbS and SnO_x nanoparticles for functional applications

Synthesis of the semiconductors PbS and SnO_x is showed to be possible with the help of carefully controlled techniques such as size fractionation and in-flight sintering. With techniques basing on electrical effects, nanoparticle composite pairs have been obtained experimentally. The process of sintering PbS has been investigated for PbS with help of a quantitative model which allowed the determination of sintering parameters. As a first indication of changing physical properties with particle size, the absorption spectrum of PbS particles is shown to shift toward the blue, indicative for quantum confinement effects. Thin films composed of SnO_x nanoparticles show gas-sensitive behavior.

8. Conclusions

There is a great deal of interest today in the special properties of nanoparticles and their potential applications. An overview of the potential functional applications, which include electronic, optical and magnetic applications, based on these special properties shows the broad range of possible applications. Most applications demand some control over particle size, width of the particle size distribution, crystallinity, stoichiometry, inter-particle connections and mixing or doping with other materials.

Gas-phase processes, although having some drawbacks, have the largest means of control and are therefore the method of choice here. Processes based on pure physical processes are used more often than chemical methods as they allow to obtain the highest purity. The evaporation-condensation method is chosen in this work as synthesis method. The Brownian coagulation inherent to this method makes it impossible to obtain narrow particle size distributions but allows to obtain a mixing of particles of different materials for the synthesis of nanocomposites.

The formation of nanoparticles by the evaporation-condensation technique was analyzed using a moment model describing nucleation, condensation and coagulation. Using the model, it was shown that the temperature in the evaporation furnace and the cooling rate determines the mean particle size and that an aerosoldynamical model allows the prediction of the temperatures needed for nanoparticle formation.

For describing more complicated systems having more degrees of freedom, such as distribution of particle sizes, different chemical compositions, distribution of charges and distribution of number of primary in an aggregate, a newly developed Direct Simulation Monte Carlo method was shown to be suitable. Two examples of practical relevance containing multi-dimensional particle dynamics were given: coagulation with chemical reaction in droplets (microreactors) and the coating of solid particles with nanoparticles.

Aggregation of mixtures of charged nanoparticles is useful for obtaining composites. This was studied by means of the Direct Simulation Monte Carlo method. The selectivity of mixing is characterized by means of the fraction of symmetric aggregates. It was shown that for each charge distribution different conditions lead to a highest possible selectivity of mixing.

Two chemical compounds were selected for further experimental study based on a literature review. One component is selected for its potential quantum confinement effects. PbS is a narrow-gap IV-VI semiconductor with a cubic rock salt structure and is an attractive candidate for the study of quantum confinement effects as its hole Bohr radius is 9 nm. This results in strong confinement effects. The

confinement results in a blue shift in the optical absorption spectrum. The other material, SnO_x, is selected for its gas-sensing properties.

A size uniformity is important in order to study or make use of quantum size effects, as a distribution of particle sizes will decrease or smear out these effects. In view of the high specific surface and activity of SnO_x nanoparticles, considerable improvement in sensing properties is expected. In order to understand the relationship between gas-sensing behaviour and particle size better it is necessary to generate monodisperse nanoparticles, because a distribution of particle sizes will decrease the special properties and complicates the interpretation of the experimental results. At the moment no gas sensors based on almost equal-sized nanoparticles are available. For this goal, size fractionation by means of a Differential Mobility Analyzer was applied. This decreases the yield, but for functional applications the quality more than the quantity of the nanoparticles is decisive, as most of the functional applications need only thin films.

Several new instruments have been developed in this work which allow to obtain more control over processes which are essential for the synthesis method chosen here. They allow nanoparticle charging, nanoparticle size fractionation and nanoparticle deposition.

A newly developed nanoparticle charger, the twin Hewitt charger, allows a larger fraction of the nanoparticles to be charged, which is important to get a higher yield. A higher yield would result in a shorter deposition time, which is important because the deposition takes at present hours to days. The instrument has been extensively investigated experimentally in order to find the optimal charging conditions.

Differential Mobility Analysis at lower pressures than atmospheric pressure has been investigated theoretically. It was found that the lower particle limit is not changed fundamentally with lower pressures when keeping the mass flow rate constant, but that the higher particle limit is decreased due to decrease of the maximum allowed field strength. A Differential Mobility Analyzer design for low pressure has been presented. It is important to perform size fractionation at pressures lower than atmospheric pressure, as usually the system pressure is decreased in order to get a higher yield of smaller nanoparticles and to increase the cleanness of the system.

An Electrostatic Precipitator has been developed which allows the investigation of electrical properties of nanoparticle films under clean conditions direct after deposition. This is especially important for semiconductor nanoparticles, where the surface influences the optical and electronic properties.

Synthesis of the semiconductors PbS and SnO_x in form of almost equal-sized monocrystalline nanoparticles is showed to be possible with the help of carefully controlled techniques such as size fractionation and in-flight sintering. The processes

of sintering of PbS has been investigated with help of a quantitative model which allowed the determination of sintering parameters, which are usually unknown for semiconducting materials. The process should be controlled such that sufficient sintering and crystallisation but no evaporation and re-condensation occurs, as this destroys the monodispersity.

As examples of the suitability of synthesized PbS and SnO_x nanoparticles for functional applications, the absorption spectrum of PbS and the gas-sensitivity of thin films composed of SnO_x nanoparticles were investigated. As a first indication of changing physical properties with particle size, the absorption spectrum of PbS particles is shown to shift toward the blue, indicative for quantum confinement effects. The measurements also indicate that the optical properties are strongly influenced by the handling of the nanoparticles directly after their formation, such as sintering and/or evaporation processes taking place in the sintering furnace. By choosing suitable initial mobility diameters, it should be possible to attain the commercially interesting bandgap range around 1.3 eV, used for very fast optical data transfer by means of GaAs solid state lasers. Further investigations should be accompanied by careful observations of the actual particle diameter and crystallinity after sintering at different temperatures, preferably by means of high-resolution transmission microscopy.

First measurements show that it is possible to create thin gas-sensitive layers composed of equal-sized SnO_2 nanoparticles. The experimental procedure allows to produce thin films, in which the properties of the nanoparticles can be independently controlled by size-fractionation and in-flight sintering and oxidation. Further properties of the films, such as the inter-particle contacts which are very important for the electrical conductivity, can be influenced by post-deposition annealing This opens a way to investigate fundamental gas-sensing properties of a better controlled microstructure than available at present.

Finally, the possibility of gas-phase synthesis of tailored composite nanoparticles by means of aggregation of oppositely charged, size-selected nanoparticles of two different materials is shown. Electrical effects are applied for size-selection, selective mixing, separating the composite nanoparticles from unaggregated nanoparticles and the deposition of nanoaggregates. Size, size dispersion and materials can be selected independently. As an illustration of the method, composite nanoparticles consisting of differently sized Ag and PbS nanoparticles have been obtained. The method allows the investigation of fundamental properties of composite nanoparticles both in-flight and after deposition in form of a thin film.

Concluding, the field of nanoparticles for functional applications is exciting and rapidly developing. Synthesis and handling methods are available, but the main challenge lies in obtaining a better control over the particle characteristics so that the desired properties of the functional applications can be attained.

Acknowledgements

At the first place, I would like to convey my sincere thanks to my mentor, Prof.Dr.-Ing. H. Fissan, whose experience in all aspects of research was invaluable. He encouraged and enabled me to start many research projects which were crucial for this Habilitation Thesis.

I am indebted to a number of persons who contributed to this work. First of all, the members of the present nanoparticle group in the process- and aerosol measurement technology section (AMT). Arkadi Maisels performed the simulations with the Monte Carlo technique, and was also responsible for the experiments with the bipolar mixing. Karuna Nanda recorded the optical absorption spectra of the PbS nanoparticles. Marcus Kennedy was responsible for the SnO_x synthesis and characterization of the gas-sensitive thin films. Frank Otten initiated the construction of the electrostatic precipitator, amongst numerous other activities. Ralf Lange performed the first SnO_x synthesis trials. Frank Jordan gave useful advise for setting up and testing the charger. Our technical assistent, Christoph Kleinert, was of great help in constructing the numerous new experimental setups, while Klaus Kubernus, Fiete Kapitza and Siegfried Neumann enabled the work in the laboratories and at personal computers. Heidi Giesen and Rongrong Wang assisted in the administrative part. Important contributions came also from the students, Kornelius Nielsch who assisted with the first synthesis experiments, Sami Kilani who constructed the charger and Willy Gerber who constructed the electrostatic precipitator. I am further indebted to our guest scientists, Aaron Peled for his critical comments on my reviewing of the functional applications and Bodh Mehta for his advise and help with the electrical characterization of the SnO_x films.

Without the help from the low-temperature physics section of the physics department, especially Bernd Rellinghaus and Mehmet Acet, the particle characterization would have been impossible. I would like to thank also the chairmen and other members of the Special Research Program “Nanoparticles from the gas phase: formation, structure, properties” (SFB 445) for their support and valuable discussions. The help of the German National Science Foundation (DFG) for financing several projects from which results were shown here is gratefully acknowledged.

Finally, I would like to thank my wife, Sabine, for her patience with my preoccupation with these invisible small particles and for her love and support.

List of references

Abeles, B., Pinch, H.L. and Gittleman, J.I. (1975) Percolation conductivity in W-Al_2O_3 granular metal films. *Phys.Rev.Lett.* **35** (4) 247-250

Adachi, M., Okuyama, K., Kousaka, Y. and Tanaka, H. (1988) Preparation of gas sensitive film by deposition of ultrafine tin dioxide particles. *J.Aerosol Sci.* **19** (2) 253-263

Agata, M., Kurase, H., Hayashi, S. and Yamamoto, K. (1990) Photoluminescence spectra of gas-evaporated CdS microcrystals. *Solid State Comm.* **76** (8) 1061-1065

Alivisatos, A.P. (1996) Semiconductor clusters, nanocrystals, and quantum dots. *Science* **271** 933-937

Andres, R.P., Averback, R.S., Brown, W.L., Brus, L.E., Goddard, W.A, Kaldor, A., Louie, S.G., Moscovits, M., Peercy, P.S., Riley, S.J., Siegel, R., Spaepen, F. and Wang, Y. (1989) Research opportunities on clusters and cluster-assembled materials - A department of energy, council on materials science panel report. *J.Mater.Res.* **4** (3) 704-734

Balachandran, U., Siegel, R.W., Liao, Y.X. and Askew, T.R. (1995) Synthesis, sintering, and magnetic properties of nanophase Cr_2O_3. *Nanostruct.Matls.* **5** 505-512

Bapat, P.M., L.L. Tavlarides and G.W. Smith (1983) Monte Carlo Simulations of Mass Transfer in Liquid-Liquid Dispersions. *Chem. Eng. Sci.*, **38** 2003-2008

Bartz, H., Fissan, H. and Liu, B.Y.H. (1987) A new generator for ultrafine aerosols below 10 nm. *Aerosol Sci. Technol.*, **6** 163-171

Bayazitoglu, Y., Brotzen, F.R. and Zhang, Y. (1996) Metal vapor condensation in a converging nozzle. *Nanostruct.Matls.* **7** 789-803

Bezryadin, A., Dekker, C. and Schmid, G. (1997) Electrostatic trapping of single conducting nanoparticles between nanoelectrodes. *Appl.Phys.Lett.* **71** (9) 1273-1275

Bird, G.A., *Molecular gas Dynamics*, Clarendon Press, Oxford (1976)

Birringer, R., Gleiter, H., Klein, H.P. and Marquardt, P. (1984) Nanocrystalline materials , an approach to a novel solid structure with gas like disorder.*Phys.Lett* **102A** 365

Blandenet, G., Court, M. and Lagarde, Y. (1981) Thin layers deposited by the pyrosol process. *Thin Solid Films* **77** 81-90

Bowles, R.S., Kolstad, J.J., Calo, J.M. and Andres, R.P. (1981) Generation of molecular clusters of controlled size. *Surf.Sci.* **106** 117-124

Brankovic, Z., Milosevic, O., Uskokovic, D., Poleti, D. and Karanovic, L. (1994) Nanostructured constituents of ZnO-based varistors prepared by mechanical attrition. *Nanostruct.Matls.* **4** 149-157

Brus, L.E. (1983) A simple model for the ionization potential, electron affinity, and aqueous redox potentials of small semiconductor crystallites. *J.Chem.Phys.* **79**(11) 5566-5571

Brus, L.E. (1984) Electron-electron and electron-hole interactions in small semiconductor crystallites: the size dependence of the lowest excited electronic state. *J.Chem.Phys.* **80(9)** 4403-4409

Brus, L. (1991) Quantum crystallites and nonlinear optics. *Appl.Phys.* A **53** 465-474

Brus, L.E., Szajowski, P.F., Wilson, W.L., Harris, T.D., Schuppler, S. and Chitrin, P.H. (1995) Electronic spectroscopy of Si nanocrystals: relationship to bulk c-Si and porous Si. *J.Am.Ceram.Soc.* **117** 2915-2922

Büscher, P., Schmidt-Ott, A., Wiedensohler, A. (1994) Performance og an Unipolar "Square Wave" Diffusion Charger with Variable *nt*-Produkt. *J. Aerosol Sci,* **25** 651-665

Cai, J. and Sorensen, C.M. (1994) Diffusion of fractal aggregates in the free molecular regime. *Phys. Rev.* E **50** 3397-3400

Camata, R.P., Atwater, H.A., Vahala, K.J. and Flagan, R.C. (1996) Size classification of silicon nanocrystals. *Appl.Phys.Lett.* **68** (22) 3162-3164

Cannon, W.R., Danforth, S.C., Flint, J.C., Haggerty, J.S. and Marra, R.A. (1982) Sinterable ceramic powders from laser-driven reactions. *J.Am.Ceram.Soc.* **65** 324-335

Carey, M.J., Young, A.P, Starr, A., Rao, D. and Berkowitz, A.E. (1992) Giant magnetoresistance in heterogeneous AgCo alloy films. *Appl.Phys.Lett* **61** (24) 2935-2937

Chadda, S., Ward, T.L., Carim, A., Kodas, T.T., Ott, K. and Kroeger, D. (1991) Synthesis of $Ba_2Cu_3O_{7-y}$ and $YBa_2Cu_4O_8$ by aerosol decomposition. *J. Aerosol Sci.* **22 (**5) 601-616

Chen, D.-R., Pui, D.Y.H. and Kaufman, S.L. (1995) Electrospraying of conducting liquids for monodisperse aerosol generation in the 4 nm to 1.8 µm diameter range. *J.Aerosol Sci.* **26** (6) 963-977

Chen, X., Hu, X. and Feng, J. (1995) Nanostructured nickel oxide films and their electrochromic properties. *Nanostruct.Matls.* **6** 309-312

Chen, D.-R., Pui, D.Y.H., Hummes, D., Fissan, H., Quant, F.R. and Sem, G.J. (1998) Design and Evaluation of a Nanometer Aerosol Differential Mobility Analyzer (Nano-DMA). *J. Aerosol Sci*. **29** (5/6) 497-509

Chen, D. and Pui, D.Y.H. (1999) A high efficiency, high throughput unipolar aerosol charger for nanoparticles. *Nanoparticle Res*. **1** 115-126

Chopra, K.L., Major, S. and Pandya, D.K. (1983) Transparent conductors - a status review. *Thin Solid Films* **102** 1-46

Chow, G.-M., Klemens, P.G. and Strutt, P.R. (1989) Nanometer-size fiber composite synthesis by laser-induced reactions. *J.Appl.Phys.* **66** (7) 3304-3308

Colvin, V.L., Schlamp, M.C. and Alivisatos, A.P. (1994) Light-emitting diodes made from cadmium selenide nanocrystals and a semiconducting polymer. *Nature* **370** 354-356

Collins, R. T., Fauchet, F. M. and Tischler, M. A. (1997) *Physics Today* **50** (January), 24

Dahneke, B (1983) “Simple kinetic theory of Brownian diffusion in vapors and aerosols”. In *Theory of Dispersed Multiphase Flow* (Edited by Meyer, R.E.), pp. 97-133. Academic Press, New York

Danek, M., Jensen, K.F., Murray, C.B. and Bawendi, M.G. (1994) Preparation of II-VI quantum dot composites by electrospray organometallic chemical vapor deposition. *J.Crystal Growth* **145** 714-720

De Marco, M., Wang, X.W., Snyder, R.L., Simmins, J., Bayya, S., White, M. and Naughton, M.J. (1993) Mössbauer and magnetization studies of nickel ferrites. *J.Appl.Phys.* **73** (10) 6287-6289

Deppert, K., Maximov, I., Samuelson, L., Hansson, H.-C. and Wiedensohler, A. (1994) Sintered aerosol masks for dry-etched quantum dots. *Appl.Phys.Lett.* **64** (24) 3293-3295

Deppert, K., Bovin, J.-O., Malm, J.-O- and Samuelson, L. (1996) A new method to fabricate size-selected compound semiconductor nanocrystals: aerotaxy. *J.Crystal Growth* **169** 13-19

Deppert,K, Nielsch, K., Magnusson, M.H., Dumpich, G., Kruis, F.E. and Fissan, H. (1998) Feasibility study of nanoparticle synthesis from powders of compounds with incongruent sublimation behavior by the evaporation/condensation method. *Nanostruct. Matls.***10** (4) 565-573

Dieguez, A., Romano-Rodriguez, A., Morante, J.R., Weimar, U., Schweizer-Berberich, M. and Göpel, W. (1996) Morphological analysis of nanocrystalline SnO_2 for gas sensor applications. *Sensors and Actuators B* **31** 1-8

Dixkens, J. and Fissan, H. (1997) Design of a Sampling System for Off-Line Particle Analysis. In “Fine Solid Particles”; Schwerpunktprogramm der DFG (1991-1997), 214-222, Shaker-Verlag GmbH, Aachen, ISBN3-8265-3050-0, ISSN 0945-1021

Dufoux, D.P. and Axelbaum, R.L. (1995) Nanoscale unagglomerated nonoxide particles from a sodium coflow flame. *Combust. Flame* **100** 350-358

Ehbrecht, M., Kohn, B., Huisken, F., Laguna, M.A. and Paillard, V. (1997) Photoluminescence and resonant Raman spectra of silicon films produced by size-selected cluster beam deposition. *Phys. Rev.* B **56** 6958-6964

El-Shall, M.E. and Edelstein, A.S. (1996) Formation of clusters and nanoparticles from a supersaturated vapor and selected properties, pp. 13-54 *in:* „Nanomaterials: synthesis, properties and applications“, ed. by A.S. Edelstein and R.C.Cammarata, Institute of Physics Publishing, Bristol, UK

El-Rahaiby, S.K. and Rao, Y.K. (1982) Kinetics of vaporization of lead sulfide. *Metall. Trans* B **13B** 633-641

Estrada, W., Andersson, A.M. and Granqvist, C.G. (1988) Electrochromic nickel-oxide-based coatings made by reactive dc magnetron sputtering: preparation and optical properties. *J.Appl.Phys.* **64** (7) 3678-3683

Fissan, H., Hummes, D., Stratmann, F., Büscher, P., Neumann, S., Pui, D.Y.H. and Chen, D.R. (1996) Experimental comparison of four Differential Mobility Analyzers for nanometer aerosol measurements. *Aerosol Sci. Technol.* **24** 1-13

Fissan, H., Pöcher, A., Neumann, S., Boulaud, D. and Pourprix, M. (1998) Analytical and empirical transfer functions of a simplidfied Spectromètre de mobilité electrique circulaire (SMEC) for nanoparticles. *J. Aerosol Sci.* **29** 289-293

Friedlander, S.K (1983) *Ann.N.Y.Acad.Sci.*, **40** 354

Friedlander, S.K. (1977) *Smoke, Dust and Haze*, Wiley, New York.

Fröhlich, K., Machajdik, D., Rosova, A., Vavra, I., Weiss, F., Bochu, B. and Senateur, J.P. (1995) Growth of $SrTiO_3$ thin epitaxial films by aerosol MOCVD. *Thin Solid Films* **260** 187-191

Fuchs, N.A. (1964) *The Mechanics of Aerosols*. Pergamon Press, Elmsford, NY.

Fujita, T., Oshima, K., Kuroishi, T. (1976) Temperature dependence of electrical conductivity in films of fine particles. *J.Phys.Soc.Japan* **40** (1) 90-92

Gacoin, T., Boilot, J.P., Gandais, M., Ricolleau, C. and Chamarro, M. (1995) Transparent sol-gel matrices doped with quantum sized PbS particles. *MRS Res.Symp. Proc.* **358** 247-252

Gangopadhyay, S., Hadjipanayis, G.C., Dale, B., Sorensen, C.M., Klabunde, K.J., Papaefthymiou, V. and Kostikas, A. (1992) Magnetic properties of ultrafine iron particles. *Phys.Rev.B* **45** (17) 9778-9787

Gao, H.J., Xue, Z.Q., Wu, Q.D. and Pang, S.J. (1995) Structure and electrical properties of Ag-ultrafine-particle-polymer thin films. *J.Vac.Sci.Technol.B* **13**(3) 1242-1246

Garcia, A.L., C. van den Broek, M. Aertsens and R. Serneels (1987) A Monte Carlo Method of Coagulation. *Physica*, **143A** 535-546

Gautheron, B., Labeau, M., Delabouglise, G. and Schmatz, U. (1993) Undoped and Pd-doped SnO_2 thin films for gas sensors. *Sensors and Actuators B* **15-16** 357-362

Gelbard, F. Tambour, Y. and Seinfeld, J.H. (1980) Sectional Representations for Simulating Aerosol Dynamics. *J. Colloid and Interface Sci.* **76** 541-550

Gelbard, F. and Seinfeld, J.H. (1980) Simulation of Multicomponent Aerosol Dynamics. *J. Colloid and Interface Sci.* **78** 485-501

Girshick, S.L. and Chiu, C.P.(1989) Kinetic nucleation theory: A new expression for the rate of homogeneous nucleation from an indeal supersaturated vapor. *J. Chem.Phys.* **93** 1273-1277

Gmelin, L.)1979) *Gmelin handbook of inorganic chemistry*, ed. by E.H.E. Pietsch, Springer, Berlin

Goldstein, A.N., Echer, C.M. and Alivisatos, A.P. (1992) Melting in semiconductor nanocrystals. *Science* **256** 1425-1427

Göpel, W. and Schierbaum, K.D. (1995) SnO2 sensors: current status and future prospects. *Sensors and Actuators* **26** (1) 71-98

Göpel, W. (1996) Ultimate limits in the miniaturization of chemical sensors. *Sensors and Actuators A* **56** 83-102

Goswami, R., Banerjee, S., Chattopadhyay, K. and Raychaudhuri, A.K. (1993) Superconductivity in rapidly quenched metallic systems with nanoscale structure. *J.Appl.Phys.* **73** (6) 2934-2940

Granqvist, C.G. and Buhrman, R.A. (1976) Ultrafine metal particles. *J.Appl.Phys.* **47** (5) 2200-2219

Grimm, S., Schultz, M., Barth, S. and Müller, R. (1997) Flame pyrolysis - a preparation route for ultrafine pure -Fe_2O_3 powders and the control of their particle size and properties. *J.Mater.Sci.* **32** (1997) 1083-1092

Günther, B. and Kumpmann, A. (1992) Ultrafine oxide powders prepared by inert gas evaporation. *Nanstruct.Matls.* **1** 27-30

Gutsch, A., S.E. Pratsinis and F. Löffler (1995) Agglomerate Structure and Growth Rate by Trajectory Calculations of Monomer-Cluster Collisions. *J. Aerosol Sci.*, **26** 187

Hadjipanayis, G.C., Klabunde, K.J. and Sorensen, C.M. (1996) Magnetic and structural properties of nanoparticles. pp. 375-394 *in:* „Nanomaterials: synthesis, properties and applications“, ed. by A.S. Edelstein and R.C.Cammarata, Institute of Physics Publishing, Bristol, UK

Hahn, H. and Averback, R.S. (1990) The production of nanocrystalline powders by magnetron sputtering. *Appl.Phys.Lett.* **67**(2) 1113-1115

Harrison, M.R., Hall, S.R., Jacobson, D.M. and Dineen, C. (1996) High-current conductors using high-temperature superconductors. *GEC J. of Res.* **13** (3) 146-158

Hayashi, C. (1987) Ultrafine particles. *J.Vac.Sci.Technol. A* **5**(4) 1375-1384

Hayashi, S., Sanda, H., Agata, M. and Yamamoto, K, (1989) Resonant Raman scattering from ZnTe microcrystals: Evidence for quantum size effects. *Phys.Rev.B.* **40** (8) 5544-5547

Herzer, G. (1990) Grain size dependence of coercivity and permeablity in nanocrystalline ferromagnets. *IEEE Trans. Magn.* **26** (5) 1397-1402

Hewitt, G.W. (1957) AIEE Trans. **76** 300

Hide, F., Schwartz, B.J., Diaz-Garcia, M.A. and Heeger; A.J. (1996) Laser emission from solutions and films containing semiconducting polymer and titanium dioxide nanocrystals. *Chem.Phys.Lett.* **256** 424-430

W.C. Hinds (1982) *Aerosol Technology*, p. 44 (John Wiley, New York)

Hodes, G., Albu-Yaron, A., Decker, F. and Motisuke, P. (1987) Three-dimensional quantum-size effect in chemically deposited cadmium selenide films. *Phys.Rev.B* **36** 4215-4221

Hogan, H. (1996) The gigachips are coming. *Industrial Physicist* 7-8

Holtz, R.L., Provenzano, V. and Imam, M.A. (1996) Overview of nanophase metals and alloys for gas sensors, getters, and hydrogen storage. *Nanostruct.Matls.* **7** 259-264

Honig, R.E. and Kramer, D.A. (1969), "Vapor Pressure Data for the Solid and Liquid Elements", report, RCA Laboratories, Princeton NJ

Horvath, J., Birringer, R. and Gleiter, H. (1987) Diffusion in nanocrystalline material. *Sol. State Comm.* **62**(5) 319-322

Hu, W.S., Liu, Z.G., Zheng, J.G., Hu, X.B., Guo, X.L., and Göpel, W. (1997) Preparation of nanocrystalline SnO_2 thin films used in chemisorption sensors by pulsed laser reactive ablation. *J.Mater Sci.Mater.Elec.* **8** 155-158

Huang, Y.K., Menovsky, A.A: and Boer, F.R. de. (1993) Electrical resistivity of nanocrystalline copper. *Nanostruct.Matls.* **2** 505-513

Hull, P.J., Hutchison, J.L., Salata, O.V. and Dobson, P.J. (1997) Synthesis of nanometer-scale silver crystallites via a room-temperature electrostatic spraying process. *Adv.Mater.* **9** (5) 413-417

Hwang, J.-H., Dravid, V.P., Teng, M.H., Host, J.J., Elliott, B.R., Johnson, D.L. and Mason, T.O. (1997) Magnetic properties of graphitically encapsulated nickel nanocrystals. *J.Mater.Res.* **12** (4) 1076-1082

Ishikawa, K., Yoshikawa, K. and Okada, N. (1988) Size effect on the ferroelectric phase transition in $PbTiO_3$ ultrafine particles. *Phys.Rev.B.* **37** (10) 5852-5855

Ito, O., Asai, T., Ogawa, T., Hasegawa, M., Ikegami, A., Endoh, Y., Araya, T., Atoh, K. and Kobayashi, T. (1991) Effect of conduction particle size on LaB_6 thick film reesistor. *Thin Solid Films* **198** 17-27

Iwama, S., Hayakawa, K. and Arizumi, T. (1982) Ultrafine powders of TiN and AlN produced by a reactive gas evaporation technique with electron beam heating. *J.Crystal Growth* **56** 265-269

Jergel, M., Hanic, F., Strbik, V., Liday, J., Plesch, G., Melisek, T. and Kubranova, M. (1992) Thin BSCCO films prepared by deposition from aerosol. *Supercond. Sci. Technol.*, **5** (11) 663-670

Johnston, G.P., Muenchausen, R., Smith, D.M., Fahrenholtz, W. and Foltyn, S. (1992) Reactive laser ablation synthesis of nanosize alumina powder. *J.Am.Ceram.Soc.* **75** (12) 3293-3298

Kaito, C., Fujita, K. and Shiojiri, M. (1976) Growth of smoke particles prepared by evaporation in inert gases. *J.Appl.Phys.* **47** (12) 5161-5166

Kaito, C., Fujita, K. and Shiojiri, M. (1983) Growth of CdTe smoke particles prepared by gas evaporation technique. *J.Crystal Growth* **62** 375-383

Kaito, C., Saito, Y. and Fujita, K. (1987) A new preparation method of ultrafine particles of metallic sulfides. *J.Appl.Phys.* 2 **26** 1973-1975

Kaito, C. and Saito, Y. (1990) Growth of ultrafine particles of II-VI compounds by a new gas evaporation technique. *J.Crystal Growth* **99** 743-746

Kanemitsu, Y., Uto, H., Matsumoto, Y. and Maeda, Y. (1992) On the origin of visible photoluminescence in nanometer-size Ge crystallites. *Appl.Phys.Lett.* **61** 2187-2189

Kanemitsu, Y., Ogawa, T., Shiraishi, K. and Takeda, K. (1993) Visible photoluminescence from oxidized Si nanometer-sized spheres: exciton confinement on a spherical shell. *Phys.Rev.B* **48** (7) 4883-4886

Kanemitsu, Y. (1995) Light emission from porous silicon and related materials. *Phys.Rep.* **263** 1-91

Kang, Y.C., Park, S.B. and Kang, Y.W. (1995) Preparation of high surface area nanophase particles by low pressure spray pyrolysis. *Nanostruct.Matls.* **5** 777-791

Kang, Y.C. and Park, S.B. (1996a) Preparation of nanometre size oxide particles using filter expansion aerosol generator. *J.Mater.Sci.* **31** 2409-2416

Kang, Y.C. and Park, S.B. (1996b) Effect of preparation conditions on the formation of primary ZnO particles in filter expansion aerosol generator. *J.Mater.Sci.*, accepted

Kato, M. (1976) Preparation of ultrafine particles of refractory oxides by gas-evaporation method.*Jap.J. Appl.Phys.* **15**(5) 757-760

Kagawa, M., Suzuki, M., Mizoguchi, Y., Hirai, T. and Syono, Y. (1993) Gas-phase synthesis of ultrafine particles and thin films of Y-Al-O by the spray-ICP technique. *J.Aerosol Sci.* **24** 349-355

Katzer, M., Weber, A. P., Schmidt, E. and Kasper, G. (1998) Collision Frequences of Fractal-like Aerosol Particles. *Advanced Technologies for Particle Processing*, **1**, pp. 93-98

Kawaguchi, T. and Miyazima, S. (1993) Visible photoluminescence from Si microcrystalline particles. *Jpn.J.Appl.Phys.* **32** L215-L217

Kear, B.H. and Strutt, P.R. (1995) Chemical processing and applications for nanostructured materials. *Nanostruct.Matls.* **6** 227-236

Kim, K. and Rye, C.K. (1994) Generation of charged liquid cluster beam of liquid-mix precursors and applications to nanostructured materials. *Nanostruct.Matls* **4** 597-602

Kizaki, Y., Osada, H. and Aoki, H. (1993) Ultrafine particle beam deposition III: Applications to thermoelectric materials. *Jpn. J. Appl. Phys.* **32** 5778-5790.

Klabunde, K.J. (1994) Free atoms ,clusters, and nanoscale particles. Academic Press, San Diego.

Knutson, E.O. and Whitby, K.T. (1975) Aerosol classification by electric mobility: Apparatus, theory, and applications. *J. Aerosol Sci*. **6** 443-451

Koch, W. and Friedlander, S.K. (1990) The effect of particle coalescence on the surface area of a coagulating aerosol. *J. Colloid Interface Sci*. **140** 419-427

Koch, F. and Petrova-Koch, V. (1996) Light from Si-nanoparticle systems - a comprehensive view. *J. of Non-Cryst. Solids* **198-200** 840-846.

Kodas, T.T., Engler, E.M., Lee, V.Y., Jacowitz, R., Baum, T.H., Roche, K., Parkin, S.S.P., Young, W.S., Hughes, S., Kleder, J. and Auser, W. (1988) Aerosol flow reactor production of fine $Y_1Ba_2Cu_3O_7$ powder: Fabrication of superconducting ceramics. *Appl. Phys. Lett.* **52** (19) 1622-1624

Kodas, T.T., Engler, E.M. and Lee, V.Y. (1989) Generation of thick $Ba_2YCU_3O_7$ films by aerosol deposition. *Appl.Phys.Lett.* **54** (19) 1923-1925

Kohl, D. (1989) Surface processes in the detection of reducing gases with SnO_2-based devices. *Sensors and Actuators* **18** 71-113

Koyama, T., Ohtsuka, S., Nagata, H. and Tanaka, S. (1992) Fabrication of microcrystallites of II-VI compound semiconductors by laser ablation method, *J.Crystal Growth* **117** 156-160

Kreibig, U. (1974) Electronic properties of small silver particles: the optical constants and their temperature dependence. *J.Phys.F: Metal Phys.* **4** 999-1014

Kruis, F.E., Scarlett, B., Bauer, R.A. and Schoonman, J. (1992) Thermodynamic Calculations on the Chemical Vapor Deposition of Silicon Nitride and Silicon from Silane and Chlorinated Silanes. *J. Am. Ceram. Soc.* **75**(3) 619-628

Kruis, F.E., Kusters, K.A., Pratsinis, S.E. and Scarlett, B. (1993) A Simple Model for the Evolution of the Characteristics of Aggregate Particles undergoing Coagulation and Sintering. *Aerosol Sci. Technol.* **19** 514-526

Kruis, F.E., Goossens, A. and Fissan, H. (1996) Synthesis of Semiconducting Nanoparticles. *J. Aerosol Sci.* **27** S1 165-166

Kruis, F.E., Otten, F., Jordan F., and Fissan, H (1998a) A new efficient unipolar charger for nanoparticles. *J. Aerosol Sci.* **29** 1021-1022

Kruis, F.E., Oostra, W., Marijnissen, J., Schoonman, J., Scarlett, B. (1998b) Particle formation paths in the synthesis of silicon nitride powder in a laser-heated aerosol reactor. *J. Eur. Ceram. Soc.* **18** 1025-1036

Kruis, F.E., Nielsch, K., Fissan, H., Rellinghaus, B. and Wassermann, E.F. (1998c) Preparation of size-classified PbS nanoparticles in the gas phase. *Appl.Phys.Lett.* **73** 4 547-549

Kruis, F.E., Fissan, H. and Peled, A. (1998d) Synthesis of nanoparticles in the gas phase for electronic, optical and magnetic applications - A review. *J.Aerosol Sci* **29** 5/6 511-535

Kruis, F.E. Maisels, A. and Fissan, H. (2000a) A Direct-Simulation Monte Carlo Method for Particle Coagulation and Aggregation. AIChE J. **46**, 1735-1742

Kruis, F.E., Fissan, H. and Rellinghaus, B. (2000b) Sintering and Evaporation Characteristics of Gas-phase Synthesis of Size-selected PbS Nanoparticles. *Mat.Sci.Eng.* **B 69-70** 329-334

Kruis, F.E. and Fissan, H. (2001) Nanoparticle charging using a twin Hewitt charger. *J. Nanoparticle Res.* **3** 39-50

Kundu, T.K. and Chakravorty, D. (1995) Nanocomposite films of lead zirconate titanate and metallic nickel by sol-gel route. *Appl.Phys.Lett.* **66** (26) 3576-3578

Kundu, T.K. and Chakravorty, D. (1996) Electrical properties of sol-gel derived films containing composites of glass-ceramics and nanocrystalline silver. *J.Mater.Res.* **11**(1) 200-203

Labeau, M., Gautheron, B., Cellier, F., Vallet-Regi, M., Garcia, E. and Gonzalez Calbet, J.M. (1993) Pt nanoparticles dispersed on SnO_2 thin films: a microstructural study. *J.Sol. St.Chem* **102** 434-439

Labeau, M., Gas'kov, A.M., Gautheron, B. and Senateur, J.P. (1994) Synthesis of Pd-doped SnO_2 films on silicon and interaction with ethnol and CO. *Thin Solid Films* **248** 6-11

Landgrebe, J.D., and S.E. Pratsinis (1990) A Discrete-sectional Model for Particulate Production by Gas-phase Chemical Reaction and Aerosol Coagulation in the Free-molecular Regime. *J. Colloid Interface Sci.,* **139** 63-86

Lee, D.H., Vuong, K.D., Williams, J.A.A., Fagan, J., Condrate, R.A. and Wang, X.W. (1996) RF aerosol plasma fabrication of indium tin oxide and tin oxide thin films. *J.Mater.Res.* **11** (4) 895-903

Leong, K.H. (1987) Morphological control of particles generated from the evaporation of solution droplets: theoretical considerations. *J.Aerosol Sci.* **18** (5) 511-524

Li, C. and Hua, B. (1997) Preparation of nanocrystalline SnO_2 thin film coated Al_2O_3 ultrafine particles by fluidized chemical vapor deposition. *Thin Solid Films*, **310** 238-240

Li,Y., Gong,W., Hadjipanayis,G.C., Sorensen,C.M., Klabunde,K.J., Papaefthymiou,V., Kostikas,A., Simopolous,A. (1994) Size effects on the magnetic properties of fine Fe-Cr particles. *J. Magn.Magn.Mater.* **130** 261-266

Liffman, K (1992) A Direct Simulation Monte Carlo Method for Cluster Coagulation. *J. Comp. Phys.*, **100** 116-127

Linderoth, S. and Moerup, S. (1990) Ultrasmall iron particles prepared by use of sodium amalgam. *J.Appl. Phys.* **67** (9) 4496-4498

Litster, J.D., D.J. Smit and M.J. Hounslow (1995) Adjustable Discretized Population Balance for Growth and Aggregation. *AIChE J.* **41** 591-603

Littau, K.A., Szajowski, P.J., Muller, A.J., Kortan, A.R. and Brus, L.E. (1993) A luminiscent silicon nanocrystal colloid via a high temperature aerosol reaction. *J.Phys.Chem.* **97** 1224-1230

Lopez-Otero, A. (1978) Hot wall epitaxy. *Thin Solid Films* **49** 1-57

Lushnikov, A.A. (1976) Evolution of Coagulating Systems. III. Coagulating Mixtures, *J. of Colloid Interface Sci.*, **54** 94-101

Lüth, H. (1995) Nanostructures and semiconductor electronics. *Phys.Stat.Sol.* B **192** 287-299

Lyons, S.W., Wang, L.M. and Kodas, T.T. (1992) Nanophase oxide formation by intraparticle reaction. *Nanostruct.Matls.* **1** 283-291

Machol, J.L., Wise, F.W., Patel, R., and Tanner, D.B. (1994) Optical studies of IV-VI quantum dots. *Physica* A **207** 427-34

Maisels, F.E. Kruis, H. Fissan, B. Rellinghaus, H. Zähres (2000) Synthesis of tailored composite nanoparticles in the gas phase. Appl.Phys.Lett. **77**, 4431-4433

Majima, T., Miyahara, T., Haneda, K., Ishii, T. and Takami, M. (1994) Preparation of Iron ultrafine particles by the dielectric breaksown of $Fe(CO)_5$ using a transversely excited atmospheric CO_2 laser and their characteristics. *Jpn.J.Appl.Phys.* **33** 4759-4763

Matsoukas, T. and Friedlander, S.K. (1991) Dynamics of Aerosol Agglomerate Formation. *J. of Colloid Interface Sci.* **146** 495-518

Maximov, I., Gustfsson, A., Hansson, H.-C., Samuelson, L., Seifert, W. and Wiedensohler, A. (1993) Fabrication of quantum dot structures using aerosol deposition and plasma etching techniques. *J.Vac.Sci.Technol. A* **11** (4) 748-753

Mezey, L.Z. and Giber (1982) *Jpn.J.Appl.Phys.* **21** 1569

Mimura, H., Matsumoto, T. and Kanemitsu, Y. (1994) Blue electroluminescence from porous silicon carbide *Appl.Phys.Lett.* **65** 3350-3352

Mizuguchi, Y., Kagawa, M., Suzuki, M., Syono, Y. and Hirai, T. (1994) Synthesis of ultrafine particles and thin films of $BaFe_{12}O_{19}$ by the spray-ICP technique. *Nanostruct.Matls.* **4** 591-596

Moulson, A.J. and Herbert, J.M. (1990) Electroceramics - Materials, properties, applications. Chapman and Hall, London, UK.

Nenadovic, M.T., Comor, M.I., Vasic, V., Micic, O.I. (1990) Transient bleaching of small PbS colloids: Influence of surface properties. *J. Phys.Chem.* **94** 6390-6396

Oda, M., Fuchita, E., Tsuneizumi, M., Kashu, S. and Hayashi, C. (1992) Gas deposition films of ultra fine particles. *Nanostruct.Matls.* **1** 203-206

Ogawa, H., Abe, A., Nishikawa, M. and Hayakawa, S. (1981a) Preparation of tin oxide films from ultrafine particles. *J.Electrochem.Soc.* **128** (3) 685-689

Ogawa, H., Abe, A., Nishikawa, M. and Hayakawa, S. (1981b) Electrical properties of tin oxide ultrafine particle films. *J.Electrochem.Soc.* **128** (9) 2020-2025

Ogawa, H., Nishikawa, M. and Abe, A. (1982) Hall measurement studies and an electrical conduction model of tin oxide ultrafine particle films. *J.Appl.Phys.* **53**(6) 4448-4455

Ohtsuka, S., Koyama, T., Tsunetomo, K., Nagata, H. and Tanaka, S. (1992) Nonlinear optical properties of CdTe microcrystallites doped glasses fabricated by laser evaporation method. *Appl.Phys.Lett.* **61** (25) 2953-2954

Okuyama, K., Shimada, M., Adachi, M. and Tohge, N. (1993) Preparation of ultrafine superconductive Bi-Ca-Sr-Cu-O particles by metalorganic chemical vapor deposition. *J. Aerosol Sci.* **24** (3) 357-366

Oron, A. and Seinfeld, J.H. (1989) The dynamic behavior of charged aerosols. Part II: Numerical solution by the sectional method. *J. Colloid Interface Sci.* **133** 66-80

Otto, E., Gutsch, A. and Fissan, H. (1996) Gas Cleaning Due to Enhanced Bipolar Coagulation. *Proc. 3d Int. Symposium and Exhibition on Gas Cleaning at High Temperatures*, Karlsruhe (edited by Eberhard Schmidt, Peter Gäng, Torsten Pilz and Achim Dittler), pp. 48-59.

Otto, E. (1997) *Modellierung Brownscher und elektrischer Koagulation submikroner Partikel.* PhD Thesis, Gerhard-Mercator-Universität GH Duisburg. Shaker Verlag, Aachen.

Otto, E. and Fissan, H. (1999) Brownian Coagulation of Submicron Particles. *Adv. Powder Technol.* **10** 1-20

Panda, S. and Pratsinis, S. (1995) *J.Nanostruct.Mater.* **5**, 755

Parker, J.C. (1996) Commercialization oppurtunities for nanophase ceramics : a small-company perspective, pp. 573-581 *in:* „Nanomaterials: synthesis, properties and applications“, ed. by A.S. Edelstein and R.C.Cammarata, Institute of Physics Publishing, Bristol, UK

Pearson, W.B. (1967) *A handbook of lattice spacings and structures of metals and alloys.* 2nd edition, Vol. 2, Part 1, p. 353 (Pergamon Press, Oxford)

Pearson, H.J. (1984) Monte Carlo Simulations of Coagulation in Discrete Particle-size Distributions. Part 1. Brownian Motion and fluid shearing. *J. Fluid Mech.* **143** 367-385
Pehnt, M., Schulz, D.L., Curtis, C.J., Jones, K.M. and Ginley, D.S. (1995) Nanoparticle precursor route to low-temperature spray deposition of CdTe thin films. *Appl.Phys.Lett.* **67** (15) 2176-2178

Peled, A., Friesem, A.A. and Shapira, Y. (eds.) (1996) Proceedings of the Second International Conference on Photo-excited Processes and Applications. *Appl.Surf.Sci.* **106** pp.1-540

Peled, A. (1997) Review: State of the art in liquid phase photodeposition processes and applications(LPPD).*Lasers in Engineering.***6** 41-72

Peyghambarian, N., Hanamura, E., Koch, S.W., Masumoto, Y. and Wright, E.M. (1996) Optical characterization and applications of semiconductor quantum dots, pp. 395-436 *in:* „Nanomaterials: synthesis, properties and applications“, ed. by A.S. Edelstein and R.C.Cammarata, Institute of Physics Publishing, Bristol, UK

Piskunov, V.N., Golubev, A.I., Goncharov, E.A. and Izmailova, N.A. (1997) Kinetic Modeling of Composite Particles Coagulation. *J. Aerosol Sci*. **28** 1215-1231

Powers, D.E., Hansen, S.G., Guesic, M.E., Pulu, A.C., Hopkins, J.B., Dietz, J.B., Duncan, M.A., Langridge-Smith, P.R.R. and Smlley, R.E. (1982) Supersonic metal cluster beams: laser photoionization studies of Cu_2. *J.Phys.Chem.* **86** 2556-2560

Pratsinis, S.E. (1988) Simultaneous Nucleation, Condensation and Coagulation in Aerosol Reactors. *J. Colloid Interface Sci.*, **124** 416

Prokes, S.M. (1996) Porous silicon nanostructures, pp. 439-457 *in:* „Nanomaterials: synthesis, properties and applications“, ed. by A.S. Edelstein and R.C.Cammarata, Institute of Physics Publishing, Bristol, UK

Prost, W., Kruis, F.E., Otten, F., Nielsch, K., Rellinghaus, B., Auer, U., Peled, A., Wassermann, E.F., Fissan, H. and Tegude, F.J. (1998) Monodisperse aerosol particle deposition: Prospects for nanoelectronics, *J. Microelect. Eng*. **41/42** 535-538

Qin, X.Y., Wu, B.M., Du, Y.L., Zhang, L.D. and Tang, H.X. (1996) An experimental study of thermal diffusivity of nanocrystalline Ag. *Nanostruct.Matls.* **7** 383-391

Rao, N., Micheel, B., Hansen, D., Fandrey, C., Bench, M., Girshick, S., Heberlein, J. and McMurry, P. (1995a) Nanoparticle formation using a plasma expansion process. *Plasma Chem.Plasma Process.* **15** (4) 581-606

Rao, N., Micheel, B., Hansen, D., Fandrey, C., Bench, M., Girshick, S., Heberlein, J. and McMurry, P. (1995b) Synthesis of nanophase silicon, carbon, and silicon carbide powders using a plasma expansion process. *J.Mater.Res.* **10** (8) 2073-2084

Reed, T.B. (1961) Induction-coupled plasma torch. *J.Appl.Phys.* **32** (5) 821-824

Rubinstein, R.Y. (1981) *Simulation and the Monte Carlo Method.* John Wiley and Sons, New York, p. 91

Rulison, A.J. and Flagan, R.C. (1994) Synthesis of yttria powders by electrospray pyrolysis. *J.Am.Ceram.Soc.* **77** 3244-3250

Salata, O.V., Dobson, P.J., Hull, P.J. and Hutchison, J.L. (1994a) Fabrication of PbS nanoparticles embedded in a polymer film by gas-aerosol reactive electrostatic deposition technique. *Adv.Mater.* **6**(10) 772-775

Salata, O.V., Dobson, P.J., Hull, P.J. and Hutchison, J.L. (1994b) Fabrication of CdS nanoparticles embedded in a polymer film by gas-aerosol reactive electrostatic deposition technique. *Thin Solid Films* **251** 1-3

Salazar, K.V., Ott, K.C., Dye, R.C., Hubbard, K.M., Peterson, E.J. and Coulter, J.Y. (1992) Aerosol assisted chemical vapor deposition of superconducting $YBa_2Cu_3O_{7-x}$. *Physica* C **198** 303-308

Sanjines, R., Demarne, V. and Levy, F. (1990) Hall effect measurements in SnOx film sensors exposed to reducing and oxidizing gases. *Thin Solid Films* **193** 935-942

Sarkas, H.W., Arnold, S.T., Hendricks, J.H., Kidder, L.H., Jones, C.A. and Bowen, K.H. (1993) An investigation of catalytic activity in mixed metal oxide nanophase materials. *Z.Phys.D* **26** 46-50

Saunders, W.A., Sercal, P.C., Atwater, H.A., Vahala, K.J. and Flagan, R.C. (1992) Vapor phase synthesis of crystalline nanometer-scale GaAs clusters. *Appl.Phys.Lett.* **60** (8) 950-952

Saunders, W.A., Sercel, P.C., Lee, R.B., Atwater, H.A., Vahala, K.J., Flagan, R.C. and Escorcia-Aparcio, E.J. (1993a) Synthesis of luminescent silicon clusters by spark ablation. *Appl.Phys.Lett.* **63** 1549-1551

Saunders, W.A., Sercel, P.C., Flagan, R.C., Atwater, H.A. and Vahala, K.J. (1993b) The role of Ga-droplet formation in nanometer-scale GaAs cluster synthesis from organometallic precursors. *Z.Phys.D.* **26** 219-221

Scheibel, H.G. and Porstendörfer, J. (1983) Generation of monodisperse Ag- and NaCl-aerosol with particle diameters between 2 and 300 nm. *J.Aerosol Sci.* **14** 113-126

Schmatz, U., Delabouglise, G., Labeau, M. and Garden, J. (1994) Electrical and microstructural studies of SnO_2 ceramics obtained by tin sulfate pyrolysis. *J.Electrochem.Soc.* **141** (11) 3254-3258

A. Schmidt-Ott, J. (1988) *J. Aerosol Sci.* **19** 553

Seraphim, A.A., Ngiam, S.-T. and Kolenbrander, K.D. (1996) Surface control of luminescence in silicon nanoparticles. *J.Appl.Phys.* **80** (11) 6429-6433

Sercel, P.C., Saunders, W.A., Atwater, H.A., Vahala, K.J. and Flagan, R.C. (1992) Nanometer-scale GaAs clusters from organometallic precursors. *Appl.Phys.Lett.* **61** (6) 696-698

Service, R.F. (1996) Small clusters hit the big time. *Science* **271** 920-922

Seto, T., Shimade, M. and Okuyama, K. (1995) Evaluation of sintering of nanometer-sized titania using aerosol method. *Aerosol Sci. Technol***. 23** 183-200

Seto ,T., Nakamoto, T., Okuyama, K., Adachi, A., Kuga, Y. and Takeuchi, K. (1996) Size distribution measurements of nanometer-sized aerosol particles using DMA under low-pressure conditions. *J. Aerosol Sci.* **28** 193-206

Shah, B.H., D. Ramkrishna and J.D. Borwanker (1977) Simulation of Particulate Systems Using the Concept of the Interval of Quiescence. *AIChE J* **23** 897-904

Shi, J., Gider, S., Babcock, K. and Awschalom, D.D. (1996) Magnetic clusters in molecular beams, metals, and semiconductors. *Science*, **271** 937-941

Siegel, R.W. (1994) Nanophase materials: Synthesis, structure, and properties. Pp. 65-105, Vol. 26 in „Series in material sciences“, Springer-Verlag, Berlin. Ed. by F.E.Fujita.

Smoluchowski, M.V. (1917) Versuch zur Mathematischen Theorie der Koagulationskinetik Kolloider Lösungen. *Z. Phys. Chem.* **92** 129-168

Spouge, J.L. (1983) Solutions and critical times for the polydisperse coagulation equation when $a(x, y) = A + B(x + y) + Cxy$. *J. Phys. A: Math. Gen.* **16** 3127-3130

Stratmann, F., Wiedensohler, A., Maximov, I., Samuelson, L., Hansson, H.-C., Fissan, H. (1993) Deposition of ultrafine particles on semiconductors for use as dry etching masks: Numerical calculation and experimental verification. *J.Aerosol Sci.* **24** (5) 687-690

Takagi, H., Ogawa, H., Yamazaki, Y., Ishizaki, A. and Nakagiri, T. (1990) Quantum size effects on photoluminescence in ultrafine Si particles. *Appl.Phys.Lett.* **56** 2379-2380

Takao, Y., Awano, M., Kuwahara, Y. and Murase, Y. (1996) Preparation of oxide superconductive composite by an electrostatic mixing process. *Sensors and Actuators* B **31 (**1-2) 131-133

Tamir, S. and Berger, S. (1995) Laser induced deposition of nanocrystalline Si with preferred crystallographic orientation. *Appl.Surf.Sci.* **86** 514-520

Tang, Z.X., Nafis, S., Sorensen, C.M., Hadjipanayis, G.C. and Klabunde, K.J. (1989) Magnetic properties of aerosol synthesized barium ferrite particles. *IEEE Trans. Magn.* **25** (5) 4236-4238

Tasaki, A., Tomiyama, S., Iida, S., Wada, N. and Uyeda, R. (1965) Magnetic properties of ferromagnetic metal fine particles prepared by evaporation in argon gas. *Jap.J.Appl.Phys.* **4** (10) 707-711

Thielsch, R., Böhme, T., Reiche, R., Schläfer, D., Bauer, H. -D. and Böttcher, H. (1998) Quantum-size effects of PbS nanocrystallites in evaporated composite films. *Nanostr. Mater.* **10** 131-149

Tolbert, S.H. and Alivisatos, A.P. (1995) High-pressure structural transformations in semiconductor nanocrystals. *Ann.Rev.Phys.Chem.* **46** 595-625

Tourtin, F., Daviero, S., Ibanez, A., Haidoux, A., Avinens, C., Philippot, E. (1995) Low temperature deposition of gallium phosphate amorphous dielectric thin films by aerosol CVD, *J. of Non-Cryst. Solids*, **187** 435-442.

Turner, J.R., Kodas, T.T. and Friedlander, S.K. (1988) Monodisperse particle production by vapor condensation in nozzles. *J.Chem.Phys.* **88** (1) 457-465

Vemury, S., K. Kusters and S.E. Pratsinis (1994) Time-Lag for Attainment of the Self-preserving Particle Size Distribution by Coagulation. *J. Colloid Interface Sci.* **165** 53-59

Vemury, S., Pratsinis, S.E. and Kibbey, L. (1997) Electrically controlled flame synthesis of nanphase TiO_2, SiO_2 and SnO_2 powders. *J.Mater.Res.* **12** 1031-1042

Vemury, S., C. Janzen, C. and S.E. Pratsinis (1997) Coagulation of Symmetric and Asymmetric Bipolar Aerosols. *J. Aerosol Sci.* **28** 599-609

Venkatesan, T. and Green, S. (1996) Pulsed-laser deposition: Thin films in a flash. *Industrial Physicist* **2** (3) 22-24

Vezzoli, G.C., Chen, M.F. and Caslavsky, J. (1994) New high dielectric constant materials: micro/nanocomposites of suspended Au clusters in SiO_2/SiO_2-Al_2O_3-Li_2O gels and relevant theory for high capacitance applications. *Nanostruct.Matls.* **4** 985-1009

Viswanath, R.N., Ramasamy, S., Ramamoorthy, R., Jayavel, P. and Nagarajan, T. (1995) Preparation and characterization of nanocrystalline ZnO based materials for varistor applications. *Nanostruct.Matls.* **6** 993-996

Volkening, F.A., Naidoo, M.N., Candela, G.A., Holtz, R.L. and Provenzano, V. (1995) Characterization of nanocrystalline palladium for solid state gas sensor applications. *Nanostruct.Matls.* **5** (3) 373-382

Vollath, D., Szabo, D.V., Taylor, R.D., Willis, J.O. and Sickafus, K.E. (1995) Synthesis and properties of nanocrystalline superparamagnetic γ-Fe_2O_3. *Nanostruct.Matls.* **6** (1995) 941-944

Vollath, D. and Sickafus, K.E. (1992) Synthesis of nanosized ceramic oxide powders by microwave plasma reactions. *Nanostruct.Matls* **1** 427-437

Wang, Y., Suna, A., Mahler, W. and Kasowski, R. (1987) PbS in polymers. From molecules to bulk solids. *J. Chem. Phys*. **87** 7315-7322

Wang, J and Xiao, G. (1994) Transition-metal granular solids: Microstructure, magnetic properties, and giant magnetoresistance. *Phys.Rev.B* **49** 3982-3996

Wang, X.W., Zhong, H.H. and Snyder, R.L. (1990) RF plasma aerosol deposition of superconductive $Y_1Ba_2Cu_3O_{7-d}$ films at atmospheric pressure. *Appl. Phys. Lett.* **57**(15) 1581-1583

Wautelet, M. (1991) Estimation of the variation of the melting temperature with the size of small particles, on the basis of a surface-phonon instability model. *J.Phys.D: Appl.Phys.* **24** 343-346

Weisbuch, C. and Vinter, B. (1991) Quantum semiconductor structures: fundamentals and applications. Acedemic Press, San Diego, USA.

Weissmüller, J. (1996) Characterization by scattering techniques and EXAFS. pp. 219-276 *in:* „Nanomaterials: synthesis, properties and applications“, ed. by A.S. Edelstein and R.C.Cammarata, Institute of Physics Publishing, Bristol, UK

Weller, H. (1993) Colloidal semiconducting Q-particles: Chemistry in the transition region between solid state and molecules. *Angew.Chem.Int.Ed.Engl.* **32** 41-53

Werwa, E., Seraphin, A.A., Chiu, L.A., Zhou, C. and Kolenbrander, K.D. (1994) Synthesis and processing of silicon nanocrystallites using a pulsed laser ablation supersonic expansion method. *Appl.Phys.Lett.* **64** (14) 1821-1823

Wiedensohler, A., Büscher, P., Hansson, H.-C., Martinsson, B.G., Stratmann, F. , Ferron, G. and Busch, B. (1994) *J. Aerosol Sci.* **25** 639

Wiedensohler, A. (1988) An Approximation of the Bipolar Charge Distribution for Particles in Submicron Size Range. *J. Aerosol Sci.* **19** 387-394

Wiedensohler, A., Hansson, H.-C., Maximov, I. and Samuelson, L. (1992) Nanometer patterning of InP using aerosol and plasma etching techniques. *Appl.Phys.Lett.* **61** (7) 837-839

Wilson, W.L., Szajowski, P.F. and Brus, L.E. (1993) Quantum confinement in size-selected, surface-oxidized silicon nanocrystals. *Science* **262** 1242-1244

Woodruff, D.W. and Redwing, J.M. (1991) Chemical vapor deposition of fine-grained equiaxed tungsten films. *Surf.Coat.Technol.* **49** 215-220

Xiao, G. and Chien, C.L. (1987) Giant magnetic coercivity and percolation effects in granular Fe-(SiO_2) solids. *Appl.Phys.Lett.* **51** (16) 1280-1282

Xiong, Y. and S.E. Pratsinis (1993) Formation of Agglomerate Particles by Coagulation and Sintering: I. A Two-Dimensional Solution to the Population Balance Equation. *J. Aerosol Sci.* **24** 283-292

Xu, C., Tamaki, J., Miura, N. and Yamazoe, N. (1991) Grain size effects on gas sensitivity of porous SnO2-based elements. *Sensors and Actuators* B **3** 147-155

Xu, C.; Hampden-Smith, M.J.; Kodas, T.T. (1994) Aerosol-assisted chemical vapor deposition (AACVD) of silver, palladium and metal alloy ($Ag_{1-x}Pd_x$, $Ag_{1-x}Cu_x$ and $Pd_{1-x}Cu_x$) films. *Adv. Mater* **6** (10) 746-748

Yamada, I., Usui, H. and Takagi, T. (1987) Formation mechanism of large clusters from vaporized solid material. *J.Phys.Chem.* **91** 2463-2468

Yamamoto, T. and Mazumder, J. (1996) Synthesis of nanocrystalline $NbAl_3$ by laser ablation technique. *Nanostruct.Matls.* **7** 305-312

Yamauchi, K. and Yoshizawa, Y. (1995) Recent development of nanocrystalline soft magnetic alloys. *Nanostruct.Matls.* **6** 247-254

Yoffe, A.D. (1993) Low-dimensional systems: quantum size effects and electronic properties of semiconductor microcrystallites (zero-dimensional systems) and some quasi-two-dimensional systems. *Adv.Phys.* **42** (2) 173-266

Yoshizawa, Y., Oguma, S. and Yamauchi, K. (1988) New Fe-based soft magnetic alloys composed of ultrafine grain structure. *J.Appl.Phys.* **64** (10) 6044-6046

Young, R.M. and Pfender, E. (1985) Generation and behavior of fine particles in thermal plasmas - A review. *Plasma Chem.Plasma Process.* **5** (1) 1-37

Yu, B., Zhu, C. and Gan, F. (1997) Exciton spectra of SnO_2 nanocrystals with surficial dipole layer. *Opt.Mater.* **7** 15-20

Zachariah, M.R., Aquino, M.I., Shull, R.D. and Steel, E.B. (1995) Formation of superparamagnetic nanocomposites from vapor phase condensation in a flame. *Nanostruct.Matls.* **5** 383-392

Zhang, S.C., Messing, G.L. and Huebner, W. (1991) $YBa_2Cu_3O_{7-d}$ superconductor powder synthesis by spray pyrolysis of organic acid solutions. *J.Aerosol Sci.***22**(5) 585-599

Zhao, X.K. and McCormick, L.D. (1992) Oriented crystal particles of semiconductor PbS on Langmuir monolayer surfaces. *Appl.Phys.Lett* **61** 849-851

Zhao, D. and Pan, X. (1994) Investigation of optical and electrical properties of ZnO ultrafine particle films prepared by direct current gas discharge activated reactive method. *J.Vac.Sci.Technol. B* **12**(5) 2880-2883

Zhu, Y., Lu, H., Lu, Y. and Pan, X. (1993) Characterization of SnO_2 films deposited by d.c. gas discharge activating reaction evaporation onto amorphous and crystalline subtrates. *Thin Solid Films* **224** 82-86